The Design and Synthesis of Metal-Organic Nanosheets for Biosensing Applications

---

Amelia Claire Wood

190184977

A thesis submitted to the University of Sheffield in partial fulfilment of the requirements for the Degree of Doctor of Philosophy

June 2023

The University of Sheffield

Faculty of Science

Department of Chemistry

Abstract

Biosensors are currently utilised in a variety of biomedical applications from disease diagnostics to drug discovery with the aim to improve quality of life. Current trends in research are focused on developing synthetic biointerfaces that mimic the standard of biomolecular recognition achieved by naturally occurring biomolecules. Two-dimensional metal-organic nanosheets (MONs) are suitable candidates for biosensing applications due to their high surface area to volume ratios which results in a large number of accessible binding sites. In this thesis, a library of water stable MONs was developed and explored as potential biosensor components through the interrogation of their interaction with different peptide sequences. Simple pre- and post-synthetic functionalisation of the nanosheets was used to influence surface properties with the long term aim of being able to selectively target the binding of biomedically important analytes.

In **Chapter 2**, a series of layered isoreticular zeolitic imidazolate frameworks (ZIFs) were synthesised based on ZIF-7 ($Zn_2(bim)_4$) and ZIF-9 ($Co_2(bim)_4$). Differing benzimidazole derivatives (bearing -Br, -NH_2 or -CH_3 side groups) were used to pre-synthetically incorporate different surface functionality. Six different systems were synthesised with varying degrees of functionalisation (10-100 %) and in some cases a mixed-linker approach resulted in multivariate ZIFs. In all cases ultrathin MONs with large aspect ratios were accessed via ultrasonic liquid-assisted exfoliation. Surface property analysis demonstrated that the zeta potential and hydrophobic character of the MONs could be tuned depending on the linker component used.

The ability of MONs to selectively bind specific peptide sequences was investigated in **Chapter 3**. A high-throughput screening of 1 x 10^{13} combinations of seven residue peptides against three different MON systems was carried out using the biopanning technique, phage display. This work demonstrated that different MON surfaces had affinity for different sequences of amino acids and for all systems only one consensus high affinity binding peptide was identified (YNYRNLL – ZIF-7, NNWWAPA - ZIF-7-NH_2 and FTVRDLS – Hf-BTB-NH_2). A Hf-BTB-NH_2 coated QCM-sensor acted as proof of concept where phage displaying selective peptides showed a 5-fold increase in selectivity over that of generic peptide sequences.

Post-synthetic functionalisation (PSF) was explored in **Chapters 4** and **5** where covalent attachment and carboxylate ligand exchange were investigated respectively. The formation of covalent bonds between the amino functionalised ZIF systems and amino acids in **Chapter 4** demonstrated irregular functionalisation. The specific reaction conditions had to be adapted for each residue, with optimised conditions obtained for valine only. Maleic anhydride was also reacted with the ZIF-NH_2 systems to introduce an alternative carboxylate functional group that resulted in an increase in hydrophobic character and reduction in zeta potential of the MON surface. A post-synthetic ligand exchange approach was adopted for the incorporation of amino acids to Hf-BTB-NH_2 MONs in **chapter 5**. This facilitated the introduction of various side chain chemistries onto the ultrathin MONs resulting in the modification of surface hydrophobicity and charge.

Overall, this thesis demonstrates that MONs are promising surfaces for selectively binding specific peptide sequences with enormous potential for further tuning through pre- and post-synthetic approaches. Through the incorporation of complimentary functionality onto MON surfaces, we anticipate progress in the targeting of biomedically relevant peptides.

Acknowledgements

Firstly, I would like to thank my supervisor **Dr Jona Foster** for being so tirelessly dedicated to supporting me throughout my PhD. Without your kindness and guidance this project would not have been possible. You have encouraged me to pursue interests outside of my research and pushed me to achieve things that I did not think were possible. Thank you for everything. I would also like to extend my gratitude to **Dr Sarah Staniland** for encouraging me to apply for this PhD. Without you I would not be where I am today. Thank you for creating this opportunity.

Thank you both to **Dr Barbara Ciani** and **Dr Darren Bradshaw** for taking on the role of my examiners. You have both shown me great kindness during my research program and it has not gone unnoticed.

To the Foster group I joined initially, I couldn't have asked for a greater group of individuals to guide me. I thank you all for your patience and nurturing. **Dr Dave Ashworth**, **Dr Josh Nicks**, **Dr Kezia Sasitharan**, **Dr Charlotte Kiker**, **Dr Freya Cleasby** and **Dr Mike Harris** thank you for imparting your excellent wisdom in both science and work-life balance. Your support has been invaluable, and you continue to inspire me. A particular thanks to **Dr Josh Nicks** for taking me under his wing and believing in me right from the off. **Dr Mike Harris,** you very kindly offered precious insights throughout my research and writing process. An extra special thanks to **Dr Freya Cleasby,** I am eternally grateful for your friendship and guidance. I hope one day to be a fraction as fierce and considerate as you. I hope you and **Sam Stevens** continue to be a presence in my life, you have both helped me immensely.

To the Foster group I leave behind, **Dr Ram Prasad**, **Benedict Smith**, **Jiangtian (Andy) Tan**, **Sanyou (Victor) Xu** and **Dr Prioti Purba**, you have all been fantastic colleagues and I wish you all every success for the future.

I am especially thankful to the staff within the Department of Chemistry at the University of Sheffield, without whom none of us would achieve our PhDs. **Dr Craig Robertson**, **Denise Richards**, **Nick Smith** and **Sharon Curl**, thank you all for your time, patience and expertise.

I am also thankful to everyone who has engaged with the CPGS. One of the things I'm most proud of from the last four years is the formation of our society. You have all helped me foster skills and feel a sense of community. I hope the legacy continues.

To the DREAM BEAM TEAM - **Beth Ritchie**, **Ellen Wilson** and **Alice Rhind-Tutt** and the +1's – **Daniel Murray**, **Luke Wilson** and **Jack Berry**. From football to board games, your constant source of light and happiness has helped me through the tough days. I feel truly celebrated by each and every one of you.

Jonny Gregg, what would I have done without you! You have been an absolute rock these last four years and I will dearly miss living with you.

To my best friends **Ammara Jamil** and **Juliet Davies**, thank you for everything. You have both been there for me from the beginning. Encouraging me to take on this challenge and showing me what true strength is. You both give me the best perspective of life, keep me grounded and definitely help me to blow off steam.

Thank you to my wonderful family who have supported me every step of the way. **Harry Wood**, you might be my baby brother, but your dedication and prowess continues to inspire me. **Charlotte Wood**, you have just brought life into the world (shout out Ava Hazel Berry!) and yet you have found the time

to support me no matter. Your attitude to life, to make the most of every moment and spread kindness, is infectious. I love you both dearly. To my incredible parents, I cannot put into words how grateful I am for everything you have done for me. From picking me up from my lows to celebrating my highs, your firm belief in me has truly made me feel that anything is possible. Afterall, what would Beyoncé do? **Mum** and **dad**, I hope I have made you both proud.

Finally, to **Alan Hoodless**, my big hottie. Thank you for the constant dad jokes, delicious meals, and your unwavering belief in me. From all the practice presentations to "cool" AFM pics, you have truly supported and celebrated me throughout this experience. You inspire me to be all I can, and I look forward to our future together, whatever it may hold.

"Ever tried. Ever failed. No matter. Try Again. Fail again. Fail better."

- Samuel Beckett

Author's Declaration

This research has been performed between the months of October 2019 and June 2023, within the Department of Chemistry at the University of Sheffield, under the supervision of Dr Jonathan Foster.

1st referee Dr Jim Reid, The University of Sheffield

2nd referee, external Dr Darren Bradshaw, The University of Southampton

I, the author, confirm that this Thesis is my own work. I am aware of the University's Guidance on the Use of Unfair Means (www.sheffield.ac.uk/ssid/unfair-means). This work has not previously been presented for an award at this, or any other, university.

List of Conference Presentations

Oral Presentations

- **Amelia Wood** and Jonathan A. Foster, “Phage display against a novel two-dimensional metal-organic nanosheet to demonstrate systematically tunable biosensors”, 7th International conference on bio-sensing technology, Sitges, **May 2022.**

- **Amelia Wood** and Jonathan A. Foster, “Phage display against a novel two-dimensional metal-organic nanosheet to demonstrate systematically tunable biosensors”, UK Porous Materials, Glasgow, **June 2022**.

- **Amelia Wood** and Jonathan A. Foster, “Phage display against a novel two-dimensional metal-organic nanosheet to demonstrate systematically tunable biosensors”, MOF2022, Dresden, **September 2022** (couldn’t do it due to illness)

Poster Presentations

- **Amelia Wood** and Jonathan A. Foster, “2D MONs for application as biosensors”, Graduate Virtual Showcase, Sheffield, **May 2021**

Table of Contents

List of Common Abbreviations

2D: Two-dimensional

3D: Three-dimensional

Ab: Antibody

Adb: 9,10-anthracene dibenzoate

AFM: Atomic force microscopy

AIE: Aggregation-induced emission

AP: Acetaminophen

ATR-IR: Attenuated total reflection - infrared spectroscopy

BDC: Benzenedicarboxylic acid

Bim: Benzimidazole

Boc: *tert*-Butyloxycarbonyl

Bpy: 2,2'-bipyridine

BPY: (4-[2-(4-methylphenyl)-6-(5-methylpyridin-2-yl)pyridin-4-yl]benzoic acid)

BTB: tricarboxylate 1,3,5-benzenetribenzoic acid

BTE: (4,4',4"-(benzene-1,3,5-triyl- tris(ethyne-2,1-diyl))tribenzoic acid)

BWMM: Bipedal walking molecular machine

CALP: Calprotectin

CEA: Carcinoembryonic antigen

CHA: Catalytic hairpin assembly

CSD: Cambridge structural database

cTnI: Cardiain c Tropin I

DA: Dopamine

Dcbpy: 4,4'-dicarboxylic acid-2,2'-bipyridyl

DLS: Dynamic light scattering

DMF: (N,N)-dimethylformamide

DMS: 2,2-dimethylsuccinate

DSBTR: Double stirring bar assisted target replacement

DSN: duplex-specific nuclease

dsDNA: double stranded DNA

DMUV: Duck Tembusu Virus

EA: Elemental analysis

E. Coli: *Escherichia coli*

ECL: Electrochemiluminescence

Fab: Antigen binding fragment

FAM: Fluorescein

Fc: Ferrocene

FRET: Förster resonance energy transfer

FTIR: Fourier-transform infrared

GCE: Glass carbon electrode

GO: Graphene oxide

H_4ETTC: 4',4''',4'''',4'''''''-(ethene-1,1,2,2-tetrayl)tetrakis(([1,1'-biphenyl]-4-carboxylic acid))

HCR: Hybridization chain reaction

Hcp: Hexagonal close packed

HP: Hairpin DNA

IM: Imidazole

IVTT: *in vitro* transcription/translation

Kgd: Kagome dual

LD: Lyme disease

LOD: Limit of detection

MAP: Mycobacterium avium subspecies paratuberculosis

MB: Methylene Blue

miRNA: microRNA

mim: Methylimidazole

MNP(s): Magnetic nanoparticle(s)

MOF(s): Metal-organic framework(s)

MOL(s): Metal-organic layer(s)

MON(s): Metal-organic nanosheet(s)

MWCNT(s): Multi-walled carbon nanotube(s)

MS: Mass spectroscopy

NMR: Nuclear magnetic resonance

OAc: Acetate

OECT: Organic electrochemical transistor

PBS: Phosphate buffer saline

PCR: Polymerase chain reaction

PEI: Polyethylenimine

POC: Point of care

PSE: post-synthetic exchange

PSF: Post-synthetic functionalisation

PTTBA: 4,4',4'',4'''- (porphine-5,10,15,20-tetrayl)tetrakis benzoic acid

PVP: Polyvinylpyrrolidone

QCM: Quartz-crystal microbalance

RIM: Restriction of intramolecular motions

ROS: Reactive oxygen species

SBU(s): Secondary building unit(s)

SEM: Scanning electron microscopy

SERS: Surface-enhanced raman spectroscopy

SPECT: Single photon emission computed tomography

SPR: Surface plasmon resonance

ssDNA: single stranded DNA

TATB: 4,4',4''-*s*-triazine-2,4,6-triyltribenzoate

TCPP: tetrakis(4-carboxy-phenyl)porphyrin

TDA: 2,2'- thiodiacetic acid

TEM: Transmission electron microscopy

TGA: Thermal gravimetric analysis

TMD(s): Transition metal dichalcogenides

TPY: 4'-(4-benzoate)-(2,2',2''-terpyridine)-5,5''- dicarboxylate)

TTPP: 5,10,15,20-tetrakis[40-(terpyridinyl)phenyl]porphyrin

UA: Uric acid

XRPD: Powder X-ray diffraction

ZIF(s): Zeolitic imidazolate framework(s)

Amino acid	3 letter code	1 letter code
Alanine	Ala	A
Arginine	Arg	R
Asparagine	Asn	N
Aspartate	Asp	D
Cysteine	Cys	C
Glutamate	Glu	E
Glutamine	Gln	Q
Glycine	Gly	G
Histidine	His	H
Isoleucine	Ile	I
Leucine	Leu	L
Lysine	Lys	K
Methionine	Met	M
Phenylalanine	Phe	F
Proline	Pro	P
Serine	Ser	S
Threonine	Thr	T
Tryptophan	Trp	W
Tyrosine	Tyr	Y
Valine	Val	V

Chapter 1:

Introduction and Aims

1.1 Introduction

Naturally occurring biomaterials achieve remarkable degrees of biomolecular recognition. Micro- and nanostructures on their surface give rise to properties that facilitate multiple highly specific weak interactions resulting in selectivity.[1] Taking inspiration from these features, control over interfacial properties on the molecular scale which direct interactions with target biomolecules is an important foundation for the development of novel biosensors.[2–4]

Two-dimensional materials represent promising artificial mimics due to their high surface areas and accessible functional groups.[5–7] A wide variety of two-dimensional nanomaterials including transition metal dichalcogenides, MXenes and graphene have displayed an ability to bind biological macromolecules such as proteins and DNA.[8–10] The simple inorganic structure of conventional 2D materials leads to stochastic functionalisation with different binding groups, therefore limiting their selectivity. Nanomaterials with complex surface structures that can be tuned on the molecular scale are predicted to achieve recognition capabilities comparable to natural biomaterials.[11,12]

Metal-organic framework nanosheets (MONs) are a class of two-dimensional materials which combine organic ligands with metal-nodes.[13] The modular structure of MONs allows for systematic tuning of surface chemistry without changing the overall topology whilst their crystalline nature affords a periodic array of recognition sites that allows multidentate binding.[11,14] This thesis explores whether programmable two-dimensional metal-organic nanosheets (MONs) can be designed for application as synthetic biointerfaces. This chapter begins with a general overview of biosensing and highlights the current trends of 2D materials in disease diagnostics. The design, synthesis, and characterisation of MONs is then discussed in more detail. This is followed by an examination of the current literature surrounding the application of MONs as biosensors. Finally, biopanning as a high-throughput selection technique is outlined and its application in gaining insight into the potential of MONs in biomolecular recognition is reviewed.

1.2 Biosensing

1.2.1 Fundamentals of Biosensing

A biosensor is defined as an analytical device, used for the detection of a biological analyte in bodily fluids for diagnostic or monitoring purposes. There are four main components to a biosensor: molecular recognition, signal generation, signal transduction, and a reader instrument.[15,16] Designing a small instrument for rapid and easy measurements of biomarkers enables patients to monitor their disease easily and regularly, reducing time spent in hospitals. There is a huge drive and desire for point of care (POC) testing to simplify diagnostics and patient monitoring within healthcare, with current examples including wearable glucose monitors for patients with diabetes.[17,18]

A key component of biosensing is biomolecular recognition, the process by which biomolecules recognise and selectively bind to their molecular target.[19] Such biomolecules are often referred to as bioreceptors, with a prime example being antibodies, which detect specific antigens (Figure 1.1). Here the specific site on the antibody that detects the antigen is called the paratope and the binding site on the antigen is called the epitope. Such recognition events require the interaction of specific sequences of amino acids, where conformation of the sequence is important for selectivity.

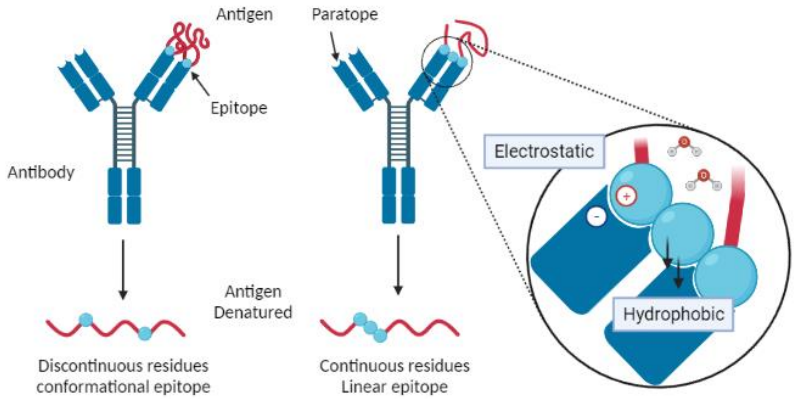

Figure 1.1: Simplified schematic of antigen-antibody interactions at the epitope and paratope, highlighting some potential binding modes. Created with BioRender.com.

The driving force for biomolecular recognition is multiple weak specific interactions working cohesively to form sensor-target complexes.[20] Examples include electrostatic interactions due to charges and dipoles and hydrophobic interactions as a result of strong forces of attraction largely arising from the entropy of the solvent. As recognition usually takes place in aqueous environments, the electrostatic and induction interactions are significantly reduced and the hydrophobic effect is often the overriding stabilisation force. Synthetic biointerfaces require control over specific surface properties on the nanoscale in order to mimic these interactions.[1]

1.2.2 Signal Generation and Transduction

The signal generated after a biomolecular recognition event comes typically in the form of light, heat, pH, charge, or mass change. Once the signal is generated the transduction component converts it into a measurable optical, electrochemical, thermometric, piezoelectric or magnetic signal.[15]

Surface plasmon resonance (SPR) based optical biosensors are among the most common (Figure 1.2).[21] The label-free nature of this approach, with real-time changes of refractive index at the sensor surface proportional to target concentration, means this technology is widely used in research regarding clinical diagnostics and pharmaceutical drug development.[22] However, in real world applications a multitude of other effects can complicate SPR analysis, including non-1:1 binding stoichiometry, non-specific absorption of molecules and limitations in mass transfer. Other optical sensing mechanisms involve Förster resonance energy transfer (FRET) and surface-enhanced Raman spectroscopy (SERS), where systems are based on fluorescence quenching and Raman scattering, respectively. [23,24]

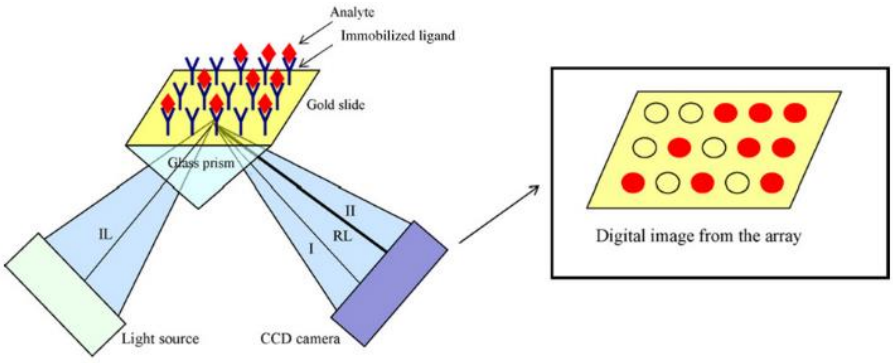

Figure 1.2 – A schematic illustration of the set-up for the SPR imaging. The molecules of ligand Y are immobilised in an array format on the surface of the gold slide attached to the glass prism. The incident light (IL) from the light source is directed on the prism. The binding of Y to the analyte ♦ causes the shift of the angle of the reflected light (RL) from position I to position II. No characteristic shift is observed at the absence of binding. Digital image from the array is recorded by CCD camera. Taken from reference 21.

Electrochemical biosensors are among the most studied and involve signal generation triggered by electron or ion transfer on a conductive transducer as a result of biomolecular recognition.[25] Devices utilise amperometric, voltammetric, potentiometric, organic electrochemical transistor (OECT), photoelectrochemical and electrochemiluminescent biosensing.[26] Sensor components include a working electrode, a counter electrode and usually a reference electrode or field-effect transistor. The successful functionalisation of the working electrode with naturally existing sophisticated biomarkers creates novel, real time molecular recognition technologies.[27] Portable, wearable and implantable electrochemical devices face engineering challenges especially for the detection of large biomolecules.[26] Signal transduction, amplification and filtering needs to be improved as well as processing to produce disposable, flexible and multielectrode electrochemical biosensors.

Quartz crystal microbalance (QCM) based biosensors (Figure 1.3) have emerged as a new class of device in the last 10-15 years.[28] Combining piezo-electronic and gravimetric analysis, QCM sensors usually comprise an electrode coated with a transducing layer (usually Au or Ti) and bridging unit or bioreceptor. The sensitivity and selectivity of the sensor is heavily reliant on the receptor as its interaction with analytes results in an effective increase in mass on the electrode surface that results

in a decrease in resonant frequency.[29] The change in mass on the electrode surface is considered proportional to the decrease in resonant frequency therefore, biomolecular recognition can be measured. Nanogram levels of mass change can be detected using a well-designed QCM set up. When considering their use in biosensing there are areas to improve including issues of baseline drift and noise with interference from non-specific binding.[28,30]

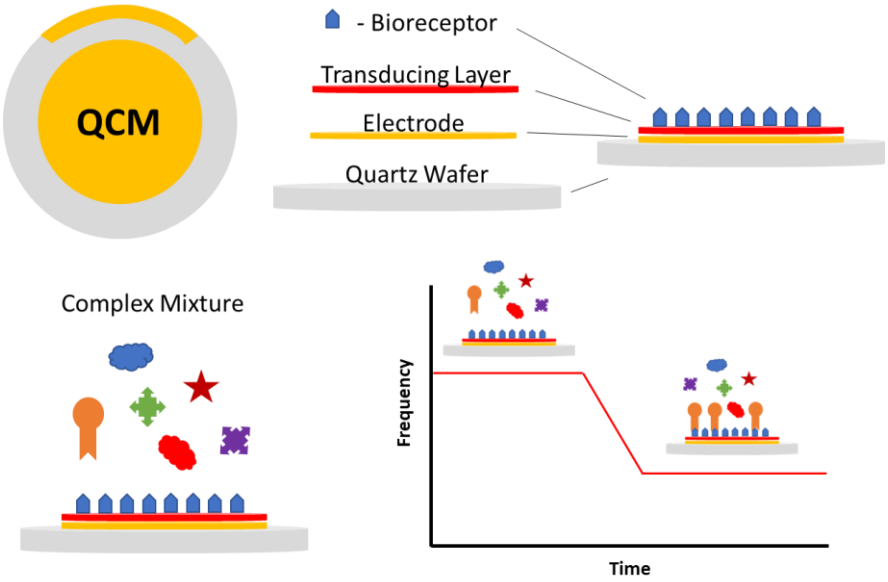

Figure 1.3: General principle of detection for a QCM biosensor. The graph shows the frequency responses of the biosensor at different stages of the assay: frequency baseline of a QCM crystal with immobilised bio receptors and then frequency change upon the binding of target molecules.

1.2.3 Move Towards 2D materials

A move towards micro- or nano-scale biosensors facilitates better signal-to-noise ratios as well as the possibility of using smaller sample volumes resulting in lower assay costs as well as improving patient comfort.[15] Miniaturisation has proved beneficial for a variety of reasons including increasing surface area-to-volume ratios of the active sensing area and in electronics the sizes of the detecting electrode and target biomarker become comparable.[5,8] This reduces non-specific binding, increasing binding efficiency towards the target analyte and resulting in improved sensitivity/resolution.

2D materials offer high surface-to-volume ratios and atomic thinness that yields a strong response to surface adsorption events and they are used as the transduction element within sensors.[6,8] Due to the simplicity of 2D inorganic surfaces resulting in no inherent biomolecular selectivity they often act as substrate supports to bioreceptor components such as antibodies and aptamers.[5] 2D materials are well-suited as transduction elements as they exhibit a broad range of optical phenomena, tunable band structure and electronic properties.[8] There are many examples of 2D material based biosensors now reported, detecting a range of bioanalytes from metabolites to whole cells, this section will focus on the most promising candidates in larger biomolecule detection where the limits of detection achieved are comparable to the current standard.

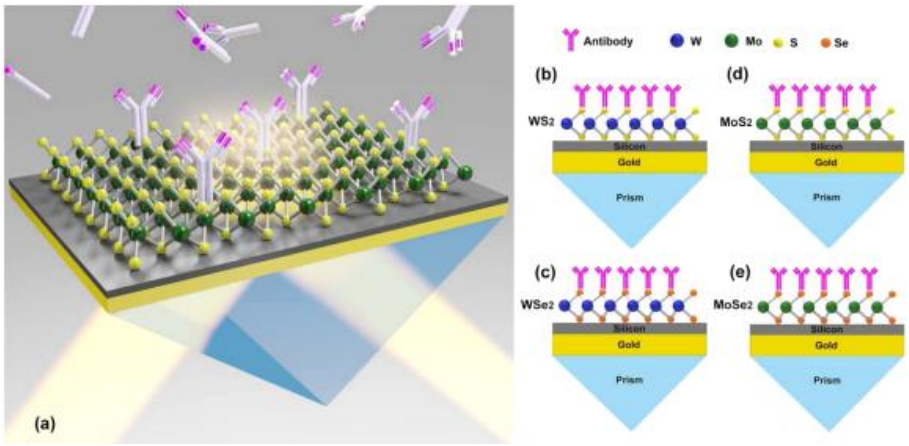

Figure 1.4 - Schematic diagram of 2D TMD structured on the plasmonic sensing substrate. (a) Antibody binding processes at the TMD sensing surface that induced a tiny refractive index change (1×10^{-6} RIU). Atomically thin (b) WS_2, (c) WSe_2, (d) MoS_2, and (e) $MoSe_2$ layers structured at the sensing interface. Taken from reference 31.

The current trend in research regarding optical biosensors has seen a drive towards optical plasmonic sensors based on 2D transition metal dichalcogenides (TMDs) such as MoS_2. It is predicted that TMDs with produce significantly stronger responses compared to commercial methods based on purely metallic substrates (such as gold) as shown in Figure 1.4.[31,32] This is attributed to extended plasmon lifetimes associated with the layered material. The band structure of TMDs has been tuned via applied electric fields, strain, and functionalisation, and has resulted in tailoring for specific optical absorption requirements and operation wavelengths.[33]

2D materials have been utilised to enhance sensitivity as they integrate well into sensor systems due to their ability to form thin films with ease.[34] Developments involving graphene oxide (GO) and MoS_2 have greatly decreased the limit of detection (LOD) of various target biomolecules including the carcinoembryonic antigen (CEA) (Figure 1.5a) and microRNA (miRNAs) (Figure 1.5b) with limits of detection (LOD) of 1.6 fM and 10 fM respectively.[35,36] For perspective, Invitrogen's commercially available CEA detection kit has a vastly larger limit of detection of 200 pg / mL.[37]

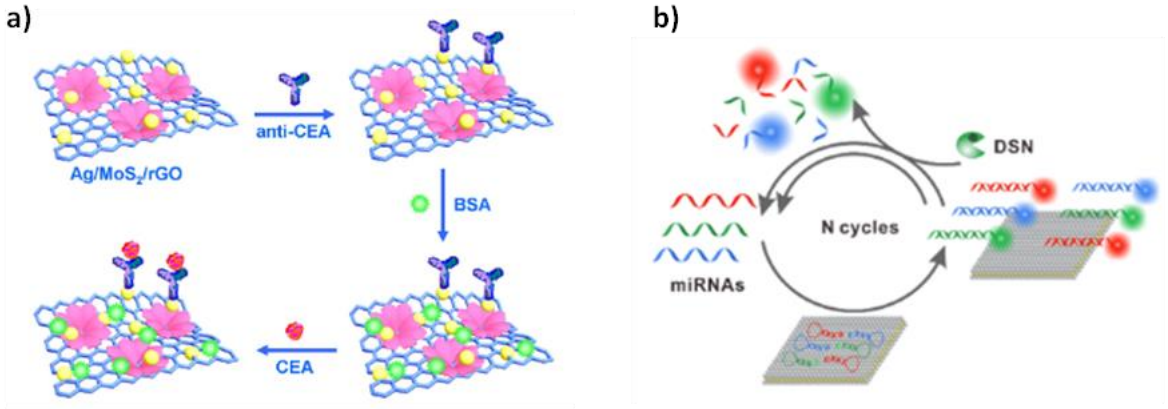

Figure 1.5 – a) Schematic illustration of label-free Ag/MoS_2/rGO based electrochemical sensor, b) Schematic illustration of MoS_2-based sensing platform for multiplexed detection of miRNAs. Taken and modified from references 35 and 36.

Pathways to detections for such systems are complex (Figure 1.5a), involving the functionalisation of electrodes with multiple nanomaterials such as gold nanoparticles (AuNPs), MoS_2 and GO as well as bioreceptors such as antibodies and other biomolecules to block non-specific binding.[35] In work by Wang *et al.*, the electrocatalytic activity of MoS_2 towards H_2O_2 reduction is enhanced by the synergistic effect of GO and AuNPs which improve conductivity. In the presence of H_2O_2, the CEA target was monitored where the specific recognition of the antibody-antigen interaction impeded catalytic efficiency. Other mechanisms (Figure 1.5b) involve the fluorescence quenching of dye-labelled ssDNA/oligonucleotides by 2D materials such as GO which are released upon binding with their target miRNAs and rely on enzyme based amplification using duplex-specific nuclease.[36]

Surface modifications of 2D materials are generally performed post-synthetically and commonly difficult to gain total uniformed surface functionality due to the poor reactivity and

solubility of inorganic surfaces.[38] Molecules often anchor to surfaces randomly or unsuccessfully resulting in defective and incomplete functionalisation of the layered material.[39] There is also a desire to avoid compromising electrical or optical properties, therefore progress in sensitivity and selectivity is impeded.[40]

In summary, 2D materials have clear advantages in progressing miniaturisation and improving the limit of detection of various biomolecules. However, their main contribution is confined to the role of transduction element.[8] Due to the simple structure of 2D materials, a separate bioreceptor element is incorporated, often stochastically, within sensors for biomolecular recognition. Taking inspiration from the remarkable degrees of selective binding found in nature this thesis aims to interrogate whether the periodic and tunable 2D surfaces of metal-organic nanosheets can mimic recognition sites such as paratopes (Figure 1.1). The following section covers the scope of MONs, including approaches to design, synthesis and characterisation and highlights the systems most appropriate for biosensing applications.

1.3 Metal-Organic Nanosheets

1.3.1 Introducing MONs

Metal-organic nanosheets (MONs) can be defined as free-standing, two-dimensional materials, approaching monolayer thickness, formed by the coordination of organic ligands with metal ions or clusters (Figure 1.6).[41] They are a subset of the metal-organic materials family which encompasses a wide variety of architectures from discrete complexes and cages to extended polymers, gels and liquid crystals.[42–46] Within this family of materials over 99,000 3D metal-organic frameworks (MOFs) have been reported on the Cambridge structural database (CSD).[47] Many of the MOFs reported are layered structures. Accessing the individual layers to produce uniform crystalline sheet-like material with single unit thickness is the basis for designing metal-organic nanosheets (MONs).[13]

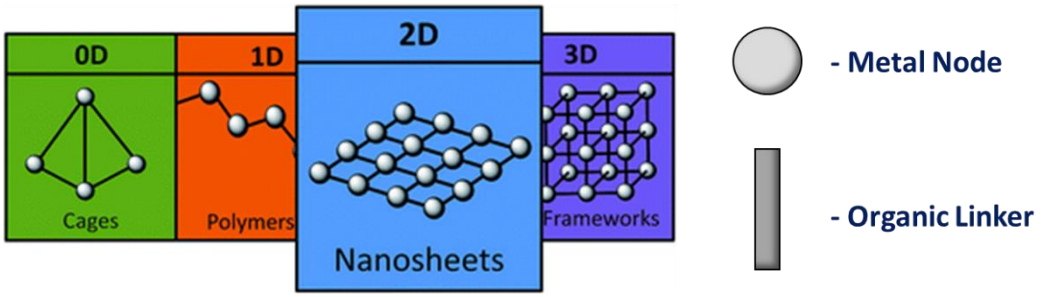

Figure 1.6: Simple schematic of a selection of the architectures found in the metal-organic materials family.

Commonly solitary layers will not be stable or cannot be isolated using a given method. Therefore, the term MON describes materials with 'nanosheet'-like structure with the potential to exist as single layers. The Foster group has established three specific qualities needed to fulfil the 'nanosheet' definition:[13]

1. Organic ligands coordinated to metal ions or clusters with continuous connectivity in two-dimensions but only non-covalently in the third dimension.
2. Highly anisotropic materials with one dimension approaching monolayer thickness and the others being at least an order of magnitude larger and approximately equal in size.
3. Materials which can be isolated in a form with the dimensions outlined above as free standing sheets, not attached to a surface or other scaffold or as layers in a bulk material.

There are various synonyms for the term MONs including metal-organic layers (MOLs), metal-organic framework nanosheets, metal-organic graphene analogues and many more.[48–50] Whilst in some cases there are slight distinctions between terminology, nanosheet can be used to describe all the two-dimensional MOFs mentioned in this work including references to literature. The advantage metal-organic nanosheets offer over conventional 2D materials is that specific chemical and physical properties can be systematically tuned.[14] Programming can be achieved through selecting specific metals and organic linker components where different structures can be accessed. Depending on the desired application it is important to consider the stability of the system. For biosensing applications MONs must be stable in physiological environments whilst retaining their tailorable nature.

1.3.2 Metal-Organic Nanosheet Design

When designing MONs, the focus is on creating strong in-layer coordination bonds and comparatively weak inter-layer interactions.[13] A number of well-established metal-organic coordination motifs exist allowing for a high degree of predictability over the topology of the 2D MONs assembled. Linker components are carboxylate, N-donor and phosphine based and coordinate to metal centres including copper, zinc, cobalt and hafnium to create a variety of structures.[51–54]

Secondary building units (SBUs) are particular molecular complexes or clusters in which differing ligand coordination modes and metal coordination environments can be used to accurately predict framework topology.[13] There are many examples of SBUs from paddlewheel motifs formed by tetracarboxybimetallic ions $[M_2(COO)_4]$ (Figure 1.7a) to hafnium clusters $Hf_6(\mu_3\text{-}O)_4(\mu_3\text{-}OH)_4(carboxylate)_{12}$ (Figure 1.7e). SBUs are incorporated into extended coordination polymers using multidentate linkers, ranging from tetrakis(4-carboxy-phenyl)porphyrins (TCPP) (Figure 1.7d) to tricarboxylate 1,3,5-benzenetribenzoic acid (BTB) ligands (Figure 1.7e) to form 2D MONs.[13,55]

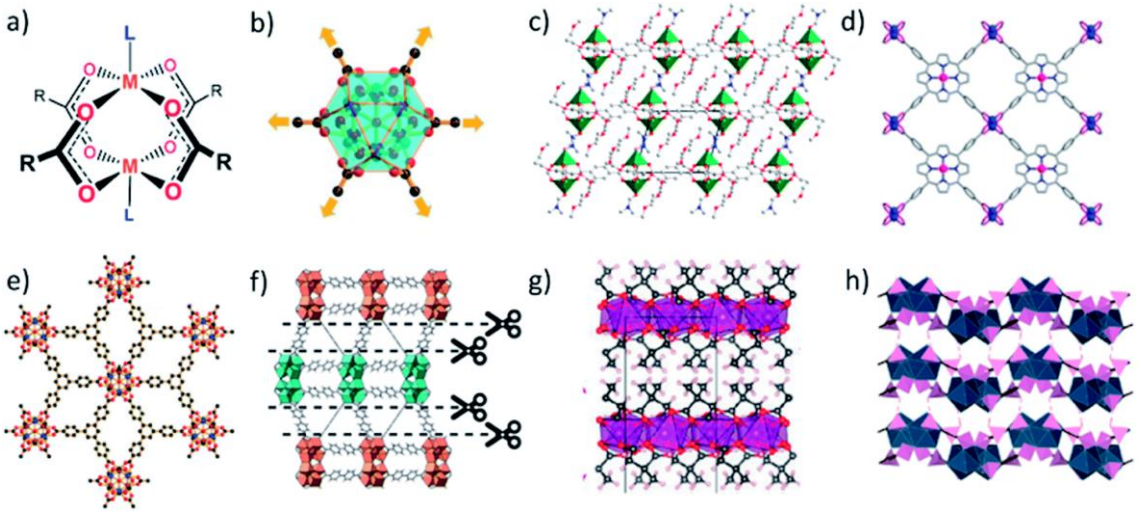

Figure 1.7 - Schemes showing (a) paddlewheel and (b) M_6L_6 secondary building units. (c–h) example crystal structures showing diversity of carboxylic acid based linkers and secondary building units used in the synthesis of MONs. Specifically, (c) $Zn_2(BDC\text{-}x_2)(DMF)_2$, where x = $O(CH_2)_3OMe$; (d) M(TCPP) where M = Zn, Cu, Cd, Co; (e) $[Hf_6(\mu_3\text{-}O)_4(\mu_3\text{-}OH)_4(carboxylate)_{12}]$; (f) hcp UiO-67; (g) Mn(DMS)(H2O); (h) lanthanum 1,3,5-benzenetriphosphonate (LBP-II). Image reproduced from reference 13.

A MON system containing hafnium clusters and a tricarboxylate linker analogous to BTB has been utilised in this thesis. When the building components are known to form 3D interpenetrated MOFs, it is crucial that synthetic procedures are modified to fulfil the geometric requirements of a 2D layer.[54,56,57] The different approaches to MON synthesis are discussed in the following section. The synthetic methodology used has a significant influence on the physiochemical properties of the nanosheets, such as size distributions, crystallinity, thickness, chemical composition, and so on.

1.3.3 Metal-Organic Nanosheet Synthesis

There are two principal routes for MON preparation: top-down exfoliation of a layered MOF, or bottom-up assembly of their molecular building blocks directly into nanosheets. A general schematic demonstrating the differing methodologies for the synthesis of MONs is given in Figure 1.8, with both approaches adopted within this thesis.[13]

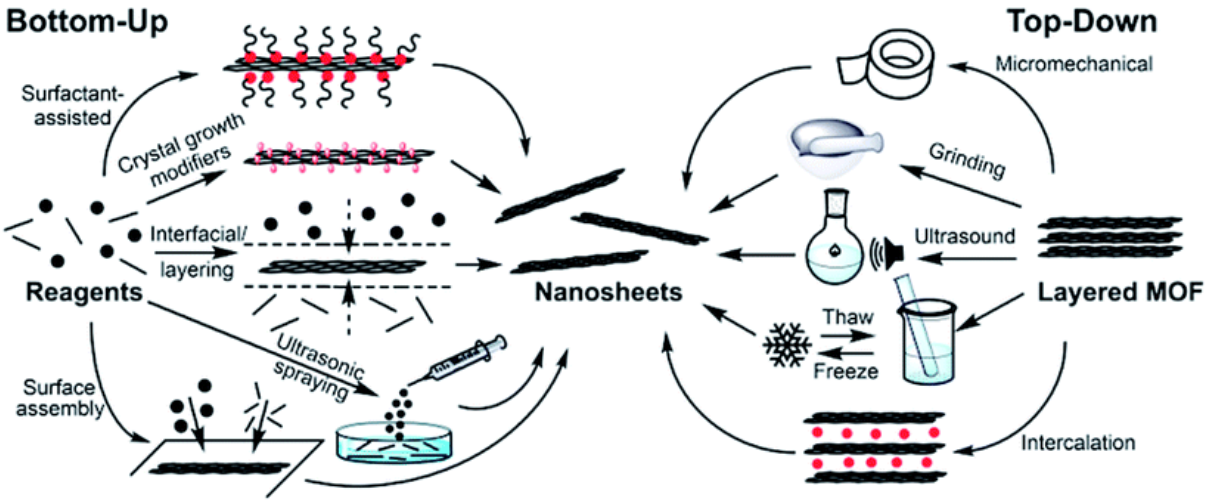

Figure 1.8 - Scheme showing different bottom-up and top-down methodologies used to produce MONs. Taken from reference 13.

1.3.3.1 Top Down

Typically, the top down approach involves synthesis of the layered metal-organic framework followed by a chemical or physical exfoliation of the layers into individual or few-layered nanosheets. "Exfoliation" describes the delamination of the bulk lamellar MOF structure through breaking weak

inter-layer interactions such as π-π interactions, hydrogen bonds and van der Waals forces without disrupting the in-plane coordination bonds. Famously graphene was isolated from its bulk graphite using the "Scotch tape" method where nanosheets down to 2 nm were accessed, though its practicality in exfoliation is limited.[58] As a result, there has been extensive work in developing more efficient and high yielding exfoliation techniques more suited to the diversity of metal-organic materials.

Whilst there is now an expanding array of MOF exfoliation techniques, with many depicted in Figure 1.8, only those most relevant to this thesis will be discussed. The most common technique is liquid phase exfoliation via sonication in which the bulk MOF is suspended in a suitable stabilising solvent system then subjected to ultrasound. The energy input from ultrasonication is enough to overcome the weak inter-layer interactions allowing solvent molecules to penetrate the structure, isolating and stabilising individual nanosheets.[59] Other energy inputs include high shear mixing using an overhead stirrer to disrupt inter-layer interaction and mechanical based wet ball-milling.[60,61] For all methods, issues arise of MON fragmentation and in-plane coordination bond breaking as a result of the indiscriminate nature of ultrasound/shearing/grinding. This leads to a broad distribution of particle sizes post-exfoliation. Solvents play a large role in the exfoliation of 3D MOFs into 2D MONs from weakening and breaking the cohesive interactions of adjacent sheets to stabilising the resulting nanosheets in colloidal suspension. In some cases, immersion of layered MOFs in solvent has resulted in spontaneous exfoliation into nanosheets.[62,63]

1.3.3.2 Bottom-up

The bottom-up approach involves the self-assembly of the metal ions and linker components often in the presence of a directing interface or chemical species. Modulating agents such as surfactants or monotopic ligands direct synthesis in two-dimensions. Interfaces (liquid/air or liquid liquid) are also utilized to direct growth along one crystal plane the interface between layers is restrictive, resulting in enhanced control over the MON thickness. Rodenas *et al.* utilized liquid layers

arranged according to density, composed of mixtures of solvents to produce Cu-BDC nanosheets approaching monolayer thickness.[42] Alternatively, restricting the stacking of layers such as with surfactants or ions can result in the production of ultrathin MONs. A commonly used surfactant is polyvinylpyrrolidone (PVP), as evidenced by Zhao *et al.* where Zn(TCPP) nanosheets were accessed < 10 nm thick via anisotropic crystal growth.[64]

Small molecules (e.g. formic acid, pyridine) that have the same functional groups as the organic ligand, competitively coordinate with metal nodes in a particular crystal plane. As discussed later in section 1.3.6, hafnium and zirconium based MON systems are synthesised using this approach, where monocarboxylic acid modulators inhibit interpenetration and control the growth of MOFs along the (220) crystal plane resulting in 2D connectivity.[54] Depending on the modulator used this approach allows for the introduction of different functional groups within the metal cluster. The tuning of surface properties via the introduction of different surface functionality is discussed further in section 1.3.7.

Overall, bottom-up methods are generally scalable and one-pot, producing larger and thicker nanosheets with a narrower size distribution in low quantities requiring minimal steps. Conversely, top-down methods result in nanosheets with a broader size distribution that are highly crystalline and phase pure. For each MON system, the most appropriate exfoliation technique might vary and optimisation is often required. The use of surfactants may aid nanosheet formation however, it can block binding sites as it can be difficult to remove. The chemical and thermal stability of the MONs within the exfoliation environment must be considered when selecting the preparation method. The method of synthesis will also depend on the properties required for a particular application, where accessing ultrathin nanosheets is a priority for electronic applications and large aspect ratios are attractive for separation applications. When considering approaches for the synthesis of MONs for biosensing, maximising the possible binding sites is a high priority along with physiological stability. Synthetic procedures that involve hydrothermal processing are likely to guarantee stability.

1.3.4 Characterisation of MONs

MONs are complex hierarchical materials which require characterisation using a wide variety of techniques in order to understand their structure and properties. Due to the nanoscale thickness of MONs the crystal structure characterisation technique single-crystal X-ray diffraction is not possible. Whilst this is a key technique for MOFs and can still be used for characterising bulk layered MOFs, it is not possible with individual nanosheets due to their reduced dimensions. Powder X-ray diffraction (XRPD) is key to phase determination by measuring the diffraction pattern of the crystalline material in powder form. This enables structural characterisation at an atomic scale, useful for determining that the bulk is in the correct layered phase and the structure of the resulting nanosheets. This often involves the comparison of powder patterns of synthesised materials to the expected pattern reported on the CSD. Through the unavoidable drying or heating of MONs there is a high potential that structural rearrangement is induced during exfoliation due to the high surface area and often labile structures of metal-organic materials.[13] The XRPD pattern of the MONs may display a loss of peaks corresponding to out of plane reflections of the parent MOF as a result of peak broadening caused by reduced dimensionality and preferred crystallite orientation.[13]

Other standard MON characterisation methods include elemental analysis (EA), Fourier-transform infrared (FTIR) spectroscopy and thermogravimetric analysis (TGA). Solid-state nuclear magnetic resonance (NMR) can also be used in order to investigate the structure of MONs. Digested MONs can be characterised by both NMR and mass spectroscopy (MS) which is particularly valuable when analysing modified MONs for example finding the ratio of organic linkers in mixed linker systems or monitoring post-synthetic functionalisation. Ideally such modifications should not affect the materials crystal structure so there would be no change in XRPD patterns. NMR and MS studies allow the efficient identification of modification success.

A large part of nanosheet analysis is determining structure on a nanoscopic level. Nanosheet dimensions and morphology can be characterised using different forms of microscopy as shown in

Figure 1.9.[65] Atomic force microscopy (AFM) is a key technique in that it is the only way to accurately determine nanosheet heights, thus whether single layers have been accessed. Scanning electron microscopy (SEM) is also used but is more suited to imaging bulk 3D MOF material and is useful in determining morphology of samples. Transmission electron microscopy (TEM) can be used for electron diffraction and imaging which determines rough particle shape, size and local features.

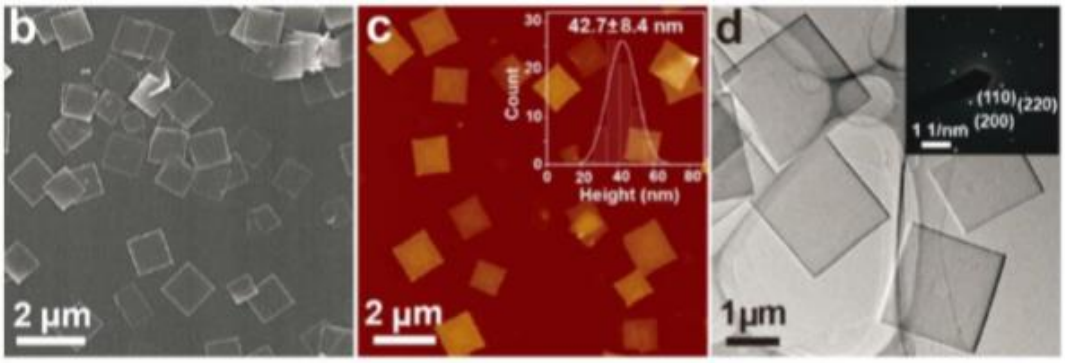

Figure 1.9 - Examples of different microscopy techniques used to image MONs b) SEM image, c) AFM image, inset: statistical analysis of the thickness of nanosheets, d) TEM image, inset: selected area electron diffraction of a nanosheet. Image reproduced from reference 65.

Sample-wide analysis of nanoscopic dimensions can be carried out using Tyndall scattering and dynamic light scattering (DLS). The simplest way to detect the presence of nanomaterial is to shine a laser through a MON suspension and observe the scattering of light by nanosheets. DLS has been used to measure the lateral size distribution of nanosheets however it assumes spherical particles and often underestimates the true value therefore corroboration of sizing with AFM analysis is critical. The same assumptions apply for zeta potential measurements which indicate the charge of a MON system. It can be used to monitor successful functionalisation and determine the prospect of attractive electrostatic interactions.[66,67] Environmental factors such as temperature, ion concentration and pH also impact results. Contact angle measurements indicate the hydrophobicity of the system but protocol remains unstandardised.[68] Surface property analysis demonstrates the potential binding interactions a MON can be involved in, aiding the design and tuning of the system for a given application.

A plethora of approaches to MON design and synthesis have been reported including a diverse range of metal ions, metal clusters and organic linkers. Access to such a diverse library has facilitated the application of MONs in functional devices,[69] gas separation,[42,52,70] and membrane separation.[53,70–72] The following sections focus on the systems suitable for application in biosensing. The key requirements are that the systems are stable in physiological environments and offer advantages over conventional 2D materials by providing opportunities for surface property tuning to facilitate selective biomolecular recognition.

1.3.5 Zeolitic Imidazolate Frameworks and Nanosheets

Zeolites are nanoporous inorganic materials and have been utilised in large numbers of industrial processes including separation, catalysis and sensing.[73,74] Crystalline zeolite structures are composed of tetrahedral $Si(Al)O_4$ units covalently joined by bridging O atoms to produce different types of framework.[75] Due to their intrinsic properties such as high surface areas, large pore volumes, tunable pore sizes and exceptional stability it is estimated that the economic contribution of zeolites annually is up to $350 billion worldwide.[76] However, simple inorganic structures are limited in the range of chemical functional groups that can be introduced and have poor compatibility with polymers, restricting applications.[76]

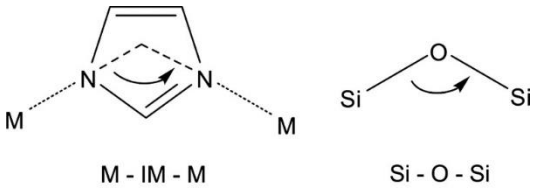

Figure 1.10 – The bridging angles in metal-imidazoles and zeolites

Zeolitic imidazolate frameworks (ZIFs) represent a special class of metal organic frameworks comprised of imidazolate linkers and metal ions, with structures similar to conventional aluminosilicate zeolites (Figure 1.10). Zeolite framework topologies have a general structure comprised of tetrahedral transition metals coordinating imidazolate (IM) type linkers. The most

common transition metals used are Co and Zn, whose structures are based on nets of linked CoN_4 or ZnN_4 where metal ions coordinate to N atoms in the 1,3-position of the imidazole ring. Notice that IM bridges make an M-IM-M angle close to 145° which is coincident with the Si-O-Si angle found in most zeolites as demonstrated in Figure 1.10.[75] The mimicking of topology and structural integrity of zeolites by ZIFs is thought to explain the exceptional thermal and chemical stability demonstrated by the ZIF family.[76] ZIFs are attractive candidates for applications where stability is key such as water purification or biosensing.[77] A study by Ruyra *et al.* demonstrated the stability of MOFs when incubated in fetal bovine serum, with ZIF-7 revealing high biostability.[78]

There are examples of different ZIF based MONs in literature with compositions such as $Zn(bim)(OAc)$,[79,80], $Zn_2(bim)_3$,[81] $Zn_2(bim)_4$,[60,61,82,83] $Co_4(bim)_{16}$,[53,84] and $Co(mim)_2$,[85,86] (bim = benzimidazole, OAc = acetate, mim = methylimidazole) used for applications including gas separation, catalysis and membrane filtration. Many of the synthetic processes for the production of 2D ZIFs resulted in MONs that were > 10 nm thick. This work focused on accessing tunable ultrathin MONs to maximise the number of possible binding sites therefore only those systems that accessed the thinnest nanosheets will be discussed.

ZIF-7, with the chemical composition $Zn_2(bim)_4$, can exist as a layered 3D structure (ZIF-7-III) where the layers are held together with weak intramolecular forces. If these interactions are interrupted, then the individual nanosheets can be accessed with the potential to get down to single layer thickness. Layered ZIF-7 was first discovered by Yang *et al.* in 2008 and has a (4,4) square planar grid structure formed by quadruply linked corner-shared networks of Zn(II) benzimidazolate tetrahedra.[87] However, ZIF-7 also exists in two other phases (ZIF-7-I / ZIF-7-II) existing as nanocrystals with differing pore sizes depending on guest occupancy as shown in Figure 1.11.[88]

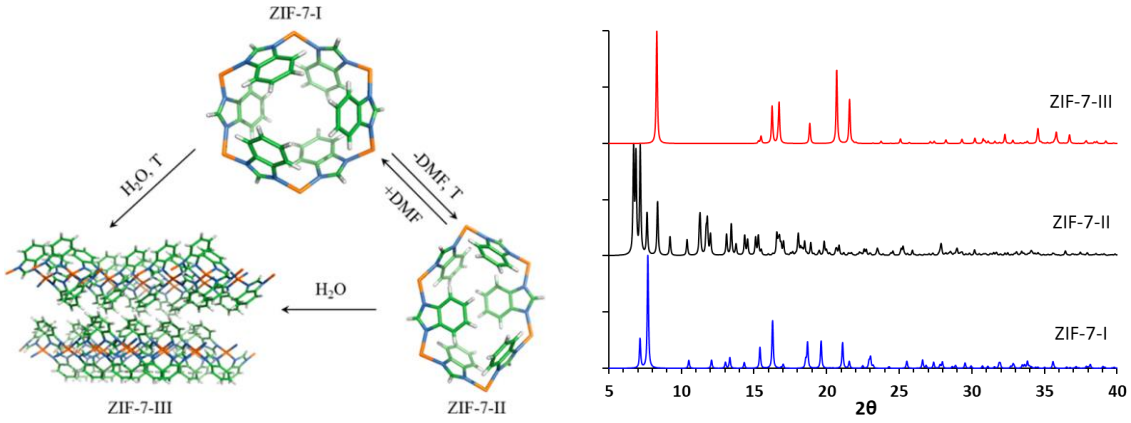

Figure 1.11 – Phase transition in ZIF-7 – Schematically and as observed by X-ray powder patterns diffraction. Figure adapted from reference 88.

Peng *et al.* were the first to demonstrate exfoliating the layered ZIF-7 MOF down to 1-nanometer-thick sheets for use as building blocks for molecular sieving membranes. Since then, a variety of synthetic methods have been reported that obtain ultrathin ZIF-7 nanosheets with impressive aspect ratios. Most methods are based on first synthesising ZIF-7 nanocrystals by combining metal salt (usually nitrate) with benzimidazole (bim) linker in DMF and then hydrothermally transforming the dried resulting powder by refluxing in distilled water. The main difference in these reported methods is the exfoliation technique in order to retrieve the 2D nanosheets.[60,61,83,89] In all cases the layered MOF is suspended in 1:1 methanol:n-propanol solution before the exfoliation technique is applied.

Wet ball milling used by Peng *et al.* is thought to facilitate the incorporation of small methanol molecules into the MOF pores and subsequent sonication resulted in nanosheets of micron diameter and 1 nm height at 15% yield.[61] Whereas the shear exfoliation technique as demonstrated by Qiu *et al.,* using an overhead stirrer to generate shear force, accessed a 28.8% yield of nanosheets ranging 3.5-5 nm in height and 100-800 nm in diameter.[60] Liu *et al.* utilises sonication only but for a longer period of time than Peng *et al.* and accessed a comparatively low yield (2 %) of ultrathin (~ 1 nm) nanosheets, likely due to the more rigorous centrifugation collection of the unexfoliated material.[83]

Ultrathin ZIF-9-III ($Co_4(bim)_{16}$) nanosheets can also be accessed, using cobalt(II) instead of zinc as the metal source (Figure 1.12).[53] The same phase transformations apply but there are examples of the direct synthesis of ZIF-9-III layered phase using sodium bicarbonate in the presence of ethanol and treatment with ultrasound to access the individual layers.[53,90] Wang *et al*. reported using a mixture of ionic liquid and ethanol to produce ZIF-9-III nanosheets directly via bottom-up synthesis where the ionic liquid acts as the intercalator to control the oriented growth, producing MONs that were on average 4.6 nm thick.[84] Hydrophobic ZIF-9-III MONs have been utilized as efficient oil-water separators and have existed as liquid marbles.[53]

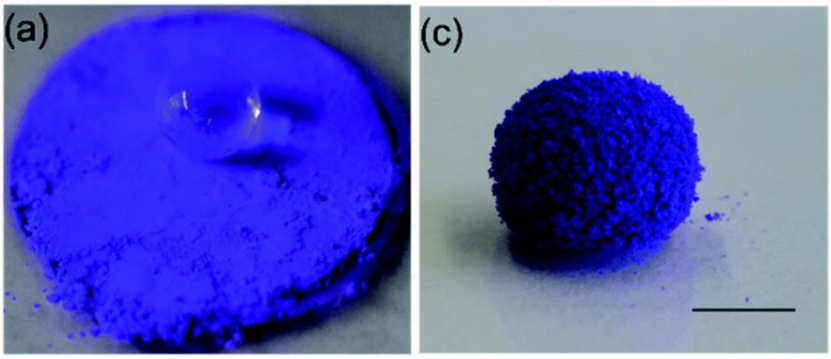

Figure 1.12: (a) Optical photograph of water droplet on a ZIF-9-III powder tablet, (c) ZIF-9-III-based liquid marbles; scale bar 5 mm. Image reproduced from reference 53.

1.3.6 Hf/Zr-Tricarboxylate Metal-Organic Nanosheets

When considering MONs for applications that require aqueous stability, hafnium and zirconium based MONs are also viable candidates. A variety of structures exist comprising metal clusters $[M_6O_4(OH)_4]$ or double clusters $[M_{12}O_8(OH)_{14}]$ coordinated by carboxylate-based linkers. 2D architectures have been accessed by restricting connectivity to the cluster via modulator addition as discussed previously (see section 1.3.3.2). Examples include hxl-UiO-67 MONs which consists of double clusters and biphenyl-4,4'-dicarboxylic acid linkers and NUS-8 MONs that consist of single clusters connected by triangular 1,3,5-benzenetribenzoic acid (BTB) linkers.[54,91] Whilst many Hf/Zr MONs demonstrate excellent aqueous stability, this section will discuss the applicability of NUS-8 based MONs for biosensing applications.

2D Hf_6-BTB ($Hf_6(\mu_3\text{-}O)_4(\mu_3\text{-}OH)_4(HCO_2)_6(BTB)_2$) (Figure 1.13) was first reported by Cao *et al.* in 2016 using a bottom-up modulated hydrothermal approach where formate capping groups directed synthesis in two dimensions, giving rise to Kagome dual (kgd) topology (Figure 1.13).[56] Ultrathin nanosheets (1.2 nm) were directly synthesised via the modulated approach, with no need for harsh exfoliation conditions.

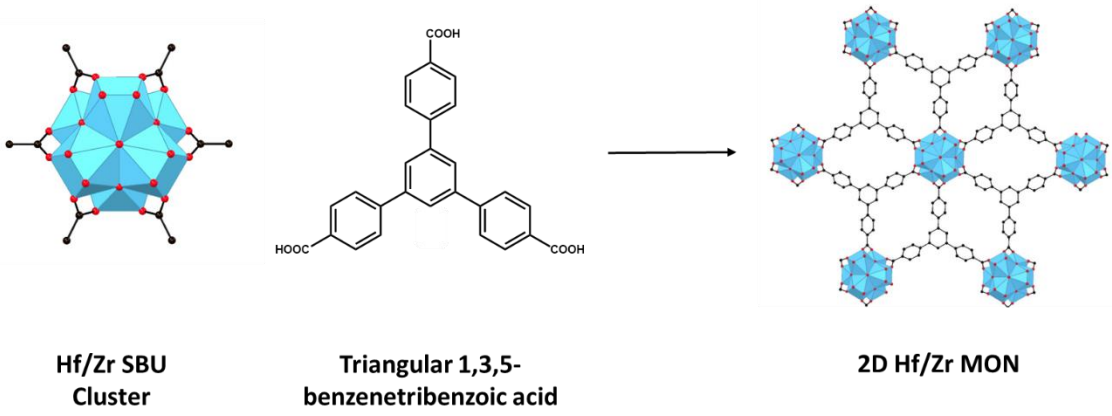

Figure 1.13: Simplified schematic of 2D Hf/Zr MON preparation

The excellent stability of the Hf/Zr-BTB based MONs is a result of the high bonding energy of the metal-carboxylate bonds with Hf–O and Zr–O bonds having values of 802 kJ mol^{-1} and 776 kJ mol^{-1} respectively which enables them to withstand refluxing in water.[54] Interestingly, 2D NUS-8 MONs display improved stability when compared to their interlocked 3D MOF analogues which has been assigned to the relief of constraints caused by interpenetration. Work by Xiong *et al.* demonstrated the stability of Hf_6-based MONs in 0.1 M phosphate buffer saline (PBS) after a 24 h incubation, highlighting it's biostability as an electrochemical sensor.[92] Other reports of Hf_6-based MONs with different triangular tricarboxylate ligands also show stability in physiological conditions for biomedical applications.[93,94]

Wenbin Lin and Cheng Wang dominate the literature surrounding these materials as well as the stacked cluster Hf_{12}/Zr_{12}-based MONs, particularly exploiting the post-synthetic functionalisation opportunities. Such materials allow for multivariate functionalisation both pre-synthetically through

the use of different metal centres, monotopic capping agents or tricarboxylate linkers and also post-synthetically through metalation, covalent conjugation or capping agent exchange which will be discussed further in the following sections.

1.3.7 Tuning of MON Surface Properties

Surface engineering of MONs can lead to the modification of surface properties (hydrophobicity, adhesivity or wettability, charge, among others) for a variety of applications including catalysis,[95–97] water purification,[98–100] and those that require cell uptake.[67,93,94,101–103] The following section discusses how MONs can be tuned pre-synthetically through the replacement of metal and/or linker components to produce materials with isoreticular structures with different functionalities. Then the scope of post-synthetic functionalisation methods will be examined. For both routes to surface modification there are a wide variety of examples from the MOF and MON literature. These sections contain the examples most relevant to the work within the thesis, including surface tuning methods available to ZIF and Hf_6/Zr_6-BTB based MONs.[30,71,72]

1.3.8 Pre-Synthetic Functionalisation

One major advantage of MONs over other 2D materials is the ability to subtly change organic linkers or metal ions/clusters without altering the topology. This enables simple pre-synthetic functionalisation to achieve periodically ordered decoration rather than the stochastic surface functionalisation observed for simple inorganic surfaces.

Recent research within the Foster group has focused introducing different chemistries via substituents on the organic linkers used to synthesise layered Cu_2-paddlewheel MOFs. The systems incorporated benzenedicarboxylate (BDC) linkers functionalised with hydrophilic methoxy-propyl chains and hydrophobic pentyl chains showed substantial differences in final concentrations after exfoliation as a result to changes in hydrophobic character. A similar study using differing alkyl chain length substituents (propyl – pentyl) resulted in higher concentrations of nanosheets accessed with

the average thickness found to decrease with increasing chain length. This work indicated that through the selection of linkers with specific substituents both the structure and properties of nanosheets could be tuned. Building on this, Ashworth and Foster reported a multi-variate approach utilising linkers with different length chains and differing hydrophilicities.[105] The synthesised MONs containing an assortment of ligands with different hydrophobic/hydrophilic character demonstrated enhanced dispersion in both polar and apolar solvents compared to the monofunctional systems. Additionally, this approach allowed for the incorporation of substituents that could not form the desired structure independently.

López-Cabrelles *et al.* demonstrated the synthesis of an isoreticular series of 2D magnetic MONs that had different surface functionality using different benzimidazole derivatives.[39] The system was similar to the previously described ZIF-7 but with Fe(II) metal centres. The 2D nanosheets synthesised retained their long-range structural order exhibiting good mechanical and magnetic properties. This work demonstrates that by incorporating functionalised (bim-X, X = Br, CH_3, NH_2) linkers the hydrophobicity of the surface was altered.

There have been reports of various Hf_6/Zr_6-based systems that involved the incorporation of different functionalised tricarboxylate based linkers whilst maintaining the kagome dual topology. Methyl- and amine-functionalised BTB,[106,107] TPY (4'-(4-benzoate)-(2,2',2''-terpyridine)-5,5''-dicarboxylate),[56,96] BTE (4,4',4''-(benzene-1,3,5-triyl- tris(ethyne-2,1-diyl))tribenzoic acid),[108] BPY (4-[2-(4-methylphenyl)-6-(5-methylpyridin-2-yl)pyridin-4-yl]benzoic acid),[48,93,94,109] TATB (4,4',4''-*s*-triazine-2,4,6-triyltribenzoate)[110] have all been utilised achieving either 100 % functionalisation or a mixed linker approach was taken. This has given rise to a huge variety of 2D MONs (Figure 1.14) with different surface functionality and active sites, with the pyridine type linkers capable of post-synthetic functionalisation to introduce photoactive compounds. Such modifications happen after the isolation of the MON layers and will be discussed in the next section.

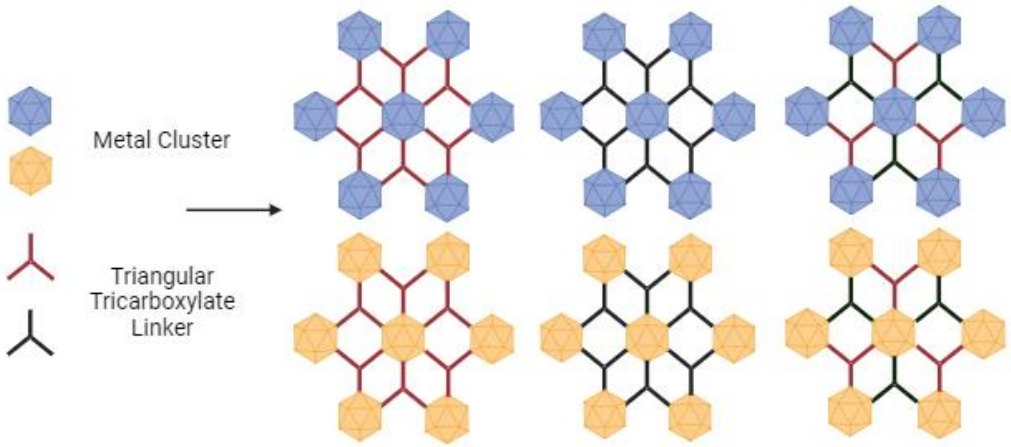

Figure 1.14: Simplified schematic demonstrating the accessibility of various 2D MONs with the same topology using different metal clusters and organic linkers.

1.3.9 Post-Synthetic Functionalisation

Post-synthetic functionalisation (PSF) involves the introduction of new functionalities following the assembly of the MON. As with analogous 3D MOF chemistry, it is not possible for certain functionalities to be introduced pre-synthetically because the desired functional group has the potential to coordinate to metal ions/clusters which may result in undesired changes to topology. Not all functional groups are compatible with or stable to the solvothermal conditions in which most metal-organic materials are synthesised, which often require high temperatures and pressures to obtain the desired crystalline phases.[104]

The major MON PSF strategies mirror those taken with MOFs and include: coordinate modification, post-synthetic exchange (PSE) and covalent functionalisation. Coordinate modification involves ligand coordination at unsaturated metal sites or more commonly metalation at linker sites.[48,49,67,93,94,111] PSE typically involves an exchange between a new coordinating ligand in solution and the MON.[48,112,113] Covalent modification describes the chemical modification of the organic linker component, with all examples in MON literature using amine binding sites.[51,114,115] These different strategies can also be combined, for example Wenbin Lin's group have developed increasingly complex systems (Figure 1.15c).[66,67,109,116]

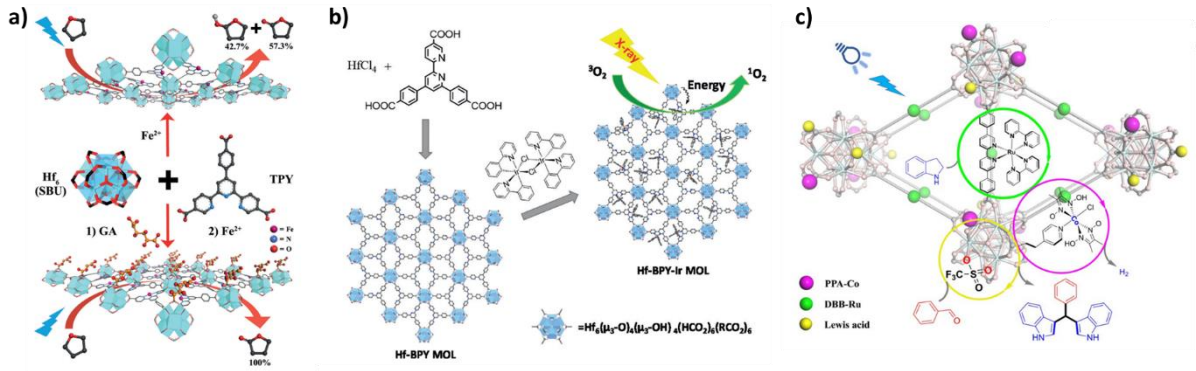

Figure 1.15: Selected representations of the types of modifications performed by Lin and Wang et al.: a) coordinative post-synthetic functionalisation and metalation of linker binding sites, b) photosensitizer based metalation, c) multivariate functionalisation including photosensitizer metalation and coordinative PSF. Taken from references 95, 94 and 109

The Lin group focus on Hf_6/Zr_6-based and Hf_{12}/Zr_{12}-based MONs, therefore these systems are the most widely reported to undergo PSF. Monotopic capping agents such as formate on the clusters can be substituted via PSE and functionalised linkers offer points of metalation or covalent attachment. The high stability of the clusters means that a large range of reaction conditions are suitable.[54] The earliest reports of post-synthetic functionalisation involved linkers such as TPY and BPY that facilitated metalation with Ru-type photosensitisers (Figure 1.15a+b) with later iterations producing photoactive MONs capable of radiodynamic therapy and photodynamic therapy.[56,93–95] Work done by shi *et al.* showed that the hydrophobic/hydrophilic character of Hf_6-TPY could be modified by PSE with various monocarboxylic acids (Figure 1.15a).[95]

A key feature of Hf_6/Zr_6-based MONs are their lewis acidic metal clusters which have enabled their use in a wide range of catalytic applications including hydrolysis, dehydrogenation and CO_2 reduction reactions, where catalytic properties were enhanced by consecutive PSF steps (Figure 1.15c).[109,112,116] Work by Quan *et al.* demonstrated three distinct PSF steps including metalation for the addition of a Ru-photosensitiser, PSE to incorporate triflate as a strong lewis acid and a separate hydrogen transfer catalyst which facilitated dehydrogenative transformations with turnover numbers of up to 500.[109]

Work done by Ling *et al*. demonstrates the only example of covalent attachment for the Hf/Zr-based MONs where amino-functionalised benzenetribenzoate linkers form a thiourea group to introduce isothiocyanate-tagged dyes which enabled effective glutathione and pH sensing.[115] The Foster group have also explored the use of covalent functionalisation where amine functionalised paddle-wheel type systems were functionalised using click-chemistry to introduce a variety of functional groups from tertiary amines to bulky pyrene molecules.[114] This approach to MON functionalisation demonstrated that the direct functionalisation of MONs resulted in much larger yields compared to their 3D layered counterparts where binding sites are less accessible. The range of both pre- and post-synthetic functionalisation reported highlights the high degree of molecular tunability of MONs.

1.4 Applications of MONs

As discussed, the programmable nature of 2D MONs has made them suitable for diverse applications.[14] The high surface areas and accessible active sites of MONs has resulted in their application in a variety of heterogeneous, photo-, and electro-catalytic processes.[56,57,85,117–119] The tunable optoelectronic properties and nanoscopic dimensions MONs possess have enabled them to be utilised in energy storage, light harvesting and emission, and other electronic devices.[106,108,120] MONs have also demonstrated their potential in a range of gas separation and water purification applications owing to their anisotropic structure and tunable porous nature.[42,99,121–123] Most relevant to this work, is the use of MONs for the detection of small molecules, ions and biomolecules.[124–126] Interest has been garnered in this area due to the diverse surface chemistries of MONs and wide range of optical and electronic properties for different pathways to detection.

1.5 MONs as Biosensors

MONs possess a number of characteristics that make them suitable for use in biosensing applications. Their high external surface areas and periodic array of binding sites are easily accessible to target analytes, facilitating rapid and sensitive detection. The modifiable structures of MONs mean each system has the potential to be tuned to improve interactions between the biological analytes and metal nodes, ligand functionalities, or adsorbates on the MON surface.

Throughout literature there are examples of MON-based sensing of small biological analytes such as glucose,[125–132] and hydrogen peroxide,[124,125,133–136] where the MON mimics horseradish peroxidase, producing reactive oxygen species (ROS) in the presence of H_2O_2. The ROS would then induce an electro- or photochemical response that is then detected. However, this review focuses on the sensing of larger biomolecules more pertinent to the work performed in later chapters. Whilst there are many sensing mechanisms, this section highlights some of the recent progress in optical, electrochemical and electrochemiluminescent (ECL) MON biosensing systems.

1.5.1 Optical sensors

The majority of MON-based optical biosensors have relied on a fluorescence quenching approach, much like many 2D material systems.[8,137] All MON-based optical biosensors are outlined in Table 1.1.[64,138–147] The most common mechanism is the quenching of fluorescing single-stranded DNA (ssDNA), where the dye-labelled ssDNA adsorbs onto the basal surface of 2D MONs resulting in quenched fluorescence due to Förster resonance energy transfer (FRET).[64,138,140–145] Following the introduction of the complementary target DNA, the fluorescence is selectively recovered as double-stranded DNA (dsDNA) is formed and no longer interacts with the MON surface. The first example was demonstrated by Zhang *et al.* using a Cu-TCPP system, where the highly accessible conjugated π-electron system of the TCPP (tetrakis(4-carboxy-phenyl)porphyrin) ligands quenched the emission of Texas red-labelled ssDNA as shown in Figure 1.16a.[64] The study compares the quenching efficiency of

the 2D MONs to the bulk MOF and H_6TCPP ligand, which both demonstrated reduced quenching capability, proving the significance of the 2D nature of the nanosheet. They go on to demonstrate the ability to detect multiple biological analytes, namely Influenza A virus subtype H5N1 gene and subtype H1N1 gene, as well as selectivity against mismatch and random DNA.

Table 1.1: Summary of 2D-MONs in optical biosensors

MON System(s)	MON Action	Analyte	Bioreceptor(s)	LOD	Ref.
Cu-TCPP	Fluorescence Quenching	Influenza A virus subtype H5N1 gene	Texas red-labeled ssDNA	20 pM	64
Co-TTPP	Fluorescence Quenching	Influenza A virus subtype H5N1 gene	Texas red-labeled ssDNA	0.1 nM	141
Cu-TCPP	Fluorescence Quenching	Salmonella enterica, Listeria monocytogenes and Vibrio parahemolyticus	Texas red-, Cy3- and FAM-labeled ssDNA	28 pM, 35 pM and 15 pM	138
$\{[Zn(HCbdcp)_2]\cdot H_2O\}_n$	Fluorescence Quenching	HIV ds-DNA	FAM-labeled ssDNA	10 pM	142
Ln-TDA (La, Nd, Eu, Tb)	Fluorescence Quenching	ATP	FAM- and TAMRA-labeled ssDNA	500 pM	144
Cu-TCPP	Fluorescence Quenching	CAP	Hairpin DNA and SYBR Green I (SG)	0.3 pg/mL	146
Cu-TCPP	Fluorescence Quenching	CAP, OTC,KANA	FAM, ROX, and Cy5-labeled ssDNA	1.5 pM, 2.4 pM and 1 pM	143
Mn-DMS	Fluorescence Quenching	microRNA	TAMRA-labeled ssDNA	0.2 pM	140
$[Fe(4\text{-}PyP)(H_2O)][Pt(CN)_4]\cdot H_2O\cdot CH_3OH$	Fluorescence Quenching	DNA	FAM-labeled ssDNA	0.3 nM	147
Zr-BTB	Fluorescence Quenching	DNA	Texas red-labeled ssDNA	0.1 nM	145
Zn-TCPP, CuTCPP, Zr-TCPP	Fluorescence Quenching	Microbial pathogens	FAM-labeled peptides	n/a	139

Following the same dye-labelled ssDNA quenching mechanism, Liu *et al.* used Co-TTPP (TTPP = 5,10,15,20-tetrakis[40-(terpyridinyl)phenyl]porphyrin) MONs also for the detection of H5N1 gene but didn't achieve the same standard in limit of detection (LOD) (0.1 nM compared to 20 pM for Cu-TCPP).[141] Other examples of ssDNA quenching based sensors include Cu-TCPP MONs for the detection of pathogen genes,[138] water-stable 2D zinc(II) zwitterionic carboxylate compound $\{[Zn(Cbdcp)(bpe)_{1/2}]\cdot 2H_2O\}_n$ was used to detect human immunodeficiency virus 1 ds-DNA (HIV ds-DNA)

sequences,[142] and Ln-TDA (2,2'- thiodiacetic acid) was used to detect ATP.[144] The Ln-TDA system demonstrated how the signal from fluorophore tags with different charge could be turned up/down. Unusually, fluorescein (FAM)-labelled *ds*DNA experienced further quenching rather than signal generation as the complex remained adsorbed to positive metal centre edges via the carboxyl and phenolic hydroxyl groups of FAM. This demonstrated the importance of surface charge in selective interactions which could be tuned via lanthanide selection.

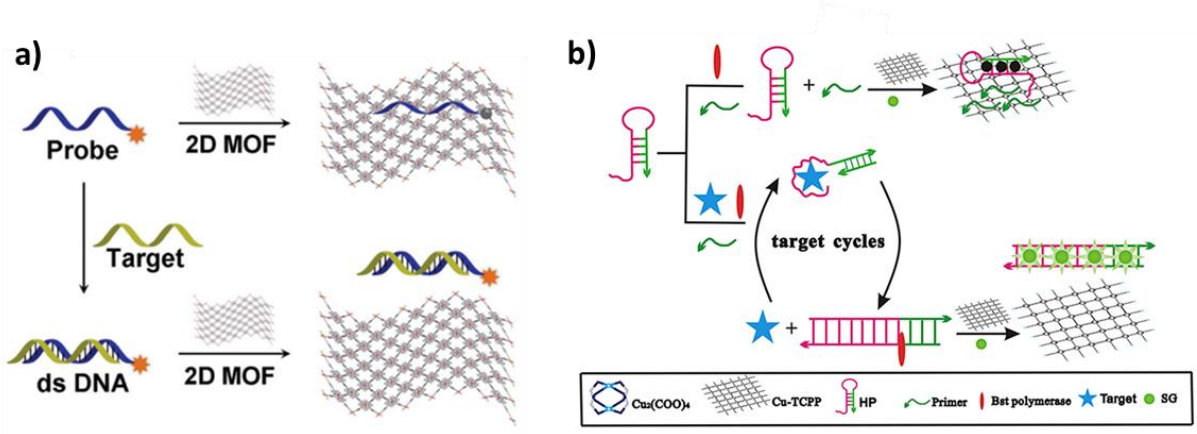

Figure 1.16 – a) Schematic illustration of 2D MOF nanosheet-based fluorescent DNA assay . Taken from reference 64, b) Schematic representation of detection of chloramphenicol (CAP) based on circular strand-replacement DNA polymerization (CSRP) and fluorescence resonance energy transfer (FRET) aptasensing platform, using Cu-TCPP nanosheets as the quencher. Taken from reference 146.

Cu-TCPP nanosheets have since been used in more complex systems to detect biomolecules such as antibiotics using the same fluorescence quenching approach (Figure 1.16b). The Gan group have developed enzyme-free systems that reported analysis of chloramphenicol (CAP) using Cu-TCPP nanosheets, claiming higher fluorescence quenching efficiency than a graphene oxide-based FRET aptasensor with a 7.5-fold improved signal-to-noise ratio.[146] The sensing capabilities were attributed to the increased number of exposed metal ion active sites of the nanosheets compared to other nanomaterials.[143,146,148] This enabled increased binding to biomolecules, enhancing sensitivity as well as reducing background signals.

The Cu-TCPP-based system has the ability to amplify the target analyte without the aid of enzymes, through a target recycling process using circular strand-replacement DNA polymerization

(CSRP) (Figure 1.16b).[146] Double stirring bar assisted target replacement (DSBTR)[143] was another enzyme-free amplification method utilised in a Cu-TCPP based sensor and hybridization chain reaction (HCR) was used in an Mn-DMS (2,2-dimethylsuccinate) based system.[140] Such approaches avoid the expense, instability and false positive results associated with enzyme assisted amplification.[97] Recycling target analytes is hugely beneficial in improving the LOD which were as low as 0.2 pM for detection of miRNA by the Mn-DMS system.[140] This combined with the manipulation of precise Y-DNA interactions facilitates highly specific sensing.

Other groups have gone on to discuss in more detail the interaction between the nanosheet surface and the *ss*DNA, to better understand the biosensing mechanism and in turn biosensing potential of various MON systems.[141,145] Lei *et al.* demonstrated that their 2D Hofmann MOF monolayer nanosheet was developed as an axial coordination platform for DNA detection via a ligand-to-metal charge-transfer of the DNA-fluorophores and Fe^{2+} active sites with a 91% quenching efficiency.[147] A comparison with the 3D bulk MOF also demonstrated the increased surface-accessible metal sites of the nanosheet improved quenching efficiency, a common theme when comparing MONs to their bulk counterparts or other 2D materials. Molecular dynamic simulations were used to investigate the different adsorption process of ssDNA and dsDNA to Zr-BTB, confirming the role of hydrogen bonding and π–π interactions for the difference in adsorption that facilitate the fluorescence quenching to “signal-on" mechanism.[145]

The work most relevant to this thesis was carried out by Sun *et al*. where three different TCPP based systems (Zn-TCPP, Cu-TCPP and Zr-TCPP) were utilized in a sensor array.[139] Two different peptide sequences (P1 - FGFGFGF and P2 - FGFKFGF) were FAM-labelled and acted as the bioreceptor, each with different isoelectric points and hydrophobicity. The different quenching abilities of the different metals within the MONs and the range in affinity the two peptides had to each MON meant six sensor elements were produced (eg. P1 and Zn-TCPP, P2 and Zn-TCPP etc.). On incubation of the systems with various pathogens the fluorescent intensities of the two peptides were recovered to

different extents. The pathogens had various compositions and could interact with nanomaterials or biomolecules through diverse nonspecific interactions. Whilst this was definitely a proof of concept assay, with limits of detection not recorded, they demonstrate that two dye-labelled peptides interact differently with similar MON surfaces. The difference in affinity was assigned to the basic side chain of lysine which carried a positive charge and was more hydrophilic under the physiological conditions. If changing just one amino acid within a peptide or swapping the metal node within a MON can influence affinity, there is potential for MON surfaces to be tuned to selectively bind specific sequences of amino acids through multiple specific interactions.

1.5.2 Electrochemical sensing

Electrochemical sensors utilize functionalised electrodes and rely on electron or ion transfer on a conductive transducer to produce a readable response. The literature surrounding MON-based electrochemical sensors is summarised in Table 1.2 and includes MON functionalised electrodes or feature the MON as a signal enhancing sandwiching component.[149–155] In all cases, immobilised bioreceptors such as aptamers and antibodies are relied on for biomolecular recognition.

A simple electrochemical aptasensor was constructed by He *et al.* utilizing zirconium based 521-MOF to coat a gold electrode.[149] PVP was used to control crystal growth in two-dimensions to maximise the surface area. Coordinative immobilisation of the aptamer was predicted as the zirconium metal nodes were thought to have strong affinity for the phosphate group of the aptamer. The target biomolecule in this case was the cancer determination marker mucin-1 and the system had a detection limit of 0.12 pg / mL. This work aimed to determine the degree of consistency between electrochemical and SPR methods, validating the electrochemical set up which showed a 5.4 fold improvement of the LOD over the SPR set up.

Table 1.2: Summary of 2D-MON based electrochemical sensors of large biomolecules.

MON System	MON Action	Analyte	Bioreceptor	LOD	Ref.
Apt/**Zr-NBB**	Electrode Coating	Mucin 1	Aptamer	0.12 pg/mL	149
PEI@GO@Ab_2/Ab_1/BSA/Ag/ **Cu-TCPP(Fe)/**MWCNT	Electrode Coating	Sulfonamides	Antibodies	0.395 ng/mL	150
Fc-Apt/BPNSs/TH/**Cu-PTTBA**	Electrode Coating	miR3123	Fc-Aptamer	0.3 pM	151
Co-BDC/ITO/MB-HPDNA/DSN (flow homogeneous assay)	Electrode Coating	microRNA	MB-Hairpin DNA	0.12 pM	152
NiCo-BDC/Ti_3C_2	Electrode Coating	Acetaminophen, Dopamine, Uric Acid	MON	0.008, 0.004 and 0.006 μM	153
(PtNi@**Cu-TCPP(Fe)**-Ab_2) – (Au@MWCNTs-Ab_1)	Signal Enhancing Sandwich	Calprotectin	Antibodies	137.7 fg/mL	154
(Ab1-**Zn-TCPP**/Fe_3O_4-COOH/Thi)-(CTAB/DES/Ab_2)	Signal Enhancing Sandwich	Cardiac Troponin I	Antibodies	0.9 pg/mL	155

Other examples of MON functionalised electrodes for electrochemical biosensing involve more complex systems than demonstrated by He *et al.*.[149] A Cu(TCPP)(Fe) based MON was employed in an immunosensor as a nanozyme where its hydrogen peroxidase mimicking activity was utilised for signal enhancement. In work done by Xiao *et al.* the proposed mechanism for detection involved the functionalisation of the electrode with multi-walled carbon nanotubes (MWCNTs), MONs, antigens and antibodies which produced a change in current on exposure to H_2O_2.[150] After incubation with polyclonal antibody functionalised PEI coated graphene oxide (PEI-GO@Ab_2) the change in current is reduced as the PEI chelates the Cu metal nodes of the MON causing degradation. Release of the photoactive TCPP(Fe) results in signal reduction. This indirect competitive electrochemical immunosensor involves the incubation of sulphonamide (target analyte) sample which interferes with antibody-antibody interactions. Increased sulphonamide concentration decreased the effect of PEI-GO@Ab_2 on the current by reducing MON degradation. The lack of recyclability of this system limits its applicability.

A copper-porphyrin based MON was utilized along with black phosphorous nanosheets (BPNSs) for microRNA detection.[151] The Cu-PTTBA (4,4',4'',4'''- (porphine-5,10,15,20-tetrayl)tetrakis benzoic acid) MON system incorporated thionine as a dopant which acted as a reference signal in current detection. A ferrocene (Fc)-labeled ssDNA aptamer was employed as the bioreceptor which via a mechanism described previously formed a complex with the target miR3123 to induce a decrease in the redox peak current of Fc (I_{Fc}, response signal). An LOD of 0.3 pM was determined and further studies demonstrated the selectivity towards the target within a mixture of biological compounds including differing microRNA. The nanocomposite of MON and BPNS experiences larger changes in current when the system is incubated with the target than with the individual components alone. The complex bioconjugate relies on all components for the enhanced electrochemical response.

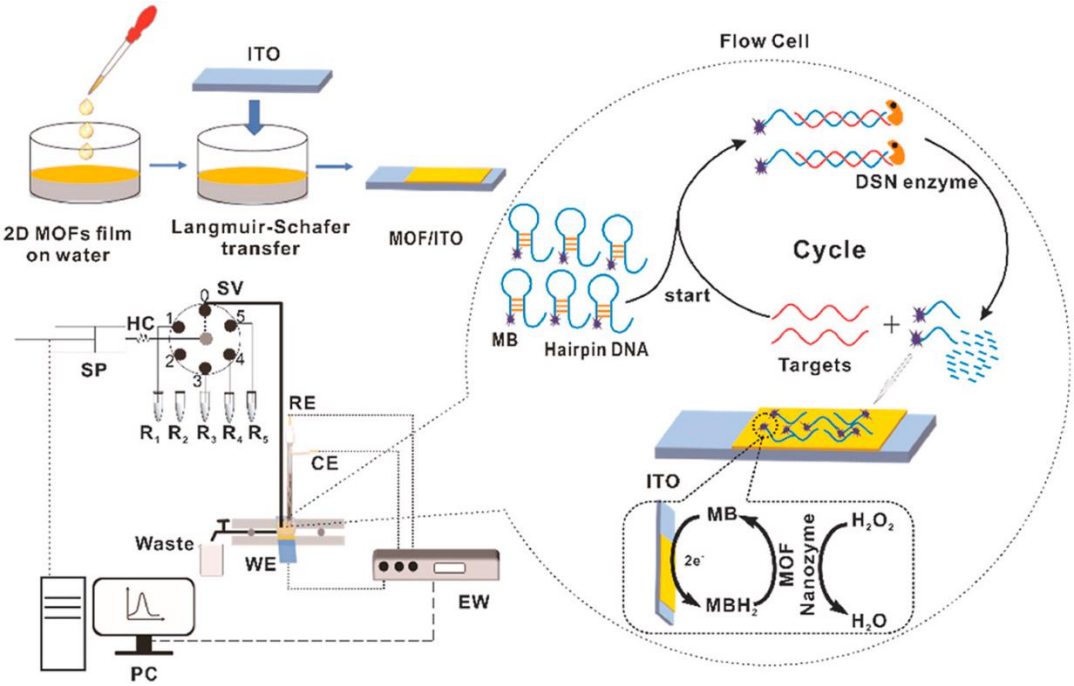

Figure 1.17: Schematic of the flow-homogeneous electrochemical assay system for microRNA based on MOF nanozyme. SP, syringe pump; HC, holding coil; SV, six-port multiposition valve; RE, reference electrode (Ag/AgCl); CE, counter electrode (Pt wire); WE, working electrode; EW: electrochemical workstation; PC, personal computer; R1–R2, sample solutions; R3, washing fluid (phosphate buffer); R4, electrolyte fluid (phosphate buffer containing 1.5 mM H_2O_2); R5, eluent (cDNA solution). Taken from reference 152.

MicroRNA was also the target analyte for a Co(BDC) (benzenedicarboxylic acid) based electrochemical biosensor where the MON again acted as a nanozyme as shown in Figure 1.17.[152] Methylene blue (MB) labelled hairpin DNA (MB-HP) hybridised with the target microRNA to form

DNA/RNA double strands. In the presence of duplex-specific nuclease (DSN) this complex would be partly hydrolysed, releasing the MB-ssDNA and microRNA into solution. The microRNA can then interact with another MB-HP and the MB-ssDNA became adsorbed on the MON coated electrode. The Co(BDC) acted as a nanozyme and in the presence of H_2O_2 oxidised the MB of the adsorbed MB-ssDNA. The oxidised MB is reduced on the surface of the electrode and an electrochemical signal is observed. The electrochemical signal is amplified by the electroactivity and enzyme-mimicking behaviour of the MON. Wang et al. demonstrated the system had excellent performance even after six regeneration cycles with a LOD of 0.12 pM.[152]

Another BDC based MON was utilized in a heterojunction for the detection of acetaminophen (AP), dopamine (DA), and uric acid (UA) via differential pulse voltammetry (DPV).[153] The catalytic active centres of the bimetallic NiCo-MON system combined with the highly conductive 2D Mxene Ti_3C_2 facilitated the electro-oxidation of AP, DA and UA without signal peak overlap. The limits of detection (LOD) of AP, DA and UA were 0.008, 0.004 and 0.006 μM respectively and the targets were also detected in samples of serum and urine to demonstrate clinical applicability. This is the only example in the MON based biosensing literature where the MON is utilised as the recognition, signal generating and transduction component, indicating that there is opportunity for multicomponent function.

Sandwich-type electrochemical immunosensors (Figure 1.18) have been extensively utilized in clinical practice owing to their high sensitivity, better selectivity, low background intensity, and broad dynamic range.[155] MONs have been selected as appropriate components of these complex systems as their tunable nature allows for the selection of highly conductive materials onto which antibodies can be immobilised. The ultrathin nature of MONs also allows for functionalisation with nanoparticles without the concerns around aggregation in pores as with 3D MOFs.

Work carried out by Dong *et al.* demonstrated the use of Cu(TCPP)(Fe) MONs functionalised with PtNi nanoparticles which increased electrocatalytic activity towards H_2O_2 reduction (Figure 1.18).[154] The platinum also provided an anchor point for the immobilisation of anti-CALP antibodies. The

electrode was functionalised with gold nanoparticle functionalised multi-walled carbon nanotubes and incubated with assembling capture antibodies. After the incubation of the functionalised electrode with the target calprotectin (CALP) and MON bioconjugate, a sandwich immunoreaction produced an electrochemical response with a LOD of 137.7 fg / mL.

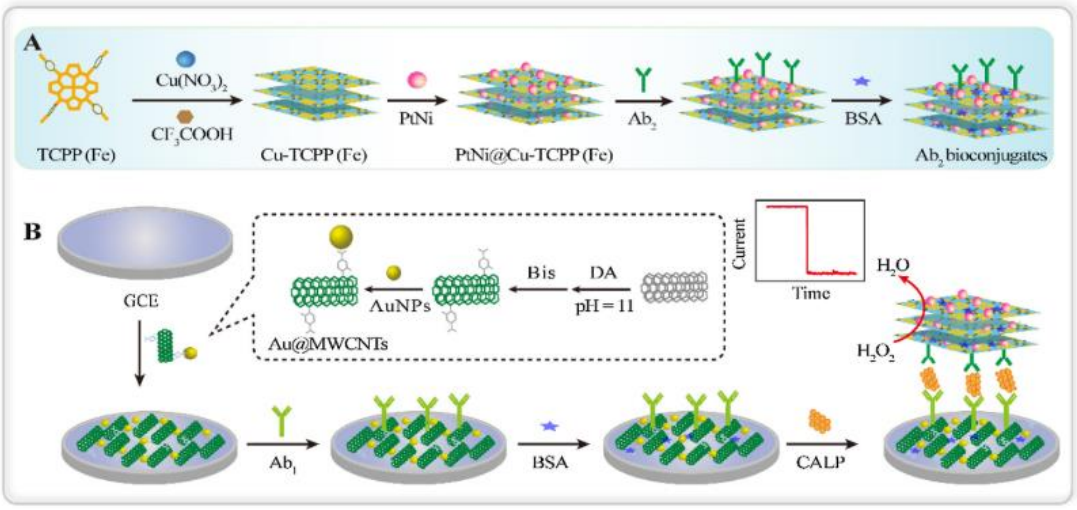

Figure 1.18: (A) The preparation procedure of PtNi@Cu-TCPP(Fe)-Ab2 bioconjugates. (B) Schematic illustration of the construction process of the sandwich electrochemical immunosensor. Taken from reference 154.

A 2D-Zn-MON nanocomposite was used as the electrochemical label in another sandwich-type immunosensors synthesised by Ahmadi *et al.* for the detection of cardiac troponin I (cTnI).[155] Zn-TCPP nanosheets were functionalised with Fe_3O_4–COOH (electrocatalyst), thionine (redox species) and anti-CTnI monoclonal antibodies (bioreceptor). The role of the nanosheet was to host the reactive components making them highly accessible and efficient in their respective roles. Compared to other reported methods to detect CTnI, the system offered lower detection limits (0.9 pg / mL) owing to the rigorously selected components.

1.5.3 Electrochemiluminescent sensing

Electrochemiluminescent (ECL) systems combine optical and electrochemical sensing. By adding a photoactive compound to an electrode-type set up, signal generation is enhanced. Through the immobilization of ECL emitters such as $Ru(bpy)_3^{2+}$ (bpy - 2,2'-bipyridine) and its derivatives onto nano-

surfaces, a variety of ECL based biosensors have been produced. The well-defined pore environments and high surface areas of metal-organic nanosheets enables increased ECL luminophore immobilisation, making them more attractive than other 2D nanomaterials.[156] It should be noted that most of the MON literature surrounding ECL biosensing have the same corresponding authors Dong-Rong Xiao and Ruo Yuan, with the groups based in two departments at Southwest University in Chongqing.[156–159] A summary of MON-based ECL sensors is shown in Table 1.3.[156–162]

Table 1.3: A summary of 2D-MON electrochemiluminescent biosensors

MON System	MON Action	Analyte	Bioreceptor	LOD	Ref.
sDNA@Ab_2/Fc-ssDNA@Ab_1/ PEI@Ru-**Hf-BTB**/Nafion	Electrode Coating	Mucin 1	Fc-/sDNA/Antibodies	0.48 fg/mL	156
AuNPs@Ru-L-Lys-**Zr-MO**L/Apt-bridge DNA-AuNPs-Fc	Electrode Coating	Mucin 1	Fc-DNA/bridge DNA/Aptamer	0.72 fg/mL	157
Zr_{12}-adb-H1/H2/H3/Apt/H4-Fc	Electrode Coating	Mucin 1	Fc-/Hairpin DNA/Aptamer	0.25 fg/mL	158
H1/Fc-sDNA/**Hf-ETTC**/Nafion (Nb·BbvCI)	Electrode Coating	Carcinoembryonic antigen (CEA)	Hairpin DNA/Fc-ssDNA	0.63 fg/mL	159
(**Ru/Zn-MON**@sDNA/MCH) - (Fe_3O_4@SiO_2@Au-cDNA)	Signal Enhancing Sandwich	miRNA-141	cDNA/sDNA	0.3 fM	160
Ru/Zn-MON@sDNA2) - (Fe_3O_4@AuNPs@HP1/HP2) – (g-C_3N_4@AuNPs-sDNA1)	Signal Enhancing Sandwich	miRNA-21	Hairpin DNA/sDNA	0.3 fM	161
(**Ru/Zn-MOF**@Ab_2) – (Ab_1-GCE)	Signal Enhancing Sandwich	Cardiac Troponin I	Antibodies	0.48 fg/mL	162

The first example of a MON-based ECL biosensor was reported in 2019 by Hu *et al.*, comprised of Hafnium clusters onto which the luminophore $Ru(bpy)_2(mcpbpy)^{2+}$ was grafted.[156] The nanosheet was chosen to solve problems faced by 3D MOF based systems, for example leakage of physically absorbed or entrapped luminophores, reducing the stability of the ECL MOF-based immunosensor.[162] Whilst ultra-stable 3D mesoporous luminescent functional MOFs have been reported, issues still arise due to the long path of ion/electron migration and diffusional constraints within bulk material. This inhibits the electrochemical activation of the interior luminophores.[156] Ultrathin 2D MONs shorten the transportation length of ions/electrons, which increases the activity of luminophores as well as there

being a vastly greater number of accessible post-modification active sites for luminophore attachment. The ECL sensing platform designed by Hu *et al.* is demonstrated in Figure 1.19, where polyethylenimine (PEI) was decorated onto Ru-Hf-MOL as a coreactant.[156]

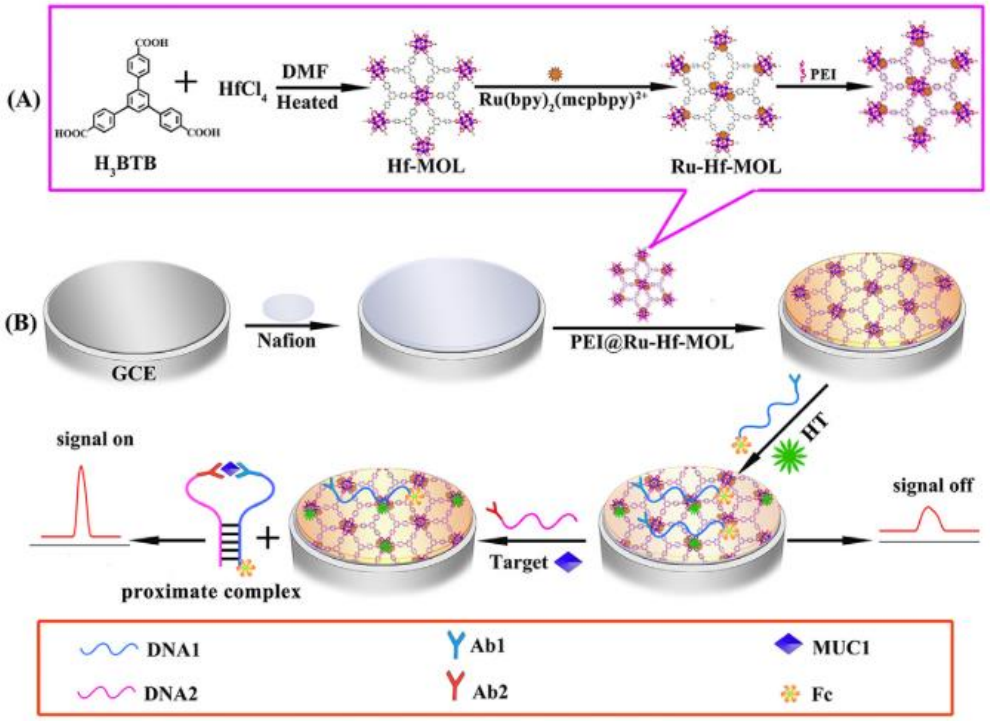

Figure 1.19 – A schematic representation of (A) The synthesis of PEI@Ru-Hf-MOL and (B) the construction of the sensor. Taken from reference 156.

The sensing mechanism involved the addition of ferrocene and antibody (Ab1) labelled ssDNA as well as blocking agent (hexanethiol - HT) to the PEI@Ru-Hf-MOL coated glass carbon electrode.[156] The ssDNA complex acted as a quencher as it absorbed strongly through π-π stacking allowing the ECL emission of $Ru(bpy)_2(mcpbpy)^{2+}$ to be effectively quenched by ferrocene (the signal off state). On addition of the target mucin 1 and antibody (Ab2) labelled ssDNA complementary to the first ssDNA, target-induced proximity hybridization occurred resulting in the formation of the proximate complex as shown in Figure 1.19 with a LOD of 0.48 fg / mL.

The same group utilised a self-enhanced ruthenium complex (Ru-L-Lys) as an ECL luminophore which grafted to the Zr-MON through lysine to produce a novel self-enhanced ECL complex (Ru-L-Lys-Zr-MON) for mucin-1 detection.[157] The self-enhanced nature of the luminophore complex is a result

of the combination of the Ru-luminophore and amino-acid (lysine) coreactant which can greatly improve the ECL intensity and efficiency due to the shorter electronic migration distance and lower energy loss compared with the observations for intermolecular interaction. The complex sensing system involves an exonuclease I-stimulated target recycling amplification strategy, introduced to enhance the ECL response. A further eight components were required including ferrocene-labelled gold nanoparticles and mucin 1 aptamers. Similar comparisons to bulk 3D MOF and other 2D materials revealed improved ECL efficiency with the Ru-l-Lys-Zr-MON system and a LOD of 0.72 fg / mL.[157]

Ru-complex free metal-organic nanosheet systems have also been developed, removing the cost and steric hinderance issues associated with $Ru(bpy)_3^{2+}$ and its derivatives.[158] Restriction of intramolecular motions (RIM) as a means to increase ECL efficiency inspired the design of a 2D Zr_{12}-adb (adb = 9,10-anthracene dibenzoate) "nanoplate". Post-synthetic modification with phosphate terminal hairpin DNA1 via strong coordination between phosphate and zirconium created a strong ECL emitter. Combined with the bipedal walking molecular machine (BWMM) amplification strategy, the sensor had a LOD of 0.25 fg mL^{-1} of mucin 1 improving upon their previous work mentioned earlier with a LODs of 0.48 fg mL^{-1} and 0.72 fg mL^{-1}.[156,157] By immobilising adb as bridging ligands the intramolecular motion is reduced, thereby supressing non-radiative energy consumption and improving ECL intensity and efficiency. Not only this but the porosity and ultrathin thickness of the "nanoplates" is thought to accelerate the migration of ions and electrons resulting in the internal and external adb to be electrically activated, which further increased utilization ratio of adb and improved ECL efficiency.[158]

A second Ru-complex free ECL platform for the ultrasensitive biosensing of carcinoembryonic antigen (CEA), utilised an aggregation-induced emission (AIE) ligand.[159] This work also refers to the RIM of the AIE ligand which promotes ECL enhancement. The AIE-ligand in this case is 4',4''',4'''',4''''''-(ethene-1,1,2,2-tetrayl)tetrakis(([1,1'-biphenyl]-4-carboxylic acid)) (H_4ETTC), which yielded a higher ECL efficiency when incorporated into the MON compared to H_4ETTC monomers, aggregates, and bulk

3D MOF. The ligand shows strong fluorescence as a result of their restricted intramolecular rotation and vibration, thereby making them extremely suitable candidates in the fabrication of MONs for ECL sensing applications. The sensing platform involved the construction of a Hf-ETTC-MOL/Nafion/GCE which strongly adhered ferrocene-labelled ssDNA to quench emission (Figure 1.20). The LOD for CEA in this case was 0.63 fg / mL where CEA is considered within normal limits at a level of < 3.0 ng / mL. CEA was also detected in spiked human serum samples with recovery values ranging from 98.6 % to 105 %.

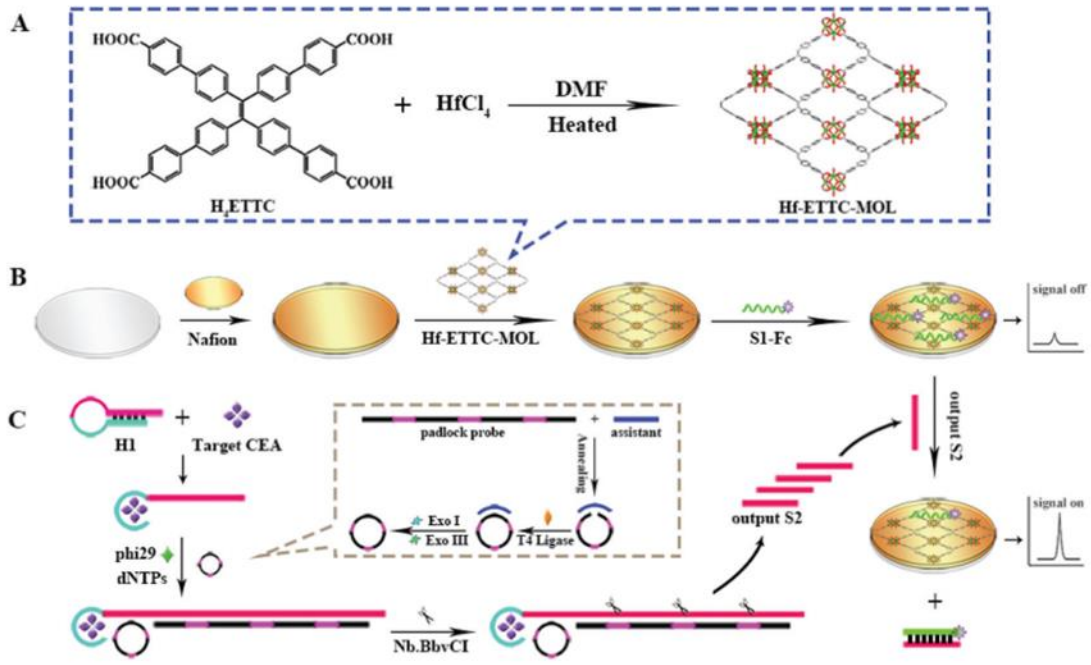

Figure 1.20: (A) Synthesis of the Hf-ETTC-MOL, (B) construction of the aptasensor, and (C) illustration of the RCA. Taken from reference 159.

A different approach was taken by Shao *et al.* where the ECL luminophore tris(4,4'-dicarboxylic acid-2,2'-bipyridyl) ruthenium(II) ($Ru(dcbpy)_3^{2+}$) was utilized as the organic linker component.[160] Another strategy to solve MOF ECL issues through incorporation of the luminophore into the system, restricted to two dimensional growth. The MON behaved as a sandwich-type signal enhancer alongside a complex capture unit (Fe_3O_4@SiO_2@Au-cDNA) with grafted sDNA employed as the bioreceptor for the detection of miRNA-141. The same group demonstrated dual miRNA detection where graphitic carbon nitride acted as another sandwich-type component.[161] The LOD in both cases was 0.3 fM, an improvement on other miRNA biosensors with various methods of detection.[160] Yan *et*

al. also used the Ru-Zn-MON system in a sandwich type immunosensor for the detection of cardiac tropin 1 (Figure 1.21) where the biomolecular recognition components were antibodies.[162] The LOD for this set up was 0.48 fg / mL significantly better than the 0.9 pg / mL LOD for the complex Zn(TCPP)-based electrochemical set up mentioned previously.[155] Demonstrating the efficacy of utilizing the photoactive component as the organic linker.

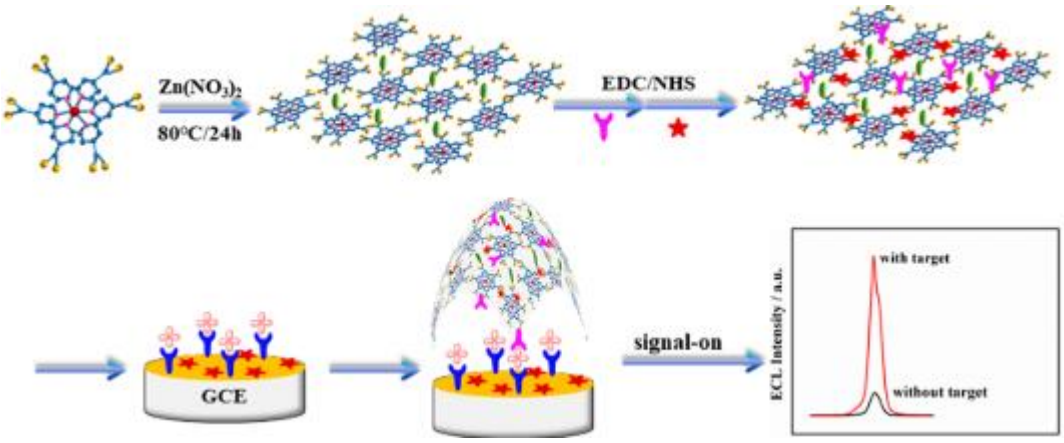

Figure 1.21 - Schematic diagram of the sandwich immunosensor based on a Zn-$(Ru(dcbpy)_3^{2+}$ metal-organic nanosheet. Taken from reference 162.

The various ECL sensors described above and summarised in Table 1.3 reveals the advantage of MONs over currently explored 2D nanomaterials as well as bulk 3D MOFs. The chemical tunability, stability and diversity of these ultrathin materials with hugely useful and vast surface-areas makes them extremely attractive candidates for biosensing applications. Previous work has provided new and efficient strategies to design ever improving, high-performance ECL materials suited to signal transduction.

1.5.4 Summary of MONs as biosensors

The reported literature thus far has utilised MONs in a variety of roles such as fluorescence quenchers, bioconjugate platforms or luminescent emitters within optical, electrochemical and electrochemiluminescent biosensors. Of the three types of MON-based biosensors discussed, electrochemiluminescent systems generally demonstrated the best limits of detection (LOD). This was

especially the case for the detection of microRNA (0.3 fM) and cardiac tropin I (0.48 fg / mL) by Ru/Zn-MONs, [130–132] and mucin 1 (0.25 fg / mL) by Zr_{12}-adb with BWMM amplification.[128] Such cases also demonstrated improved sensitivity over current methods reported for the detection of the respective target biomolecule. For some perspective, commercially available mucin 1 ELISA (enzyme linked immunosorbent assay) detection kits by FineTest® have a sensitivity of 9.375 pg / mL and cardiac troponin I ELISA detection kits by Invitrogen have a sensitivity of 100 pg / mL.[163,164]

The sensitivity was achieved through the rational selection of linker components such Ru-based luminophores or extended aromatic compounds showing enhanced ECL properties through the restriction of intramolecular motion (RIM). Despite such promising examples, there are only a handful of ECL based MON biosensors reported with the majority involving expensive Ru-complexes. In all cases, the system relies on ferrocene-labelled ssDNA or antibodies as bioreceptor components to provide biomolecular recognition.

Electrochemical based-biosensors were less sensitive, where microRNA was detected by Co-BDC (LOD = 0.12 pM),[152] cardiac tropin I was detected by Zn-TCPP (LOD = 0.9 pg / mL),[127] and mucin 1 was detected by Zr-NBB (LOD = 0.12 pg / mL).[149] The MONs acted as bioconjugate platforms and often relied on multiple components such as bioreceptors, nanoparticles as electrocatalysts and enzymes for target amplification for the achieved degree of sensitivity. Unlike the ECL systems the active components were not incorporated as linkers therefore sensitivity was reliant on their efficient loading.

The optical MON-based sensors proved to be the least sensitive, where LODs were in the nM – pM range. In some cases, there were clear advantages of the periodic array of metal-centres that provide an improved quenching performance over simple 2D materials. For example, Cu-TCPP nanosheets claimed higher fluorescence quenching efficiency than a graphene oxide-based sensor for the detection of CAP owing to its accessible metal nodes.[146] However, due to the similarity in sensing mechanism for MONs and other 2D material generally the detection limits were similar. Nonetheless,

the range in quenching efficiencies afforded by different metal centres has gained interest in assay based detection.[139]

Whilst there are a huge number of biomedically relevant targets to detect, current trends in MON based literature have focused on a few examples where bioreceptors are already well defined and easily incorporated. The tunable 2D array of metal-organic nanosheets has already demonstrated improved sensing capabilities over simple 2D materials and commercially available detection kits, particularly for the ECL based set ups. The unique ability to incorporate metal-centres and organic linkers with specific properties that can also be post-synthetically tuned offers a considerable advantage for biosensor design. However, such properties have only been interrogated and optimised in regards to signal transduction.

The inherent biomolecular recognition capabilities of MONs have not yet been explored. The excellent ECL sensors proved the advantages of including the photoactive component as the linker within the MON structure for improved sensitivity. We hypothesise that the same approach can be taken for the biomolecular recognition element. We predict the specific periodic array of functionalisable linkers and modifiable metal nodes can mimic bioreceptor sites. This project aims to interrogate whether MONs can selectively bind different peptide sequences, driving miniaturisation, and increasing both the sensitivity and selectivity towards a given target. However, the diversity of both MONs and peptide sequences and the complexity of interactions between the two means identifying strongly binding combinations for use as highly selective sensors is a formidable challenge.

1.6 Biopanning

One approach to exploring peptide-substrate interactions is through biopanning. Biopanning is an affinity selection technique where a target is exposed to a library of possible binding compounds via molecular display.[165] The library contains a large number of subtly different possible binding complexes, usually peptides, of which the strongest target binders are fished out and identified. Much

like natural selection, this technique sequentially and efficiently identifies compounds which bind with the highest affinity through competitive binding and eliminates weaker binders.[166] The target is generally defined as the substrate used to screen the library and the equivalent binding partner of the target is referred to as the template. The target-binding compound is described as the mimotope, as it mimics the template in its binding to the target.[167]

Biopanning is an umbrella term for many selection techniques including phage display, bacterial display, yeast display, ribosome display and mRNA display.[165,166,168–170] Such techniques are often described as protein evolution techniques as whilst the display system involves the protein expressed on various biological entities, it is only the binding protein that is of interest. Bacteriophage display is the most common type of display system used and is utilised in this work therefore will be discussed in detail.

1.6.1 Phage display

Bacteriophage are viruses that can infect bacteria, replicate inside them, and can be extracted and purified easily. Phage display technology takes advantage of the simplicity of phage amplification as well as its tolerance of a broad range of selection conditions. Filamentous phage M13 is the most commonly used vector to create random peptide and protein displaying libraries.[171] Foreign DNA is inserted into the genome of the filamentous phage, which results in the pentavalent display of foreign peptides. Such peptides are expressed on a coat protein on the surface of phage, most commonly the PIII protein. This creates a physical link between each discrete peptide expressed on the phage surface and the DNA encoding it within the phage, therefore DNA sequencing of each phage determines the displayed peptide sequences.[171–174] A library of phage, each expressing distinct peptides, enables the efficient identification of peptides that bind to a desired target (Figure 1.22). The phage library is added to the target, non-binding phage are washed away, and the specifically bound phage are eluted. The eluted phage are then amplified and the process is repeated at least another two times to enrich the pool of phage with competitive binders.

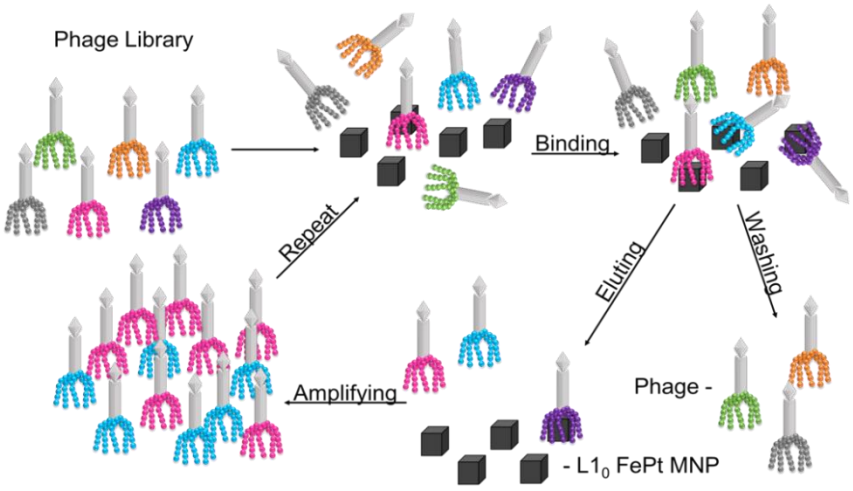

Figure 1.22: Simplified schematic of the phage display process including addition of phage library, phage binding, washing of magnetic nanoparticles (MNPs), elution of phage from MNPs, amplification of eluted phage which completes one panning round.

The phage display protocol requires stringent measures to avoid phage contamination. The library of M13KE differs from wild-type filamentous phage as the lacZα-peptide cloning sequence, which enables detection of phage plaques, is inserted into phage DNA. This insertion results in plaques appearing blue when plated on media containing XGAL and IPTG but also results in a longer phage replication cycle. As well as this, displaying foreign peptides on the N-termini may attenuate infectivity of the library phage relative to wild-type phage M13. Therefore, there is the potential for *in vivo* selection of any infecting wild phage during the amplification step. In the absence of a high affinity *in vitro* binding selection, minute amounts of contamination can lead to the majority of the resulting phage pool being wild-type after multiple panning rounds.[172]

Morton *et al.* utilized phage display to determine peptide binders that were able to distinguish *Listeria monocytogenes* from other *Listeria* species. [175] The group identified an expressed peptide with a 43-fold binding preference for *L. monocytogenes* through the sequential biopanning using a phage library. The biopanning regime employed subtraction biopanning against *L. innocua*, the strain genetically closest to *L. monocytogenes* to successfully increase the probability of identifying *L. monocytogenes*-specific binders.[176] The binders identified have the potential to be used for the development of more rapid and specific detection methods for *L. monocytogenes* in food and clinical

samples.[175] Identifying disease recognition molecules is one example of the wide range of uses of phage display. It has also been used in the development of techniques for the rapid detection of Mycobacterium avium subspecies paratuberculosis (MAP), for single photon emission computed tomographic (SPECT) imaging of resistance-susceptible breast cancer and for epitope mapping of radioimmunotherapy drugs.[177–179]

Phage display was also used to select peptides with high binding affinity to serum antibodies from patient with Lyme disease (LD) by Kouzmitcheva *et al.*.[180] The selected peptides were surveyed for reactivity with a panel of positive sera (LD patients) and negative sera (patients without LD), thus identifying 17 peptides with a diagnostically useful binding pattern: reactivity with at least three positive sera and no reactivity with any of the negative sera. Peptides like these could be the basis of a new diagnostic enzyme-linked immunosorbent assay for LD, with sufficient specificity and sensitivity to replace expensive immunoblotting tests that are currently required for definitive serological diagnosis.[180]

Another use of phage display is in materials synthesis where peptides/proteins have been used to impart control over particle nucleation, size and morphology.[181] Highly uniformed nanoscale crystals exist throughout nature, often formed under ambient conditions.[182] One way this level of control is achieved is through organic matrix-mediated biomineralisation. The specificity of a protein for a given synthetic material can be linked to both chemical and structural recognition mechanisms. The remarkable control via biomineralisation observed in nature has inspired investigations into new methods for synthesising inorganic materials. Through biomimicry, hybrid materials can be assembled from the molecular level using the recognition properties of proteins under the premise that inorganic surface-specific polypeptides could be used as binding agents to control the ordering and specific function of materials. Biomolecules have been utilised as biomineralisation templates for a range of nanomaterials including magnetic particles and MOFs.[182–184]

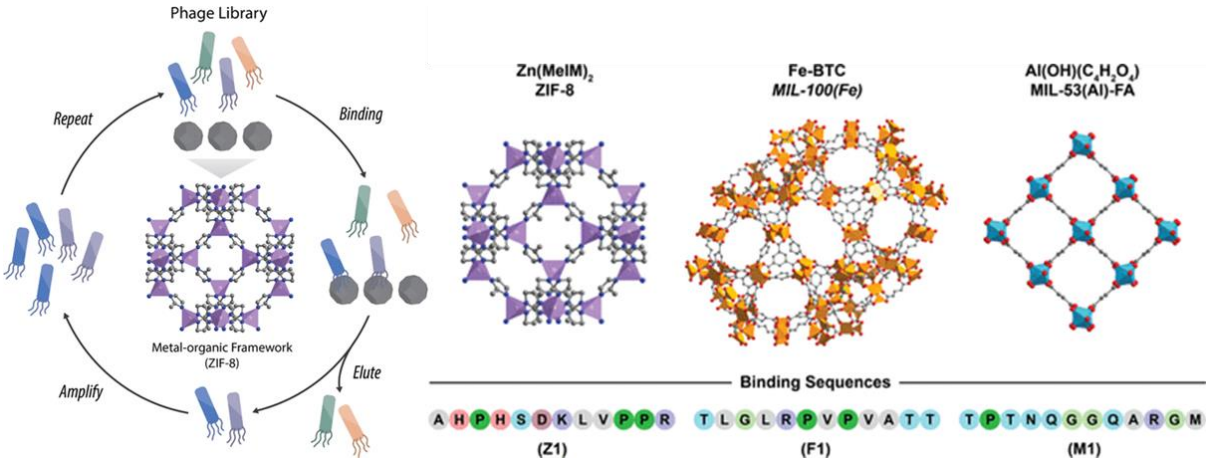

Figure 1.23: Schematic of phage display for identification of MOF-binding short peptide sequences and the structures of ZIF-8, $Fe_3X(H_2O)_2(BTC)_2{\cdot}nH_2O$ (iron carboxylate, MIL-100, an analogue to the semi amorphous Fe-BTC structure is shown), MIL-53(Al)–FA, and their corresponding MOF-binding peptide sequences. Taken from reference 185.

As well as epitope mapping and biomineralisation, phage display has been employed for the identification of sequence specific peptides that bind with high affinity to MOFs for noncovalent functionalisation (Figure 1.23).[185] Work done by Fan *et al.* demonstrated that peptides could differentiate between different metal–organic framework systems with on-target binding measuring dissociation constants (K_d) as low as 12 ± 5 μM. This is consistent with previous reports where noncovalent interactions between biological macromolecules, including peptides, and inorganic materials have dissociation constants between 10^{-5} and 10^{-7} M.

This work has inspired the investigation of peptide-MON interactions in order to examine biomolecular recognition capabilities. The two-dimensional nanoscopic periodic array of binding sites are predicted to selectively bind specific sequences of amino acids. Due to the low dimensionality of MONs it is predicted that a consensus peptide would be identified.

Whilst phage display is the oldest and most common molecular display technique it is more susceptible to contamination (by wild phage) which could render a panning round useless. Phage concentration, is determined by time-consuming microbiological titration, in which dilutions of phage suspension are used to infect plated bacterial hosts.[186] Elution of phage can only be achieved by breaking the peptide-target interaction. In general, interactions can be overcome specifically with

competitive ligand to the target of interest or nonspecifically by changing the target conformation. Elution is achieved via exposure to glycine-HCl buffer (pH 2.2) followed by alkaline triethylamine-based elution buffer (pH 11).[168] Phage expressing peptides with very high affinity to the target may never be eluted, even after multiple attempts.[186] Considerations must be made regarding the suitability of MONs towards phage display conditions with aqueous stability a primary concern.

1.7 Aims

This thesis aims to explore the use of MONs within biosensors as biomolecular recognition components. This is moving away from the current trends in research that utilises MONs as the transduction element and relies on additional bioreceptors for selectivity. The rational selection of linkers and metal building blocks has already demonstrated advantages in incorporating chemistries that enhance biosensing capabilities. This work focuses on designing and synthesising a library of physiologically stable MONs and investigating their inherent selectivity towards different peptides.

Chapter 2 explores the use of pre-synthetic functionalisation through the introduction of different linker derivatives (bim-X, where X = H, Br, NH_2, CH_3) and metal nodes (Zn and Co) and the impact this has on the dimensions, surface properties and biostability of ZIF MONs. **Chapter 3** interrogates whether different MON systems selectively bind to different peptides through the use of phage display. It also explores the viability of MONs as the biomolecular recognition element within a QCM biosensor. **Chapter 4** investigates whether amine functionalised ZIF MONs from chapter 1 can undergo covalent post-synthetic functionalisation to further tune binding sites. **Chapter 5** explores the modification of Hf-BTB-NH_2 MON surfaces through the use of coordinative ligand exchange to incorporate amino acids. Finally, **Chapter 6** draws the previous four chapters together in an overall conclusion and outlook.

1.8 References

1 T. Sun, G. Qing, B. Su and L. Jiang, *Chem. Soc. Rev.*, 2011, **40**, 2909–2921.

2 Y. Ma, X. Tian, L. Liu, J. Pan and G. Pan, *Acc. Chem. Res.*, 2019, **52**, 1611–1622.

3 L. Farzin, M. Shamsipur, L. Samandari and S. Sheibani, *J. Pharm. Biomed. Anal.*, 2018, **161**, 344–376.

4 C. Doonan, R. Riccò, K. Liang, D. Bradshaw and P. Falcaro, *Acc. Chem. Res.*, 2017, **50**, 1423–1432.

5 N. Rohaizad, C. C. Mayorga-Martinez, M. Fojtů, N. M. Latiff and M. Pumera, *Chem. Soc. Rev.*, 2021, 50, 619–657.

6 H. Huang, W. Feng and Y. Chen, *Chem. Soc. Rev.*, 2021, 50, 11381–11485.

7 C. Zhu, D. Du and Y. Lin, *Biosens. Bioelectron.*, 2017, **89**, 43–55.

8 A. Bolotsky, D. Butler, C. Dong, K. Gerace, N. R. Glavin, C. Muratore, J. A. Robinson and A. Ebrahimi, *ACS Nano*, 2019, **13**, 9781–9810.

9 A. Murali, G. Lokhande, K. A. Deo, A. Brokesh and A. K. Gaharwar, *Mater. Today*, 2021, 50, 276–302.

10 S. Su, Q. Sun, X. Gu, Y. Xu, J. Shen, D. Zhu, J. Chao, C. Fan and L. Wang, *TrAC - Trends Anal. Chem.*, 2019, **119**, 115610.

11 S. Arun Kumar, B. Balasubramaniam, S. Bhunia, M. K. Jaiswal, K. Verma, Prateek, A. Khademhosseini, R. K. Gupta and A. K. Gaharwar, *WIREs Nanomedicine and Nanobiotechnology*, 2021, **13**, e1674.

12 M. T. Ulhakim, M. Rezki, K. K. Dewi, S. A. Abrori, S. Harimurti, N. L. W. Septiani, K. A. Kurnia, W. Setyaningsih, N. Darmawan and B. Yuliarto, *J. Electrochem. Soc.*, 2020, **167**, 136509.

13 D. J. Ashworth and J. A. Foster, *J. Mater. Chem. A*, 2018, **6**, 16292–16307.

14 J. Nicks, K. Sasitharan, R. R. R. Prasad, D. J. Ashworth and J. A. Foster, *Adv. Funct. Mater.*, 2021, **31**, 2103723.

15 N. Bhalla, P. Jolly, N. Formisano and P. Estrela, *Essays Biochem.*, 2016, **60**, 1–8.

16 S. Ahmad Dar, M. Sharjeel Sofi, S. Ahmad Dar and M. Nabi, in *Trends in Engineering, Applied Science and Management*, Hyderabad, 2018, pp. 414–420.

17 Point-of-Care Testing | Lab Tests Online-UK, https://labtestsonline.org.uk/articles/point-care-testing, (accessed 21 May 2020).

18 J. A. Goble and P. T. Rocafort, *J. Pharm. Pract.*, 2017, **30**, 229–237.

19 J. A. McCammon, *Curr. Opin. Struct. Biol.*, 1998, **8**, 245–249.

20 K. Kahn and K. W. Plaxco, in *Recognition Receptors in Biosensors*, Springer New York, New York, NY, 2010, pp. 3–45.

21 G. Safina, *Anal. Chim. Acta*, 2012, **712**, 9–29.

22 P. Damborský, J. Švitel and J. Katrlík, *Essays Biochem.*, 2016, **60**, 91–100.

23 X. Qiu and N. Hildebrandt, *ACS Nano*, 2015, **9**, 8449–8457.

24 C. H. Camp and M. T. Cicerone, *Nat. Photonics*, 2015, **9**, 295–305.

25 J. L. Hammond, N. Formisano, P. Estrela, S. Carrara and J. Tkac, *Essays Biochem.*, 2016, **60**, 69–80.

26 J. Wu, H. Liu, W. Chen, B. Ma and H. Ju, *Nat. Rev. Bioeng.*, 2023, **1**, 346–360.

27 O. A. Sadik, A. O. Aluoch and A. Zhou, *Biosens. Bioelectron.*, 2009, **24**, 2749–2765.

28 J. P J, K. Prabakaran, J. Luo and D. H. M G, *Sensors Actuators A Phys.*, 2021, **331**, 113020.

29 G. Sauerbrey, *Zeitschrift für Phys.*, 1959, **155**, 206–222.

30 H. J. Lim, T. Saha, B. T. Tey, W. S. Tan and C. W. Ooi, *Biosens. Bioelectron.*, 2020, **168**, 112513.

31 Q. Ouyang, S. Zeng, L. Jiang, J. Qu, X. Q. Dinh, J. Qian, S. He, P. Coquet and K. T. Yong, *J. Phys. Chem. C*, 2017, **121**, 6282–6289.

32 N. Zakirov, S. Zhu, A. Bruyant, G. Lérondel, R. Bachelot and S. Zeng, *Biosensors*, 2022, **12**, 810.

33 Q. Li, L. Xu, K. W. Luo, X. F. Li, W. Q. Huang, L. L. Wang and Y. Bin Yu, *J. Mater. Chem. C*, 2017, **5**, 4426–4434.

34 S. Das, R. Gulotty, A. V. Sumant and A. Roelofs, *Nano Lett.*, 2014, **14**, 2861–2866.

35 Y. Wang, Y. Wang, D. Wu, H. Ma, Y. Zhang, D. Fan, X. Pang, B. Du and Q. Wei, *Sensors Actuators, B Chem.*, 2018, **255**, 125–132.

36 M. Xiao, T. Man, C. Zhu, H. Pei, J. Shi, L. Li, X. Qu, X. Shen and J. Li, *ACS Appl. Mater. Interfaces*, 2018, **10**, 7852–7858.

37 Invitrogen CEA Human ELISA Kit, https://www.thermofisher.com/elisa/product/CEA-Human-ELISA-Kit/EHCEA.

38 A. Faghani, I. S. Donskyi, M. Fardin Gholami, B. Ziem, A. Lippitz, W. E. S. Unger, C. Böttcher, J. P. Rabe, R. Haag and M. Adeli, *Angew. Chemie*, 2017, **129**, 2719–2723.

39 J. López-Cabrelles, S. Mañas-Valero, I. J. Vitórica-Yrezábal, P. J. Bereciartua, J. A. Rodríguez-Velamazán, J. C. Waerenborgh, B. J. C. Vieira, D. Davidovikj, P. G. Steeneken, H. S. J. van der Zant, G. Mínguez Espallargas and E. Coronado, *Nat. Chem.*, 2018, **10**, 1001–1007.

40 A. J. Clancy, H. Au, N. Rubio, G. O. Coulter and M. S. P. Shaffer, *Dalt. Trans.*, 2020, **49**, 10308–10318.

41 R. Sakamoto, K. Takada, T. Pal, H. Maeda, T. Kambe and H. Nishihara, *Chem. Commun.*, 2017, **53**, 5781–5801.

42 T. Rodenas, I. Luz, G. Prieto, B. Seoane, H. Miro, A. Corma, F. Kapteijn, F. X. Llabrés I Xamena and J. Gascon, *Nat. Mater.*, 2015, **14**, 48–55.

43 N. R. Champness and M. Schröder, *Curr. Opin. Solid State Mater. Sci.*, 1998, **3**, 419–424.

44 S. R. Batten, N. R. Champness, X. Chen, J. Garcia-martinez, S. Kitagawa, L. Öhrström, M. O. Keeffe, M. P. Suh and J. Reedijk, *Pure Appl. Chem.*, 2013, **85**, 1715–1724.

45 R. W. Corkery, *Curr. Opin. Colloid Interface Sci.*, 2008, **13**, 288–302.

46 J. K. Wychowaniec, H. Saini, B. Scheibe, D. P. Dubal, A. Schneemann and K. Jayaramulu, *Chem. Soc. Rev.*, 2022, **51**, 9068–9126.

47 P. Z. Moghadam, A. Li, S. B. Wiggin, A. Tao, A. G. P. Maloney, P. A. Wood, S. C. Ward and D. Fairen-Jimenez, *Chem. Mater.*, 2017, 29, 2618–2625.

48 G. Lan, Z. Li, S. S. Veroneau, Y. Y. Zhu, Z. Xu, C. Wang and W. Lin, *J. Am. Chem. Soc.*, 2018, **140**, 12369–12373.

49 Y. Shu, J. Chen, Z. Xu, D. Jin, Q. Xu and X. Hu, *J. Electroanal. Chem.*, 2019, **845**, 137–143.

50 D. Sheberla, L. Sun, M. A. Blood-Forsythe, S. Er, C. R. Wade, C. K. Brozek, A. Aspuru-Guzik and M. Dincă, *J. Am. Chem. Soc.*, 2014, **136**, 8859–8862.

51 J. Nicks, J. Zhang and J. A. Foster, *Chem. Commun.*, 2019, **55**, 8788–8791.

52 Y. Li, F. Liang, H. Bux, W. Yang and J. Caro, *J. Memb. Sci.*, 2010, **354**, 48–54.

53 H. Saini, P. Kallem, E. Otyepková, F. Geyer, A. Schneemann, V. Ranc, F. Banat, R. Zbořil, M. Otyepka, R. A. Fischer and K. Jayaramulu, *J. Mater. Chem. A*, 2021, **9**, 23651–23659.

54 Z. Hu, E. M. Mahdi, Y. Peng, Y. Qian, B. Zhang, N. Yan, D. Yuan, J. C. Tan and D. Zhao, *J. Mater. Chem. A*, 2017, **5**, 8954–8963.

55 M. Eddaoudi, D. B. Moler, H. Li, B. Chen, T. M. Reineke, M. O'Keeffe and O. M. Yaghi, *Acc. Chem. Res.*, 2001, **34**, 319–330.

56 L. Cao, Z. Lin, F. Peng, W. Wang, R. Huang, C. Wang, J. Yan, J. Liang, Z. Zhang, T. Zhang, L. Long, J. Sun and W. Lin, *Angew. Chemie - Int. Ed.*, 2016, **55**, 4962–4966.

57 A. Dhakshinamoorthy, A. M. Asiri and H. Garcia, *Adv. Mater.*, 2019, **31**, 1900617.

58 K. S. Novoselov, D. Jiang, F. Schedin, T. J. Booth, V. V. Khotkevich, S. V. Morozov and A. K. Geim, *Proc. Natl. Acad. Sci. U. S. A.*, 2005, **102**, 10451–10453.

59 C. Backes, T. M. Higgins, A. Kelly, C. Boland, A. Harvey, D. Hanlon and J. N. Coleman, *Chem. Mater.*, 2017, **29**, 243–255.

60 Q. Qiu, H. Chen, Z. You, Y. Feng, X. Wang, Y. Wang and Y. Ying, *ACS Appl. Mater. Interfaces*, 2020, **12**, 5429–5436.

61 Y. Peng, Y. Li, Y. Ban, H. Jin, W. Jiao, X. Liu and W. Yang, *Science (80-.).*, 2014, **346**, 1356–1359.

62 B. Garai, A. Mallick, A. Das, R. Mukherjee and R. Banerjee, *Chem. - A Eur. J.*, 2017, **23**, 7361–7366.

63 A. Gallego, C. Hermosa, O. Castillo, I. Berlanga, C. J. Gõmez-García, E. Mateo-Martí, J. I. Martínez, F. Flores, C. Gõmez-Navarro, J. Gõmez-Herrero, S. Delgado and F. Zamora, *Adv. Mater.*, 2013, **25**, 2141–2146.

64 M. Zhao, Y. Wang, Q. Ma, Y. Huang, X. Zhang, J. Ping, Z. Zhang, Q. Lu, Y. Yu, H. Xu, Y. Zhao and H. Zhang, *Adv. Mater.*, 2015, **27**, 7372–7378.

65 F. Cao, M. Zhao, Y. Yu, B. Chen, Y. Huang, J. Yang, X. Cao, Q. Lu, X. Zhang, Z. Zhang, C. Tan and H. Zhang, *J. Am. Chem. Soc.*, 2016, **138**, 6924–6927.

66 G. Lin, G. T. Nash, T. Luo, I. Ghosh, S. Sohoni, A. J. Christofferson, G. Liu, G. S. Engel and W. Lin, *Adv. Mater.*, 2023, **2212069**, 2212069.

67 G. T. Nash, T. Luo, G. Lan, K. Ni, M. Kaufmann and W. Lin, *J. Am. Chem. Soc.*, 2021, **143**, 2194–2199.

68 K. Jayaramulu, F. Geyer, A. Schneemann, Š. Kment, M. Otyepka, R. Zboril, D. Vollmer and R. A.

Fischer, *Adv. Mater.*, 2019, **31**, 1900820.

69 W. Zhao, J. Peng, W. Wang, S. Liu, Q. Zhao and W. Huang, *Coord. Chem. Rev.*, 2018, **377**, 44–63.

70 Y. Peng, Y. Li, Y. Ban and W. Yang, *Angew. Chemie Int. Ed.*, 2017, **56**, 9757–9761.

71 Y. Wen, X. Zhang, X. Li, Z. Wang and C. Y. Tang, *ACS Appl. Nano Mater.*, 2020, **3**, 9238–9248.

72 P. H. Bessette, J. J. Rice and P. S. Daugherty, *Protein Eng. Des. Sel.*, 2004, **17**, 731–739.

73 B. Yilmaz and U. Müller, in *Topics in Catalysis*, 2009, vol. 52, pp. 888–895.

74 Y. Li, L. Li and J. Yu, *Chem*, 2017, 3, 928–949.

75 K. S. Park, Z. Ni, A. P. Cô, J. Y. Choi, R. Huang, F. J. Uribe-Romo, H. K. Chae, M. O'keeffe and O. M. Yaghi, *Proc. Natl. Acad. Sci. U. S. A.*, 2006, **103**, 10186–10191.

76 B. Chen, Z. Yang, Y. Zhu and Y. Xia, *J. Mater. Chem. A*, 2014, 2, 16811–16831.

77 X. Li, Y. Liu, J. Wang, J. Gascon, J. Li and B. Van Der Bruggen, *Chem. Soc. Rev.*, 2017, 46, 7124–7144.

78 A. Ruyra, A. Yazdi, J. Espín, A. Carné-Sánchez, N. Roher, J. Lorenzo, I. Imaz and D. Maspoch, *Chem. - A Eur. J.*, 2015, **21**, 2508–2518.

79 K. Zhao, S. Liu, G. Ye, Q. Gan, Z. Zhou and Z. He, *J. Mater. Chem. A*, 2018, **6**, 2166–2175.

80 F. Xue, P. Kumar, W. Xu, K. A. Mkhoyan and M. Tsapatsis, *Cite This Chem. Mater*, 2018, **30**, 69–73.

81 Y. Peng, Y. Li, Y. Ban and W. Yang, *Angew. Chemie*, 2017, **129**, 9889–9893.

82 D. Liu, B. Liu, C. Wang, W. Jin, Q. Zha, G. Shi, D. Wang, X. Sang and C. Ni, *ACS Sustain. Chem. Eng.*, 2020, **8**, 2167–2175.

83 H.-L. Liu, Y.-J. Chang, T. Fan and Z.-Y. Gu, *Chem. Commun.*, 2016, **52**, 12984–12987.

84 Y. Wang, J. Zhang, X. Cheng, Y. Sha, M. Xu, Z. Su, J. Hu and L. Yao, *Nanoscale*, 2022, **14**, 11012–11017.

85 J. Cao, C. Lei, J. Yang, X. Cheng, Z. Li, B. Yang, X. Zhang, L. Lei, Y. Hou and K. Ostrikov, *J. Mater. Chem. A*, 2018, **6**, 18877–18883.

86 S. Wang, D. Xu, L. Ma, J. Qiu, X. Wang, Q. Dong, Q. Zhang, J. Pan and Q. Liu, *Anal. Bioanal. Chem.*, 2018, **410**, 7145–7152.

87 Q.-F. Yang, X.-B. Cui, J.-H. Yu, J. Lu, X.-Y. Yu, X. Zhang, J.-Q. Xu, Q. Hou and T.-G. Wang, *CrystEngComm*, 2008, **10**, 1534.

88 P. Zhao, G. I. Lampronti, G. O. Lloyd, M. T. Wharmby, S. Facq, A. K. Cheetham and S. A. T. Redfern, *Chem. Mater.*, 2014, **26**, 1767–1769.

89 Y. Peng, Y. Huang, Y. Zhu, B. Chen, L. Wang, Z. Lai, Z. Zhang, M. Zhao, C. Tan, N. Yang, F. Shao, Y. Han and H. Zhang, *J. Am. Chem. Soc.*, 2017, **139**, 8698–8704.

90 K. Jayaramulu, J. Masa, D. M. Morales, O. Tomanec, V. Ranc, M. Petr, P. Wilde, Y.-T. Chen, R. Zboril, W. Schuhmann and R. A. Fischer, *Adv. Sci.*, 2018, **5**, 1801029.

91 M. J. Cliffe, E. Castillo-Martínez, Y. Wu, J. Lee, A. C. Forse, F. C. N. Firth, P. Z. Moghadam, D. Fairen-Jimenez, M. W. Gaultois, J. A. Hill, O. V Magdysyuk, B. Slater, A. L. Goodwin and C. P.

Grey, *J. Am. Chem. Soc.*, 2017, **139**, 5397–5404.

92 Y. Xiong, C. Wang, Y. F. Wu, C. Luo, D. Zhan and S. Wang, *Molecules*, 2022, **27**, 8599.

93 G. Lan, K. Ni, S. S. Veroneau, Y. Song and W. Lin, *J. Am. Chem. Soc.*, 2018, **140**, 16971–16975.

94 G. Lan, K. Ni, R. Xu, K. Lu, Z. Lin, C. Chan and W. Lin, *Angew. Chemie*, 2017, **129**, 12270–12274.

95 W. Shi, L. Cao, H. Zhang, X. Zhou, B. An, Z. Lin, R. Dai, J. Li, C. Wang and W. Lin, *Angew. Chemie - Int. Ed.*, 2017, **56**, 9704–9709.

96 Y. Quan, W. Shi, Y. Song, X. Jiang, C. Wang and W. Lin, *J. Am. Chem. Soc.*, 2021, **143**, 3075–3080.

97 Y. Fan, H. Zheng, S. Labalme and W. Lin, *J. Am. Chem. Soc.*, 2023, **145**, 4158–4165.

98 Y. Peng, R. Yao and W. Yang, *Chem. Commun.*, 2019, **55**, 3935–3938.

99 H. Ang and L. Hong, *ACS Appl. Mater. Interfaces*, 2017, **9**, 28079–28088.

100 J. Hong, L. Kang, X. Shi, R. Wei, X. Mai, D. Pan, N. Naik and Z. Guo, *J. Mater. Sci. Technol.*, 2022, **98**, 212–218.

101 G. Lan, K. Ni, E. You, M. Wang, A. Culbert, X. Jiang and W. Lin, *J. Am. Chem. Soc.*, 2019, **141**, 18964–18969.

102 L. Hang, T. Zhang, H. Wen, L. Liang, W. Li, X. Ma and G. Jiang, *Nano Res.*, 2021, **14**, 660–666.

103 H. Cheng, Y. Liu, Y. Hu, Y. Ding, S. Lin, W. Cao, Q. Wang, J. Wu, F. Muhammad, X. Zhao, D. Zhao, Z. Li, H. Xing and H. Wei, *Anal. Chem*, 2017, **89**, 11552–11559.

104 K. K. Tanabe and S. M. Cohen, *Chem. Soc. Rev.*, 2011, **40**, 498–519.

105 D. J. Ashworth and J. A. Foster, *Nanoscale*, 2020, **12**, 7986–7994.

106 H. Yuan, G. Liu, Z. Qiao, N. Li, P. J. S. Buenconsejo, S. Xi, A. Karmakar, M. Li, H. Cai, S. J. Pennycook and D. Zhao, *Adv. Mater.*, 2021, **33**, 2101257.

107 Y. Pu, Z. Yang, V. Wee, Z. Wu, Z. Jiang and D. Zhao, *J. Memb. Sci.*, 2022, **641**, 119912.

108 L. Cao, Z. Lin, W. Shi, Z. Wang, C. Zhang, X. Hu, C. Wang and W. Lin, *J. Am. Chem. Soc.*, 2017, **139**, 7020–7029.

109 Y. Quan, G. Lan, W. Shi, Z. Xu, Y. Fan, E. You, X. Jiang, C. Wang and W. Lin, *Angew. Chemie Int. Ed.*, 2021, **60**, 3115–3120.

110 Z. Wang, Y. Liu, Z. Wang, L. Cao, Y. Zhao, C. Wang and W. Lin, *Chem. Commun.*, 2017, **53**, 9356–9359.

111 J. Xiao, S. S. Yang, J. X. Wu, H. Wang, X. Yu, W. Shang, G. Q. Chen and Z. Y. Gu, *Anal. Chem.*, 2019, **91**, 9093–9101.

112 J. Zhao, R. Chen, J. Huang, F. Wang, C.-A. Tao and J. Wang, *ACS Appl. Mater. Interfaces*, 2021, **13**, 40863–40871.

113 G. Lan, Y. Fan, W. Shi, E. You, S. S. Veroneau and W. Lin, *Nat. Catal.*, 2022, **5**, 1006–1018.

114 J. Nicks and J. A. Foster, *Nanoscale*, 2022, **14**, 6220–6227.

115 X. Ling, D. Gong, W. Shi, Z. Xu, W. Han, G. Lan, Y. Li, W. Qin and W. Lin, *J. Am. Chem. Soc.*, 2021, **143**, 1284–1289.

116 Y. Guo, W. Shi, H. Yang, Q. He, Z. Zeng, J. Ye, X. He, R. Huang, C. Wang and W. Lin, *J. Am. Chem.*

Soc., 2019, **141**, 17875–17883.

117 Y. Fan, E. You, Z. Xu and W. Lin, *J. Am. Chem. Soc.*, 2021, **143**, 18871–18876.

118 Y. Wang, L. Feng, J. Pang, J. Li, N. Huang, G. S. Day, L. Cheng, H. F. Drake, Y. Wang, C. Lollar, J. Qin, Z. Gu, T. Lu, S. Yuan and H. Zhou, *Adv. Sci.*, 2019, **6**, 1802059.

119 A. Goswami, D. Ghosh, V. V Chernyshev, A. Dey, D. Pradhan and K. Biradha, *ACS Appl. Mater. Interfaces*, 2020, **12**, 33679–33689.

120 K. Sasitharan, D. G. Bossanyi, N. Vaenas, A. J. Parnell, J. Clark, A. Iraqi, D. G. Lidzey and J. A. Foster, *J. Mater. Chem. A*, 2020, **8**, 6067–6075.

121 Y. Peng, R. Yao, W. Yang, R. Li, / Chemcomm and C. Communication, *Chem. Commun*, 2019, **55**, 3935.

122 L. Huang, X. Zhang, Y. Han, Q. Wang, Y. Fang and S. Dong, *J. Mater. Chem. A*, 2017, **5**, 18610–18617.

123 Y. Peng and W. Yang, *Sci. China Chem.*, 2019, **62**, 1561–1575.

124 J. Chen, Y. Shu, H. Li, Q. Xu and X. Hu, *Talanta*, 2018, **189**, 254–261.

125 A. Yuan, Y. Lu, X. Zhang, Q. Chen and Y. Huang, *J. Mater. Chem. B*, 2020, **8**, 9295–9303.

126 N. Zhu, L. Gu, J. Wang, X. Li, G. Liang, J. Zhou and Z. Zhang, *J. Phys. Chem. C*, 2019, **123**, 9388–9393.

127 D. Ning, Q. Liu, Q. Wang, X. M. Du, W. J. Ruan and Y. Li, *Sensors Actuators, B Chem.*, 2019, **282**, 443–448.

128 W. Li, S. Lv, Y. Wang, L. Zhang and X. Cui, *Sensors Actuators B Chem.*, 2019, **281**, 652–658.

129 B. Tan, H. Zhao, W. Wu, X. Liu, Y. Zhang and X. Quan, *Nanoscale*, 2017, **9**, 18699–18710.

130 H. Chen, Q. Qiu, S. Sharif, S. Ying, Y. Wang and Y. Ying, *ACS Appl. Mater. Interfaces*, 2018, **10**, 24108–24115.

131 Y. Li, J.-J. Li, Q. Zhang, J.-Y. Zhang, N. Zhang, Y.-Z. Fang, J. Yan and Q. Ke, *Sensors Actuators B Chem.*, 2022, **354**, 131140.

132 M. Y. Shi, M. Xu and Z. Y. Gu, *Anal. Chim. Acta*, 2019, **1079**, 164–170.

133 J. Chen, Y. Xu, F. Xu, Q. Zhang, S. Li and X. Lu, *Anal. Methods*, 2021, **13**, 4228–4237.

134 S. Chen, P. Zhao, L. Jiang, S. Zhou, J. Zheng, X. Luo, D. Huo and C. Hou, *Anal. Bioanal. Chem.*, 2021, **413**, 613–624.

135 A. Portorreal-Bottier, S. Gutiérrez-Tarriño, J. J. Calvente, R. Andreu, E. Roldán, P. Oña-Burgos and J. L. Olloqui-Sariego, *Sensors Actuators B Chem.*, 2022, **368**, 132129.

136 C. Wang, S. Huang, L. Luo, Y. Zhou, X. Lu, G. Zhang, H. Ye, J. Gu and F. Cao, *J. Electroanal. Chem.*, 2019, **835**, 178–185.

137 H. S. Wang, *Coord. Chem. Rev.*, 2017, **349**, 139–155.

138 Q. Qiu, H. Chen, S. Ying, S. Sharif, Z. You, Y. Wang and Y. Ying, *Microchim. Acta*, 2019, **186**, 93.

139 Z. Sun, S. Wu, Y. Peng, M. Wang, M. Jalalah, M. S. Al-Assiri, F. A. Harraz, J. Yang and G. Li, *Chem. Eng. J.*, 2021, **405**, 126707.

140 W. J. Song, *Talanta*, 2017, **170**, 74–80.

141 C. Liu, T. Wang, J. Ji, C. Wang, H. Wang, P. Jin, W. Zhou and J. Jiang, *J. Mater. Chem. C*, 2019, **7**, 10240–10246.

142 H. Q. Zhao, G. H. Qiu, Z. Liang, M. M. Li, B. Sun, L. Qin, S. P. Yang, W. H. Chen and J. X. Chen, *Anal. Chim. Acta*, 2016, **922**, 55–63.

143 Q. Yang, J. Hong, Y. X. Wu, Y. Cao, D. Wu, F. Hu and N. Gan, *ACS Appl. Mater. Interfaces*, 2019, **11**, 41506–41515.

144 H. S. Wang, J. Li, J. Y. Li, K. Wang, Y. Ding and X. H. Xia, *NPG Asia Mater.*, 2017, **9**, 1–9.

145 H. Zhang, B. Luo, P. An, X. Zhan, F. Lan and Y. Wu, *ACS Appl. Bio Mater.*, 2022, **5**, 3500–3508.

146 Q. Yang, L. Zhou, Y. X. Wu, K. Zhang, Y. Cao, Y. Zhou, D. Wu, F. Hu and N. Gan, *Anal. Chim. Acta*, 2018, **1020**, 1–8.

147 B. J. Córdova Wong, D. M. Xu, S. S. Bao, L. M. Zheng and J. Lei, *ACS Appl. Mater. Interfaces*, 2019, **11**, 12986–12992.

148 X. Wang, A. Jiang, T. Hou, H. Li and F. Li, *Biosens. Bioelectron.*, 2015, **70**, 324–329.

149 L. He, F. Duan, Y. Song, C. Guo, H. Zhao, J.-Y. Tian, Z. Zhang, C.-S. Liu, X. Zhang, P. Wang, M. Du and S.-M. Fang, *2D Mater.*, 2017, **4**, 025098.

150 J. Xiao, X. Hu, K. Wang, Y. Zou, E. Gyimah, S. Yakubu and Z. Zhang, *Biosens. Bioelectron.*, 2020, **150**, 111883.

151 Y. Sun, H. Jin, X. Jiang and R. Gui, *Sensors Actuators, B Chem.*, 2020, **309**, 127777.

152 Z. Wang, Y. Zhang, X. Wang and L. Han, *Biosens. Bioelectron.*, 2022, **206**, 114120.

153 X. Lu, F. Zhang, Y. Sun, K. Yu, W. Guo and F. Qu, *Dalt. Trans.*, 2021, **50**, 16593–16600.

154 L. Dong, L. Yin, G. Tian, Y. Wang, H. Pei, Q. Wu, W. Cheng, S. Ding and Q. Xia, *Sensors Actuators, B Chem.*, 2020, **308**, 127687.

155 A. Ahmadi, S. M. Khoshfetrat, Z. Mirzaeizadeh, S. Kabiri, J. Rezaie and K. Omidfar, *Talanta*, 2022, **237**, 122911.

156 G.-B. Hu, C.-Y. Xiong, W.-B. Liang, Y. Yang, L.-Y. Yao, W. Huang, W. Luo, R. Yuan and D.-R. Xiao, *Biosens. Bioelectron.*, 2019, **135**, 95–101.

157 Y. Yang, G. B. Hu, W. Bin Liang, L. Y. Yao, W. Huang, R. Yuan and D. R. Xiao, *Nanoscale*, 2019, **11**, 10056–10063.

158 L.-Y. Yao, F. Yang, G.-B. Hu, Y. Yang, W. Huang, W.-B. Liang, R. Yuan and D.-R. Xiao, *Biosens. Bioelectron.*, 2020, **155**, 112099.

159 Y. Yang, G. B. Hu, W. Bin Liang, L. Y. Yao, W. Huang, Y. J. Zhang, J. L. Zhang, J. M. Wang, R. Yuan and D. R. Xiao, *Nanoscale*, 2020, **12**, 5932–5941.

160 H. Shao, J. Lu, Q. Zhang, Y. Hu, S. Wang and Z. Guo, *Sensors Actuators, B Chem.*, 2018, **268**, 39–46.

161 H. Shao, H. Lin, J. Lu, Y. Hu, S. Wang, Y. Huang and Z. Guo, *Biosens. Bioelectron.*, 2018, **118**, 247–252.

162 M. Yan, J. Ye, Q. Zhu, L. Zhu, J. Huang and X. Yang, *Anal. Chem.*, 2019, **91**, 10156–10163.

163 FineTest Human MUC-1(Mucin-1) ELISA Kit, https://www.fn-test.com/product/eh0406/, (accessed 24 June 2023).

164 Invitrogen Cardiac Troponin I (TNNI3) Human ELISA Kit, https://www.thermofisher.com/elisa/product/Cardiac-Troponin-I-TNNI3-Human-ELISA-Kit/EHTNNI3, (accessed 24 June 2023).

165 A. M. Levin and G. A. Weiss, *Mol. Biosyst.*, 2006, **2**, 49–57.

166 S. D. Stellwagen, D. A. Sarkes, B. L. Adams, M. A. Hunt, R. L. Renberg, M. M. Hurley and D. N. Stratis-Cullum, *BMC Biotechnol.*, 2019, **19**, 1–12.

167 B. He, G. Chai, Y. Duan, Z. Yan, L. Qiu, H. Zhang, Z. Liu, Q. He, K. Han, B. Ru, F. B. Guo, H. Ding, H. Lin, X. Wang, N. Rao, P. Zhou and J. Huang, *Nucleic Acids Res.*, 2016, **44**, D1127–D1132.

168 G. P. Smith, *Science (80-.).*, 1985, **228**, 1315–1317.

169 G. M. Cherf and J. R. Cochran, in *Methods in Enzymology*, 2015, pp. 155–175.

170 M. He and M. J. Taussig, *Briefings Funct. Genomics Proteomics*, 2002, **1**, 204–212.

171 J. Pande, M. M. Szewczyk and A. K. Grover, *Biotechnol. Adv.*, 2010, **28**, 849–858.

172 N. E. B. GmbH, *Construction*.

173 M. Vodnik, U. Zager, B. Strukelj and M. Lunder, *Molecules*, 2011, **16**, 790–817.

174 B. D. Reiss, C. Mao, D. J. Solis, K. S. Ryan, T. Thomson and A. M. Belcher, *Nano Lett.*, 2004, **4**, 1127–1132.

175 J. Morton, N. Karoonuthaisiri, R. Charlermroj, L. D. Stewart, C. T. Elliott and I. R. Grant, *PLoS One*, 2013, **8**, 1–11.

176 Z. Lan, F. Fiedler and S. Kathariou, *J. Bacteriol.*, 2000, **182**, 6161–6168.

177 L. D. Stewart, A. Foddai, C. T. Elliott and I. R. Grant, *J. Appl. Microbiol.*, 2013, 115, 808–817.

178 B. M. Larimer and S. L. Deutscher, *Am. J. Nucl. Med. Mol. Imaging*, 2014, **4**, 435–47.

179 B. He, C. Mao, B. Ru, H. Han, P. Zhou and J. Huang, *Comput. Math. Methods Med.*, 2013, **2013**, 1–6.

180 G. A. Kouzmitcheva, V. A. Petrenko and G. P. Smith, *Clin. Diagnostic Lab. Immunol.*, 2001, **8**, 150–160.

181 F. B. Mehmet Sarikaya, Tamerler, Candan, Alex K. -Y. Jen, Klaus Schulten, *Nat. Mater.*, 2003, **2**, 577–585.

182 A. E. Rawlings, J. P. Bramble, A. A. S. Tang, L. A. Somner, A. E. Monnington, D. J. Cooke, M. J. McPherson, D. C. Tomlinson and S. S. Staniland, *Chem. Sci.*, 2015, **6**, 5586–5594.

183 Q. Li, Y. Wang, G. Zhang, R. Su and W. Qi, *Chem. Soc. Rev.*, 2023, 52, 1549–1590.

184 D. Zhang, Y. Fan, G. Li, W. Du, R. Li, Y. Liu, Z. Cheng and J. Xu, , DOI:10.1016/j.snb.2019.127187.

185 G. Fan, C. M. Dundas, C. Zhang, N. A. Lynd and B. K. Keitz, *ACS Appl. Mater. Interfaces*, 2018, **10**, 18601–18609.

186 M. Lunder, T. Bratkovič, B. Doljak, S. Kreft, U. Urleb, B. Štrukelj and N. Plazar, *Appl. Biochem. Biotechnol.*, 2005, **127**, 125–131.

Chapter 2:

Pre-Synthetic Functionalisation of Metal-Organic Nanosheets for Biosensing Applications

---

2.1 Introduction and Aims

High chemical stability under aqueous conditions is a key requirement of biosensing surfaces. Zeolitic imidazolate framework (ZIF) systems were selected to be investigated as suitable candidates due to various attractive properties including high stability, tunability and large surface areas.[1] ZIF-7 ($Zn_2(bim)_4$, where bim is benzimidazole) has previously been reported by a range of research groups and has been synthesised in a variety of ways depending on the desired phase of the product.[2–4] The MOF can exist as different phases as discussed previously and shown in Figure 1.11, with ZIF-7-III existing as a layered 3D structure which can be exfoliated to produce nanosheets as demonstrated by Liu *et al*..[5,6] ZIF-9 ($Co_2(bim)_4$) with a cobalt metal centre instead of zinc undergoes the same phase transformations with ZIF-9-III also existing as nanosheets.[7–9]

Work done by Saini *et al.* demonstrates the use of ZIF-9-III in oil-water separation, highlighting its hydrolytic stability.[8] Both ZIF-7-III and ZIF-9-III are the densest of the possible phases and this plays an important role in the stability of these materials.[5] Studies have demonstrated the high stability of ZIF-7(-I/-II) MOF in a culture medium containing 10 % fetal bovine serum (37°C for 24 hr) by comparing XRPD patterns pre- and post-incubation.[10] As well as oil-water separation, ZIF-9-III nanosheets have been used as catalysts in aqueous conditions.[7–9] Both MON systems, therefore, have the potential to be stable in biological media, a crucial feature in biosensor design.[11]

The $Fe(bimX)_2$ nanosheet system, analogous to ZIF-7/9, reported by López-Cabrelles *et al.* demonstrated pre-synthetic modifications that resulted in different surface functionality through the use of a variety of organic linkers (Figure 2.1).[12] The series of magnetic MONs based on Fe(II) centres retained their long-range structural order exhibiting good mechanical and magnetic properties. This work demonstrated that through a rational selection of the functional substituent of the organic ligand, different surfaces could be produced with periodic decoration. This in turn resulted in the modification of the surface properties of the nanosheets.[12] Introducing functional groups from halogens to amine groups altered the surface hydrophobicity. Hydrophobic interactions are a key driving force in biomolecular recognition therefore this degree of control over MON surface hydrophobicity is an attractive feature in biosensor design. Owing to the similarities of the systems, it should be possible to form the same ZIF-7 nanosheet topology with a range of different benzimidazole derivatives. Previously, 2-aminobenzimidazole has been post-synthetically introduced into a ZIF-7 synthesis to form a mixed linker system (ZIF-7-NH_2) via solvent assisted ligand exchange in work done by Xiang *et.al.*.[13] There are further examples of multivariate ZIFs with a mixtures of imidazolate-based linkers retaining crystallinity.[14] This is further evidence of the scope of tunability of ZIF-7 and ZIF-9.

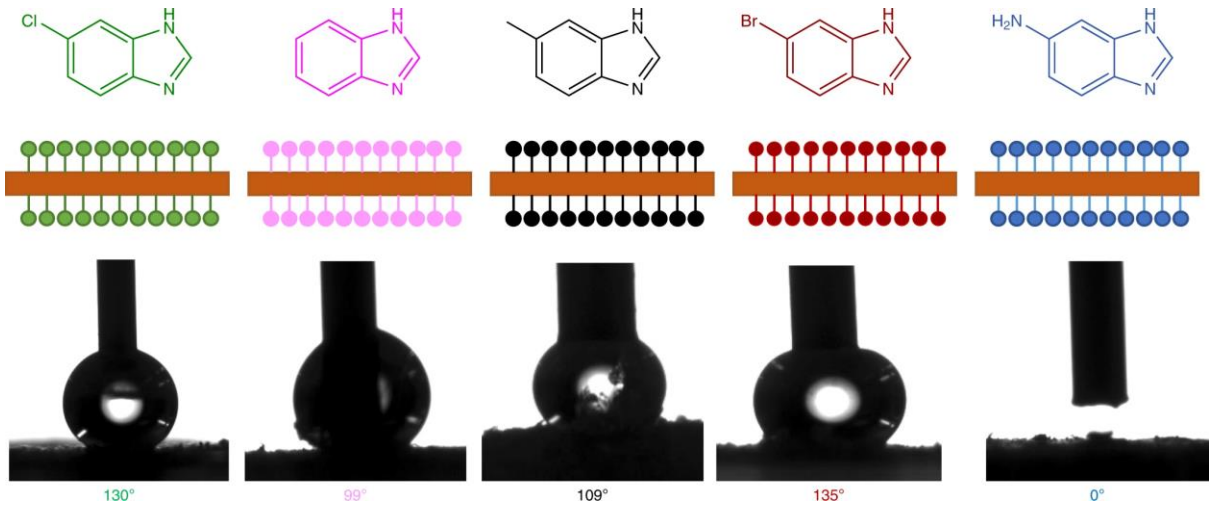

Figure 2.1 - Surface modification in MUV-1-X. Atoms at the surface of MUV-1-X can be changed by chemical design (X = Cl, H, CH_3 , Br, NH_2) in a pre-synthetic manner to obtain different surface behaviours that change the water contact angle. The structure of each derivatized ligand is shown (top) with a schematic representation of each functionalized 2D layer (middle) and a picture of a water droplet deposited on each surface (bottom), from which the contact angles are measured. Taken from reference 12.

The primary aim of the research in this chapter was to synthesise and characterise a series of MONs suitable for biosensing applications, with a focus on producing MONs that have high physiological stability. We anticipate building an understanding of how the tunable nature of MONs can be exploited in the design of MON-based biosensors. This work explores how surface engineering can lead to rational modifications of surface properties such as charge and hydrophobicity.

The objectives of this chapter was to synthesise and fully characterise ZIF-7 and ZIF-9 metal-organic nanosheets by reproducing previous methodologies. Following that, the aim was to introduce different benzimidazole derivatives (bim-Br, bim-NH_2 and bim-CH_3) pre-synthetically to those systems and fully characterise the resulting material. The effect of the pre-synthetic functionalisation on surface properties such as charge and hydrophobicity would then be determined. The final objective was to interrogate the biostability of the MONs produced to determine their applicability in biosensing.

2.2 Results and Discussion

2.2.1 Synthesis and Characterisation of ZIF-7

Liu *et al.* outlined a method to produce monolayer nanosheets of $Zn_2(bim)_4$.[6] In this method, a three-dimensional structure ZIF-7-I was first produced via a 72 h room temperature synthesis, this was then hydrolysed for 24 h to form the layered ZIF-7-III phase. Previous literature reports that the hydrothermal phase transition is irreversible as while the Zn-N bonding in ZIF-7-I/II is susceptible to hydrolysis, the ZIF-7-III phase is more thermodynamically stable.[5] The resulting material was exfoliated in methanol-propanol mixtures to form ZIF-7-III nanosheets. This material had the desired XRPD

pattern of layered $Zn_2(bim)_4$, which matched the pattern simulated based on the single-crystal data (CCDC - 675375).[6,15] This method was adapted from seminal work on the system by Peng *et al*. with slight modifications.[15]

In this work, the metal salt and organic linker were left in DMF at room temperature for 72 h to form ZIF-7 nanocrystals (ZIF-7-I) where the pores are filled with guest DMF molecules. The material was then collected, dried and characterised by XRPD to establish the phase present. Figure 2.2a shows the ZIF-7-I MOF XRPD pattern which matched the expected pattern in blue beneath it. The ZIF-7-I MOF nanocrystal is also depicted schematically in Figure 2.2b and the SEM image of such nanocrystals is shown in Figure 2.2c as expected.[16] ZIF-7-I nanocrystals were hydrothermally transformed via refluxing in distilled water (100°C for 24 hr) to the ZIF-7-III 3D layered phase. The bulk 3D layered material was characterised as shown in Figure 2.2a, where the experimental XRPD pattern matches the expected CCDC (675375) pattern in red. The layers are visible via SEM as shown in Figure 2.2d and depicted schematically in Figure 2.2b labelled ZIF-7-III 3D bulk.

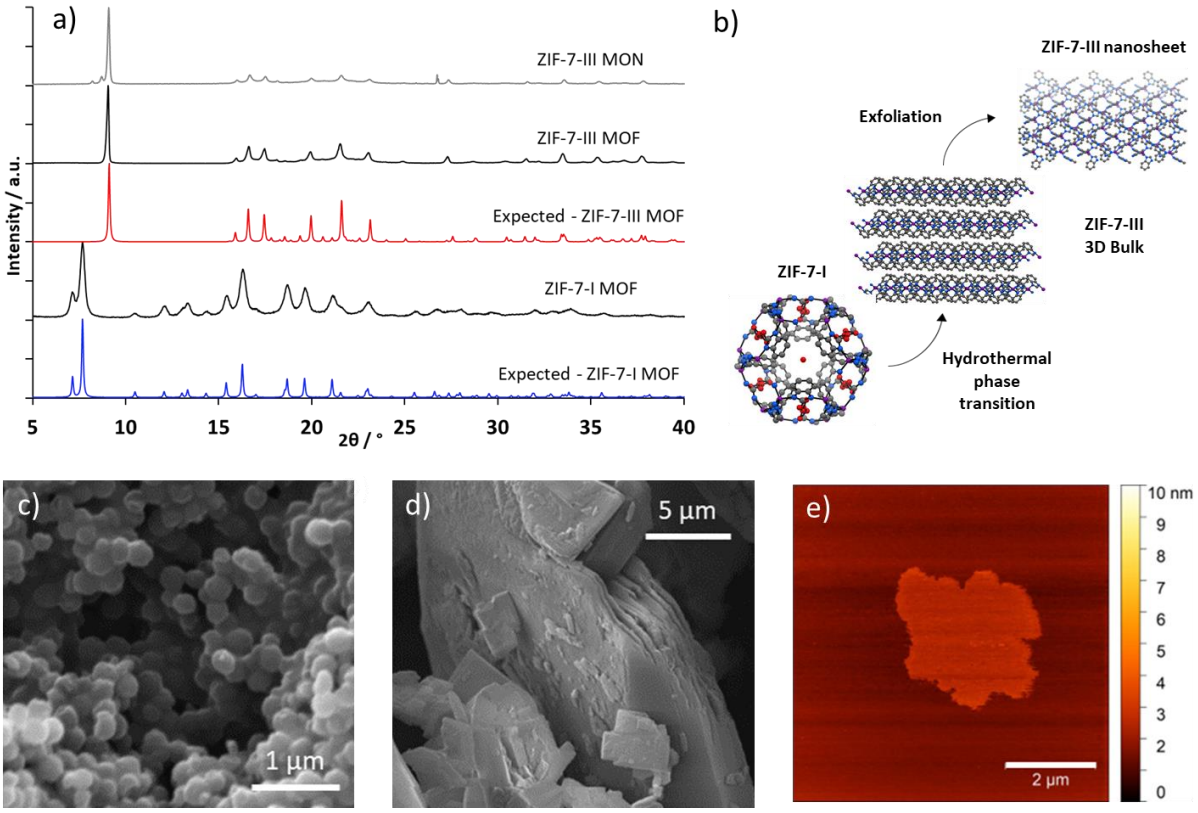

Figure 2.2 – a) XRPD patterns of the different phases of ZIF-7 MOF and nanosheet with comparison to the expected pattern found in CCDC (602541,675375), b) Schematic illustration of the phase change of ZIF-7 from nanocrystal to layered MOF, then exfoliation to nanosheet, c) SEM image of ZIF-7-I, d) SEM image of ZIF-7-III MOF, e) AFM image of a ZIF-7-III nanosheet.

Having established that the bulk material was in the layered phase, exfoliation to access nanosheets was attempted. Liquid-assisted exfoliation using ultrasonication is most common for this system along with ball-milling.[6,15] A range of exfoliation conditions were investigated, and the optimal protocol was found to be a 2 h ultrasonication in a solvent mixture of methanol:n-propanol (1:1 v) followed by 500 rpm 5 min centrifugation which accessed nanosheets with a yield of 27 %. Figure 2.3a shows a comparison of particle sizes in this work to those reported in literature. The synthesised nanosheets in this work were consistently ultrathin.

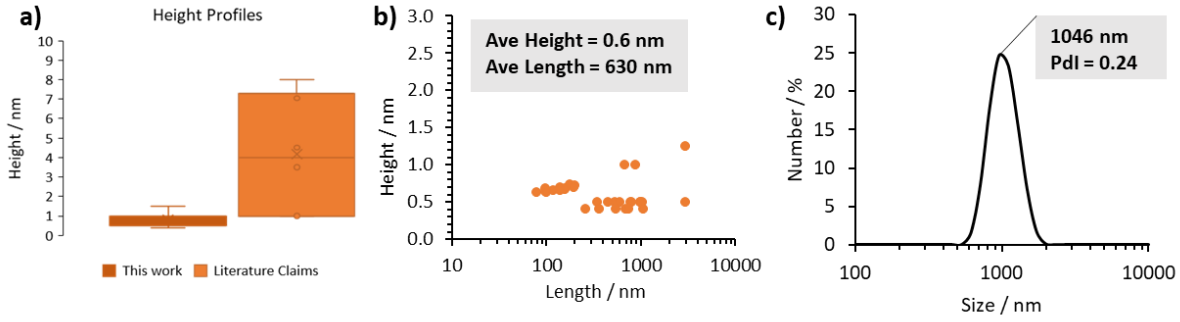

Figure 2.3: a) Comparison of nanosheet height profiles of ZIF-7 nanosheets in this work and those in literature, b) comparison of ZIF-7 nanosheet heights and lengths accessed from the optimised exfoliation method in this work, c) DLS data of ZIF-7 nanosheets.

A single layer of ZIF-7-III is thought to be 0.988 nm based on the interlayer distance in the single crystal structure.[15] The intense ultrasonication often results in uneven 'peeling' of layers causing layer fragmentation. AFM was used to determine the dimensions of the nanosheets (Figure 2.3b). The ultrasonication resulted in MONs that were one or two layers thick where the second layer was often fragmented which is consistent with those reported by Peng e*t al.* and Liu *et al.*.[6,15] Ranging in heights from 0.5 – 1.5 nm and lengths from 78 nm to 3 µm, nanosheets were isolated giving large aspect ratios reaching > 1000.[15] Due to the nature of AFM analysis it is likely the areas of samples imaged represents smaller particles found around drying lines that are more easily imaged.

Further size analysis using dynamic light scattering (DLS) supported this data with a peak at 1046 nm as shown in Figure 2.3c. DLS measures Brownian motion and relates this to the hydrodynamic diameter of particles, which are assumed to be homogenous hard spheres. The data produced can be affected by solvent choice, concentration, preparation method and the algorithms used to determine size. Limitations include sedimentation, multiple light scattering and low resolution as well as the incorrect assumptions of particle shape when considering MONs. Multiple peaks indicate multiple size distributions within a single sample, or an effect of agglomeration within samples as a result of poor suspension within the selected solvent system. Due to the limitations of DLS, it is therefore used as a comparison of similar systems in the same solvent at the same concentration to obtain trends and not

to accurately determine particle size. In the case of ZIF-7/9 nanosheets methanol was used to suspend the nanosheets for DLS measurements. The single peak observed at 1046 nm for ZIF-7 showed that the MONs isolated were 500 nm – 2000 nm, a size distribution that falls within the range observed via AFM.

Overall, ZIF-7-III nanosheets could be successfully synthesised with an average height of 0.6 nm and an average length of 630 nm. The synthesised nanosheets were some of the thinnest in comparison to the literature data. Such high surface area material is ideal for applications demanding surface activity such as biosensing. This investigation also demonstrates the potential to improve the yield of high surface area nanosheets for current and future functionalised ZIF-7-III systems.

2.2.2 Synthesis and Characterisation of ZIF-7-Br

In order to develop an isoreticular series, the ZIF-7 system was synthesised with different benzimidazole derivatives. Following the same method outlined by Liu *et al.*, ZIF-7-Br was synthesised using 6-bromo-1H-benzimidazole as an equimolar replacement for benzimidazole.[6] The bromo functionality increases the basicity of the imidazole by deactivating the benzene ring as a result of its electronegativity. The high reactivity of organo-bromides allows for easy subsequent conversion into various functional groups opening up possibilities to fine-tune the surface properties of the nanosheets post-synthetically.[17]

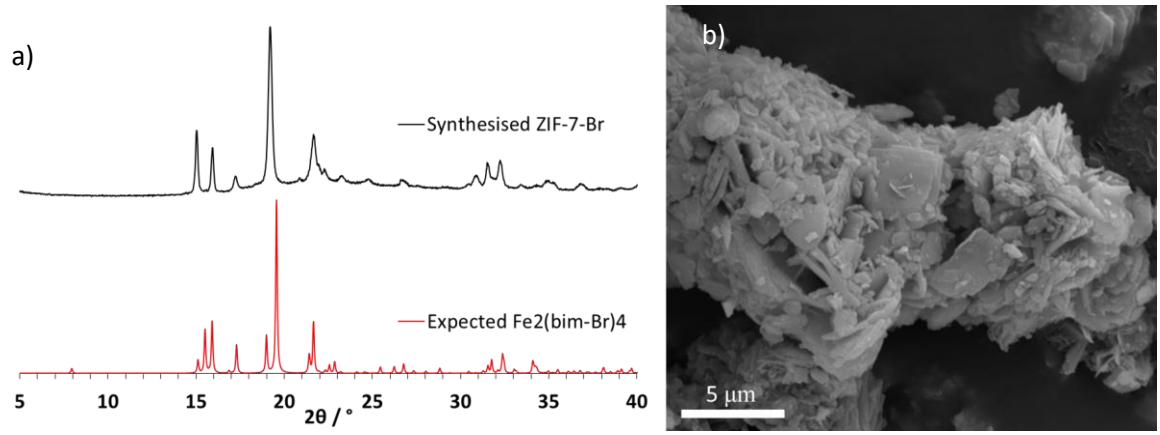

Figure 2.4: a) Comparison of XRPD pattern of synthesised layered ZIF-7-Br-III and a comparable literature XRPD pattern, b) SEM image of ZIF-7-Br MOF

The XRPD pattern (Figure 2.4a) for the bulk ZIF-7-Br MOF compared with the previously reported Fe (II) structure showed a close match indicating they have isoreticular structures (CCDC - 1849147).[12] The comparable Fe structure is known to have the same equivalent powder pattern for $Fe_2(bim)_4$ as ZIF-7-III, therefore it is indicative that the bromo functionalised MOF shares the same XRPD pattern. The SEM image (Figure 2.4b) indicated the layered bulk was formed and elemental analysis of the

material matched that of the expected ratio of elements indicating the correct molecular composition. The ATR-IR spectrum (Figure 2.5) showed the presence of bromine functionality with an additional peak at 586 cm^{-1} when compared to the synthesised ZIF-7 spectrum and peaks appear at 800 – 820 cm^{-1} to indicate that a benzene substituent was present.

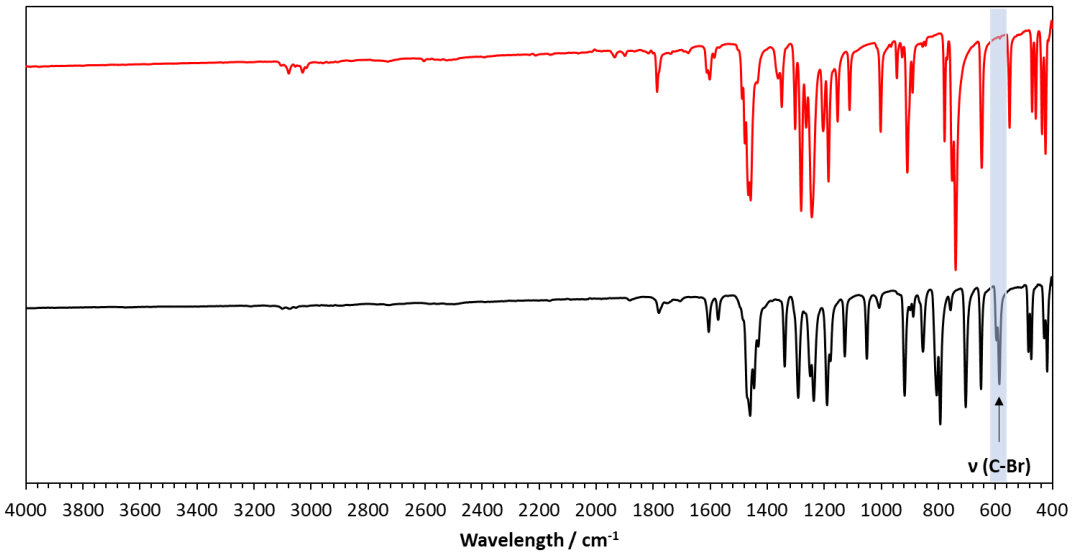

Figure 2.5: ATR-IR of synthesised ZIF-7-Br (black) compared to synthesised ZIF-7 (red)

The same exfoliation conditions previously optimised for ZIF-7 (experimental) were applied to ZIF-7-Br to allow direct comparison of the nanosheets. AFM was used to characterise the resulting material where the nanosheets had a range in height of 0.9 nm to 25 nm and lateral dimensions between 115 nm and 971 nm. In comparison to ZIF-7, the aspect ratios for the bromine functionalised nanosheets were more varied, with two distinct groups of nanosheets formed. There is a smaller and thicker group averaging 13 nm in height and around 144 nm long and a group with larger lateral dimensions that are ultrathin (~ 0.9 nm). The DLS data (Figure 2.6c) supports this with two distinct peaks at 164 nm and 1106 nm. The introduction of the bromo functional group onto the surfaces of the layers results in different interlayer interactions when compared to ZIF-7. The liquid-assisted exfoliation protocol for ZIF-7 is therefore unlikely to be the optimum for ZIF-7-Br as the solvents will interact with the surface differently. For isolation of monolayer nanosheets different solvents and/or centrifugation speeds should be employed. Overall, ZIF-7-Br nanosheets were accessed down to 0.9 nm thick with particle sizes reaching up to 1 μm in length.

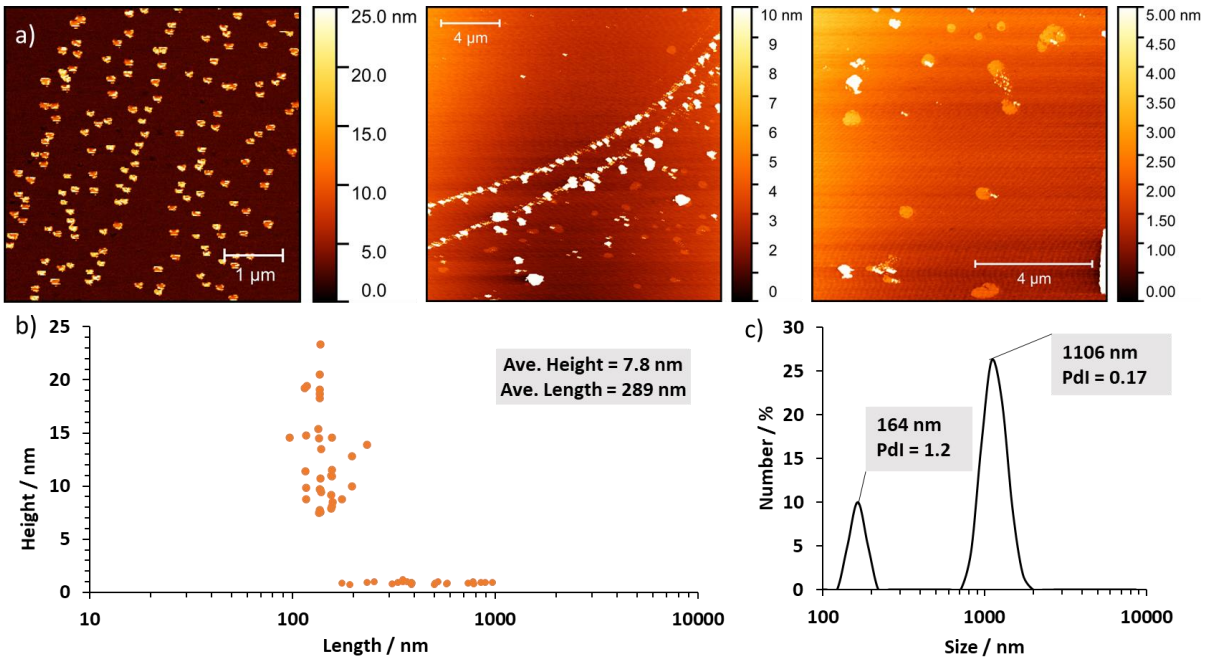

Figure 2.6: a) AFM images of ZIF-7-Br nanosheets, b) the associated dimensions data of ZIF-7-Br nanosheets, c) DLS data for ZIF-7-Br nanosheets.

2.2.3 Synthesis and Characterisation of ZIF-7-NH_2

Synthesis of ZIF-7 with an additional amino functionality was attempted by the direct replacement of (32.57 mmol) benzimidazole (bim) with the (32.57 mmol) 5-amino-benzimidazole linker (bim-NH_2, Figure 2.7) in the initial reactant mixture in the same way as for ZIF-7-Br.[6] However, the initial experiments were unsuccessful with XRPD indicating the formation of amorphous material. It is thought that the amine group increases the electron density of the benzene ring which decreases the basicity of the imidazole, therefore, influencing its ability to coordinate to the zinc metal nodes.

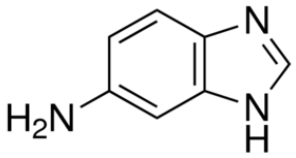

Figure 2.7: 5-amino-benzimidazole

The advantage of amino functionality of ZIF-7-I/III polycrystalline membranes has been highlighted in the literature, where mixed linker systems have been used for improved gas separation.[13,18] In such cases 2-aminobenzimidazole is introduced to the ZIF-7 system pre-synthetically or via solvent-assisted ligand exchange at various ratios with respect to benzimidazole reaching up to 26 mol.%. This inspired us to introduce benzimidazole as a 'dopant' in order to nucleate and control nanoparticle growth so that ZIF-7-I could form. As the amino derivative formed significantly less

crystalline material, bim was doped into the initial reactant mixture due to the previously successful attempts to enhance crystallinity. Another reason for the introduction of bim into the bim-NH_2 system is to demonstrate the potential of multivariate ZIF MONs.

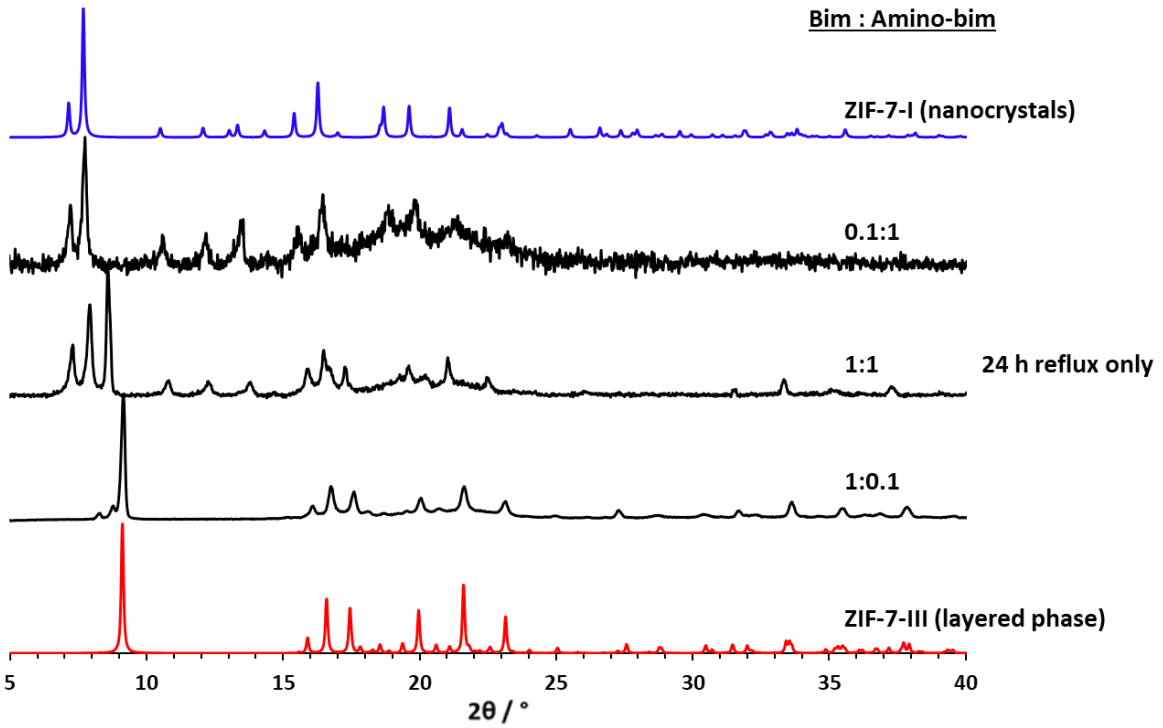

Figure 2.8: XRPD pattern of synthesised ZIF-7-NH_2 frameworks with varying ratios of benzimidazole (bim) to 5-amino-benzimidazole (amino-bim) as well as the expected XRPD patterns of ZIF-7-I phase (blue) and ZIF-7-III phase (red).

The first dosage of benzimidazole investigated was 10% by mole (with 90% bim-NH_2) which resulted in a bulk material XRPD pattern having slight amorphous character but a significant improvement upon the pure 5-amino-benzimidazole based framework. This improvement in phase purity inspired a set of experiments with varying ratios of benzimidazole and 5-amino-benzimidazole, where XRPD patterns (Figure 2.8) of the resulting materials showed different phase compositions. In each case, the total moles of the organic linker were unchanged from the original method.

On increasing the content of bim-NH_2 the resulting material contains increased proportions of the ZIF-7-I phase. This indicates that the metal-linker bonds are less susceptible to hydrolysis with the bim-NH_2 and/or there is a higher activation barrier for formation of the more thermodynamically stable ZIF-7-III phase. The 1:1 MOF that contains an equal number of moles of the two organic linkers has both ZIF-7-I and ZIF-7-III phases as shown in the XRPD pattern (Figure 2.8). Further optimisation of the synthetic method, where reflux time was increased from 24 hr to 1 week resulted in bulk-layered material as the XRPD data showed a good match to the expected and synthesised ZIF-7 powder patterns (Figure 2.9c). There is a slight shift in the [002] plane which can be assigned to the

amine groups sticking up between the layers in this plane as shown schematically in Figure 2.9b. SEM of the material confirmed it was layered as shown in Figure 2.9a.

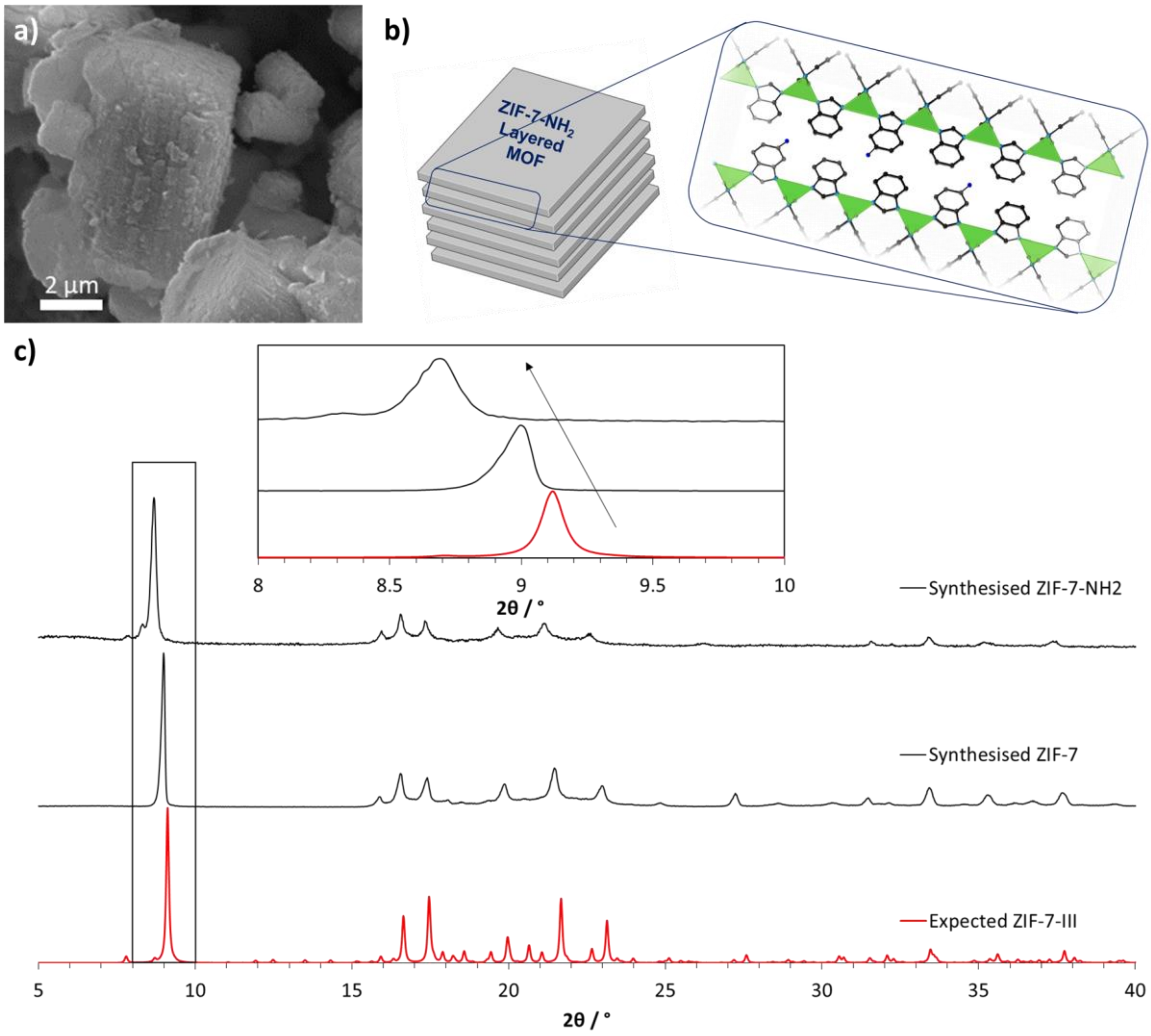

Figure 2.9: a) SEM of ZIF-7-NH_2 MOF, b) Schematic of bulk layered ZIF-7-NH_2 with zoom in of the layers to see the amine groups (blue) sticking into the [002] plane, c) XRPD pattern for expected ZIF-7-III, the synthesised ZIF-7 and the synthesised ZIF-7-NH_2 MOF. Insert is zoomed into 8-10 2θ / °.

Up to 17 % amine functionality was achieved according to NMR (Figure 2.29, experimental) when comparing the integral values of the imidazole hydrogen. The amine groups can also be identified by the ATR-IR spectra (Figure 2.11) where two ν(N–H) stretching bands appear in the 3500–3350 cm^{-1} region.

After confirmation that the bulk layered phase was synthesised, the material underwent the same exfoliation conditions as ZIF-7 (ultrasonication in methanol : n-propanol 1:1, 2 h) to access nanosheets. The AFM data (Figure 2.10) shows the dimensions of the resulting ultrathin nanosheets that ranged in height from 1 nm to 4.5 nm and were on average 395 nm in length. Typically, the nanosheets were one or two layers thick with comparable aspect ratios to the ZIF-7 system. The DLS data shows a larger average particle size with a peak at 846 nm.

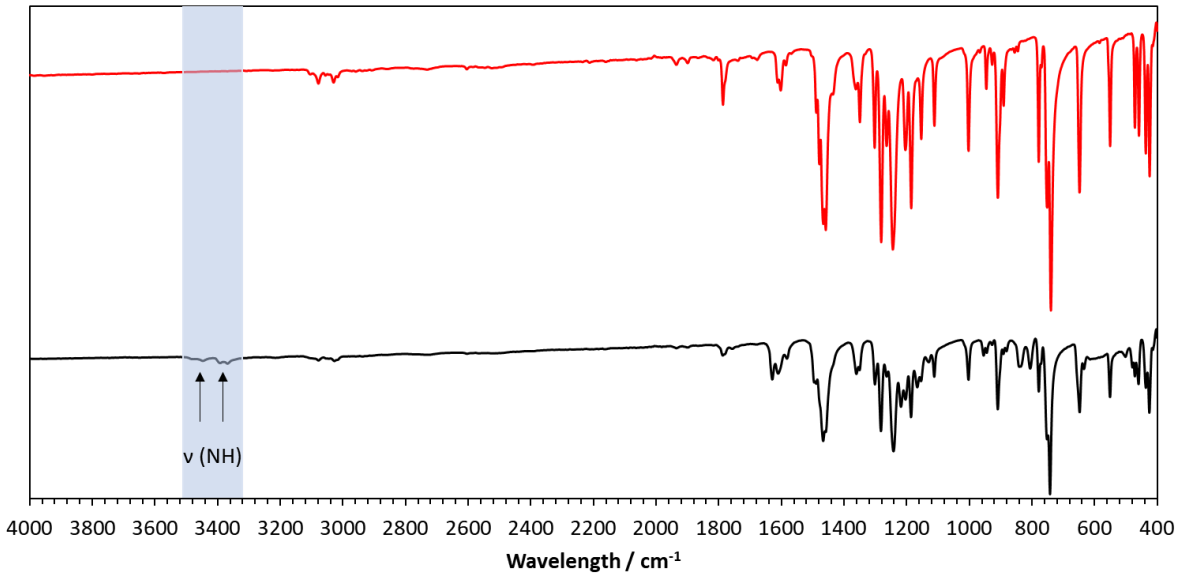

Figure 2.11: ATR-IR spectra of synthesised ZIF-7-NH_2 MOF(black) and synthesised ZIF-7 MOF(red).

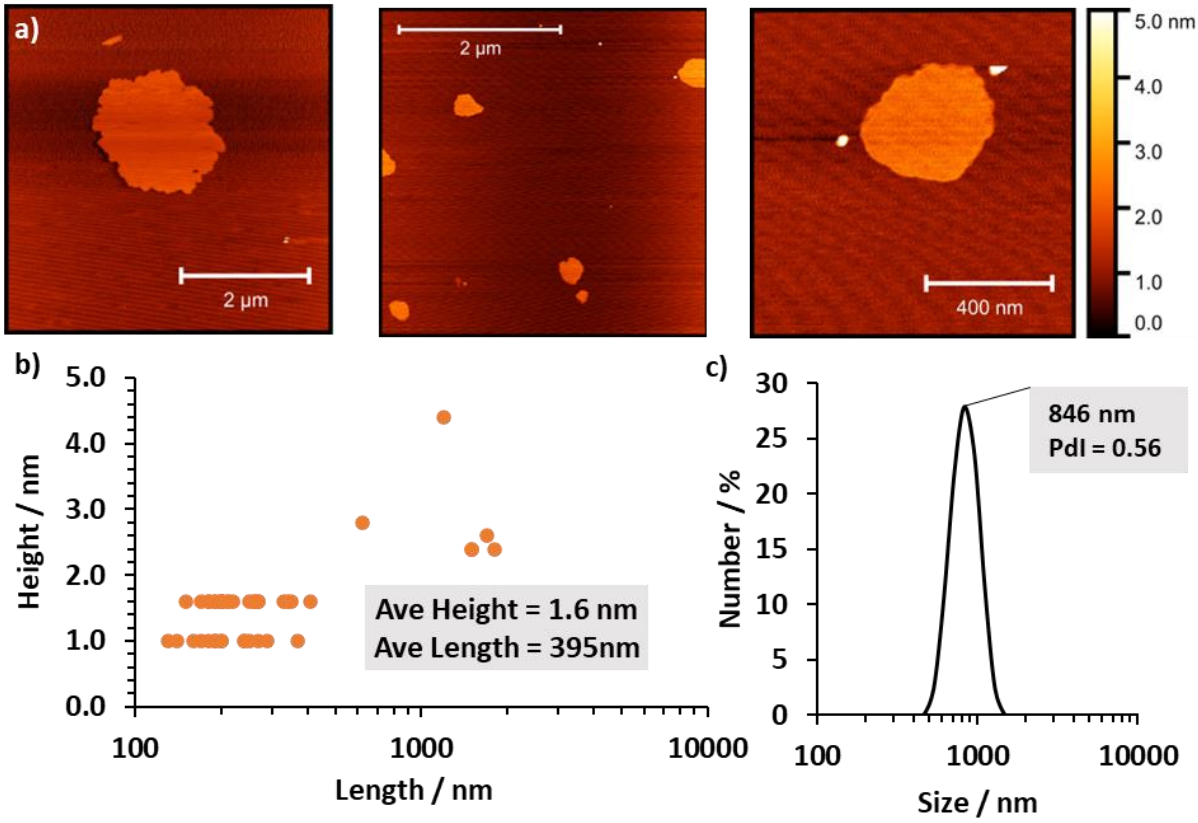

Figure 2.10: a) AFM images and b) the associated dimensions data of ZIF-7-NH_2 nanosheets with c) the associated DLS data.

2.2.4 Synthesis and Characterisation of ZIF-7-CH_3

The next example in the isoreticular ZIF-7-based series was ZIF-7-CH_3 where methyl-benzimidazole was used as the linker. The same adapted method used to synthesise ZIF-7-NH_2 was used where a mixed ligand system was produced as a result of using benzimidazole to nucleate growth and direct synthesis. The aromatic methyl group is weakly electron donating through conjugation which is likely to decrease the basicity of the imidazole in the same way as bim-NH_2. XRPD (Figure 2.12a) and SEM (Figure 2.12b) were used to confirm that bulk layered material had been synthesised, with a similar shift in the [002] peak as seen when introducing a functional group on the surface of the layers as seen previously in the schematic in Figure 2.9b.

The NMR spectra showed 20% functionality (Figure 2.30, experimental), which is a similar amount of pre-synthetic functionalisation as seen with ZIF-7-NH_2 (17 %). The IR spectrum (Figure 2.12c) confirmed that a benzene substituent was present with peaks 800 – 820 cm^{-1} and the peak at 2.48 ppm on the NMR spectrum proves this is a methyl group.

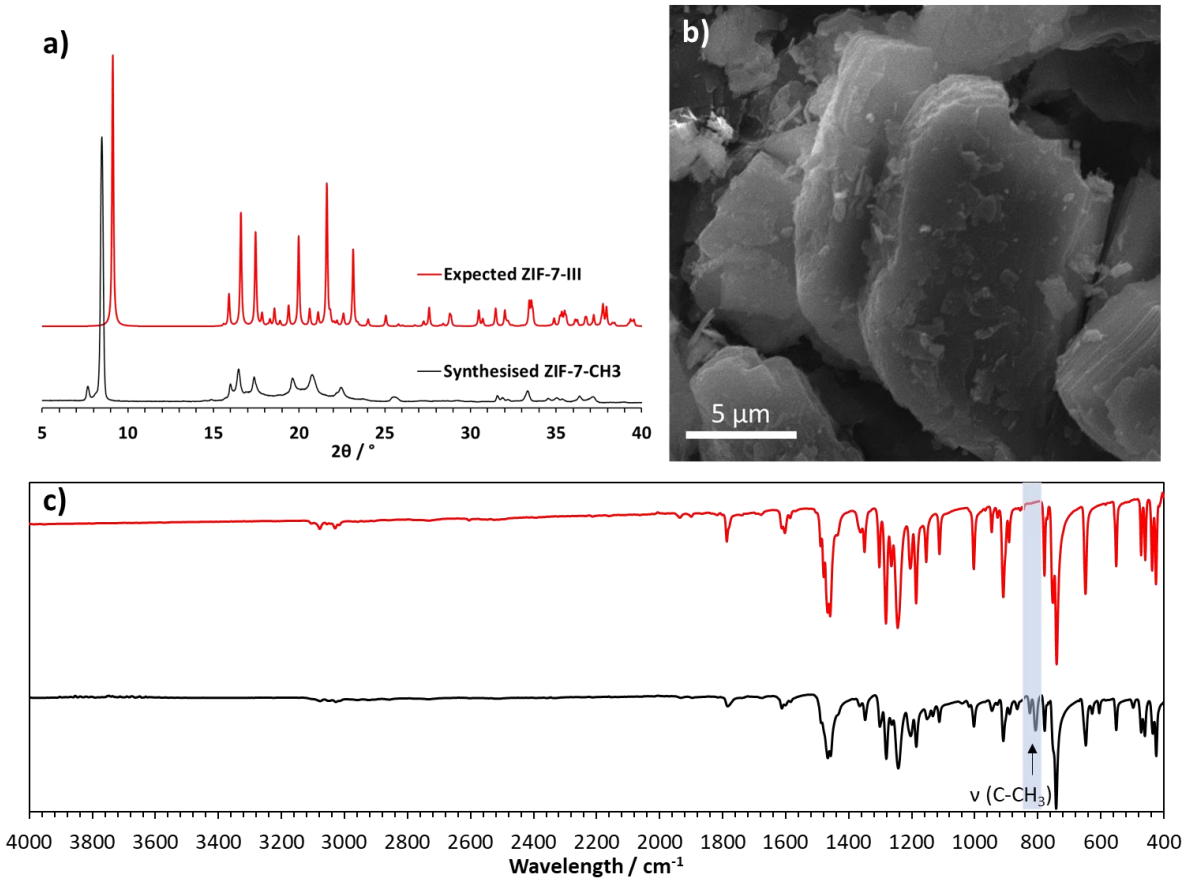

Figure 2.12: a) XRPD pattern of synthesised ZIF-7-CH_3 MOF and the expected patter of ZIF-7-III MOF, b) SEM of synthesised ZIF-7-CH_3 MOF, c) ATR-IR spectra of synthesised ZIF-7-CH_3 MOF (black) and synthesised ZIF-7 MOF (red).

Having confirmed the material was layered it underwent the same exfoliation conditions used for all previous ZIF-7-based MOFs. The size analysis data revealed two populations of nanosheets were accessed, with a laterally smaller group ~ 1.1 nm thick and ~ 100 nm in diameter and then another ultrathin group of nanosheets only ~ 0.7 nm thick and 100 – 1000 nm in length (Figure 2.13). The DLS data showed a peak at 779 nm which is smaller than the peak for ZIF-7 (1046 nm). Interestingly there was only one peak observed in the DLS even with the two groups of nanosheets identified by AFM, indicating that there could be larger nanosheets that were not imaged that results in the broad distribution around 779 nm.

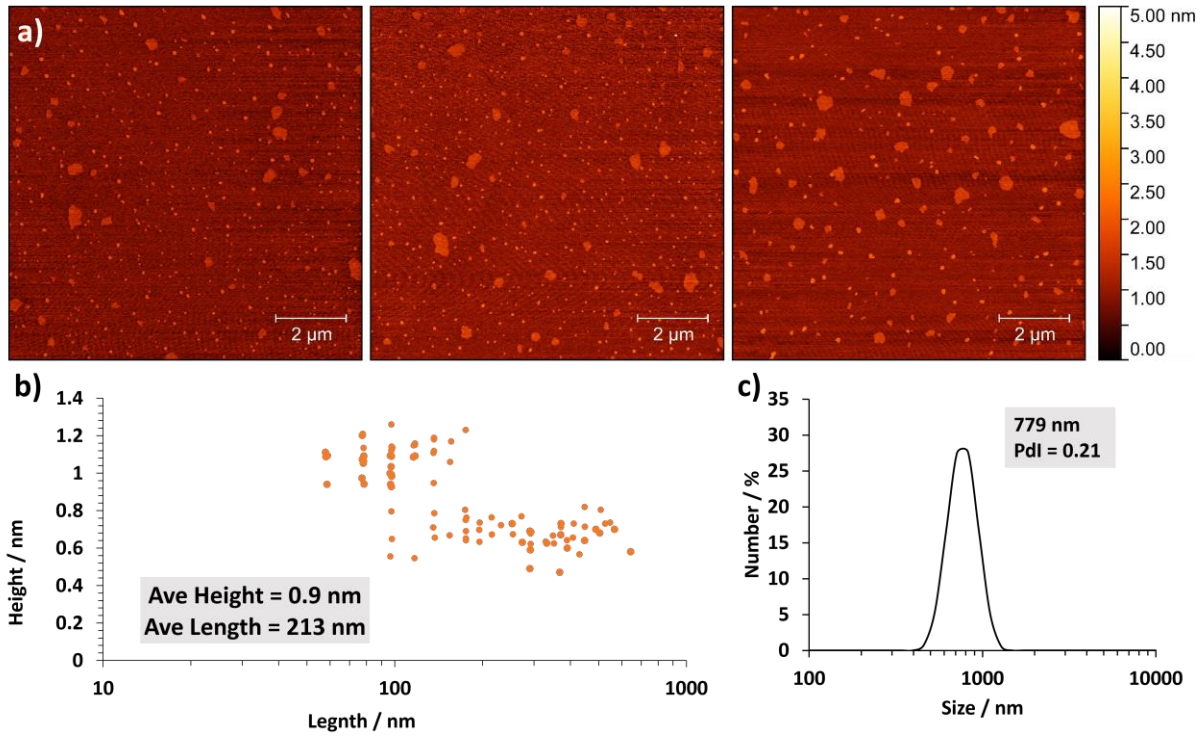

Figure 2.13: a) AFM images and b) the associated dimensions data of ZIF-7-CH_3 nanosheets with c) the associated DLS data.

2.2.5 Synthesis and Characterisation of ZIF-9

As well as swapping out the linker molecule to effect surface property changes, metal node exchange can also be employed. Here ZIF-9 was synthesised which contains the same organic linker molecule as ZIF-7 (benzimidazole) but has cobalt metal nodes. Following work carried out by Saini *et al.,* ZIF-9 nanosheets were accessed with slight modifications to the previously published method.[8] XRPD and SEM showed the direct synthesis of the bulk layered phase (Figure 2.14). This was a rapid room-temperature reaction where the metal salt, organic linker and sodium hydrocarbonate were dissolved in ethanol. The red solid metal salt turned purple in a matter of seconds as cobalt carbonate formed. This synthetic method was attempted using the zinc salt to form ZIF-7-III but did not work indicating the reactivity of the metal salt is important here.

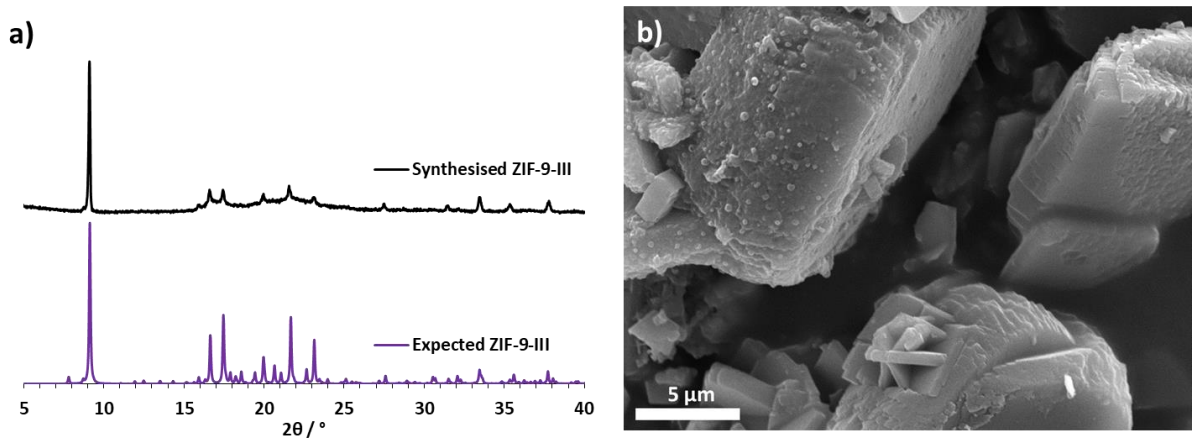

Figure 2.14: a) XRPD pattern of synthesised ZIF-9 MOF and the expected patter of ZIF-9-III, b) SEM of synthesised ZIF-9 MOF.

A 2 h ultrasonication (80 KHz) in ethanol produced ultrathin nanosheets as shown by the AFM images (Figure 2.15a). The AFM particle size analysis revealed that nanosheets ranged from 1.2 – 7 nm thick but were typically 1.6 nm. This is thinner than the current reported ZIF-9-III nanosheets that range from 2 - 4.6 nm in height.[7,19] The average length of the ZIF-9 nanosheets was 301 nm which is consistent with the current literature. The DLS measurement for this system was 891 nm (Figure 2.15c), which is a higher estimation than the nanosheets imaged using AFM. This may be due to the fact that all systems were suspended in methanol to make measurements comparable, and ZIF-9 may be more likely to aggregate in these conditions.

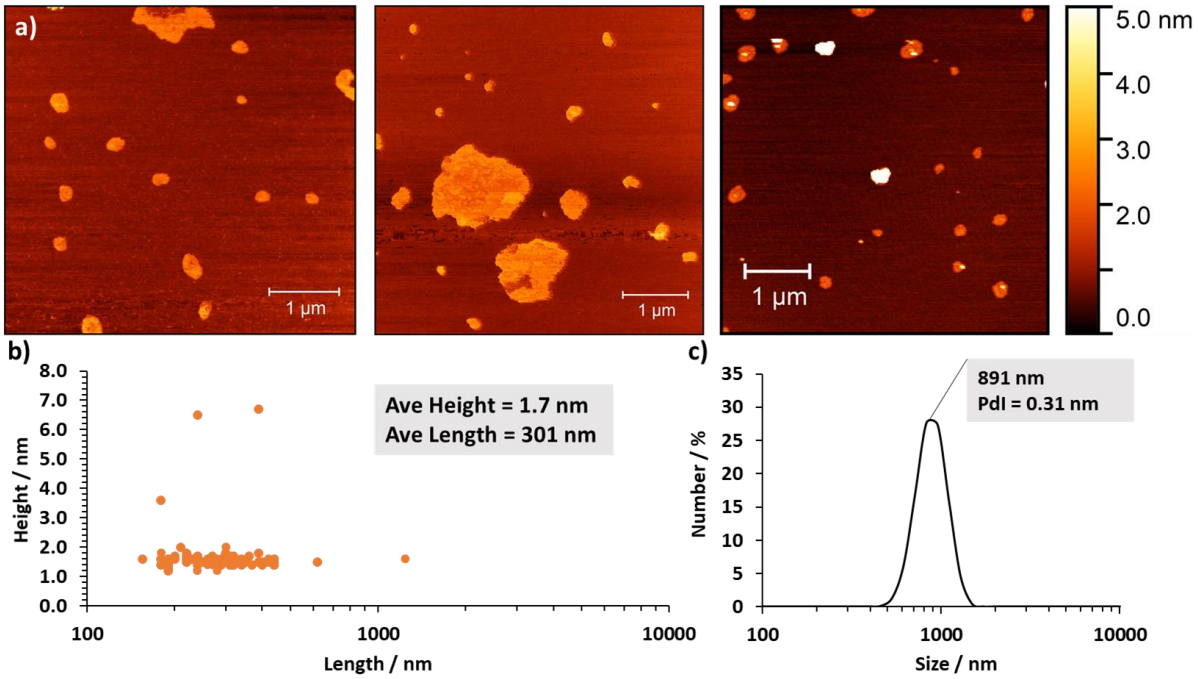

Figure 2.15: a) AFM images and b) the associated dimensions data of ZIF-9 nanosheets with c) the associated DLS data

2.2.6 Synthesis and Characterisation of ZIF-9-NH_2

To demonstrate the extent to which pre-synthetic modifications access a range of isoreticular materials with completely different surface properties attempts were made to synthesise ZIF-9 with amino functionality. When comparing to ZIF-7, both the metal node and linker are different for ZIF-9-NH_2 but the crystal structure was predicted to not change significantly. The same method used to synthesise ZIF-9 nanosheets was implemented with the direct replacement of benzimidazole with 5-amino-benzimidazole. This resulted in the formation of amorphous material, which was the same result as for the initial attempts at ZIF-7-NH_2 synthesis therefore the same mixed linker approach was taken again.

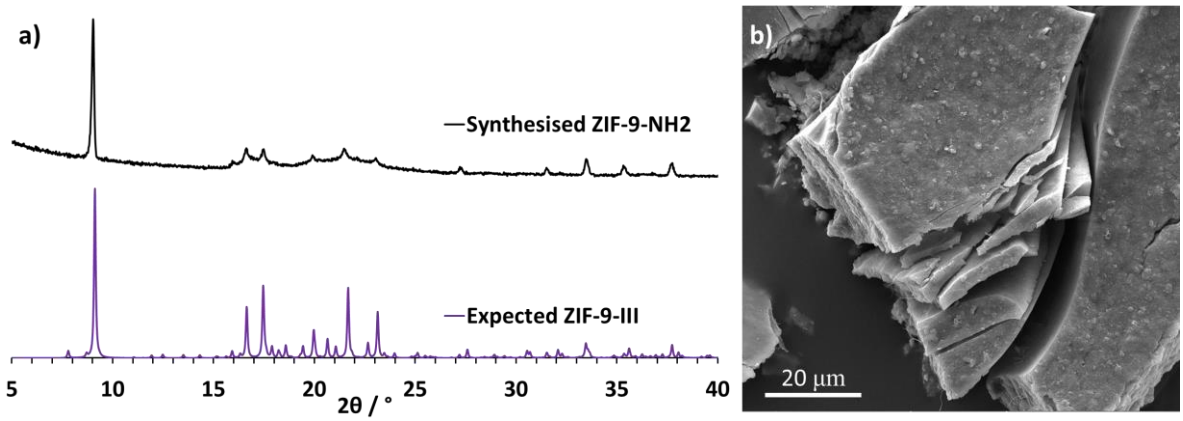

Figure 2.16: a) XRPD of synthesised ZIF-9-NH_2 MOF and expected ZIF-9-III (CCDC 988184), b) SEM image of synthesised ZIF-9-NH_2 MOF.

A 1:3 molar ratio of bim-NH_2 to bim was used to access bulk-layered ZIF-9-NH_2 material. This was confirmed using XRPD and SEM (Figure 2.16). The ^{1}H NMR spectrum showed that these conditions resulted in 10 % functionality of the amine group which is less than the ZIF-7-NH_2 system but this is likely a result of cobalt being less reactive than zinc. The ATR-IR spectrum (Figure 2.17) showed the characteristic ν(N–H) stretching bands appearing in the 3500–3350 cm^{-1} region.

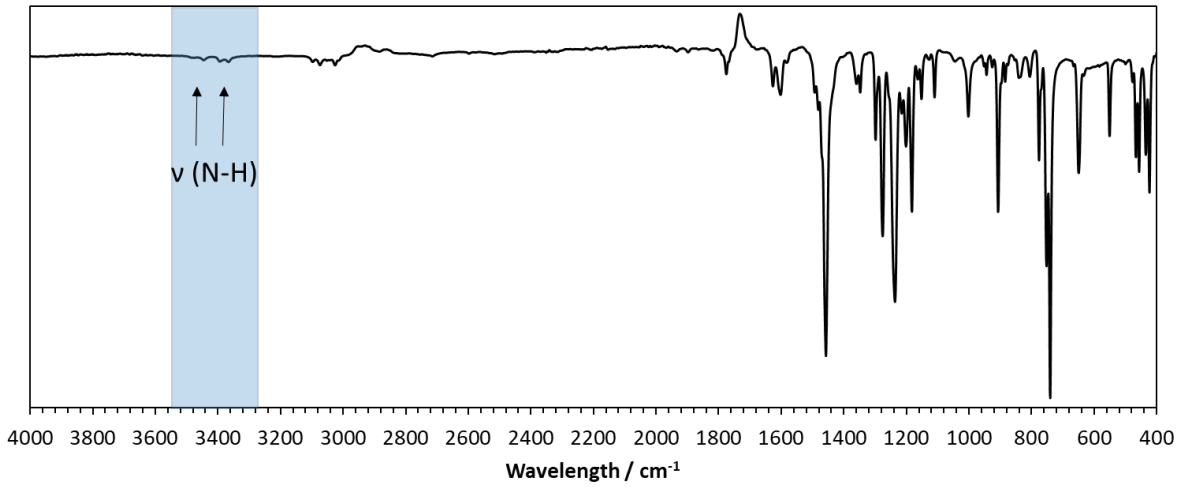

Figure 2.17: ATR-IR spectrum of ZIF-9-NH_2 MOF.

The ZIF-9 exfoliation protocol (2h ultrasonication in ethanol) was used to access individual nanosheets, with particle size analysis revealing ultrathin nanosheets were accessed. AFM analysis (Figure 2.18a+b) captured nanosheets that could be categorised into two populations with one group of MONs ~2.5 nm thick around 150 nm in length and single layer MONs ~1 nm thick with larger lateral dimensions reaching micrometres in scale. The DLS data in this case was more representative of the larger group of nanosheets. On comparison to the ZIF-9 system larger nanosheets were accessed. There is a similar size distribution of nanosheets as ZIF-7-CH_3 with two groups formed. The DLS data (Figure 2.18c) in both instances have number average peaks around the average height of the thinner and larger group of nanosheets.

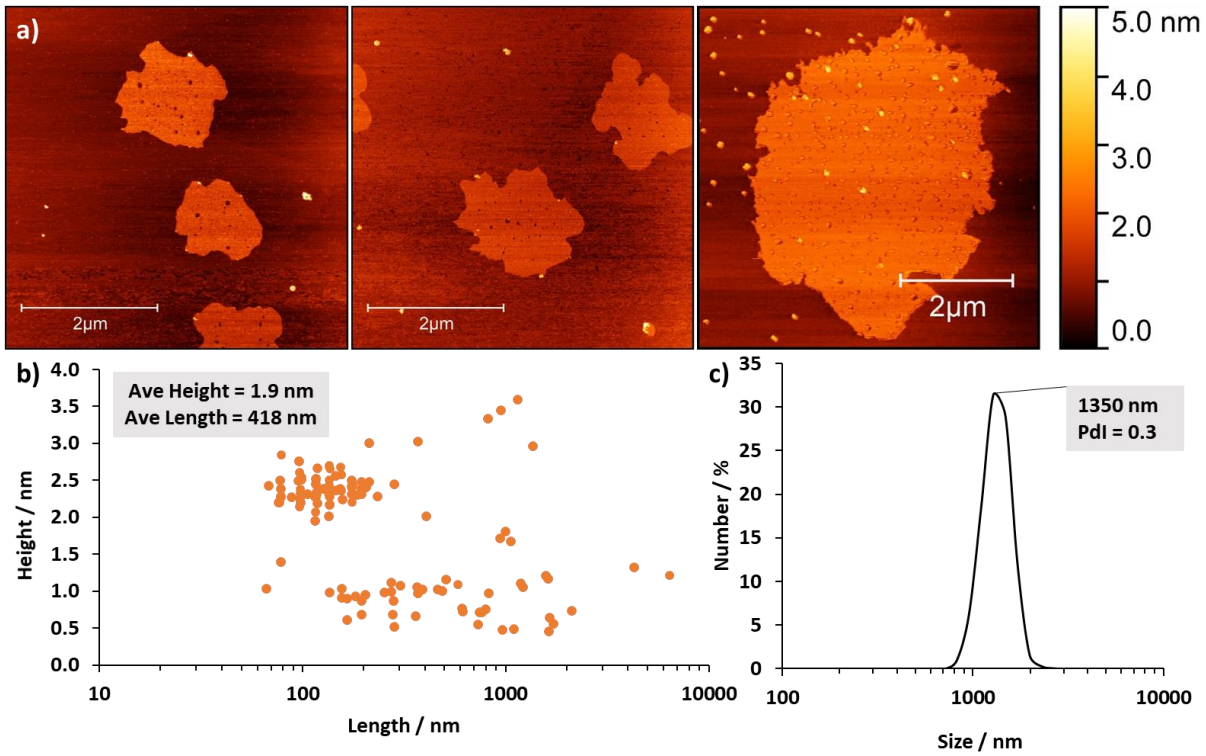

Figure 2.18: a) AFM images and b) the associated dimensions data of ZIF-9-NH_2 nanosheets with c) the associated DLS data

2.2.7 Stability Tests

Having successfully synthesised ZIF-7/9-III nanosheets and a series of isostructural functionalised MONs, the next step towards demonstrating their utility in biosensing was to test their stability in biological conditions. The physiologically relevant buffer, phosphate buffer saline (PBS) was used to incubate the MONs in order to determine any degradation of the MONs and effects on their crystallinity. XRPD patterns were compared before and after 24 h incubation in PBS (1 mg / mL, pH 7.4) at room temperature. Figure 2.19 shows the XRPD spectra for each MON, with no change in crystallinity observed for ZIF-7-Br and ZIF-7-CH_3. There were changes in powder pattern observed for ZIF-7 and ZIF-7-NH_2 with peaks appearing at 8.23 ° and 11.51 ° respectively. For the ZIF-9 MONs there were more peaks appearing, with a new peak at 13.37 ° as well as at ~ 8.3 ° and 11.36 °. The systems most suitable for biosensing applications are ZIF-7-Br and ZIF-7-CH_3 as they show no changes in the XRPD pattern after incubation. The other ZIF systems retain the major peaks associated with the MON structure, but new peaks appear that suggest other crystalline material is forming. This is likely a result of the phosphates in the buffer that are known to have high affinity to polyvalent cationic metal centres disrupting metal-linker bonds.[20]

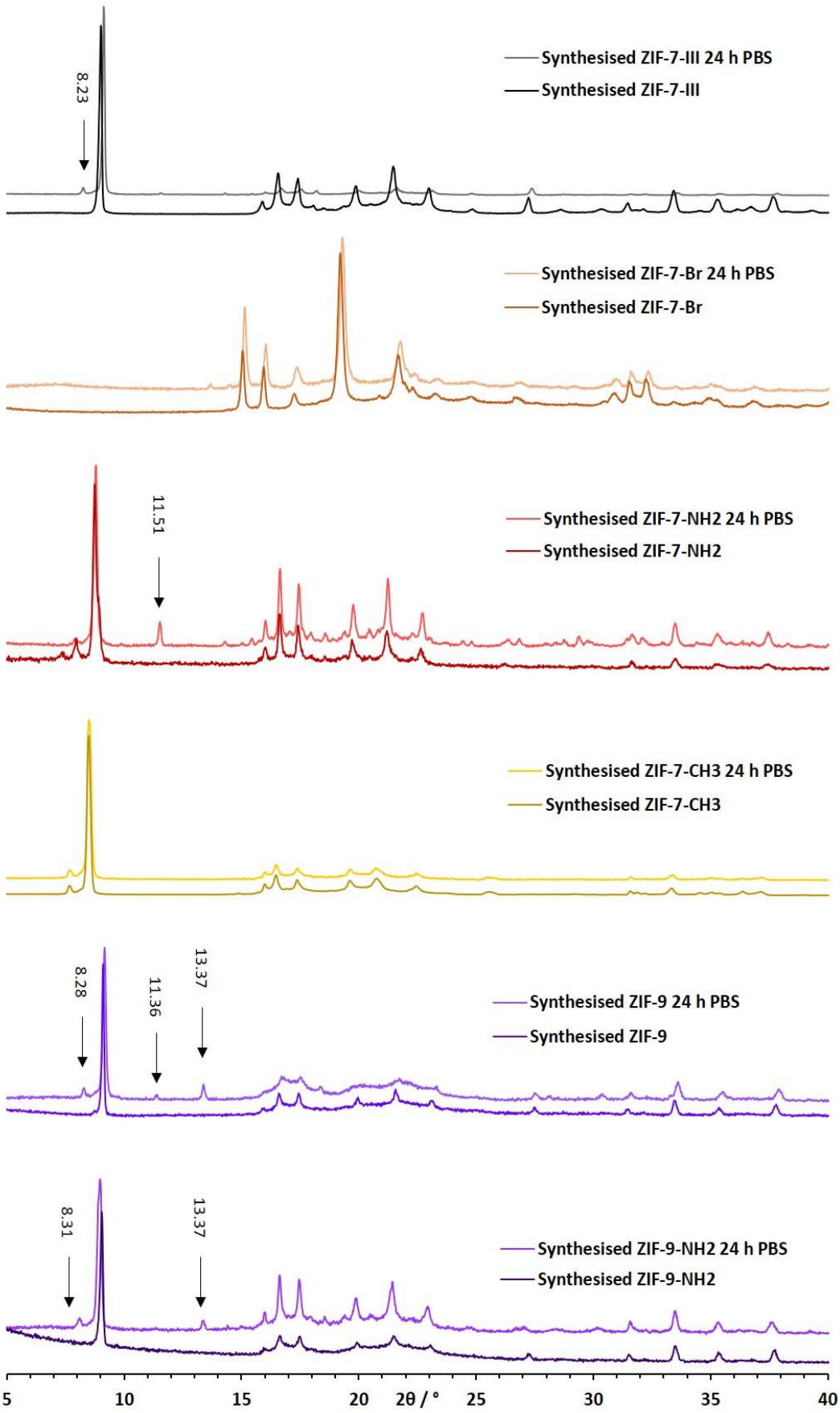

Figure 2.19: Comparison of the XRPD patterns for the synthesised ZIF MONs before and after incubation with PBS for 24 h.

2.2.8 Outcomes of Pre-Synthetic Functionalisation

When comparing the particle size analysis using DLS and AFM there is a consistent disagreement where the DLS measurement provides a higher estimate of the mean particle size (difference in blue (DLS) and green (AFM) line in Figure 2.20). Despite this, there is a similar trend for both types of analysis, with agreement that ZIF-7-Br and ZIF-7-CH_3 have the smallest particle sizes and ZIF-7 and ZIF-9-NH_2 have the largest.

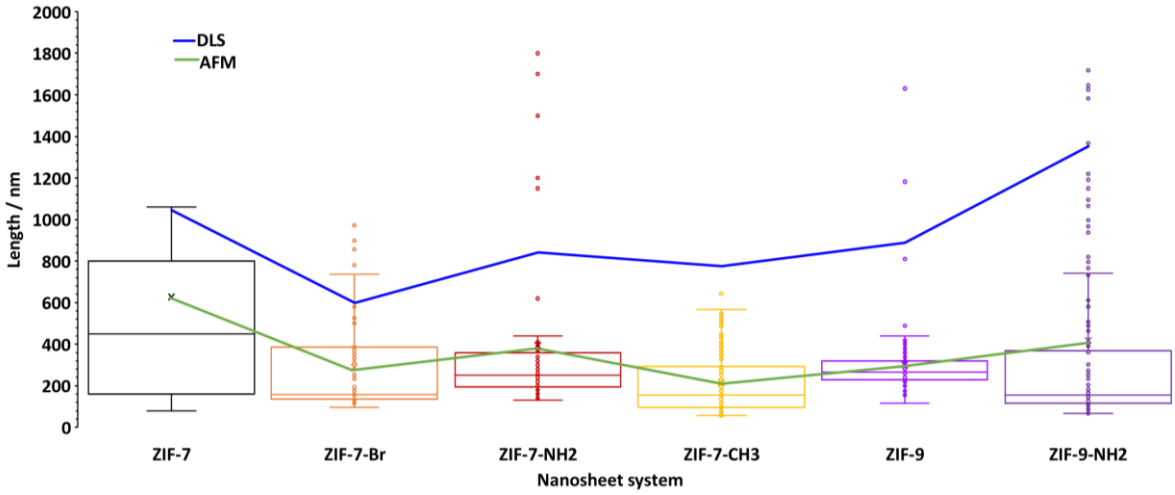

Figure 2.20: A zoomed in (0 - 2000 nm) comparison of AFM size analysis for each nanosheet system compared to the number mean (d.nm) determined using DLS.

Further comparison of the nanosheet dimensions are based off the AFM data only as issues of stability within the measurement environment plays less of a role. When evaluating the surface properties of the nanosheet series it is important to consider how/if the size of the nanosheet may affect performance. The particle sizes of the different ZIF-7 type systems will first be compared to determine the impact the linker has and then the same comparisons will be made for the similar ZIF-7 and ZIF-9 type systems to determine the effect of metal node and linker exchange.

First a comparison of the size analysis data for the different ZIF-7 based systems showed that for all four systems it was possible to access ultrathin nanosheets that were between 100-1000 nm in length (Figure 2.21). The ZIF-7 system ($Zn_2(bim)_4$) produced on average the thinnest nanosheets at 0.6 nm and the functionalised systems averaged at 0.9 – 7.8 nm. For ZIF-7-Br there was one population of ultrathin nanosheets ~ 0.9 nm in height which was consistent with the thinnest nanosheets from the other functionalised systems. A second population existed reaching heights of 25 nm with much smaller aspect ratios. The functionalised nanosheets were on average thicker than the standard ZIF-7 system (0.6 nm) which is as a result of the functional groups sticking into the [002] plane, off the surface of the nanosheet.

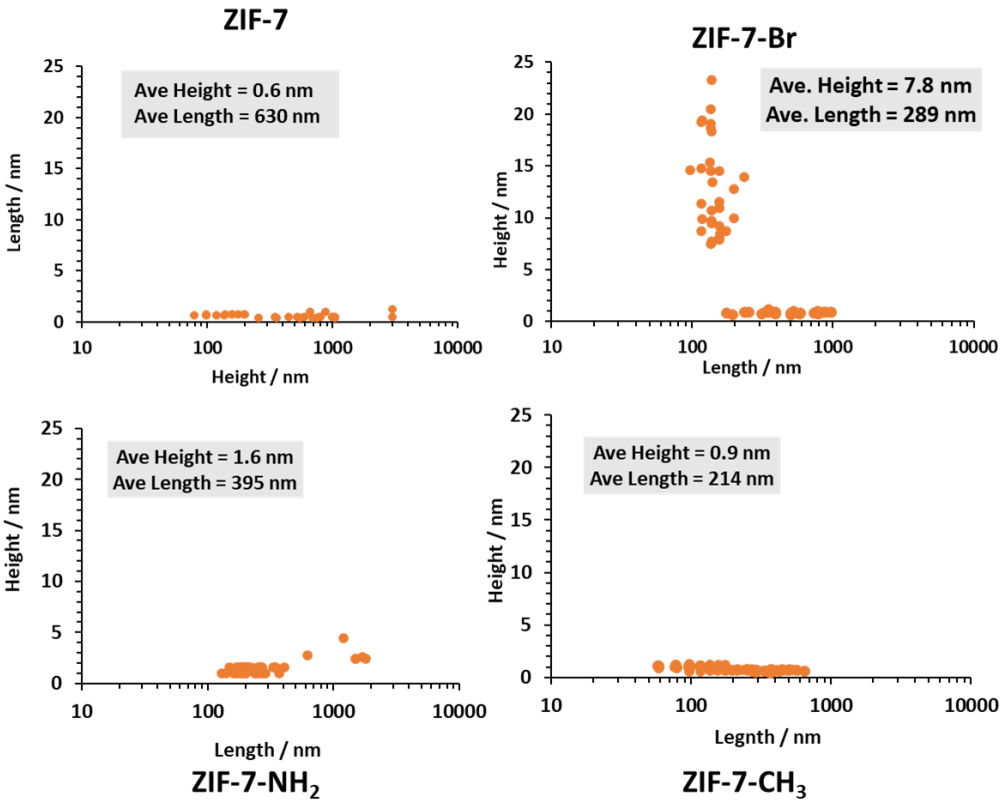

Figure 2.21: Comparison of the size analysis for ZIF-7, ZIF-7-Br, ZIF-7-NH_2 and ZIF-7-CH_3

Comparison of how metal and ligand exchange impacted size distribution is shown in Figure 2.22. Here a direct comparison of ZIF-7, ZIF-9, ZIF-7-NH_2 and ZIF-9-NH_2 is made where both zinc and cobalt metal nodes are used as well as benzimidazole and 5-amino-benzimidazole. Overall, all systems produced ultrathin layers with the majority of nanosheets between 100 nm and 1 µm, giving high aspect ratios. Again, the nanosheets were comparable in particle size therefore differences in surface properties is likely a result of the pre-synthetic modifications.

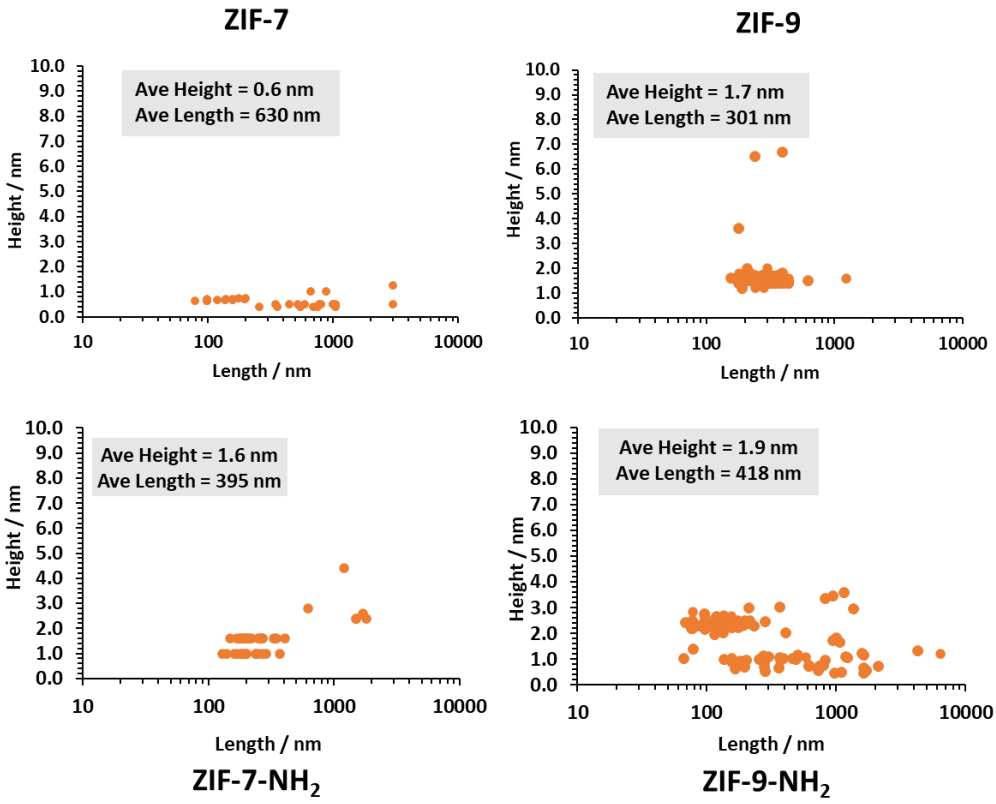

Figure 2.22: Comparison of the size analysis for ZIF-7, ZIF-9, ZIF-7-NH_2 and ZIF-9-NH_2

The charge of a biosensor surface plays a huge role in the recognition of the desired target. Understanding how tuning the composition of MONs can enable the tuning of surface charge will facilitate smart MON-based biosensor design. Due to the similarities in dimensions, it is likely that any difference in properties of the nanosheets is to do with chemical composition.

ZIF-7 pre-synthetic surface modifications effected zeta potential as shown in Figure 2.24, where MONs (1 mg / mL) were suspended in diluted PBS (1.37 mM wrt NaCl). Introducing a bromine group at 100 % functionality significantly increased the zeta potential to -6.7 mV. The bromo substituents are electron withdrawing meaning that orbital overlap within the benzene ring is expected to be disrupted altering the overall charge distribution. ZIF-7-CH_3 had only a small increase in zeta potential (-21.6 mV) which is likely due to the methyl substituents weak electron donation. Introducing amine functionality onto the surface significantly increases the zeta potential to 2.3 mV as at pH 7.7 the amine groups will introduce positive charge on the nanosheets surface. Due to the different degrees of functionalisation, direct trends cannot be established but it is clear that ligand substitution impacts zeta potential.

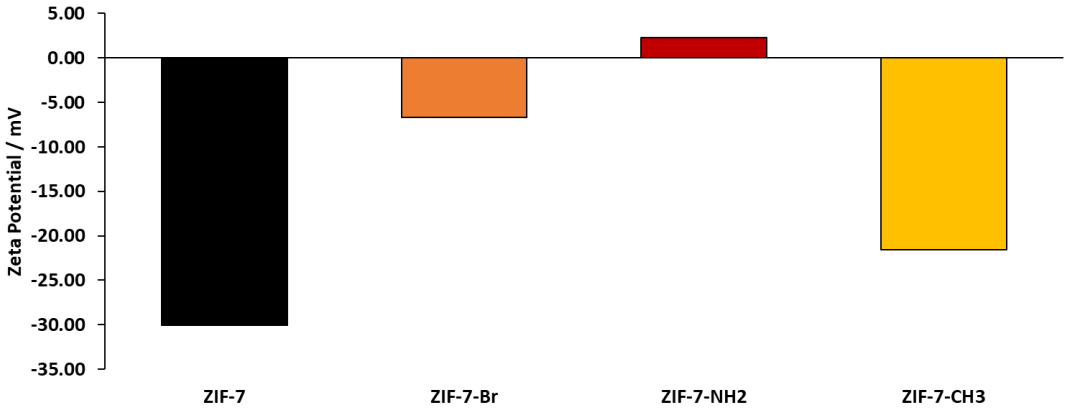

Figure 2.24: Zeta potential measurements of ZIF-7, ZIF-7-Br, ZIF-7-NH_2 and ZIF-7-CH_3 MONs (1 mg / mL, 1.37 mmol PBS wrt NaCl)

The comparison of zeta potential data of ZIF-7, ZIF-7-NH_2, ZIF-9 and ZIF-9-NH_2 MONs suspended in diluted PBS is shown in Figure 2.23. ZIF-7 and ZIF-9 ($Co_2(bim)_4$) have similar values of - 30.1 mV and - 27.9 mV, therefore metal node exchange has little impact. Introducing amine functionality onto the surface in both cases significantly increases the zeta potential to 2.3 mV for ZIF-7-NH_2 and to -20.5 mV for ZIF-9-NH_2. There was a greater level of amine functionality introduced onto the ZIF-7-NH_2 surface (17 %) compared to the ZIF-9-NH_2 system (10%) and this may explain the larger change in zeta potential for the zinc based MONs.

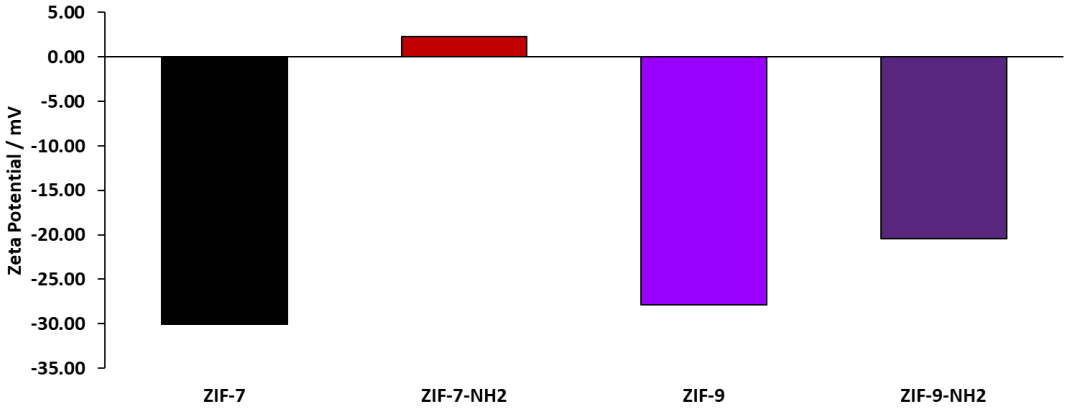

Figure 2.23: Zeta potential data for ZIF-7, ZIF-9 , ZIF-7-NH_2 and ZIF-9-NH_2 in diluted PBS (1.37 mmol wrt NaCl).

Contact angle measurements (Figure 2.25) revealed the effect of functionalisation on the hydrophobicity of the MONs. ZIF-7 and ZIF-9 gave angles of 149 ° and 145.9 ° respectively, consistent with the literature values (ZIF-9 = 144 °).[8] Introducing the bromine and methyl groups onto the ZIF-7 surface increased the contact angle to 161.3 ° and 154.9 °, indicating increased hydrophobicity. This is consistent with the effects seen in the pre-synthetic functionalisation work done by Lopez-Cabrelles *et al.* with the $Fe(bimX)_2$ based systems.[12] The amine group reduced the contact angle for both the ZIF-7-NH_2 and ZIF-9-NH_2 system as a result of its polarity. This study shows that the functional linkers introduced different hydrophobic characteristics to the MON surface, even at 10 % functionalisation (ZIF-9-NH_2).

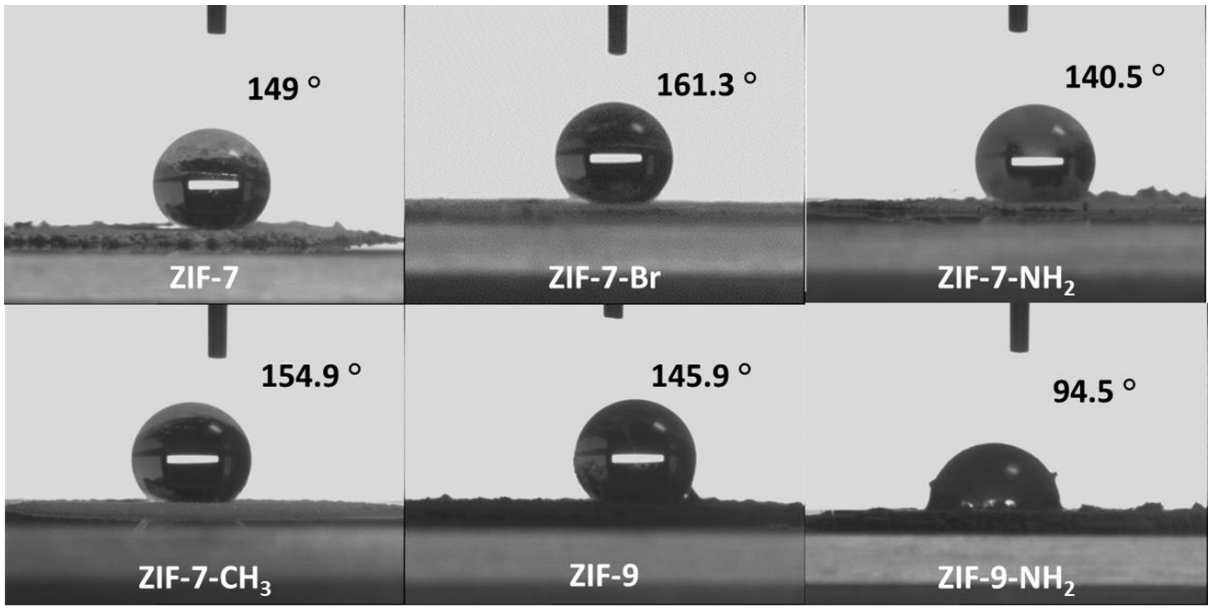

Figure 2.25: Contact angle images for all the synthesised ZIF MONs.

2.3 Conclusion

In this chapter six layered MOFs, four of which were novel, were synthesised using two different metal ions and four different linkers and exfoliated to form nanosheets. Their structure and properties were characterised and their potential for use in biosensing applications evaluated. Benzimidazole and three of its derivatives (bim-Br, bim-NH_2 and bim-CH_3) along with zinc (ZIF-7 type) and cobalt (ZIF-9 type) were selected to create a series of isoreticular MONs with a variety of surface functionalities. The components were incorporated in the initial synthetic step and underwent a hydrothermal phase transition to access the layered MOF. Previously reported ZIF-7 and ZIF-9 nanosheets were accessed via liquid-assisted exfoliation down to 0.6 nm and 1.7 nm in height respectively, with both systems producing nanosheets with large aspect ratios ranging ~ 100-1000.

Pre-synthetic functionalisation of ZIF-7 with bim-Br resulted in nanosheets with 100 % bromine functionality. The direct replacement of bim with bim-br was possible in this instance due to the electron withdrawing nature of the substituent increasing the basicity of the imidazole. For the introduction of bim-NH_2 and bim-CH_3 a different approach had to be taken as the basicity of the imidazole was reduced by the functional groups and amorphous material was produced. A 1:1 mixture of bim and bim-NH_2 meant nucleation of the desired particle growth was possible and a mixed linker system was produced with 17 % amine functionality (ZIF-7-NH_2). Using the same approach was taken for the synthesis of ZIF-7-CH_3 (using bim-CH_3) where 20 % methyl functionality was achieved and ZIF-9-NH_2 was synthesised where 10 % amine functionalisation was achieved. Having successfully synthesised six layered MOFs the material was exfoliated using ultrasonication to access the individual layers with particle size and surface properties analysed.

The ZIF-7-Br nanosheets were thicker than those of ZIF-7 with the thinnest nanosheets having heights of 0.9 nm. Two different groups of ZIF-7-Br MONs were accessed (multilayer ~ 164 nm and monolayer ~ 1106 nm) suggesting the exfoliation protocol needed to be optimised in order to isolate the group of monolayer nanosheets. All other pre-synthetic functionalisation resulted in no significant changes to lateral dimensions and monolayer heights increased relative to the functional group incorporated into the [002] plane.

The different MON systems underwent a stability test under physiological conditions (24 h, PBS, pH 7.4) where the XRPD pattern after incubation determined whether there was any changes to the crystal structure. This biostability test revealed that ZIF-7-Br and ZIF-7-CH_3 were the most stable systems as there was no changes to the overall XRPD pattern. ZIF-7, ZIF-7-NH_2, ZIF-9 and ZIF-9-NH_2 all saw some slight changes to the pattern after incubation where new crystal peaks appeared. The cobalt based systems showed more new peaks than the zinc based systems indicating reduced stability therefore they might be suitable candidates for controlled drug delivery.[20] As the key peaks remained unchanged, the biostability of all the systems was confirmed. Extended stability testing in PBS combined with particle size analysis would confirm the maximum time of incubation before significant changes are observed.

Whilst the lack of 100 % functionality resulted in the unpredictable arrangement of functional groups in some cases, information as to the impact this had on surface properties could be established. All synthesised MONs had differing zeta-potential values and contact angle measurements with respect to their parent system. With all modifications leading to an increased zeta potential but both increased and decreased hydrophobicity. The incorporation of bim-NH_2 dramatically increased the zeta potential, even at low levels of functionalisation indicating the potential control over surface

charge by varying the ratio of linker components. Bim-Br had the largest impact on contact angle measurements where the hydrophobic character of ZIF-7-Br was increased dramatically compared to ZIF-7, indicating the same approach to linker blending could be used to tune surface hydrophobicity.

Overall, pre-synthetic functionalisation of the ZIF-7/9 systems resulted in MONs with different surface properties. By producing an isoreticular MON series through exchanging the metal node and/or linker it is possible to tune the charge and hydrophobicity. Surface analysis could be compared meaningfully as all nanosheets were ultrathin and of similar lengths. The majority of the changes to surfaces properties can be assigned to the linker components as the metal node didn't significantly change zeta potential or contact angle measurements. Due to the range in surface properties available it is predicted that the systems described will be appropriate candidates for biosensing applications, where each system is likely to bind to different biomolecules with different affinities. Further tuning could be attempted through using a multivariate linker approach using more than two different linkers.

2.4 Experimental

2.4.1 Synthesis and Exfoliation of ZIF-7

Zinc nitrate hexahydrate (755 mg, 2.54 mmol) and benzimidazole (1.92 g, 16.28 mmol) were dissolved in DMF (250 mL, 3.25 mol). After stirring for 1 h, the solution is kept statically at room temperature for 72 h. ZIF-7 nanoparticles were then collected by centrifugation and thoroughly washed with methanol and dried at 50 °C overnight. Then subsequently dried at 120 C for 48 h in a vacuum oven. The obtained ZIF-7-I was redispersed in distilled water at a concentration of 0.5 wt % and then refluxed at 100 C for 24 h. The turbid mixture was washed with distilled water once and methanol three times, and then dried at 50 C overnight to obtain ZIF-7-III (486 mg, 0.805 mmol, 42 %) as a white powder. Elemental Analysis: Expected Mass %: C 56.1, H 3.3, N 18.7 Found Mass %: C 56.21, H 3.51, N 18.6; (ESI-NEG): $[M]^+$ 119.1 (benzimidazole). ^{1}H NMR (DCl/DMSO-d_6): 11.84 (s, 1H), 10.08 (m, 2H), 9.80 (m, 2H). Phase purity confirmed by XRPD with a comparison to the CCDC (675375) powder pattern for ZIF-7-III.

80 mg ZIF-7-III was ultrasonicated in 120 mL of a mixed solvent of methanol and n-propanol (1:1, v/v) at 80 KHz for 2 hr to access nanosheets. After being centrifuged at 500 rpm for 5 min, the collected supernatant containing the nanosheets was the centrifuged at 12,000 rpm for 1 hr.

Table 2.1: Elemental analysis data for ZIF-7-III MOF.

Element	Expected ZIF-7-III	Synthesised ZIF-7-III
Carbon	56.1	56.1
Hydrogen	3.4	3.5
Nitrogen	18.7	18.5

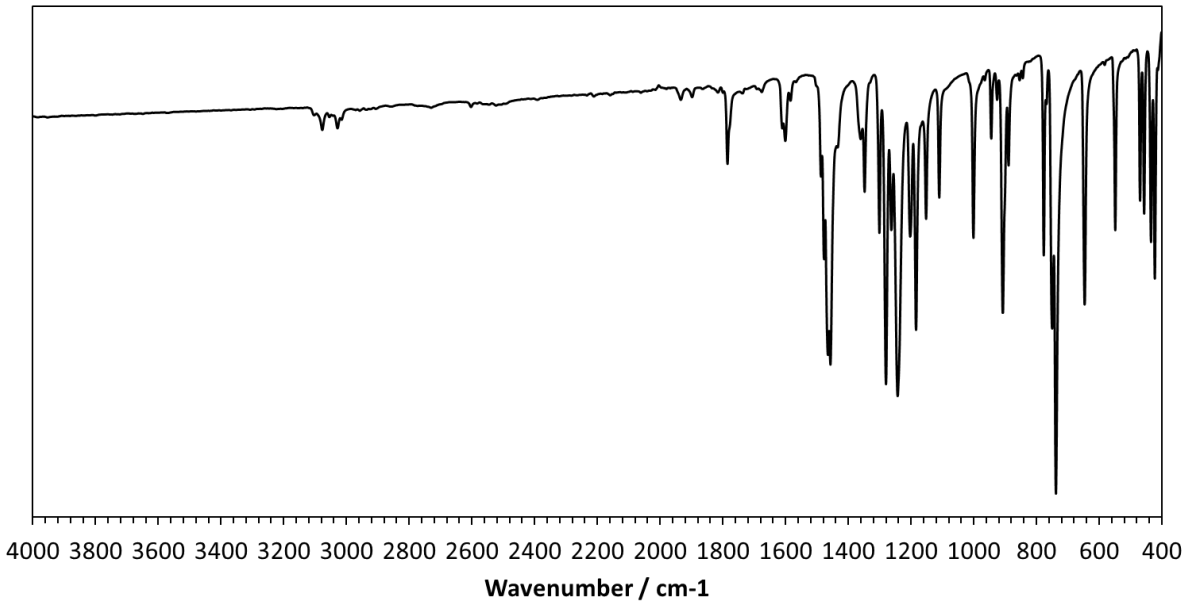

Figure 2.26: ATR-IR spectrum of ZIF-7 MOF

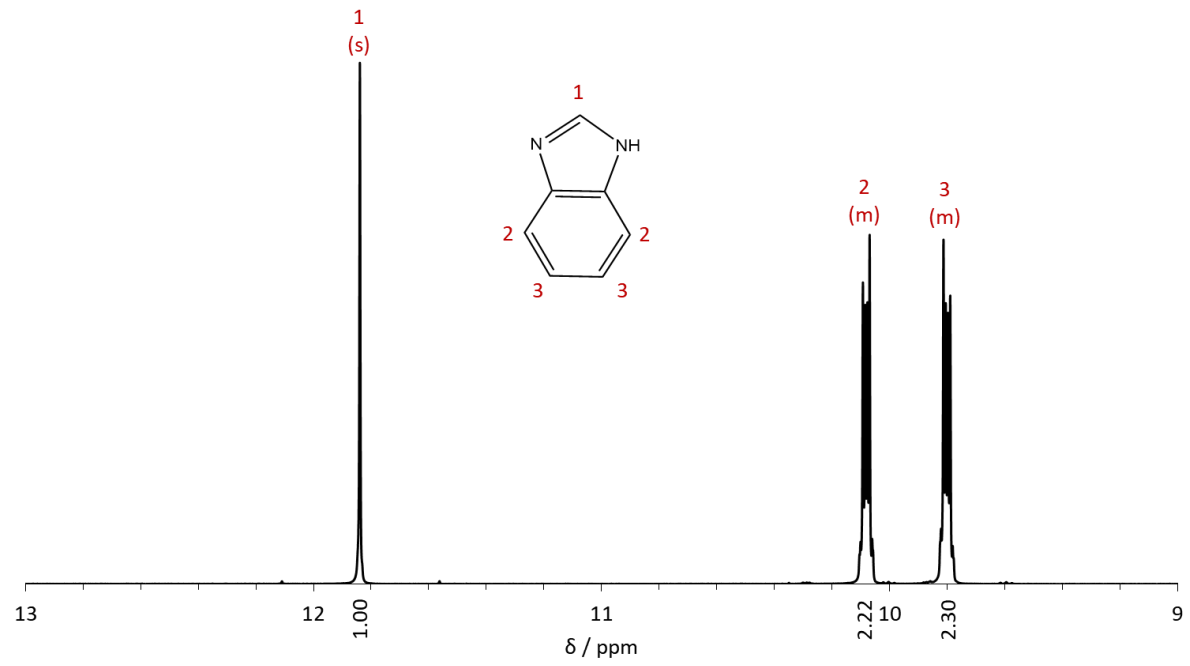

Figure 2.27: ^{1}H NMR spectrum of ZIF-7 in DMSO after digestion using DCl.

2.4.2 Synthesis and Exfoliation of ZIF-7-Br

Zinc nitrate hexahydrate (755 mg, 2.54 mmol) and 5-bromobenzimidazole (1.92 g, 16.28 mmol) were dissolved in DMF (250 mL, 3.25 mol). After stirring for 1 h, the solution is kept statically at 30 °C for 2 weeks. ZIF-7-Br nanoparticles were then collected by centrifugation and thoroughly washed with methanol and dried at 50 °C overnight. Then subsequently dried at 80 °C for 48 hr in a vacuum oven. ZIF-7-Br-I was redispersed in distilled water at a concentration of 0.5 wt % and refluxed in a microwave for 5 hrs at 150 °C. The turbid mixture was washed with distilled water once and methanol three times, and then dried at 50 °C overnight to obtain ZIF-7-Br-III (370 mg, 0.806 mmol, 32 %) as a yellow powder. Elemental Analysis: Expected Mass %: C 36.7, H 1.97, N 12.2, Br 34.7 Found Mass %: C 36.39, H 1.98, N 11.96, Br 33.89; (ESI-NEG): $[M]^+$ = 198.03 (5-bromobenzimidazole). ^{1}H NMR (400 MHz, DCl/DMSO-d_6): δ 9.65 (s, 1H), 8.11 (d, J = 1.8 Hz, 1H), 7.84 (d, J = 5.5 Hz, 1H), 7.74 (m, 1H). Phase purity confirmed by XRPD with a comparison to the CCDC (1849147) powder pattern for MUV-1-Br.

80 mg ZIF-7-Br-III was ultrasonicated in 120 mL of a mixed solvent of methanol and n-propanol (1:1, v/v) at 80 KHz for 2 hr to access nanosheets (21.6 mg, 27 %). After being centrifuged at 500 rpm for 5 min, the collected supernatant containing the nanosheets was the centrifuged at 12,000 rpm for 1 hr.

Table 2.2: Elemental data for ZIF-7-Br MOF.

Element	Expected ZIF-7-Br	Synthesised ZIF-7-Br
Carbon	36.7	36.39
Hydrogen	1.97	1.98
Nitrogen	12.2	11.96
Bromine	34.7	33.89

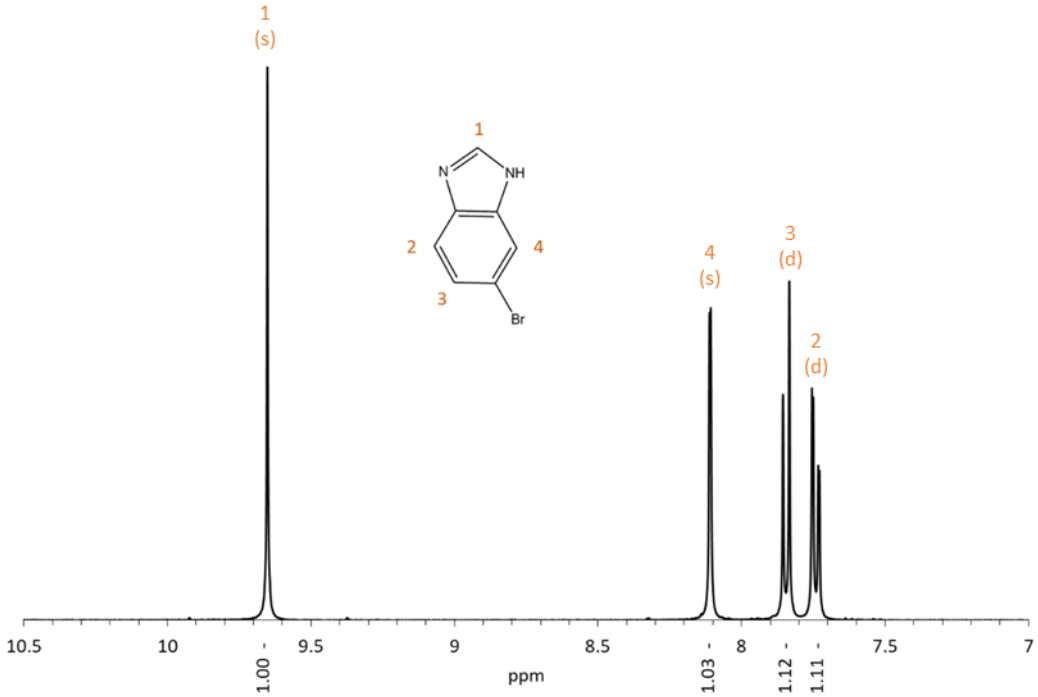

Figure 2.28: ^{1}H NMR spectra of ZIF-7-Br MOF in DMSO after digestion using DCl.

2.4.3 Synthesis and Exfoliation of ZIF-7-NH_2

Zinc nitrate hexahydrate (755 mg, 2.54 mmol), (962 mg, 8.14 mmol) benzimidazole and (1.08 g, 8.11 mmol) 5-aminobenzimidazole were dissolved in DMF (125 mL, 1.63 mol). After stirring for 1 h, the solution is kept statically at 30 °C for 2 weeks. ZIF-7-NH_2 nanoparticles were then collected by centrifugation and thoroughly washed with methanol and dried at 50 °C overnight. Then subsequently dried at 120 °C for 48 h in a vacuum oven. The obtained ZIF-7-NH_2-I was redispersed in distilled water at a concentration of 0.5 wt % and then refluxed at 100 C for 1 week. The turbid mixture was washed with distilled water once and methanol three times, and then dried at 50 °C overnight to obtain ZIF-7-NH_2-III (436 mg, 0.694 mmol, 27 %) as a purple powder. Elemental Analysis: Expected Mass %: C 54.6, H 3.4, N 20.0 Found Mass %: C 53.2, H 3.5, N 19.9; (ESI-NEG):$[M]^+$ 134.1 (Bim-NH_2), $[M]^+$ 119.1 (Bim). ^{1}H NMR (DCl/DMSO-d_6): 9.73 (s, 1H, **Bim-NH_2**), 9.66 (s, 1H, **Bim**), 8.03 (d, 1H, **Bim-NH_2**), 8.00 (s, 1H, **Bim-NH_2**), 7.92 – 7.83 (m, 2H, **Bim**), 7.64 (d, *J* = 2.0 Hz, 1H, **Bim-NH_2**), 7.63 – 7.55 (m, 2H, **Bim**). Phase purity confirmed by XRPD with a comparison to the CCDC (675375) powder pattern for ZIF-7-III.

80 mg ZIF-7-NH_2-III was ultrasonicated in 120 mL of a mixed solvent of methanol and n-propanol (1:1, v/v) at 80 KHz for 2 hr to access nanosheets (22.9 mg, 29 %). After being centrifuged

at 500 rpm for 5 min, the collected supernatant containing the nanosheets was the centrifuged at 12,000 rpm for 1 hr.

Table 2.3: Elemental analysis data for ZIF-7-NH_2 MOF.

Element	Expected ZIF-7-NH_2	Synthesised ZIF-7-NH_2
Carbon	54.6	53.2
Hydrogen	3.4	3.5
Nitrogen	20.0	19.9

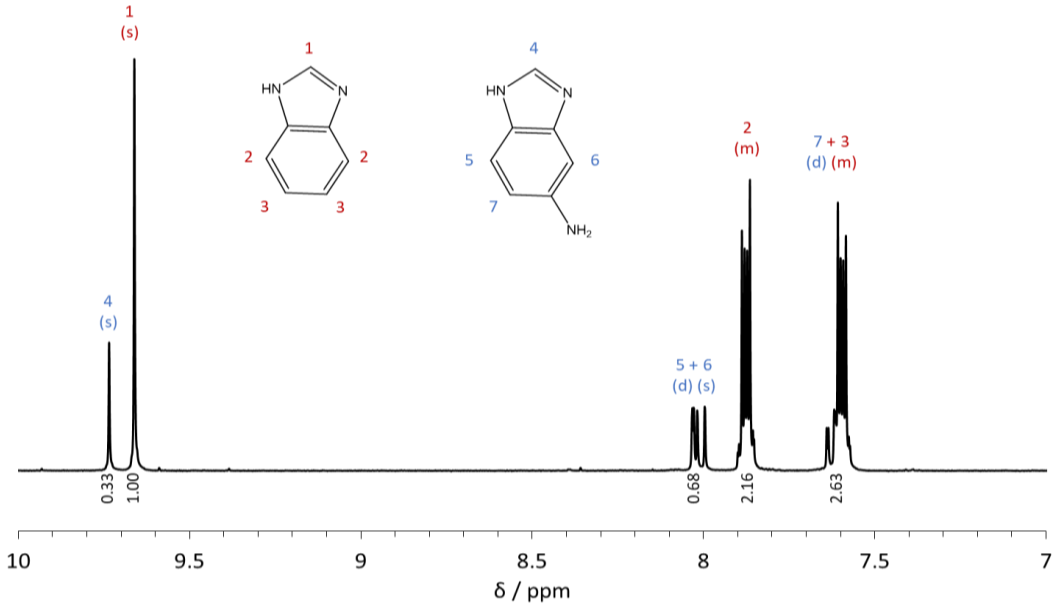

Figure 2.29: ^{1}H NMR spectrum of ZIF-7-NH_2 digested with DCl/DMSO-d6, with peaks assigned according to the inset molecular structures.

2.4.4 Synthesis and Exfoliation of ZIF-7-CH_3

Zinc nitrate hexahydrate (755 mg, 2.54 mmol), (962 mg, 8.14 mmol) benzimidazole and (1.07 g, 8.11 mmol) 5-methylbenzimidazole were dissolved in DMF (125 mL, 1.63 mol). After stirring for 1 h, the solution is kept statically at 30 °C for 2 weeks. ZIF-7-CH_3 nanoparticles were then collected by centrifugation and thoroughly washed with methanol and dried at 50 °C overnight. Then subsequently dried at 120 °C for 48 h in a vacuum oven. The obtained ZIF-7-I was redispersed in distilled water at a concentration of 0.5 wt % and then refluxed at 100 C for 1 week. The turbid mixture was washed with distilled water once and methanol three times, and then dried at 50 °C overnight to obtain ZIF-7-III (436 mg, 0.694 mmol, 27 %) as a yellow powder. Elemental Analysis: Expected Mass %: C 56.7, H 3.6, N 18.4 Found Mass %: C 55.1, H 3.4, N17.6; (ESI-NEG):$[M]^+$ 134.1 (Bim-NH_2), $[M]^+$ 119.1 (Bim). ^{1}H NMR (400 MHz, DCl/DMSO-d_6): δ 9.63 (s, 1H, **Bim**), 9.55 (s, 1H, **Bim-CH_3**), 7.90 – 7.84 (m, 2H, **Bim**), 7.74 (d, J = 8.5 Hz, 1H, **Bim-CH_3**), 7.65 (s, 1H, **Bim-CH_3**), 7.63 – 7.55 (m, 2H, **Bim**), 7.44 – 7.38 (m,

1H, **Bim-CH_3**), 2.48 (s, 3H, **Bim-CH_3**). Phase purity confirmed by XRPD with a comparison to the CCDC (675375) powder pattern for ZIF-7-III.

80 mg ZIF-7-CH_3-III was ultrasonicated in 120 mL of a mixed solvent of methanol and n-propanol (1:1, v/v) at 80 KHz for 2 hr to access nanosheets (30 mg, 38 %). After being centrifuged at 500 rpm for 5 min, the collected supernatant containing the nanosheets was the centrifuged at 12,000 rpm for 1 hr.

Table 2.4: Elemental analysis of ZIF-7-CH_3 MOF.

Element	Expected ZIF-7-CH_3	Synthesised ZIF-7-CH_3
Carbon	56.7	55.1
Hydrogen	3.6	3.4
Nitrogen	18.4	17.6

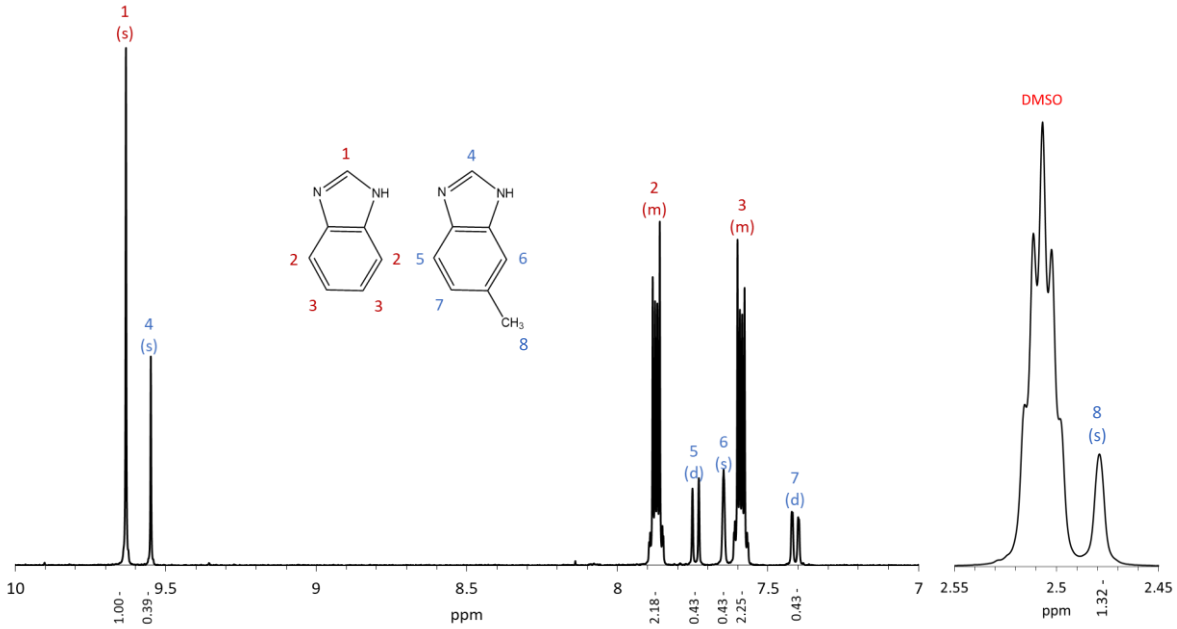

Figure 2.30: ^{1}H NMR of ZIF-7-CH_3 MOF in DMSO after digestion using DCl with peak assignments (red – benzimidazole, blue – methyl-benzimidazole).

2.4.5 Synthesis and Exfoliation of ZIF-9

Cobalt nitrate hexahydrate (87 mg, 0.30 mmol), benzimidazole (71 mg, 0.60 mmol) and sodium hydrocarbonate (47 mg, 0.56 mmol) was suspended in ethanol (2 ml, 72.7 mmol) and sonicated for 1 min. The solution was kept statistically at 50 °C for 72 h. The obtained ZIF-9-III was washed three times with ethanol and three times with water then dried in at 80 °C for 48 h in a vacuum oven producing a purple powder (79.7 mg, 0.037 mmol, 49 %). Elemental Analysis: Expected Mass %:

C 57.3, H 3.4, N 19.1 Found Mass %: C 56.1, H 3.7, N 18.3; (ESI-NEG): $[M]^+$ 119.1 (Bim). ^{1}H NMR (400 MHz, DCl/DMSO-d_6): δ 9.63 (s, 1H, **Bim**) 7.90 – 7.84 (m, 2H, **Bim**), 7.63 – 7.55 (m, 2H, **Bim**). Phase purity confirmed by XRPD with a comparison to the CCDC (988184) powder pattern for ZIF-9-III.

8 mg ZIF-9-III was ultrasonicated in 10 mL of ethanol at 80 KHz for 2 hr to access nanosheets (1.9, 23 %). After being centrifuged at 500 rpm for 5 min, the collected supernatant containing the nanosheets was the centrifuged at 12,000 rpm for 1 hr.

Table 2.5: Elemental Analysis of ZIF-9 MOF.

Element	Expected ZIF-9	Synthesised ZIF-9
Carbon	57.3	56.1
Hydrogen	3.4	3.7
Nitrogen	19.1	18.3

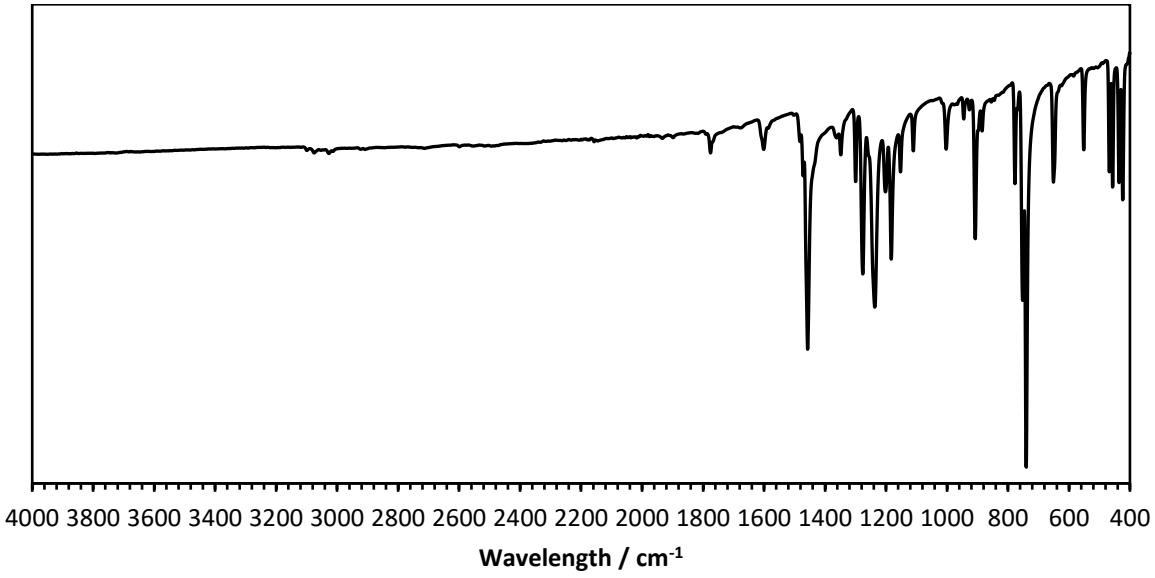

Figure 2.31: ATR-IR of ZIF-9 MOF.

2.4.6 Synthesis and Exfoliation of ZIF-9-NH_2

Cobalt nitrate hexahydrate (87 mg, 0.30 mmol), benzimidazole (53 mg, 0.45 mmol), 5-aminobenzimidzole (20 mg, 0.15) and sodium hydrocarbonate (47 mg, 0.56 mmol) was suspended in ethanol (2 ml, 72.7 mmol) and sonicated for 1 min. The solution was kept statistically at 50 °C for 72 h. The obtained ZIF-9-NH_2-III was washed three times with ethanol and three times with water then dried in at 80 °C for 48 h in a vacuum oven producing a dark purple powder (71.8 mg, 0.033 mmol, 44%). Elemental Analysis: Expected Mass %: C 57.3, H 3.4, N 19.1 Found Mass % C 54.0, H 3.5, N 19.0. (ESI-

NEG):$[M]^+$ 134.1 (Bim-NH_2), $[M]^+$ 119.1 (Bim). ^1H NMR (DCl/DMSO-d_6): 9.73 (s, 1H, **Bim-NH_2**), 9.66 (s, 1H, **Bim**), 8.03 (d, 1H, **Bim-NH_2**), 8.00 (s, 1H, **Bim-NH_2**), 7.92 – 7.83 (m, 2H, **Bim**), 7.64 (d, *J* = 2.0 Hz, 1H, **Bim-NH_2**), 7.63 – 7.55 (m, 2H, **Bim**). Phase purity confirmed by XRPD with a comparison to the CCDC (988184) powder pattern for ZIF-9-III.

8 mg ZIF-9-NH_2-III was ultrasonicated in 10 mL of ethanol at 80 KHz for 2 hr to access nanosheets (3.5 mg, 44 %). After being centrifuged at 500 rpm for 5 min, the collected supernatant containing the nanosheets was the centrifuged at 12,000 rpm for 1 hr.

Table 2.6: Elemental Analysis of ZIF-9-NH_2 MOF.

Element	Expected ZIF-9-NH_2	Synthesised ZIF-9
Carbon	57.3	54.0
Hydrogen	3.5	3.5
Nitrogen	19.9	19.0

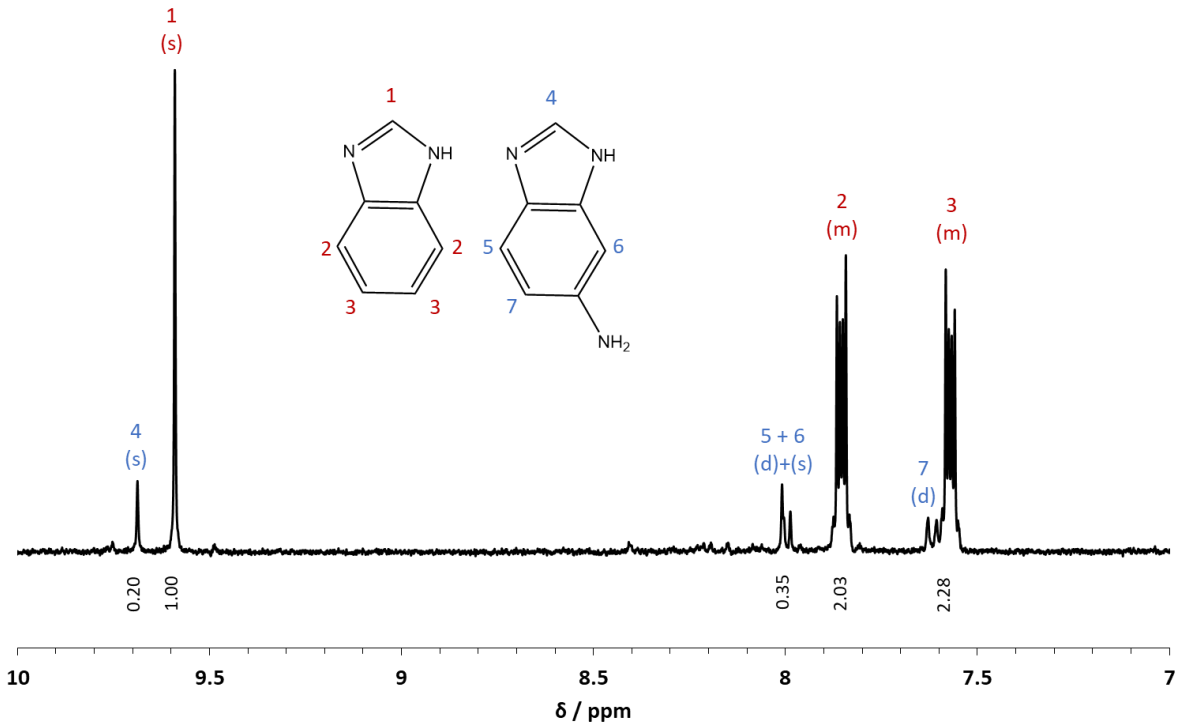

Figure 2.32: ^1H NMR of ZIF-9-NH_2 MOF in DMSO after digestion using DCl with peak assignments (red – benzimidazole, blue – 5-amino-benzimidazole).

2.5 References

1 K. S. Park, Z. Ni, A. P. Cô, J. Y. Choi, R. Huang, F. J. Uribe-Romo, H. K. Chae, M. O'keeffe and O. M. Yaghi, *Proc. Natl. Acad. Sci. U. S. A.*, 2006, **103**, 10186–10191.

2 Y. Sun, Y. Li and J. C. Tan, *ACS Appl. Mater. Interfaces*, 2018, **10**, 41831–41838.

3 T. Xiao and D. Liu, *Mater. Today Energy*, 2019, **14**, 100357.

4 W. Cai, T. Lee, M. Lee, W. Cho, D. Y. Han, N. Choi, A. C. K. Yip and J. Choi, *J. Am. Chem. Soc.*, 2014, **136**, 7961–7971.

5 P. Zhao, G. I. Lampronti, G. O. Lloyd, M. T. Wharmby, S. Facq, A. K. Cheetham and S. A. T. Redfern, *Chem. Mater.*, 2014, **26**, 1767–1769.

6 H.-L. Liu, Y.-J. Chang, T. Fan and Z.-Y. Gu, *12984 | Chem. Commun*, 2016, **52**, 12984.

7 K. Jayaramulu, J. Masa, D. M. Morales, O. Tomanec, V. Ranc, M. Petr, P. Wilde, Y.-T. Chen, R. Zboril, W. Schuhmann and R. A. Fischer, *Adv. Sci.*, 2018, **5**, 1801029.

8 H. Saini, P. Kallem, E. Otyepková, F. Geyer, A. Schneemann, V. Ranc, F. Banat, R. Zbořil, M. Otyepka, R. A. Fischer and K. Jayaramulu, *J. Mater. Chem. A*, 2021, **9**, 23651–23659.

9 Y. Wang, J. Zhang, X. Cheng, Y. Sha, M. Xu, Z. Su, J. Hu and L. Yao, *Nanoscale*, 2022, **14**, 11012–11017.

10 A. Ruyra, A. Yazdi, J. Espín, A. Carné-Sánchez, N. Roher, J. Lorenzo, I. Imaz and D. Maspoch, *Chem. - A Eur. J.*, 2015, **21**, 2508–2518.

11 N. Gu and S. Liu, *J. Mater. Chem. B*, 2020, 3168–3170.

12 J. López-Cabrelles, S. Mañas-Valero, I. J. Vitórica-Yrezábal, P. J. Bereciartua, J. A. Rodríguez-Velamazán, J. C. Waerenborgh, B. J. C. Vieira, D. Davidovikj, P. G. Steeneken, H. S. J. van der Zant, G. Mínguez Espallargas and E. Coronado, *Nat. Chem.*, 2018, **10**, 1001–1007.

13 L. Xiang, L. Sheng, C. Wang, L. Zhang, Y. Pan and Y. Li, *Adv. Mater.*, 2017, **29**, 1606999.

14 J. A. Thompson, C. R. Blad, N. A. Brunelli, M. E. Lydon, R. P. Lively, C. W. Jones and S. Nair, *Chem. Mater.*, 2012, **24**, 1930–1936.

15 Y. Peng, Y. Li, Y. Ban, H. Jin, W. Jiao, X. Liu and W. Yang, *Science (80-.).*, 2014, **346**, 1356–1359.

16 M. Tu, C. Wiktor, C. Rösler and R. A. Fischer, *Chem. Commun.*, 2014, **50**, 13258–13260.

17 R. Van Kerrebroeck, P. Naert, T. S. A. Heugebaert, M. D'hooghe and C. V Stevens, *Molecules*,

2019, **24**, 2116.

18 H. Chang, Y. Wang, L. Xiang, D. Liu, C. Wang and Y. Pan, *Chem. Eng. Sci.*, 2018, **192**, 85–93.

19 Y. Wang, J. Zhang, X. Cheng, Y. Sha, M. Xu, Z. Su, J. Hu and L. Yao, *Nanoscale*, 2022, **14**, 11012–11017.

20 M. D. J. Velásquez-Hernández, R. Ricco, F. Carraro, F. T. Limpoco, M. Linares-Moreau, E. Leitner, H. Wiltsche, J. Rattenberger, H. Schröttner, P. Frühwirt, E. M. Stadler, G. Gescheidt, H. Amenitsch, C. J. Doonan and P. Falcaro, *CrystEngComm*, 2019, **21**, 4538–4544.

Chapter 3:

Phage Display Against Two-Dimensional Metal-Organic Nanosheets as a Route-Towards Tunable Biosensors

---

Author contributions (Manuscript in Preparation)

Amelia C. Wood	Synthesised the ZIF-7 and ZIF-7-NH_2 MONs, characterised all MONs including surface property analysis, carried out biopanning against each MON system and peptide binding studies, prepared the MON-QCM sensor and carried out sensing experiments, analysed the experimental results and drafted the manuscript.
Edwin C. Johnson	Provided training on QCM preparation and analysis and aided with data discussion and editing of the manuscript
Ram R. R. Prasad	Synthesised the Hf-BTB-NH_2 MONs used for biopanning
Steven P. Armes	Provided the QCM equipment
Sarah S. Staniland	Co-supervised the project
Jonathan A. Foster	Supervised the project, aided with data discussion and drafting of the manuscript.

The aim for following chapter was to investigate how the periodic array of binding sites presented by MONs, particularly unsaturated metal clusters and functionalised organic linkers can be exploited for selectively binding biomolecules. Of the three MON systems to feature in this chapter details for the synthesis of ZIF-7 and ZIF-7-NH_2 MONs can be found in chapter 2 and the synthesis of Hf-BTB-NH_2 is in chapter 5. The affinity between peptide sequences and different physiologically stable MONs was interrogated via the high throughput screening technique phage display. The trends in peptide binding are discussed along with further binding studies including dissociation constant calculations. A quartz-crystal microbalance was coated with Hf-BTB-NH_2 MONs to produce a MON based biosensor for the detection of phage where there is a 5-fold increase in selectivity was demonstrated for phage displaying the consensus peptide compared to phage displaying generic peptides.

Phage display against two-dimensional metal-organic nanosheets as a route towards tunable biosensors

Amelia C. Wood, Edwin C. Johnson, Ram R. R. Prasad, Steven P. Armes, Sarah S. Staniland, Jonathan A. Foster

Dainton Building, Department of Chemistry, University of Sheffield, Brook Hill, Sheffield S3 7HF, UK

KEYWORDS. Phage Display, Metal-Organic Nanosheet, Biopanning, Quartz-crystal microbalance

ABSTRACT: We present the first example of phage display biopanning against metal−organic nanosheets and demonstrate their use for the design of a next-generation biosensor. Three MONs (ZIF-7, ZIF-7-NH_2 and Hf-BTB-NH_2) were chosen as initial targets to demonstrate how simple synthetic modifications can enhance selectivity towards sequences of amino acids. Each MON system was added to a solution containing every possible combination of 7-residue peptides attached to bacteriophage hosts and, through a succession of panning rounds, the highest affinity binding peptides for each system was identified. In each case only a single peptide sequence was isolated (YNYRNLL – ZIF-7, NNWWAPA - ZIF-7-NH_2 and FTVRDLS – Hf-BTB-NH_2). This indicates that the MONs are highly selective, which is attributed to the 2D structure of the nanosheets. Zeta potential and contact angle measurements of the MONs were used in conjunction with calculated properties for the peptide sequences and binding studies to provide insights into the relative importance of electrostatic, hydrophobic and co-ordination bonding interactions. Further studies focusing on Hf-BTB-NH_2 confirmed that the sequence VRDL was highly conserved, and the on-target binding sequence exhibited up to a 19-fold lower dissociation constant than for off-target sequences. The Hf-BTB-NH_2 MONs were coated onto a quartz crystal microbalance and produced a 5-fold higher signal for FTVRDLS compared to phage with generic peptide sequences. We anticipate that the highly tunable nature of MONs will enhance our understanding of binding interactions and enable targeting of biomedically important peptides.

INTRODUCTION

Complex surface structures are responsible for the remarkable degree of biomolecular selectivity found in nature. Macromolecules bind to these bio-interfaces through multiple weak interactions, with electrostatic and hydrophobic interactions critical in determining selectivity.[1] Two-dimensional materials represent promising artificial mimics due to their high specific surface areas and accessible functional groups.[2,3] A wide range of nanomaterials including transition metal dichalcogenides, MXenes and graphene have displayed an ability to bind biological macromolecules such as proteins and DNA.[4–6] However, the simple inorganic structure of these surfaces leads to stochastic functionalization with different binding groups, therefore limiting their selectivity.

Metal-organic framework nanosheets (MONs) are a class of two-dimensional materials that combine organic ligands with metal nodes.[7,8] The modular structure of MONs enables systematic tuning of surface chemistry without changing the overall topology, while their crystalline nature affords a periodic array of recognition sites that promotes multidentate binding.[9] Presentation of these functional groups on the surface of the nanosheets, rather than within the pores of a three-dimensional metal-organic framework (MOF), removes any size limitations.[10] Early generations of MON-based biosensors have typically involved fluorescence quenching of dye-labeled single-stranded DNA, functionalization with bioreceptors and nanozyme behavior.[3,11–16] In these examples, much of the sensitivity and selectivity is conferred by other components, such as aptamers and antibodies, enzymes, nanoparticles or other 2D-materials.[9]

To the best of our knowledge, there are currently no studies investigating the interaction of specific sequences of amino acids with MONs, although several studies have investigated their interactions with their three dimensional analogs, MOFs. Indeed, several MOFs are promising catalysts for the formation and cleavage of peptides, as well as the selective hydrolysis of proteins.[17–20] Parac-Vogt and co-workers investigating the adsorption of a diverse range of dipeptides onto various Zr-based metal-organic frameworks. Extensive screening revealed that affinity depended on hydrophobic, aromatic and cation–π interactions arising from the hydrophobic/aromatic nature of the linkers and cluster connectivity.[21] However, the diversity of both MOFs and peptide sequences and the complexity of their interactions means that identifying strong-binding combinations for use as highly selective sensors remains a formidable challenge.

Phage display biopanning provides an alternative approach to exploring peptide-substrate interactions.[22,23] A

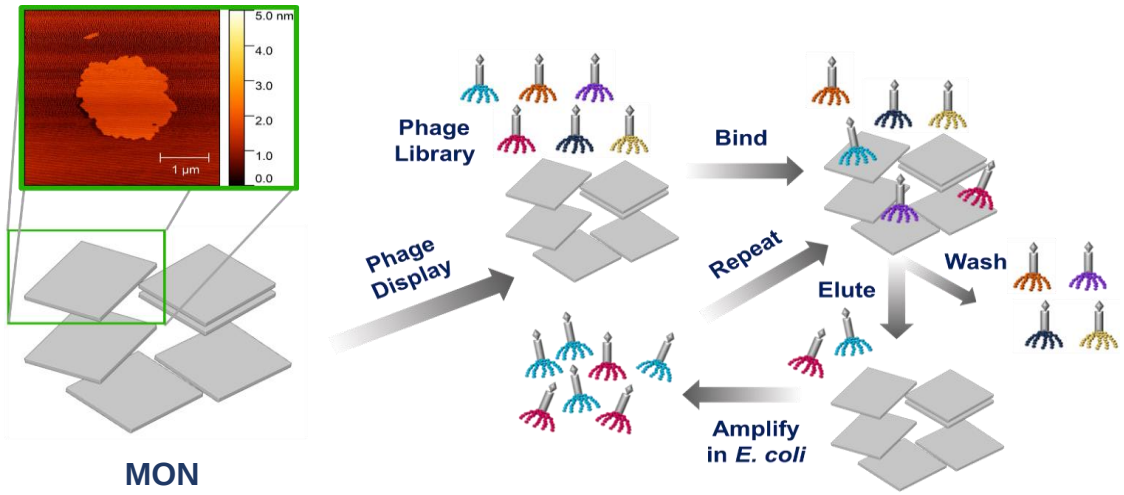

Figure 1. Schematic illustration of phage display against MONs (inset AFM image shows ZIF-7-NH_2), which includes phage incubation with MON to encourage binding, washing and elution steps, and phage amplification using *E. coli.*

library of bacteriophages presenting various combinations of peptides are incubated with a given target under competitive binding conditions to identify the most strongly binding sequences (Figure 1). This approach has been used to interrogate antigen-antibody interactions through epitope mapping as well as to identify suitable peptides for bioinspired mineralization.[24–26] In particular, Fan and co-workers used phage display to identify strongly binding peptides to a series of water-stable MOFs, which they used to control nucleation, modify their surface properties and tune the release of cargo.[27]

We hypothesized that biopanning could be used to identify strongly binding peptide sequences and hence design highly selective MON based sensors for biomedical applications. Three different 2D MON systems (ZIF-7, ZIF-7-NH_2 and Hf-BTB-NH_2) were selected to explore the effect of subtly different components on biosensor performance. Phage display was utilized to determine which peptides would exhibit strong binding to the surface of each MON out of a library of 1×10^{13} possible combinations of 7 amino acids. In each case, a consensus binding peptide sequence with strong affinity to its nanosheet system was identified, highlighting the intrinsic bio-selectivity of these ultrathin MONs. Finally, we demonstrate a MON-based quartz-crystal microbalance (QCM) biosensor which exhibits a 5-fold increase in signal for the selective peptide functionalized phage compared to generic peptide sequences. Overall, our results demonstrate that specific peptide sequences can exhibit strong selective binding to metal−organic nanosheets which enables the design of next-generation biosensors.

RESULTS AND DISCUSSION

Synthesis and characterization of layered MOFs and their exfoliation to form MONs. Three layered MOFs, chosen for their aqueous stability and subtle differences in their chemical structure, were synthesized and exfoliated to form nanosheets.

The first system, ZIF-7 (Figure 2d), has previously been reported by a number of groups and used for gas separation, solid-phase extraction, and membrane filtration.[28–30] Here we adapted a method developed by Liu *et al.* and Peng *et al.* for its synthesis.[31,32] Benzimidazole and zinc nitrate hexahydrate were reacted under ambient conditions in DMF to produce a 3D ZIF-7-I phase material prior to refluxing in water to induce a hydrothermal phase transition that produced the bulk layered phase, ZIF-7-III (ESI – Figure S1). X-ray powder diffraction pattern (XRPD) of the resulting white microcrystalline powder matched that of the predicted ZIF-7-III pattern (Figure 2i) while scanning electron microscopy (SEM) studies also confirmed the formation of a layered material (Figure 2a).

Liquid exfoliation was achieved through ultrasonication of layered ZIF-7-III for 2 h in a 1:1 methanol/*n*-propanol mixture. Ultrathin nanosheets of 0.6 nm mean height and approximately 630 nm length were obtained, as indicated by atomic force microscopy images (Figure 2e and Figure S18). Dynamic light scattering reported a spherical equivalent diameter of 1063 nm (Figure S21).

The second MON system, ZIF-7-NH_2 was inspired by the work of Lopez-Cabrelles *et al.*, who produced an isoreticular series of iron-based ZIFs incorporating a range of functional groups.[33] However, initial attempts to prepare 100% ZIF-7-NH_2 via the route reported for ZIF-7 resulted in only partial conversion to ZIF-7-NH_2-III during reflux of ZIF-7-NH_2-I in water, resulting in mixed phase material (Figure S7). A mixed ligand system was therefore produced by adding 50 mol% of 5-amino-benzimidazole alongside benzimidazole in the initial step (see section 3.3 in the Supporting Information). The XRD powder pattern for the final material matched that reported for ZIF-7-III, confirming successful formation of this novel layered material (Figure 2i). Introducing the amine group produced a small shift in the [002] peak, which is attributed to an increase in the inter-layer distance owing to incorporation of this bulky group (Figure S8). The presence of both ligands within the MOF was confirmed by IR spectroscopy as well as mass spectrometry analysis of the MOF after acid digestion. ^{1}H NMR spectroscopy of the digested material indicated the presence of 20% bim-NH_2: this is consistent with a $Zn_2(bim)_{3.2}(bim\text{-}NH_2)_{0.8}$ composition, as calculated from elemental microanalysis (Figure S5).

ZIF-7-NH_2 nanosheets were accessed in the same way as for ZIF-7 and AFM studies indicated mean heights and lengths of 1.6 nm and 400 nm respectively for ZIF-7-NH_2 (Figure 2f and Figure S19). ZIF-7-NH_2 nanosheets had a relatively broad lateral size distribution reaching lengths of 2 µm but the mean height only ranged from 1 to 5 nm. Dynamic light scattering studies indicated a slight increase in the apparent z-average

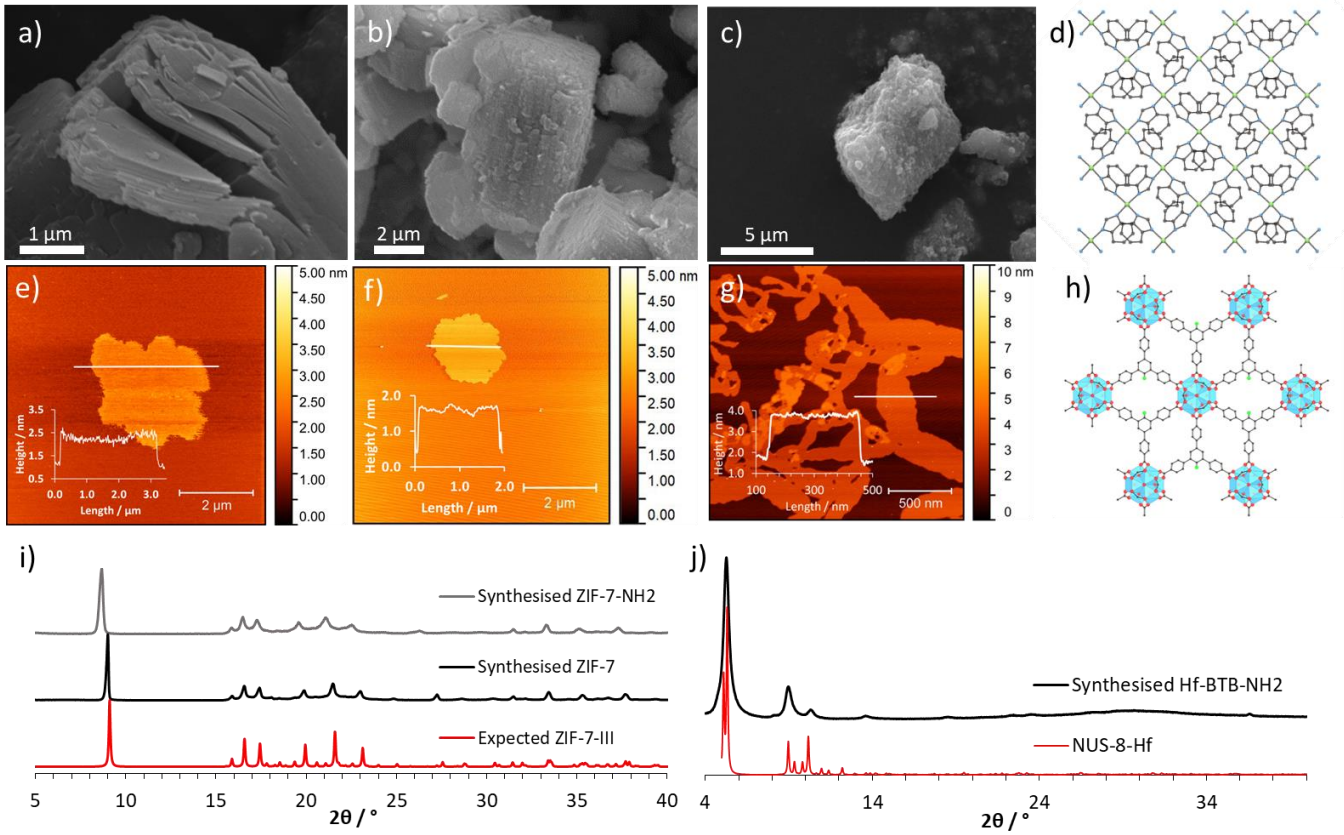

Figure 2: a) Scanning electron microscopy (SEM) image of as-synthesized ZIF-7 layered MOF, b) SEM image of ZIF-7-NH_2 layered MOF, c) SEM image of Hf-BTB-NH_2, d) Schematic of ZIF-7, e) Atomic force microscopy (AFM) image of ZIF-7 nanosheets, f) AFM image of ZIF-7-NH_2 nanosheets, g) AFM image of Hf-BTB-NH_2 nanosheets h) Schematic of Hf-BTB-NH_2, i) expected X-ray powder diffraction (XRPD) pattern of ZIF-7-III (CCDC - 675375) compared to synthesized ZIF-7-III and synthesized ZIF-7-NH_2, j) XRPD pattern of synthesized Hf-BTB-NH_2 compared to NUS-8-Hf.

diameter for ZIF-7-NH_2 with a narrower particle size distribution compared to ZIF-7 (Figure S20).

A third MON system was also evaluated. A wide range of nanosheets formed from tricarboxylate linkers connected to Zr_6 or Hf_6 clusters have been reported for use in catalytic,[34–36] and photo- or radio-dynamic therapy applications.[37–40] Here Hf-BTB-NH_2, was prepared by modifying the synthetic protocol reported by Ling *et al.* to introduce hafnium metal clusters.[41] Accordingly, hafnium chloride and BTB-NH_2 linker were dissolved in DMF then water and formic acid were added as modulating agents. This mixture was heated for 48 h at 120 °C and the resulting pale viscous colloidal suspension became a homogeneous suspension after washing. Figure 2j shows the XRPD pattern obtained for the Hf-BTB-NH_2 system compared to BTB-Hf (NUS-8) which contains the same key features. The only difference is the introduction of the amine group on the central benzene ring of the BTB linker, see Figure 2h. Further comparison to studies by Ling et al. can be found in Figure S13, which shows a good match to a simulated pattern for Hf_6-BTB MOL.[41] The bulk material was then ultrasonicated in water (37 KHz, 12 h) to access nanosheets. The AFM image in Figure 2g shows an example of Hf-BTB-NH_2 nanosheets (average height = 2.7 nm, mean length = 504 nm) with dynamic light scattering reporting an apparent z-average diameter of 493 nm (Figure S20-S21).

Before phage display was attempted, stability tests were conducted to confirm structural integrity of the MONs under incubation conditions. Each system was exposed to phosphate buffer saline (PBS) for 1 h and 24 h and any change in structure was determined via XRPD. After incubation for 1 h, the XRPD pattern remained unchanged for each system. After 24 h, only small changes were observed for the ZIFs and no change for Hf-BTB-NH_2 (Figure S23-S25). Moreover, AFM studies revealed no significant change in particle size after incubation (Figure S26).

Selection of Peptide-Functionalized Bacteriophage with High-Affinity MON Binding. Biopanning studies against the three different MON systems were undertaken using genetically modified M13 bacteriophage hosts with a mean length of 880 nm and a mean height of 6.6 nm incorporating a pentavalent display of identical peptides (Figure 1).[42,43] The library of phage- displaying peptides was added to the MONs and incubated for 1 h. Subsequently, a washing step removed any unbound phage, leaving only phage bound to the MONs. The pH of the system was adjusted to enable bound phage elution, which were then amplified through the infection of *E. coli*. This protocol constituted one panning round.

This process was repeated twice by adding the amplified phage from the previous panning round to create increasingly competitive binding conditions and hence identify peptides with the highest affinities. After the third panning round, twelve phage clones were isolated in each case and their DNA was sequenced to determine those peptide sequences that bound with the highest affinity to each MON system.

Table 1. Summary of the dominant binding peptides identified by phage display for each MON system.

MON System	MON Zeta Potential / mV	MON Contact Angle / °	Peptide Binding Sequence (N'-C'amidated)	Peptide Binding Sequence (N'-C'amidated)	Peptide Isoelectric Point / pH	Predicted overall charge in PD
ZIF-7	-30.1	149	YNYRNLL	Tyr, Asn, Tyr, Arg, Asn, Leu, Leu	10.15	+2
ZIF-7-NH_2	2.3	141	NNWWAPA	Asn, Asn, Trp, Trp, Ala, Pro, Ala	14.00	+1
Hf-BTB-NH_2	-36.9	25	FTVRDLS	Phe, Thr, Val, Arg, Asp, Leu, Ser	10.59	+1

The identified peptide sequences are shown in Table 1. Only one dominant peptide sequence was isolated for each MON system after three panning rounds, suggesting high selectivity towards that specific peptide. In contrast, Fan et. al. reported 2-3 high affinity binding peptides after the final panning round when using phage display against MOFs.[27] One possible explanation for this difference is that the ultrathin nature of the 2D-MONs means there is essentially just one type of surface available for binding, whereas 3D-MOFs offer multiple faceted surfaces.

Discussion of peptide binding trends. To gain further insight regarding the selection of each preferred peptide sequence, the surface properties of the MONs were compared with those of the consensus peptide. Based on related studies,[21] we hypothesized that three different factors could be important for binding: 1) electrostatic interactions, 2) hydrophobic interactions, 3) specific R-group interactions. Experimental and calculated data to test the relative importance of each type of interaction are presented in Table 1.

To investigate the importance of electrostatic interactions, aqueous electrophoresis studies of the nanosheets were undertaken in the presence and absence of each peptide. Zeta potentials of the three nanosheet systems were determined in dilute PBS (1.37 mmol with respect to NaCl) at 20℃ to replicate phage display conditions as closely as possible while meeting instrumental requirements. ZIF-7 and Hf-BTB-NH_2 nanosheets exhibited moderately negative zeta potentials of –30.1 mV and –36.9 mV, respectively. Thus the surface chemistry of the ZIF systems is dominated by the anionic imidazole ligands, rather than the zinc cations. The negative zeta potential for Hf-BTB-NH_2 most likely indicates the presence of surface hydroxyl and phosphate groups, which would confer overall anionic charge. The weakly positive zeta potential observed for ZIF-7-NH_2 is attributed to the presence of surface amine groups. Such a low zeta potential is often associated with an unstable colloidal suspension. However, no sedimentation was observed over the timescale of the experiment and the zeta potential data proved to be reproducible.

Amino acid side-chain and *N*-terminus pK_a values were used to calculate the isoelectric point of the binding peptide and to predict the overall charge under phage display (PD) conditions (see section 5.3 in the Supporting Information). All three peptides contain a free terminal amine, which should be protonated under PD conditions and hence contribute a +1 charge. The ZIF-7-NH_2 sequence contained no ionizable R-groups; both ZIF-7 and Hf-BTB-NH_2 contained arginine, which confers an additional +1 charge. However, this results in charge balance in the case of Hf-BTB-NH_2 owing to its ionizable aspartic acid residue. The change in zeta potential (ΔZP) was determined upon MON incubation with excess binding peptide (Figure S30). A large ΔZP is observed for ZIF-7 (+56.2 mV) and Hf-BTB-NH_2 (+40.0 mV) but a rather smaller difference is observed for ZIF-7-NH_2 (+20.9 mV). Thus, electrostatic interactions seem to be important for the binding of cationic peptides to the anionic surfaces of ZIF-7 and Hf-BTB-NH_2, but this effect is less significant for peptide binding to ZIF-7-NH_2. As the guanidinium moiety within arginine is most likely charged under the experimental conditions, we infer that it contributes to the overall electrostatic interactions. The importance of arginine interactions with aromatic residues is well-documented in the biomolecular recognition literature.[44,45]

The hydrophobicity of the MON surfaces was investigated using contact angle measurements using DSA100 and compared to the proportion of hydrophobic/hydrophilic residues within the peptide sequences. Nanosheets were packed onto a glass slide, water drops were added using a micro-syringe and the contact angle was measured using a drop shape analyser image system (Figure S22). Although there are some limitations to this approach owing to surface roughness effects, clear differences were observed between the two types of nanosheets.[46] Hf-BTB-NH_2 nanosheets were considerably more hydrophilic (contact angle = 25 °) compared to the ZIF-7 and ZIF-7-NH_2 nanosheets (contact angles of 149 ° and 141 °, respectively). This correlates with the known properties of these MOF classes: the surface chemistry of Hf-BTB-NH_2 systems is dominated by their $Hf_6(\mu_3\text{-}O)_4(\mu_3\text{-}OH)_4(HCO_2)_6$ clusters,[47] while the Zn^{2+} ions of the ZIF systems are largely shielded by the relatively hydrophobic imidazole rings.[48]

This trend in hydrophobicity is mirrored by the consensus binding peptides. The ZIF-7 binding sequence, YNYRNLL, contains several hydrophobic tyrosine and leucine residues, while the ZIF-7-NH_2 peptide sequence, NNWWAPA, contains multiple hydrophobic tryptophan and alanine residues. Benzimidazole derivatives are known enzyme inhibitors owing to π- π interactions between aromatic residues.[49,50] The presence of aromatic Tyr and Trp residues suggest probable π-π interactions with the electron-rich aromatic benzimidazole ligands of ZIF-7. The two peptides for the ZIF MONs both contain two polar asparagine residues, which may confer stability in aqueous solution. In contrast, the Hf-BTB-NH_2 sequence, FTVRDLS, contains a broader range of amino acids, with only three hydrophobic residues (phenylalanine, valine and leucine) alongside hydrophilic residues such as threonine and serine, as well as anionic aspartic acid and cationic arginine residues. This suggests that hydrophobic binding effects are most likely dominant for the ZIF-7-NH_2 but are much less important for the more polar Hf-BTB-NH_2 nanosheets.

Table 2. Summary of the binding peptides identified by phage display in panning round 1 and 3 against Hf-BTB-NH_2 with similarities highlighted in yellow.

MON System	Panning round	Peptide Binding Sequence (N'-C'amidated)	Peptide Isoelectric Point / pH	Predicted overall charge in PD
Hf-BTB-NH_2	3	FTVRDLS	10.59	+1
	1	FTVRDLS	10.59	+1
	1	FPVRDLS	10.59	+1
	1	STVRDFS	10.57	+1
	1	SPVRDNW	10.57	+1
	1	YPERDLC	6.19	-0.1
	1	ISPHPGS	14	+1.1

At first sight, the presence of the aspartic acid residue in the consensus peptides for the Hf-BTB-NH_2 nanosheets appears to be counter-intuitive given the overall anionic surface character of this MON. However, Lan *et al.* demonstrated that various amino acids can bind to the surface of closely-related Hf_{12}-cluster nanosheets via ligand exchange.[51] In principle, the anionic carboxylate form of aspartic acid (which has a side-chain pK_a of 3.90) may similarly displace the capping formate ligand (pK_a 3.75) to bind to the Hf clusters.

To further explore these trends, strongly binding peptides from the first panning round of Hf-BTB-NH_2 were sequenced (see Table 2). Interestingly, the sequence VRD was conserved in four of the six most strongly binding cases, with RDL conserved in three out of six cases. The conserved nature of this sequence indicates that multiple amino acids are involved in cooperative binding interactions, rather than individual amino acids acting in isolation. Furthermore, the combination of an anionic carboxylate group adjacent to a cationic arginine group and a hydrophobic valine/leucine group appears to be important for effective binding of the consensus peptide sequence.

For the sixth sequence, ISPHPGS, only the final serine is conserved compared to the consensus peptide. In this case, arginine is replaced by a cationic histidine residue in the central fourth position, with the latter flanked by hydrophobic proline residues but no residues with co-ordinating carboxylate R-groups. The constrained proline rings means that this peptide is likely to have a significantly different set of interactions with the MON surface. Presumably, this produces a local minimum on the energy binding landscape.

The dissociation constant (K_d) for the consensus peptide for each MON binding to Hf-BTB-NH_2 was calculated. A saturation binding experiment was conducted in which zeta potential measurements were recorded for a stock MON solution (1 mg/ml in 1.37 mmol PBS w.r.t. NaCl) incubated with various peptide concentrations (Figure S31). The dissociation constant for FTVRDLS binding to Hf-BTB-NH_2 was calculated to be 74 ± 22 μM. Off-target binding studies of YNYRNLL and NNWWAPA against Hf-BTB-NH_2 were also conducted, with the K_d determined to be 285 ± 23 μM and 1393 ± 200 μM respectively. This corresponds to an approximate 4-fold and 19-fold increase in the dissociation constant relative to the on-target binding of FTVRDLS. This is consistent with the phage display identified 12-mer peptide binding studies against MOFs reported by Fan et. al., with all values lying within the micromolar range.[27] The smaller difference in K_d for YNYRNLL most likely reflects similarities between these arginine-bearing peptides, which leads to strong binding to the anionic MON surfaces. Thus, Hf-BTB-NH_2 shows a high degree of selectivity for the consensus peptide identified through the biopanning studies, which makes it a promising candidate for the design of a biosensor.

MON-coated QCM sensing of bacteriophage-displaying peptides. Over the past decade, various quartz crystal microbalance (QCM) based biosensors have been developed that offer high sensitivity and rapid detection times.[52–56] A typical QCM biosensor contains either a natural or synthetic recognition element such as antibodies or molecularly-imprinted polymers (MIPs) coated on a QCM surface. Natural receptors suffer from instability problems while technical issues associated with MIPs lead to sub-optimal detection limits.[54] We hypothesized that 2D-MONs might offer an alternative biomolecular recognition platform because they constitute a highly stable periodic array of active sites and can be easily processed to form thin films. Examples of 3D-MOF based QCM sensors for vapor/gas detection have been reported but such coatings are relatively thick (~ 1 μm).[57,58] A 2D-MON based QCM sensor has been produced for ammonia detection but as far as we are aware there have been no other studies involving MON-based QCM sensors.[59] QCM was used to assess intrinsic structural changes within MON-based water filtration membranes but not used as a sensor.[60] Xie *et al.* designed a covalent-organic framework nanosheet QCM sensor to detect miRNA but in this case the nanosheet was simply used to enhance signal generation in a complex probe DNA system.[61]

One major advantage of a QCM sensor is its sensitivity: detectable changes in adsorbed mass are of the order of one nanogram per cm^2. The simplest model relating Δf to m is the Sauerbrey equation,[62] which is used to calculate the mass of the adsorbate.

Silica-based QCM substrates were coated with MONs to investigate their performance in sensing various viruses at a constant flow rate of 0.018 ml min^{-1}. The Hf-BTB-NH_2 system was selected as it was the most stable in PBS (Figure S25) and minimal signal drift was observed. This QCM sensor had a Hf-BTB-NH_2 coating of mean thickness of approximately 100 nm, see Figure 3c. Phage-displaying FTVRDLS, the consensus peptide for Hf-BTB-NH_2, was compared with generic 7-mer peptides as a control to assess the extent of non-specific binding.

QCM data obtained using a sensor with no MON coating (grey) and two sensors coated with Hf-BTB-NH_2 MON (black and blue) are shown in Figure 3. Uncoated and MON-coated

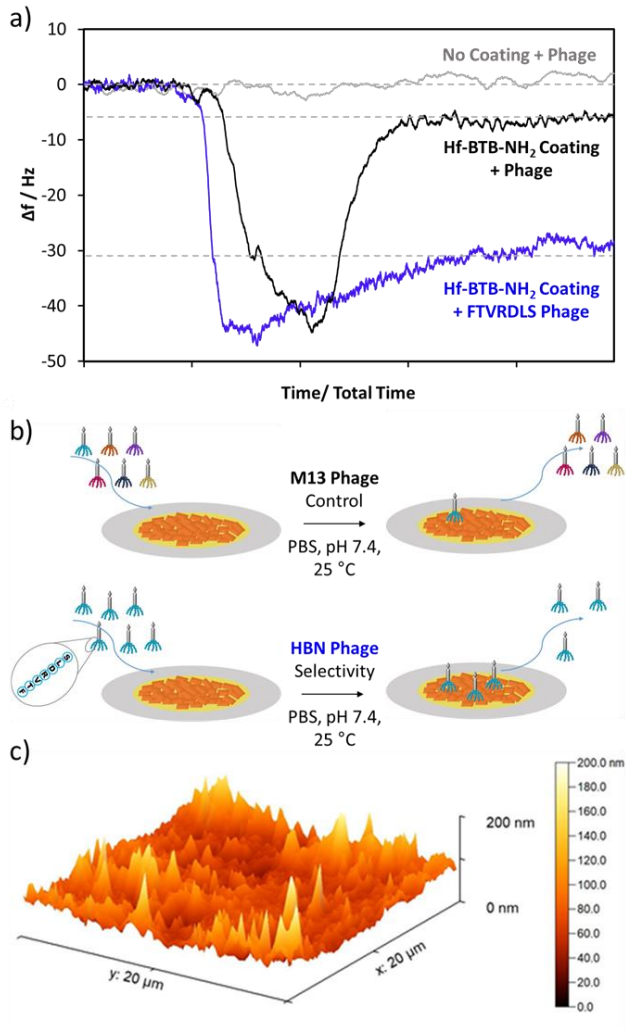

Figure 3: a) Change in frequency, Δ*f*, observed for a silica QCM sensor with no coating (grey) and a ~100 nm Hf-BTB-NH_2 coating after exposure to an aqueous solution of M13 phage in PBS at pH 7.4. Δ*f* was also determined for a ~100 nm Hf-BTB-NH_2-coated silica QCM sensor after exposure to a FTVRDLS-functionalized phage in PBS at pH 7.4, b) Schematic illustration of the difference between exposing this Hf-BTB-NH_2-coated QCM sensor to phage and FTVRDLS phage, c) AFM image of the Hf-BTB-NH_2 coated silica QCM used to determine the mean coating thickness of ~100 nm.

QCM sensors were exposed to control phage (grey and black). The uncoated QCM sensor showed no Δ*f* and the MON-coated sensor with generic phage exhibited only a small Δ*f*, which corresponds to an adsorbed amount of just 0.38 mg·m^{-2}. These observations indicate a weak interaction between the MON surface and the generic phage but no detectable interaction with the uncoated silica sensor control. In contrast, the selective phage (displaying FTVRDLS) exhibited a much greater Δ*f* corresponding to an adsorbed amount of 1.87 mg·m^{-2}, which is a 5-fold increase compared to the control phage. This confirms that phage display identified a selective peptide and that MON-based QCM sensors can be readily constructed.

CONCLUSION

Achieving high selectivity for a specific peptide sequence amongst the myriad of possibilities is a formidable challenge with enormous potential for the development of next-generation biosensors. Here we demonstrate that MONs confer selectivity through multiple weak interactions with peptides. Three ultrathin MON systems were prepared: ZIF-7 and ZIF-7-NH_2 possess similar chemical structures while Hf-BTB-NH_2 differs significantly. PD biopanning was exploited to screen a library of 1×10^{13} possible combinations of 7 amino acids and hence identify the strongest binding peptide sequence for each of the three different MONs. In contrast to previous biopanning studies on MOFs, only a single consensus peptide sequence was identified in each case; this is attributed to the MONs surface comprising only a single facet.

Comparing zeta potential data and contact angle measurements obtained for these MONs with calculated properties for the peptide sequences indicates that a combination of electrostatic, hydrophobic and coordination bonding interactions are important for strong peptide-MON binding. In particular, the VRDL sequence is highly conserved for peptides that bind strongly to Hf-BTB-NH_2. The consensus sequence for Hf-BTB-NH_2 binds up to 19 times more strongly to Hf-BTB-NH_2 than the preferred peptide sequences identified for the other two MONs. A proof-of-concept QCM-MON biosensor was constructed and a 5-fold increase in selectivity was demonstrated for phage displaying the consensus peptide compared to phage displaying generic peptides. Thus we anticipate that the diverse and highly tunable surface chemistry of MONs, in conjunction with the rapid sampling of binding peptides provided by phage display and the high sensitivity of QCM sensors will inform the design of a new generation of exquisitely selective sensors for biomedically important peptides.

MATERIALS AND METHODS

Materials

Synthesis of ZIF-7 nanosheets. First, ZIF-7-I nanoparticles were prepared by adding DMF (250 mL, 3.25 mol) to $Zn(NO_3)\cdot 6H_2O$ (755 mg, 2.54 mmol) and benzimidazole (1.92 g, 16.28 mmol). This mixture was left at room temperature for 72 h, stirring for the first hour only. The precipitate was then collected by centrifugation (12,000 rpm for 1 h). Particles were purified by thoroughly washing via redispersion in methanol then centrifugation (12,000 rpm for 1 h). This wash-centrifugation cycle was repeated three times before drying at 50 °C for 18 h in a vacuum oven. The particles were further dried at 120 °C for 48 h in a vacuum oven.

ZIF-7-I was redispersed in distilled water (0.5 wt%) and refluxed at 100 °C for 24 h. The turbid mixture was washed with distilled water once and methanol three times by redispersion and centrifuging (12,000 rpm for 1 h). The white solid was then dried at 50 °C overnight to obtain ZIF-7-III. Finally, ZIF-7-III (80 mg) was ultrasonicated in a 1:1 v/v methanol/*n*-propanol mixture (120 mL) at 80 KHz for 2 h to access nanosheets. After centrifugation at 500 rpm for 5 min, the resulting supernatant containing the nanosheets was then centrifuged at 12,000 rpm for 1 h.

Synthesis of ZIF-7-NH_2 nanosheets. First, ZIF-7-NH_2-I nanoparticles were prepared by adding DMF (125 mL, 1.63 mol) to $Zn(NO_3)\cdot 6H_2O$ (755 mg, 2.54 mmol) and benzimidazole (962 mg, 8.14 mmol) and 5-aminobenzimidazole (1.08 g, 8.11 mmol). This mixture was left at 30 °C for 2 weeks, stirring for the first hour only. ZIF-7-NH_2 nanoparticles were then collected by centrifugation

(12,000 rpm for 1 h). Particles were purified by thoroughly washing via redispersion in methanol followed by centrifugation (12,000 rpm for 1 h). This wash-centrifugation cycle was repeated three times before drying at 50 °C for 18 h in a vacuum oven. The particles were further dried at 120 °C for 48 h in a vacuum oven.

ZIF-7-NH_2-I was redispersed in distilled water at a concentration of 0.5 wt % and refluxed at 100 °C for 1 week. The turbid mixture was washed with distilled water once and methanol three times, and then dried at 50 °C overnight to obtain ZIF-7-NH_2-III. 80 mg ZIF-7-NH_2-III was ultrasonicated in 1:1 v/v methanol/*n*-propanol (120 mL) at 80 KHz for 2 h to access nanosheets. After centrifugation at 500 rpm for 5 min, the resulting supernatant containing the nanosheets was then centrifuged at 12,000 rpm for 1 h.

Synthesis of Hf-BTB-NH_2 nanosheets. To prepare Hf-BTB-NH_2 MONs, $HfCl_4$ (34.59 mg, 0.108 mmol) and 2,4,6-tris(4-carboxyphenyl)aniline (32.87 mg, 0.072 mmol) were added to a 20 mL screw-cap glass vial. DMF (12.5 mL) was added and the mixture was dissolved with the aid of ultrasonics to obtain a clear solution. Formic acid (2.5 mL) and H_2O (0.7 mL) were added, then the vial was sealed and placed in a 120 °C oven for 48 h. The vial was taken out of the oven and cooled to room temperature. The turbid solution was centrifuged to collect Hf-BTB-NH_2 as a pale-yellow precipitate. The precipitate was washed multiple times with DMF, followed by ethanol. To prevent stacking of the MON layers, Hf-BTB-NH_2 was stored in ethanol until needed for further studies.

Phage Display. MON binding peptides were isolated from a random 7-mer peptide library (New England Biolabs, Inc.) using the phage display protocol. The DNA sequences of the 7-mer peptides from the combinatorial peptide library are fused to the gIII of the bacteriophage M13. The peptides are separated from the pIII major coat protein by a short spacer sequence (GGGS). The peptide library has complexities on the order of 10^{13} independent clones, which is sufficient to encode the 1.28 x 10^9 possible 7-mer peptide sequences. General phage methods were conducted according to the manufacturer's recommendations.

MONs were incubated with the phage library in 2x blocking buffer (BB) phosphate buffered saline for 1 h on a rotating blood wheel. The particles were washed three times with PBS to remove unbound phage. After each wash, the frameworks were isolated by centrifugation (relative centrifugal force (RCF) 10 000 × g) for 10 min, and the supernatant was discarded. Bound phage were eluted with 0.2 M glycine pH 2.2, followed by trimethylamine. This resulted in MON digestion for ZIF-7 and ZIF-7-NH_2 so it is assumed that all bound phage were eluted. The eluted phage were amplified in E. coli (ER2738) and purified by poly(ethylene glycol)-8000/sodium chloride (PEG/NaCl) precipitation with subsequent centrifugation steps. In subsequent biopanning rounds, at least 5×10^{10} phage were applied. A total of three panning rounds were conducted to enrich the peptide pool with the highest affinity binders. For each MON system, 12 phage clones were analyzed by DNA sequencing.

Peptide binding study. Hf-BTB-NH_2 solution (1 mg/ml) in diluted PBS (1.37 mmol wrt. NaCl) was incubated for 1 h with various concentrations of the three identified binding peptides. Zeta potentials were determined after 1 h of incubation to examine any change in this parameter for the various peptides. The equation for K_d is provided in section 4.1 of the Supporting Information.

Preparation of MON-based QCM sensors. Quartz crystal microbalance (QCM) sensors coated with a 50 nm silica overlayer (QSX 303, ~5 MHz fundamental frequency) were purchased from Q-Sense (Sweden). Each sensor was cleaned according to the manufacturer's instructions. This protocol involved (i) UV/O_3 treatment for 15 min (Bioforce UV/O_3 cleaner, ~9 mW cm^{-2}, λ = 254 nm), (ii) exposure to 2% w/w sodium dodecylsulfate solution for 30 min, (iii) copious rinsing with deionized water and drying under N_2, (iv) a final UV/O_3 treatment for 15 min.

The sensor was prepared by adding 10 x 10 µL of MON solution (1 mg/ml, ethanol) dropwise to the clean QCM substrate while spin coating at 3,000 rpm for 10 min. The thickness of the resulting MON coating was measured using AFM to be approximately 100 nm.

QCM measurements were performed using an openQCM NEXT instrument (Novatech Srl., Italy) equipped with a temperature-controlled cell connected to a Masterflex Digital Miniflex peristaltic pump (Cole-Parmer Instrument Company, UK). All experiments were conducted in PBS buffer (pH 7.4) and no measurements were undertaken until the sensor frequency exhibited a drift of less than 0.1 Hz·min^{-1}; this typically occurred within 1 h of filling the cell. Once a stable signal was obtained, the phage solutions (1 x 10^{12} PFU / mL) in PBS were passed through the cell at a constant flow rate of 0.018 mL·min^{-1} (minimum flow volume = 0.20 mL).

The adsorbed amount can be calculated using various models.[63–65] The simplest and most widely applied of these is based on the Sauerbrey equation, which relates the change in frequency, Δf, directly to the change in adsorbed mass per unit area, m,

$$m = C \times \frac{\Delta f}{n}$$

where C is a sensitivity constant (-0.177 (mg·m^{-2}) × Hz^{-1}), Δf is the change in the resonant frequency (Hz), and n is the overtone number. The third harmonic (n = 3) was used to calculate the adsorbed amount to avoid experimental artifacts associated with the fundamental harmonic that may occur if the sample is imperfectly mounted on the sensor.[65–67]

ASSOCIATED CONTENT

Supporting Information. Materials synthesis and characterization, XRPD, ATR-IR, SEM, TGA, Tyndall scattering images, AFM, DLS, zeta potential data, contact angle images, binding study data and calculations.

AUTHOR INFORMATION

Corresponding Author

* E-mail: jona.foster@sheffield.ac.uk

Funding Sources

EPSRC

ACKNOWLEDGMENTS

The authors acknowledge the EPSRC for funding (EP/T012455/1) and Michael Harris, Jiangtian Tan, Chris Hill and the University of Sheffield BioMedical Sciences EM unit are thanked for SEM analysis. Dr. Raffaele Battaglia and Marco Mauro at Novaetech S.r.l. (Pompeii, Italy) are thanked for their excellent technical support regarding the QCM studies.

ABBREVIATIONS

2D-MON, two-dimensional metal-organic nanosheet; 3D-MOF, three-dimensional metal-organic framework; bim, benzimidazole; bim-NH_2, 5-aminobenzimidazole; BTB-NH_2, 2,4,6-tris(4-carboxyphenyl)aniline; *C*, sensitivity constant; K_d, dissociation constant; *m*, mass; MIPS, molecularly imprinted polymers; MOF, metal-organic framework; n, overtone number; MON, metal-organic nanosheet; PBS, phosphate buffered saline; QCM, quartz crystal microbalance; ZIF, zeolitic imidazolate framework.

REFERENCES

(1) Kahn, K.; Plaxco, K. W. Principles of Biomolecular Recognition. In *Recognition Receptors in Biosensors*; Springer New York: New York, NY, **2010**, 3–45. https://doi.org/10.1007/978-1-4419-0919-0_1.

(2) Rohaizad, N.; Mayorga-Martinez, C. C.; Fojtů, M.; Latiff, N. M.; Pumera, M. Two-Dimensional Materials in Biomedical, Biosensing and Sensing Applications. *Chemical Society Reviews*. **2021**, 619–657. https://doi.org/10.1039/d0cs00150c.

(3) Huang, H.; Feng, W.; Chen, Y. Two-Dimensional Biomaterials: Material Science, Biological Effect and Biomedical Engineering Applications. *Chemical Society Reviews*. **2021**, 11381–11485. https://doi.org/10.1039/d0cs01138j.

(4) Bolotsky, A.; Butler, D.; Dong, C.; Gerace, K.; Glavin, N. R.; Muratore, C.; Robinson, J. A.; Ebrahimi, A. Two-Dimensional Materials in Biosensing and Healthcare: From in Vitro Diagnostics to Optogenetics and Beyond. *ACS Nano* **2019**, *13*, 9781–9810. https://doi.org/10.1021/acsnano.9b03632.

(5) Murali, A.; Lokhande, G.; Deo, K. A.; Brokesh, A.; Gaharwar, A. K. Emerging 2D Nanomaterials for Biomedical Applications. *Materials Today*. **2021**, 276–302. https://doi.org/10.1016/j.mattod.2021.04.020.

(6) Su, S.; Sun, Q.; Gu, X.; Xu, Y.; Shen, J.; Zhu, D.; Chao, J.; Fan, C.; Wang, L. Two-Dimensional Nanomaterials for Biosensing Applications. *TrAC - Trends Anal. Chem.* **2019**, *119*, 115610. https://doi.org/10.1016/j.trac.2019.07.021.

(7) Cun, J.-E.; Fan, X.; Pan, Q.; Gao, W.; Luo, K.; He, B.; Pu, Y. Copper-Based Metal–Organic Frameworks for Biomedical Applications. *Adv. Colloid Interface Sci.* **2022**, *305*, 102686. https://doi.org/10.1016/j.cis.2022.102686.

(8) Arun Kumar, S.; Balasubramaniam, B.; Bhunia, S.; Jaiswal, M. K.; Verma, K.; Prateek; Khademhosseini, A.; Gupta, R. K.; Gaharwar, A. K. Two-dimensional Metal Organic Frameworks for Biomedical Applications. *WIREs Nanomedicine and Nanobiotechnology* **2021**, *13*, e1674. https://doi.org/10.1002/wnan.1674.

(9) Nicks, J.; Sasitharan, K.; Prasad, R. R. R.; Ashworth, D. J.; Foster, J. A. Metal–Organic Framework Nanosheets: Programmable 2D Materials for Catalysis, Sensing, Electronics, and Separation Applications. *Adv. Funct. Mater.* **2021**, *31*, 2103723. https://doi.org/10.1002/adfm.202103723.

(10) Zhao, D.; Zhang, W.; Wu, Z. H.; Xu, H. Nanoscale Metal−Organic Frameworks and Their Nanomedicine Applications. *Frontiers in Chemistry*. Frontiers Media S.A. **2022**, 1243. https://doi.org/10.3389/fchem.2021.834171.

(11) Zhao, M.; Wang, Y.; Ma, Q.; Huang, Y.; Zhang, X.; Ping, J.; Zhang, Z.; Lu, Q.; Yu, Y.; Xu, H.; Zhao, Y.; Zhang, H. Ultrathin 2D Metal-Organic Framework Nanosheets. *Adv. Mater.* **2015**, *27*, 7372–7378. https://doi.org/10.1002/adma.201503648.

(12) Zhang, H.; Luo, B.; An, P.; Zhan, X.; Lan, F.; Wu, Y. Interaction of Nucleic Acids with Metal-Organic Framework Nanosheets by Fluorescence Spectroscopy and Molecular Dynamics Simulations. *ACS Appl. Bio Mater.* **2022**, *5*, 3500–3508. https://doi.org/10.1021/acsabm.2c00431.

(13) Yang, Y.; Hu, G. B.; Liang, W. Bin; Yao, L. Y.; Huang, W.; Zhang, Y. J.; Zhang, J. L.; Wang, J. M.; Yuan, R.; Xiao, D. R. An AIEgen-Based 2D Ultrathin Metal-Organic Layer as an Electrochemiluminescence Platform for Ultrasensitive Biosensing of Carcinoembryonic Antigen. *Nanoscale* **2020**, *12*, 5932–5941. https://doi.org/10.1039/c9nr10712f.

(14) Yan, M.; Ye, J.; Zhu, Q.; Zhu, L.; Huang, J.; Yang, X. Ultrasensitive Immunosensor for Cardiac Troponin i Detection Based on the Electrochemiluminescence of 2D Ru-MOF Nanosheets. *Anal. Chem.* **2019**, *91*, 10156–10163. https://doi.org/10.1021/acs.analchem.9b02169.

(15) Lin, Y.; Sun, Y.; Dai, Y.; Sun, W.; Zhu, X.; Liu, H.; Han, R.; Gao, D.; Luo, C.; Wang, X. A "Signal-on" Chemiluminescence Biosensor for Thrombin Detection Based on DNA Functionalized Magnetic Sodium Alginate Hydrogel and Metalloporphyrinic Metal-Organic Framework Nanosheets. *Talanta* **2020**, *207*, 120300. https://doi.org/10.1016/j.talanta.2019.120300.

(16) Zeng, Y.; Wang, M.; Sun, Z.; Sha, L.; Yang, J.; Li, G. Colorimetric Immunosensor Constructed Using 2D Metal–Organic Framework Nanosheets as Enzyme Mimics for the Detection of Protein Biomarkers. *J. Mater. Chem. B* **2022**, *10*, 450–455. https://doi.org/10.1039/d1tb02192c.

(17) de Azambuja, F.; Loosen, A.; Dragan, C.; van den Besselaar, M.; Harvey, J. N.; Parac-Vogt, T. N. En Route to a Heterogeneous Catalytic Direct Peptide Bond Formation by Zr-Based Metal-Organic Framework Catalysts. *ACS Catal.* **2021**, *11*, 7647–7658. https://doi.org/10.1021/acscatal.1c01782.

(18) Loosen, A.; De Azambuja, F.; Smolders, S.; Moons, J.; Simms, C.; De Vos, D.; Parac-Vogt, T. N. Interplay between Structural Parameters and Reactivity of Zr6-Based MOFs as Artificial Proteases. *Chem. Sci.* **2020**, *11* (26), 6662–6669. https://doi.org/10.1039/d0sc02136a.

(19) Giang, H.; Ly, T.; Fu, G.; Kondinski, A.; Bueken, B.; De Vos, D.; Parac-Vogt, T. N. Superactivity of MOF-808 toward Peptide Bond Hydrolysis. *J. Am. Chem. Soc* **2018**, *140*, 2023. https://doi.org/10.1021/jacs.8b01902.

(20) Ly, H. G. T.; Fu, G.; De Azambuja, F.; De Vos, D.; Parac-Vogt, T. N. Nanozymatic Activity of UiO-66 Metal-Organic Frameworks: Tuning the Nanopore Environment Enhances Hydrolytic Activity toward Peptide Bonds. *ACS Appl. Nano Mater.* **2020**, *3*, 8931–8938. https://doi.org/10.1021/acsanm.0c01688.

(21) Loosen, A.; de Azambuja, F.; Parac-Vogt, T. N. Which Factors Govern the Adsorption of Peptides to Zr(Iv)-Based Metal–Organic Frameworks? *Mater. Adv.* **2022**, *3*, 2475–2487. https://doi.org/10.1039/d1ma01027a.

(22) Smith, G. P.; Petrenko, V. A. Phage Display. *Chem. Rev.* **1997**, *97*, 391–410. https://doi.org/10.1021/cr960065d.

(23) Rawlings, A. E.; Bramble, J. P.; Tang, A. A. S.; Somner, L. A.; Monnington, A. E.; Cooke, D. J.; McPherson, M. J.; Tomlinson, D. C.; Staniland, S. S. Phage Display Selected Magnetite Interacting Adhirons for Shape Controlled Nanoparticle Synthesis. *Chem. Sci.* **2015**, *6*, 5586–5594. https://doi.org/10.1039/c5sc01472g.

(24) Li, C.; Liu, J.; Shaozhou, W.; Bai, X.; Zhang, Q.; Hua, R.; Liu, J.-H.; Liu, M.; Zhang, Y. Epitope Identification and Application for Diagnosis of Duck Tembusu Virus Infections in Ducks. *Viruses* **2016**, *8*, 306. https://doi.org/10.3390/v8110306.

(25) Kouzmitcheva, G. A.; Petrenko, V. A.; Smith, G. P. Identifying Diagnostic Peptides for Lyme Disease through Epitope Discovery. *Clin. Diagnostic Lab. Immunol.* **2001**, *8*, 150–160. https://doi.org/10.1128/CDLI.8.1.150-160.2001.

(26) Reiss, B. D.; Mao, C.; Solis, D. J.; Ryan, K. S.; Thomson, T.; Belcher, A. M. Biological Routes to Metal Alloy Ferromagnetic Nanostructures. *Nano Lett.* **2004**, *4*, 1127–1132. https://doi.org/10.1021/nl049825n.

(27) Fan, G.; Dundas, C. M.; Zhang, C.; Lynd, N. A.; Keitz, B. K. Sequence-Dependent Peptide Surface Functionalization of Metal-Organic Frameworks. *ACS Appl. Mater. Interfaces* **2018**, *10*, 18601–18609. https://doi.org/10.1021/acsami.8b05148.

(28) Li, Y.; Liang, F.; Bux, H.; Yang, W.; Caro, J. Zeolitic Imidazolate Framework ZIF-7 Based Molecular Sieve Membrane for Hydrogen Separation. *J. Memb. Sci.* **2010**, *354*, 48–54. https://doi.org/10.1016/j.memsci.2010.02.074.

(29) Zhang, S.; Yao, W.; Ying, J.; Zhao, H. Polydopamine-Reinforced Magnetization of Zeolitic Imidazolate Framework ZIF-7 for Magnetic Solid-Phase Extraction of Polycyclic Aromatic Hydrocarbons from the Air-Water Environment. *J. Chromatogr. A* **2016**, *1452*, 18–26. https://doi.org/10.1016/j.chroma.2016.05.039.

(30) Kang, C.-H.; Lin, Y.-F.; Huang, Y.-S.; Tung, K.-L.; Chang, K.-S.; Chen, J.-T.; Hung, W.-S.; Lee, K.-R.; Lai, J.-Y. Synthesis of ZIF-7/Chitosan Mixed-Matrix Membranes with Improved Separation Performance of Water/Ethanol Mixtures. *J. Memb. Sci.* **2013**, *438*, 105–111. https://doi.org/10.1016/j.memsci.2013.03.028.

(31) Liu, H.-L.; Chang, Y.-J.; Fan, T.; Gu, Z.-Y. Two-Dimensional Metal–Organic Framework Nanosheets as a Matrix for Laser Desorption/Ionization of Small Molecules and Monitoring Enzymatic Reactions at High Salt Concentrations. *Chem. Commun.* **2016**, *52*, 12984–12987. https://doi.org/10.1039/C6CC07371A.

(32) Peng, Y.; Li, Y.; Ban, Y.; Jin, H.; Jiao, W.; Liu, X.; Yang, W. Metal-Organic Framework Nanosheets as Building Blocks for Molecular Sieving Membranes. *Science (80-.).* **2014**, *346*, 1356–1359. https://doi.org/10.1126/science.1254227.

(33) López-Cabrelles, J.; Mañas-Valero, S.; Vitórica-Yrezábal, I. J.; Bereciartua, P. J.; Rodríguez-Velamazán, J. A.; Waerenborgh, J. C.; Vieira, B. J. C.; Davidovikj, D.; Steeneken, P. G.; van der Zant, H. S. J.; Mínguez Espallargas, G.; Coronado, E. Isoreticular Two-Dimensional Magnetic Coordination Polymers Prepared through Pre-Synthetic Ligand Functionalization. *Nat. Chem.* **2018**, *10*, 1001–1007. https://doi.org/10.1038/s41557-018-0113-9.

(34) Zhao, J.; Chen, R.; Huang, J.; Wang, F.; Tao, C.-A.; Wang, J. Facile Synthesis of Metal–Organic Layers with High Catalytic Performance toward Detoxification of a Chemical Warfare Agent Simulant. *ACS Appl. Mater. Interfaces* **2021**, *13*, 40863–40871. https://doi.org/10.1021/acsami.1c08365.

(35) Quan, Y.; Lan, G.; Shi, W.; Xu, Z.; Fan, Y.; You, E.; Jiang, X.; Wang, C.; Lin, W. Metal–Organic Layers Hierarchically Integrate Three Synergistic Active Sites for Tandem Catalysis. *Angew. Chemie Int. Ed.* **2021**, *60*, 3115–3120. https://doi.org/10.1002/anie.202011519.

(36) Guo, Y.; Shi, W.; Yang, H.; He, Q.; Zeng, Z.; Ye, J.; He, X.; Huang, R.; Wang, C.; Lin, W. Cooperative Stabilization of the [Pyridinium-CO 2 -Co] Adduct on a Metal–Organic Layer Enhances Electrocatalytic CO 2 Reduction. *J. Am. Chem. Soc.* **2019**, *141*, 17875–17883. https://doi.org/10.1021/jacs.9b09227.

(37) Luo, T.; Fan, Y.; Mao, J.; Yuan, E.; You, E.; Xu, Z.; Lin, W. Dimensional Reduction Enhances Photodynamic Therapy of Metal–Organic Nanophotosensitizers. *J. Am. Chem. Soc.* **2022**, *144*, 5241–5246. https://doi.org/10.1021/jacs.2c00384.

(38) Lan, G.; Ni, K.; Xu, R.; Lu, K.; Lin, Z.; Chan, C.; Lin, W. Nanoscale Metal-Organic Layers for Deeply Penetrating X-Ray-Induced Photodynamic Therapy. *Angew. Chemie* **2017**, *129*, 12270–12274. https://doi.org/10.1002/ange.201704828.

(39) Nash, G. T.; Luo, T.; Lan, G.; Ni, K.; Kaufmann, M.; Lin, W. Nanoscale Metal–Organic Layer Isolates Phthalocyanines for Efficient Mitochondria-Targeted Photodynamic Therapy. *J. Am. Chem. Soc.* **2021**, *143*, 2194–2199. https://doi.org/10.1021/jacs.0c12330.

(40) Lan, G.; Ni, K.; Veroneau, S. S.; Song, Y.; Lin, W. Nanoscale Metal–Organic Layers for Radiotherapy–Radiodynamic Therapy. *J. Am. Chem. Soc.* **2018**, *140*, 16971–16975. https://doi.org/10.1021/jacs.8b11593.

(41) Ling, X.; Gong, D.; Shi, W.; Xu, Z.; Han, W.; Lan, G.; Li, Y.; Qin, W.; Lin, W. Nanoscale Metal–Organic Layers Detect Mitochondrial Dysregulation and Chemoresistance via Ratiometric Sensing of Glutathione and PH. *J. Am. Chem. Soc.* **2021**, *143*, 1284–1289. https://doi.org/10.1021/jacs.0c11764.

(42) Hess, G. T.; Cragnolini, J. J.; Popp, M. W.; Allen, M. A.; Dougan, S. K.; Spooner, E.; Ploegh, H. L.; Belcher, A. M.; Guimaraes, C. P. M13 Bacteriophage Display Framework That Allows Sortase-Mediated Modification of Surface-Accessible Phage Proteins. *Bioconjug. Chem.* **2012**, *23*, 1478–1487. https://doi.org/10.1021/bc300130z.

(43) Burton, D. R. Phage Display. *Immunotechnology* **1995**, *1*, 87–94. https://doi.org/10.1016/1380-2933(95)00013-5.

(44) Burley, S. K.; Petsko, G. A. Amino-Aromatic Interactions in Proteins. *FEBS Lett.* **1986**, *203*, 139–143. https://doi.org/10.1016/0014-5793(86)80730-X.

(45) Patwardhan, S. V.; Patwardhan, G.; Perry, C. C. Interactions of Biomolecules with Inorganic Materials: Principles, Applications and Future Prospects. *J. Mater. Chem.* **2007**, *17*, 2875. https://doi.org/10.1039/b704075j.

(46) Jayaramulu, K.; Geyer, F.; Schneemann, A.; Kment, Š.; Otyepka, M.; Zboril, R.; Vollmer, D.; Fischer, R. A. Hydrophobic Metal–Organic Frameworks. *Adv. Mater.* **2019**, *31*, 1900820. https://doi.org/10.1002/adma.201900820.

(47) Pu, Y.; Yang, Z.; Wee, V.; Wu, Z.; Jiang, Z.; Zhao, D. Amino-Functionalized NUS-8 Nanosheets as Fillers in PIM-1 Mixed Matrix Membranes for CO2 Separations. *J. Memb. Sci.* **2022**, *641*, 119912. https://doi.org/10.1016/j.memsci.2021.119912.

(48) Zhao, P.; Lampronti, G. I.; Lloyd, G. O.; Wharmby, M. T.; Facq, S.; Cheetham, A. K.; Redfern, S. A. T. Phase Transitions in Zeolitic Imidazolate Framework 7: The Importance of Framework Flexibility and Guest-Induced Instability. *Chem. Mater.* **2014**, *26*, 1767–1769. https://doi.org/10.1021/cm500407f.

(49) Singla, P.; Luxami, V.; Paul, K. Benzimidazole-Biologically Attractive Scaffold for Protein Kinase Inhibitors. *RSC Adv.* **2014**, *4*, 12422. https://doi.org/10.1039/c3ra46304d.

(50) Osmaniye, D.; Evren, A. E.; Sağlık, B. N.; Levent, S.; Özkay, Y.; Kaplancıklı, Z. A. Design, Synthesis, Biological Activity, Molecular Docking, and Molecular Dynamics of Novel Benzimidazole Derivatives as Potential AChE/MAO-B Dual Inhibitors. *Arch. Pharm. (Weinheim).* **2022**, *355*, e210045. https://doi.org/10.1002/ardp.202100450.

(51) Lan, G.; Fan, Y.; Shi, W.; You, E.; Veroneau, S. S.; Lin, W. Frameworks for Artificial Photosynthesis. *Nat. Catal.* **2022**, *5*, 1006–1018. https://doi.org/10.1038/s41929-022-00865-5.

(52) Pohanka, M. The Piezoelectric Biosensors: Principles and Applications, a Review. *Int. J. Electrochem. Sci.* **2017**, *12*, 496–506. https://doi.org/10.20964/2017.01.44.

(53) Afzal, A.; Mujahid, A.; Schirhagl, R.; Bajwa, S.; Latif, U.; Feroz, S. Gravimetric Viral Diagnostics: QCM Based Biosensors for Early Detection of Viruses. *Chemosensors* **2017**, *5*, 7. https://doi.org/10.3390/chemosensors5010007.

(54) Lim, H. J.; Saha, T.; Tey, B. T.; Tan, W. S.; Ooi, C. W. Quartz Crystal Microbalance-Based Biosensors as Rapid Diagnostic Devices for Infectious Diseases. *Biosens. Bioelectron.* **2020**, *168*, 112513. https://doi.org/10.1016/j.bios.2020.112513.

(55) Pohanka, M. Quartz Crystal Microbalance (QCM) Sensing Materials in Biosensors Development. *Int. J. Electrochem. Sci.* **2021**, *16*, 211220. https://doi.org/10.20964/2021.12.15.

(56) P J, J.; Prabakaran, K.; Luo, J.; M G, D. H. Effective Utilization of Quartz Crystal Microbalance as a Tool for Biosensing Applications. *Sensors Actuators A Phys.* **2021**, *331*, 113020. https://doi.org/10.1016/j.sna.2021.113020.

(57) Wang, L. Metal-Organic Frameworks for QCM-Based Gas Sensors: A Review. *Sensors Actuators A Phys.* **2020**, *307*, 111984. https://doi.org/10.1016/j.sna.2020.111984.

(58) Kosuru, L.; Bouchaala, A.; Jaber, N.; Younis, M. I. Humidity Detection Using Metal Organic Framework Coated on QCM. *J. Sensors* **2016**, *2016*, 1–8. https://doi.org/10.1155/2016/4902790.

(59) Chowdhury, S.; Torad, N. L.; Ashok, A.; Gumilar, G.; Chaikittisilp, W.; Xin, R.; Cheng, P.; Ul Hoque, M. I.; Wahab, M. A.; Karim, M. R.; Yuliarto, B.; Hossain, M. S.; Yamauchi, Y.; Kaneti, Y. V. Template- and Etching-Free Fabrication of Two-Dimensional Hollow Bimetallic Metal-Organic Framework Hexagonal Nanoplates for Ammonia Sensing. *Chem. Eng. J.* **2022**, *450*, 138065. https://doi.org/10.1016/j.cej.2022.138065.

Biomimetic Active Sites on Monolayered Metal–Organic

(60) Wen, Y.; Zhang, X.; Li, X.; Wang, Z.; Tang, C. Y. Metal-Organic Framework Nanosheets for Thin-Film Composite Membranes with Enhanced Permeability and Selectivity. *ACS Appl. Nano Mater.* **2020**, *3*, 9238–9248. https://doi.org/10.1021/acsanm.0c01860.

(61) Xie, B.; Yan, Y.; Wu, J.; Cai, X.; Zheng, J.; Lan, Y.; Tang, X.; Fan, J.; Zheng, S.; Cai, S. Three-Component Covalent Organic Framework Nanosheets for the Detection of MicroRNAs. *Crystals* **2022**, *12* , 1628. https://doi.org/10.3390/cryst12111628.

(62) Sauerbrey, G. Verwendung von Schwingquarzen Zur Wägung Dünner Schichten Und Zur Mikrowägung. *Zeitschrift für Phys.* **1959**, *155*, 206–222. https://doi.org/10.1007/BF01337937.

(63) Adamczyk, Z.; Sadowska, M.; Żeliszewska, P. Applicability of QCM-D for Quantitative Measurements of Nano- and Microparticle Deposition Kinetics: Theoretical Modeling and Experiments. *Anal. Chem.* **2020**, *92*, 15087–15095. https://doi.org/10.1021/acs.analchem.0c03115.

(64) Reviakine, I.; Johannsmann, D.; Richter, R. P. Hearing What You Cannot See and Visualizing What You Hear: Interpreting Quartz Crystal Microbalance Data from Solvated Interfaces. *Anal. Chem.* **2011**, *83*, 8838–8848. https://doi.org/10.1021/ac201778h.

(65) Luan, Y.; Li, D.; Wei, T.; Wang, M.; Tang, Z.; Brash, J. L.; Chen, H. "Hearing Loss" in QCM Measurement of Protein Adsorption to Protein Resistant Polymer Brush Layers. *Anal. Chem.* **2017**, *89*, 4184–4191. https://doi.org/10.1021/acs.analchem.7b00198.

(66) Reviakine, I.; Johannsmann, D.; Richter, R. P. Hearing What You Cannot See and Visualizing What You Hear: Interpreting Quartz Crystal Microbalance Data from Solvated Interfaces. *Anal. Chem.***2011**, *83*, 8838–8848. https://doi.org/10.1021/ac201778h.

(67) Tellechea, E.; Johannsmann, D.; Steinmetz, N. F.; Richter, R. P.; Reviakine, I. Model-Independent Analysis of QCM Data on Colloidal Particle Adsorption. *Langmuir* **2009**, *25*, 5177–5184. https://doi.org/10.1021/la803912p.

Phage display against two-dimensional metal-organic nanosheets as a route-towards tunable biosensors

Amelia C. Wood, Edwin C. Johnson, Ram R. R. Prasad, Steven P. Armes, Sarah S. Staniland, Jonathan A. Foster

Department of Chemistry, University of Sheffield, Brook Hill, Sheffield S3 7HF

KEYWORDS. Phage Display, Metal-Organic Nanosheet, Biopanning, Quartz-crystal microbalance

2. General Details

2.1 Materials

Commercial solvents, reagents and spectroscopic grade deuterated solvents were used as purchased without further purification, as listed: 5-aminobenzimidazole (fluorochem), benzimidazole (99 %, Alfa Aesar), deuterium oxide (99.9 atom % D, Sigma-Aldrich), dimethylformamide (≥99 %, Fisher), dimethyl sulfoxide-d6 (99.5 atom % D, Sigma-Aldrich), deuterium chloride solution (35 wt. % in D_2O, ≥99 atom % D, Sigma-Aldrich), ethanol (≥99.8 %, Fisher), formic acid (98+%, Acros Organics), hafnium chloride (98+ %, Alfa Aesar), n-propanol (SLS), sodium deuteroxide (40 wt. %, Sigma-Aldrich), zinc nitrate hexahydrate ($Zn(NO_3)_2{\cdot}6H_2O$, 98 %, Acros Organics)

7aa-Phage display kit (New England Biolabs), Miniprep Kit (Thermo Scientific GeneJET Plasmid)

2.2 Analytical Procedures

Elemental analysis was performed by the microanalytical service at the Department of Chemistry, University of Sheffield using a Vario MICRO Cube in an atmosphere of pure O_2. Elemental CHN contents are determined to a tolerance of ± 0.5 % for organometallics.

FT-IR spectra were recorded using a Perkin Elmer Spectrum 100 FT-IR spectrophotometer, equipped with a SenseIR diamond ATR module. Samples were analysed without further preparation, and spectra were obtained in reflectance mode between 4000 – 400 cm^{-1}, using 12 scans with a spectral resolution of 1 cm^{-1}.

NMR spectra were recorded at 300 K using a Bruker AV 400 spectrometer with a 5mm solution state probe at 400 MHz (1H). Supramolecular frameworks were digested prior to submission, using DCl (30 µL) and DMSOd6 (750 µL) for the ZIF systems and NaOD (100 µL) and D_2O (750 µL) for Hf-BTB-NH_2 with ultrasonication (24 h). NMR spectra were processed using MestreNova. Mass spectra were recorded directly from NMR solutions using an Agilent 6530 QTOF LC-MS in negative ionisation mode.

Powder X-ray diffraction (XRPD) data were collected using a Bruker-AXS D8 diffractometer using Cu Kα (λ=1.5418 Å) radiation and a LynxEye position sensitive detector in Bragg Brentano parafocussing geometry using a packed glass capillary or a flat silicon plate.

Thermogravimetric analyses (TGA) were performed using a Perkinelmer pyris 1 instrument. Approximately 4 mg of sample was weighed into a ceramic pan, held under nitrogen flow of 20 cm^3 min^{-1} at 25 °C for 10 minutes to purge the sample and allow for equilibration, then ramped to varying end temperatures (see individual traces for details) at 1 °C min^{-1} . The samples were then held at the final temperature for 10 minutes.

Dynamic light scattering (DLS) data were collected using a Malvern Zetasizer Nano Series particle size analyser, using a He-Ne laser at 633 nm, operating in backscatter mode (173 °). Samples were equilibrated at 298 K for 60 s prior to analysis. Zeta potential data were collected using the same instrument in zeta potential mode, using disposable polycarbonate capillary electrophoresis cells and according to the Smoluchowski method. All materials were dispersed in diluted PBS (pH 7.4) to 1.37 mmol with respect to NaCl. Samples were incubated with peptide for exactly 1 h before measurements were taken. Contact angle measurements were obtained using a Drop Shape Analyzer using the Sessile drop method.

Atomic force microscopy (AFM) images were recorded using a Bruker Multimode 5 Atomic Force Microscope, operating in soft-tapping mode in air under standard ambient temperature and pressure, fitted with Bruker OTESPA-R3 silicon cantilevers operated with a drive amplitude between 5-20 mV and resonance frequency of ~236 kHz. ZIF MON solutions were prepared (0.2 mg / mL, methanol-propan-1-ol, 1:1 volume) and Hf-BTB-NH_2 MON solutions (2.5 mg / mL ethanol, 2 drops into 20 mL vial of ethanol and vigorous shaking). AFM samples were prepared by drop-casting 10 µL drops of suspension onto the centre of freshly cleaved mica sheets heated to 120 °C on a hot plate. These sheets were stuck to stainless steel, magnetic Agar scanning probe microscopy specimen discs. Images were processed using Gwyddion software.

Scanning electron microscopy (SEM) samples were prepared by loading powdered samples onto carbon sticky tabs placed on aluminium SEM sample stubs, coated with approximately 20 nm gold using an Edwards S150B sputter coater and loaded into a TESCAN VEGA3 LMU SEM, operated at 15 keV. Images were collected at 10,000x magnification using the secondary electron detector.

For peptide sequencing, phage plasmid was extracted using a miniprep kit. The samples were sent off to GENEWIZ for sanger sequencing.

3. Synthesis of Metal-Organic Materials

3.1 Synthesis of ZIF-7-III MOF

Zinc nitrate hexahydrate (755 mg, 2.54 mmol) and benzimidazole (1.92 g, 16.28 mmol) were dissolved in DMF (250 mL, 3.25 mol). After stirring for 1 h, the solution is kept statically at room temperature for 72 h. ZIF-7 nanoparticles were then collected by centrifugation and thoroughly washed with methanol and dried at 50 °C overnight. Then subsequently dried at 120 C for 48 h in a vacuum oven. The obtained ZIF-7-I was redispersed in distilled water at a concentration of 0.5 wt % and then refluxed at 100 C for 24 h. The turbid mixture was washed with distilled water once and methanol three times, and then dried at 50 C overnight to obtain ZIF-7-III (486 mg, 0.805 mmol, 42 %) as a white powder. Elemental Analysis %: C 56.1, H 3.3, N 18.7 Found Mass %: C 56.21, H 3.51, N 18.6; (ESI-NEG): $[M]^+$ 119.1 (benzimidazole). ^{1}H NMR (DCL/DMSO-d_6): 9.66 (s, 1H), 7.92 – 7.83 (m, 2H), 7.63 – 7.55 (m, 2H). Phase purity confirmed by XRPD with a comparison to the CCDC (675375) powder pattern for ZIF-7-III.

3.2 Characterisation of ZIF-7-III MOF

XRPD

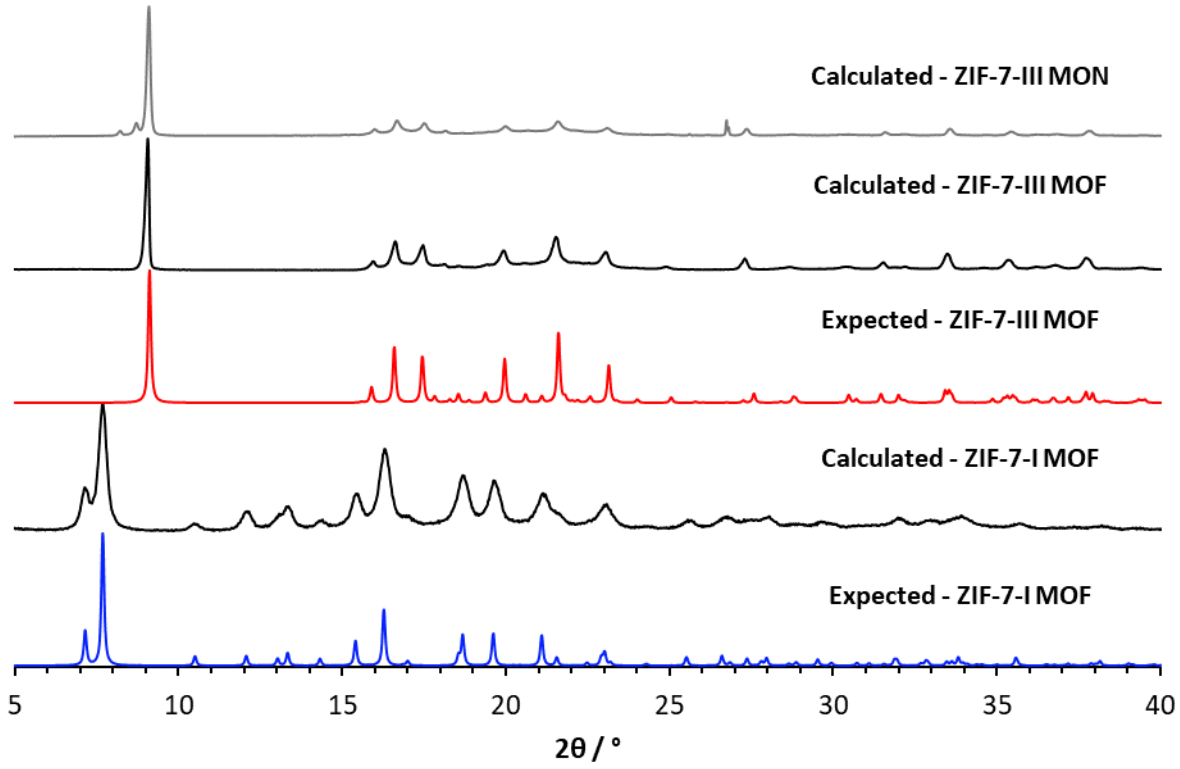

Figure S1: XRPD of the different phases of ZIF-7 MOF and 2D MON. The expected pattern of ZIF-7-I MOF found in CCDC (602541) (blue) with comparison to the calculated ZIF-7-I MOF (black). The expected pattern of ZIF-7-III MOF found in CCDC (675375) (red) with comparison to the calculated ZIF-7-III MOF (black) and the calculated ZIF-7-III MON (grey).

ATR-IR

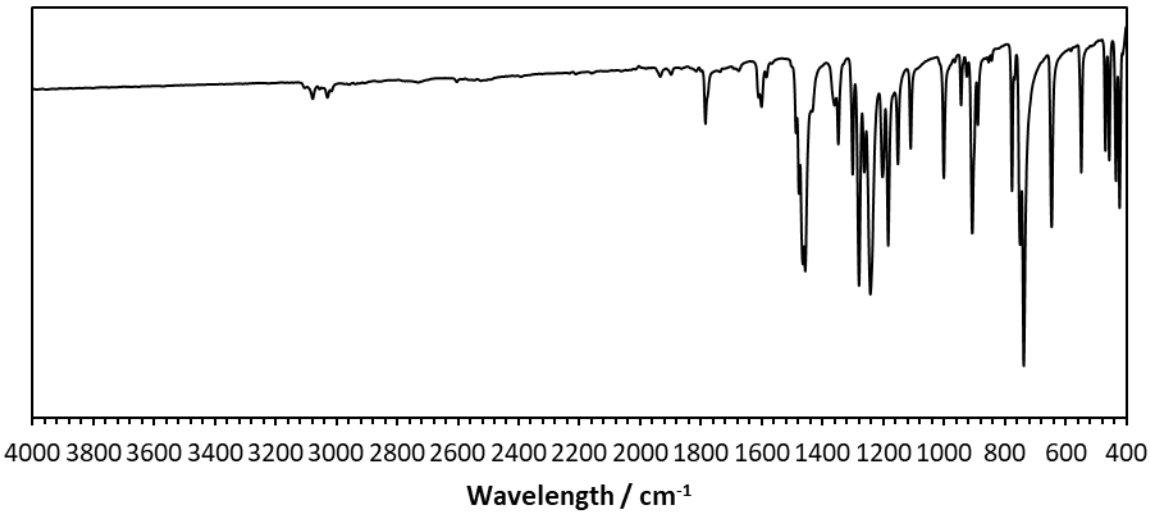

Figure S2: ATR-IR spectrum of ZIF-7

Scanning Electron Microscopy

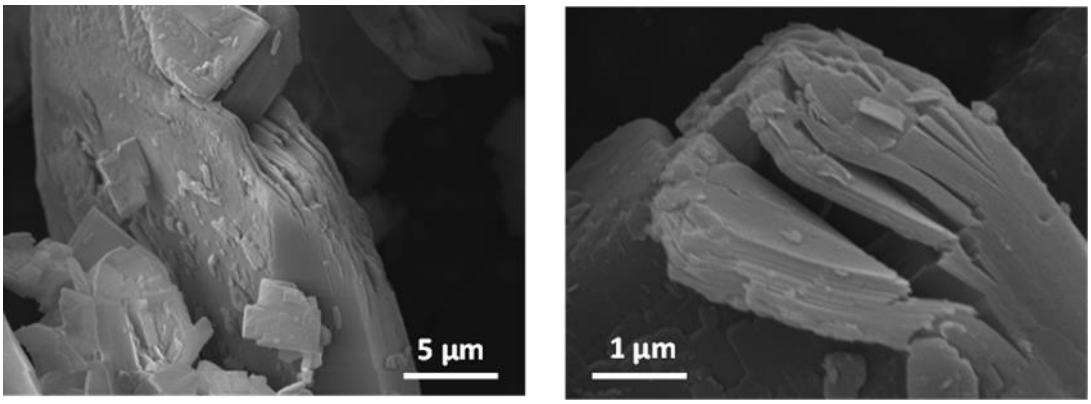

Figure S3: SEM of synthesised ZIF-7-III bulk MOF

TGA

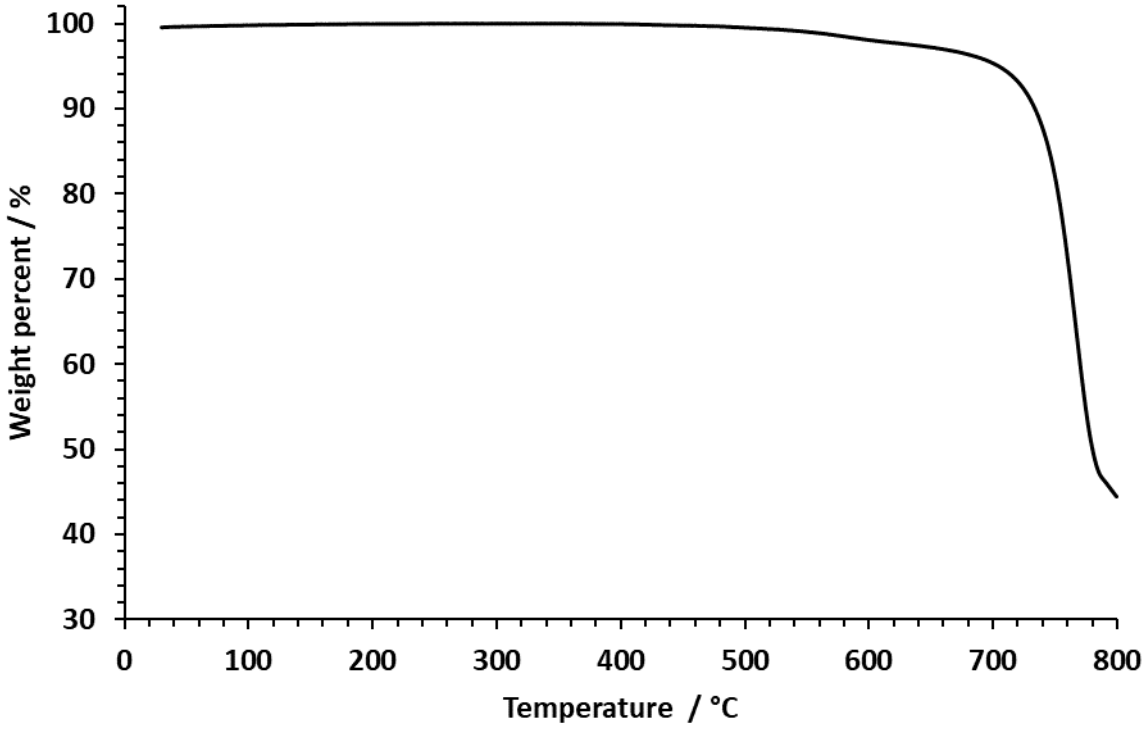

Figure S4: TGA plot for ZIF-7

3.3 Synthesis of ZIF-7-NH_2-III MOF

Zinc nitrate hexahydrate (755 mg, 2.54 mmol), (962 mg, 8.14 mmol) benzimidazole and (1.08 g, 8.11 mmol) 5-aminobenzimidazole were dissolved in DMF (125 mL, 1.63 mol). After stirring for 1 h, the solution is kept statically at 30 °C for 2 weeks. ZIF-7 nanoparticles were then collected by centrifugation and thoroughly washed with methanol and dried at 50 °C overnight. Then subsequently dried at 120 C for 48 h in a vacuum oven. The obtained ZIF-7-I was redispersed in distilled water at a concentration of 0.5 wt % and then refluxed at 100 C for 1 week. The turbid mixture was washed with distilled water once and methanol three times, and then dried at 50 C overnight to obtain ZIF-7-III (436 mg, 0.694 mmol, 27 %) as a purple. Elemental Analysis %: C 56.1, H 3.3, N 18.7 Found Mass %: C 56.21, H 3.51, N 18.6; (ESI-NEG):$[M]^+$ 134.1 (Bim-NH_2), $[M]^+$ 119.1 (Bim). 1H NMR (DCl/DMSO-d_6): 9.73 (s, 1H, **Bim-NH_2**), 9.66 (s, 1H, **Bim**), 8.03 (d, 1H, **Bim-NH_2**), 8.00 (s, 1H, **Bim-NH_2**), 7.92 – 7.83 (m, 2H, **Bim**), 7.64 (d, *J* = 2.0 Hz, 1H, **Bim-NH_2**), 7.63 – 7.55 (m, 2H, **Bim**). Phase purity confirmed by XRPD with a comparison to the CCDC (675375) powder pattern for ZIF-7-III.

3.4 Characterisation of ZIF-7-NH_2-III MOF

NMR

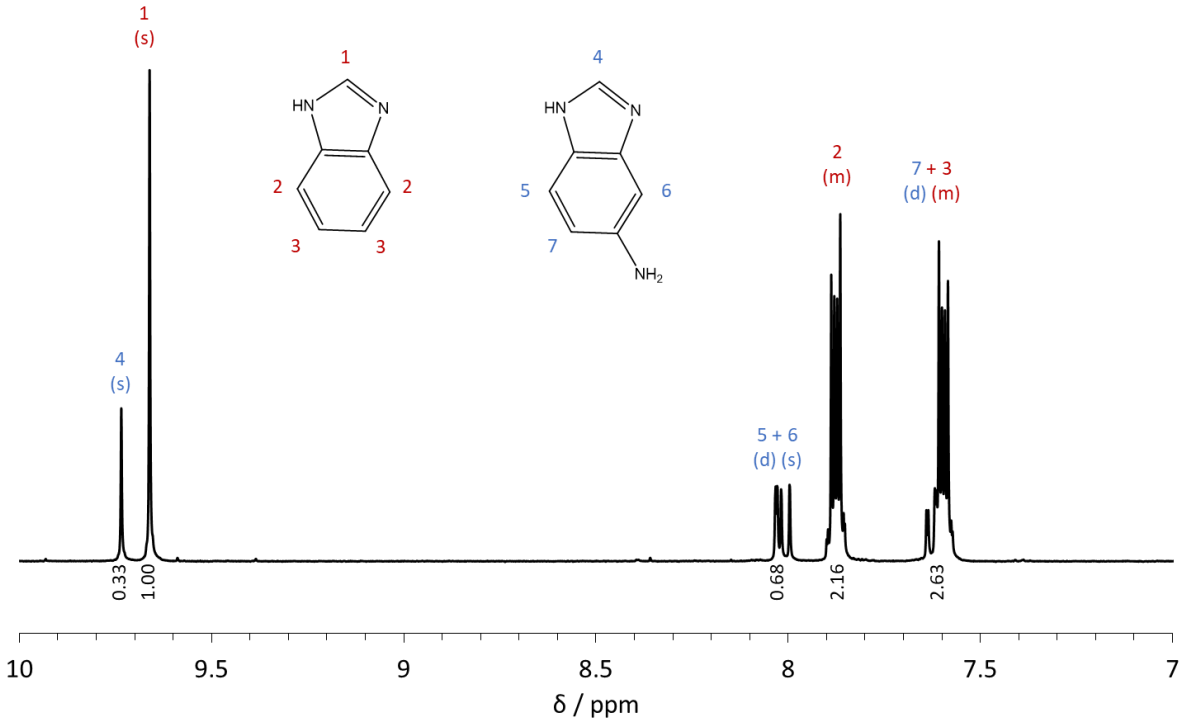

Figure S5: ^{1}H NMR spectrum of ZIF-7-NH_2 digested with DCl/DMSO-d_6, with peaks assigned according to the inset molecular structures.

XRPD

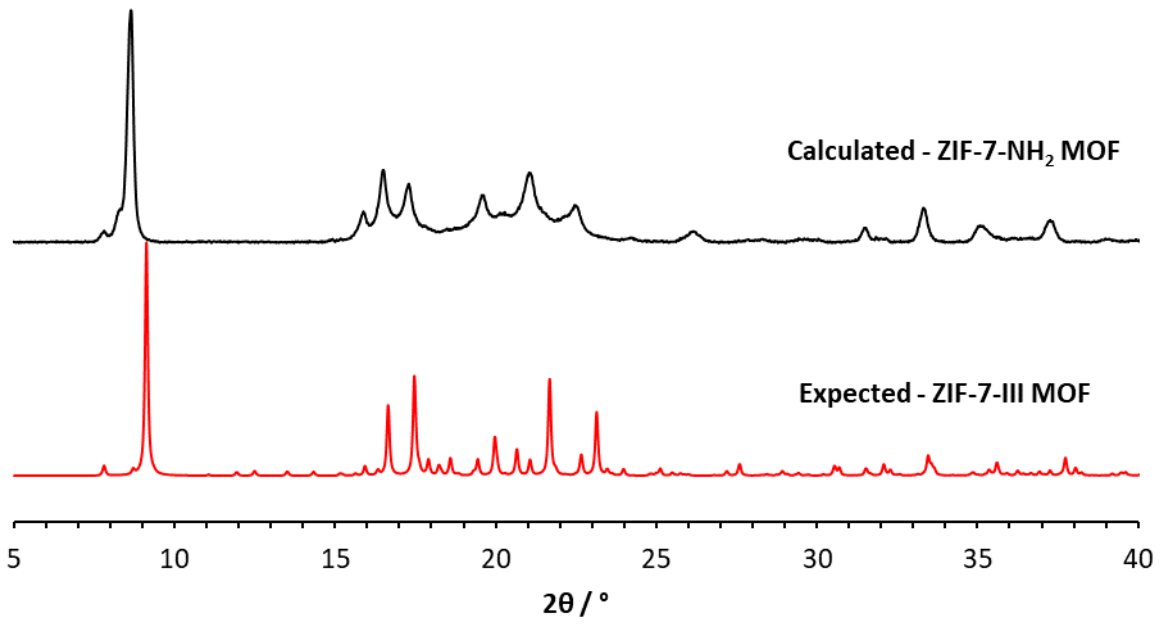

Figure S6: XRPD of synthesised ZIF-7-NH_2 (black) with comparison to the expected pattern found in CCDC (675375) (red).

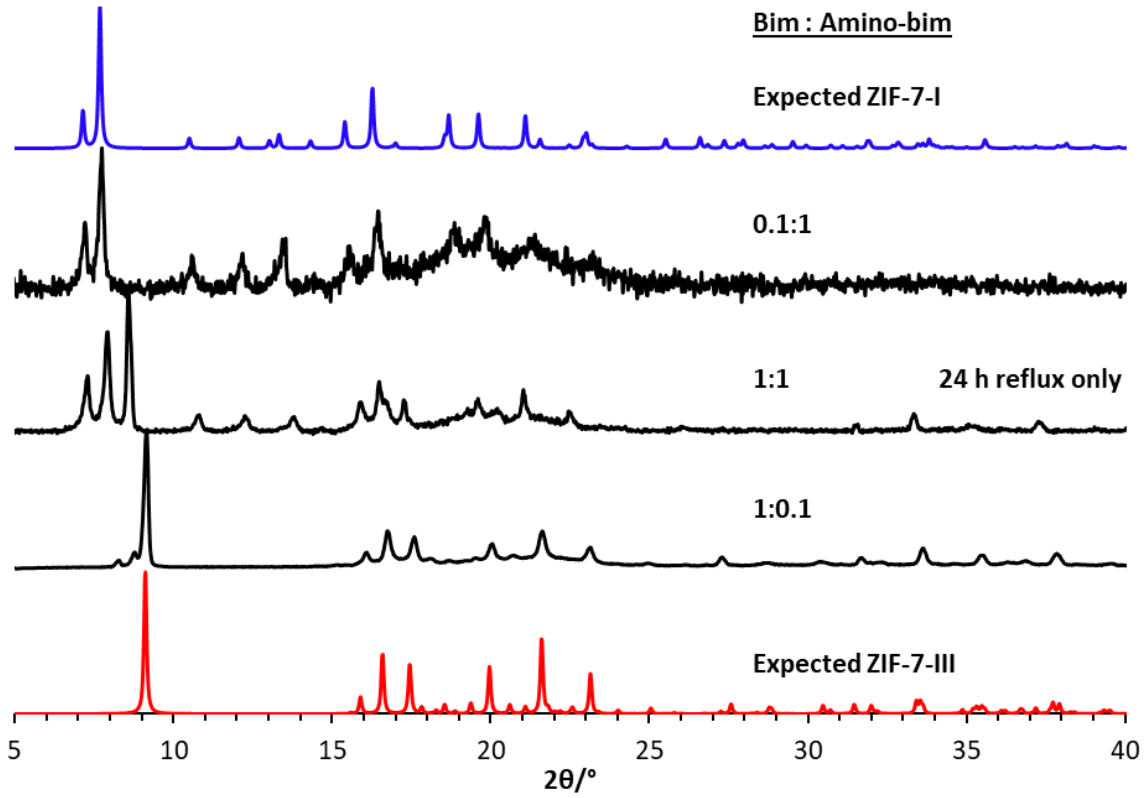

Figure S7: XRPD of synthesised ZIF-7-NH_2 with different ratio of benzimidazole and 5-amino-benzimidazole added (black) compared to ZIF-7-III (red) and ZIF-7-I (blue).

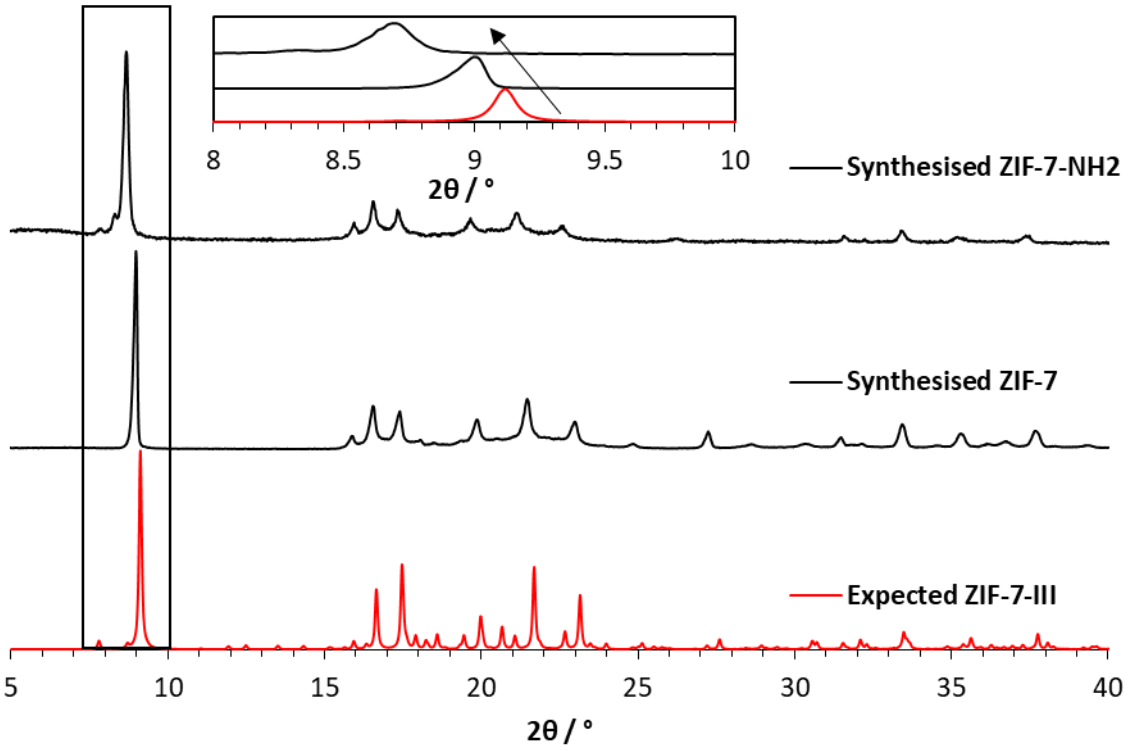

Figure S8: XRPD of synthesised ZIF-7-NH_2 (black top) with comparison to synthesised ZIF-7 (black bottom) the expected pattern found in CCDC (675375) (red) with inserted zoom of section 8-10 ° 2θ to show shift in [002].

ATR-IR

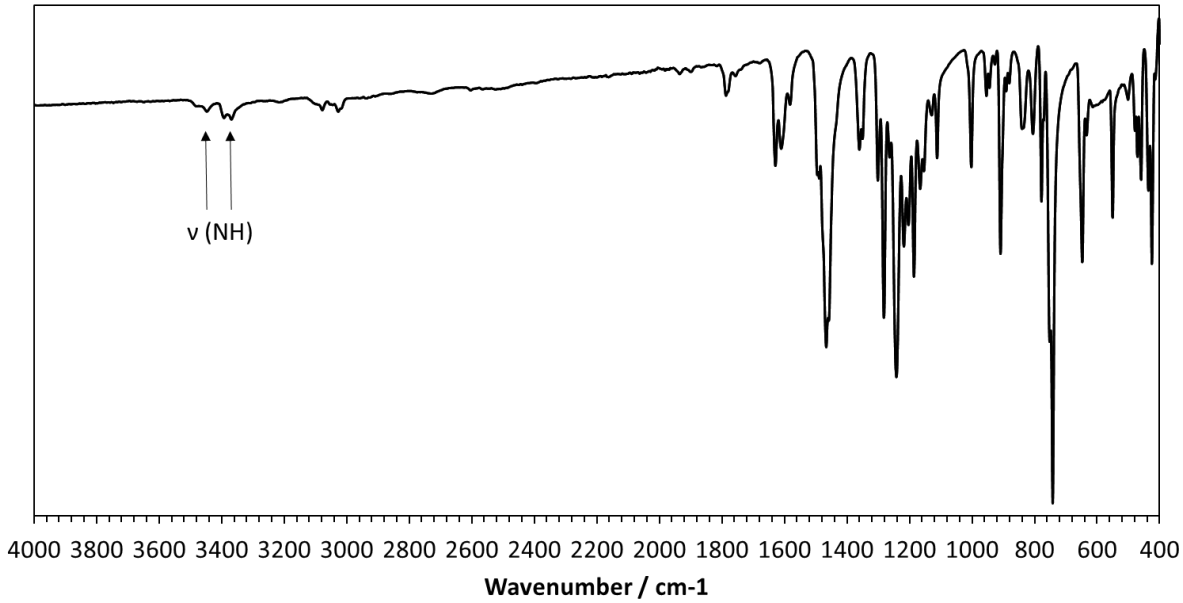

Figure S9: ATR-IR spectrum of ZIF-7-NH_2

SEM

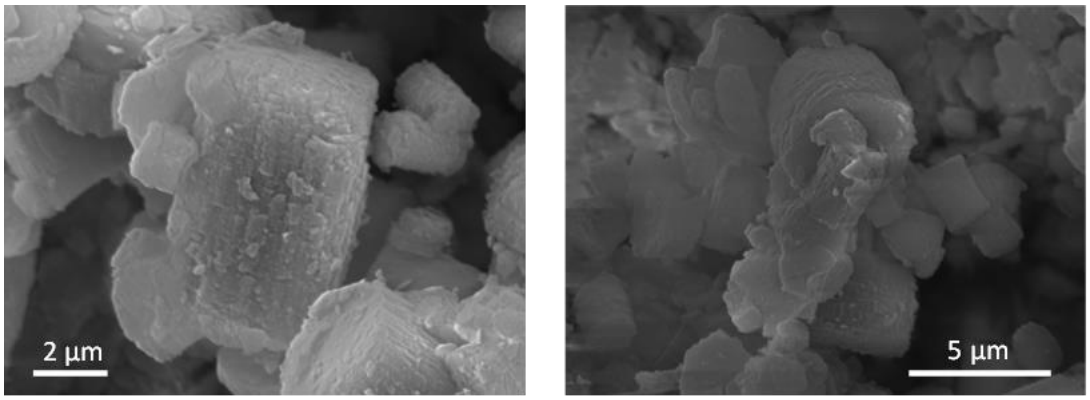

Figure S10: SEM of synthesised ZIF-7-NH_2-III bulk MOF

TGA

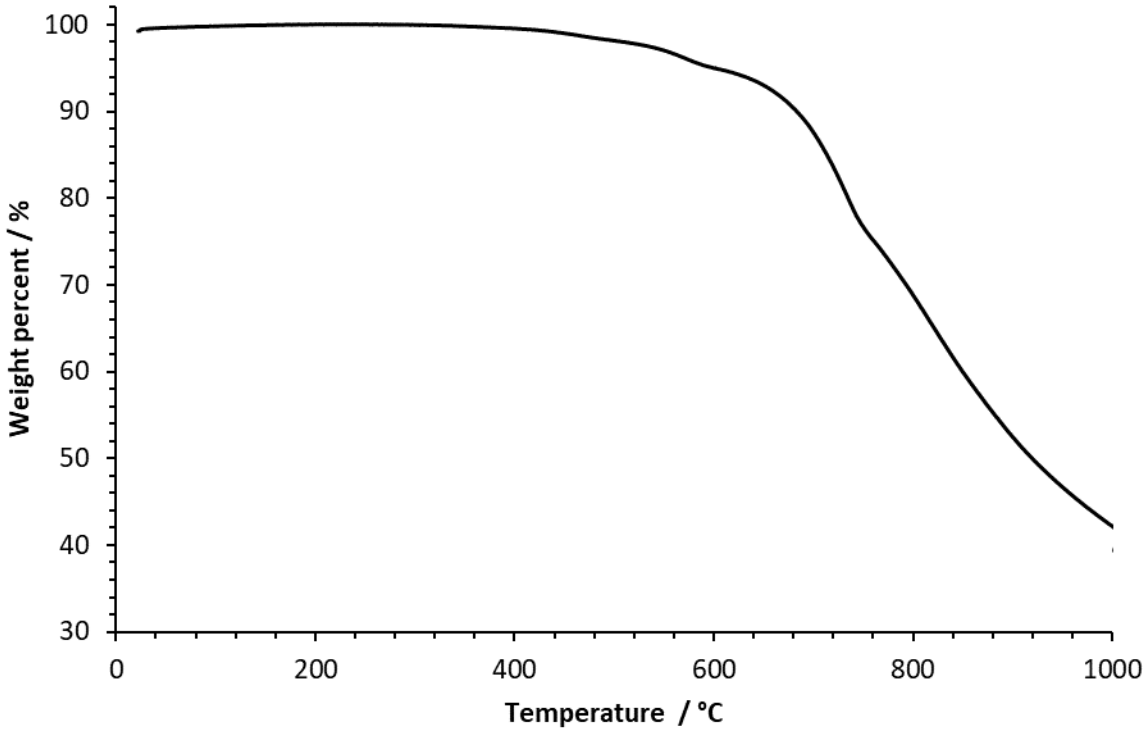

Figure S11: TGA plot for ZIF-7-NH_2

3.5 Synthesis of Hf-BTB-NH_2

To prepare Hf-BTB-NH_2 MONs, hafnium chloride (34.59 mg, 0.108 mmol) and 2,4,6-Tris(4-carboxyphenyl)aniline (32.87 mg, 0.072 mmol) were added to a 20 mL screw-cap glass vial. DMF (12.5 mL) was added and the mixture ultrasonically dissolved to obtain a clear solution. Formic acid (2.5 mL) and H_2O (0.7 mL) were added, the vial sealed and placed in a 120 °C oven for 48 h. The vial was taken out of the oven and cooled to room temperature. The turbid solution was centrifuged to collect Hf-BTB-NH_2 as a pale-yellow precipitate. The precipitate was washed multiple times with DMF, followed by ethanol. To prevent the stacking of the MON layers, Hf-BTB-NH_2 was kept in ethanol until needed for further studies. For analysis purposes the solid was collect via centrifugation and dried 120 °C overnight. Elemental Analysis %: C 27.3, H 2.04, N 1.18 Found Mass %: C 24.8, H 2.9, N 1.0. ^{1}H NMR ($NaOD/D_2O$, 24 hr sonication): 8.24 (s, 2H), 7.72 – 7.65 (m, 4H), 7.58 (d, *J* = 8.4 Hz, 2H), 7.21 (d, *J* = 8.3 Hz, 2H), 7.11 (d, *J* = 8.2 Hz, 4H), 7.03 (s, 2H). Phase purity confirmed by XRPD with a comparison to NUS-8-Hf found in CCDC (1567189).

3.6 Characterisation of Hf-BTB-NH_2

NMR

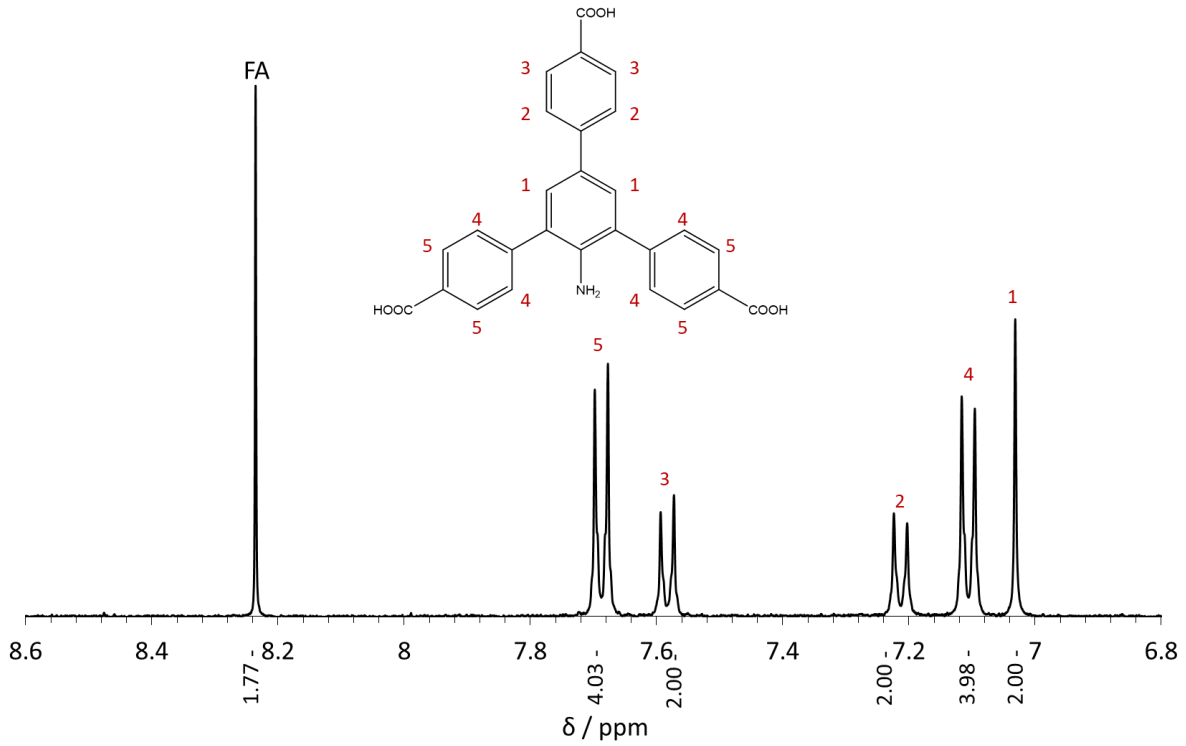

Figure S12: ^{1}H NMR spectrum of Hf-BTB-NH_2 digested with $NaOD/D_2O$ and a 24 hr sonication, with peaks assigned according to the inset molecular structure of BTB-NH_2.

XRPD

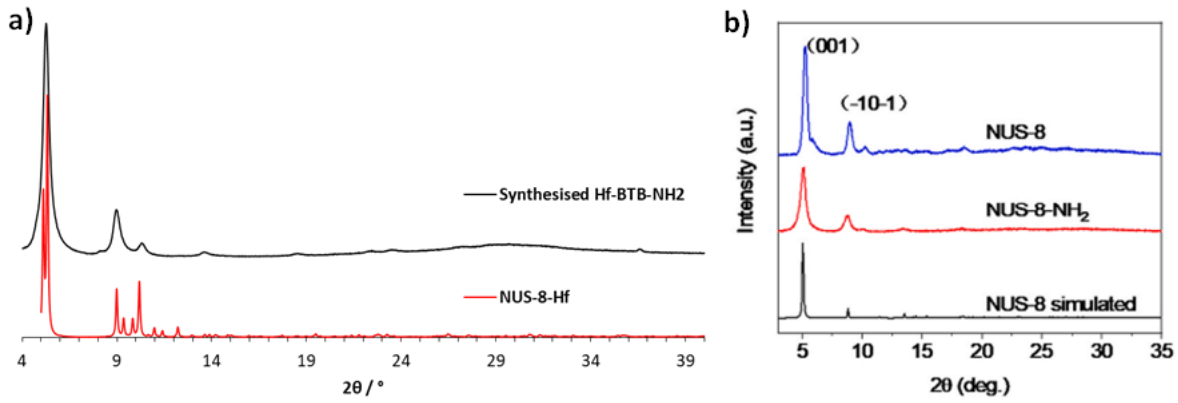

Figure S13: XRPD of synthesised Hf-BTB-NH_2 (black) with comparison to the pattern for NUS-8-Hf found in CCDC (1567189) (red). Insert of XRPD patterns of Zr-BTB-NH_2 (red) taken from paper by Pu *et al.*.[1]

ATR-IR

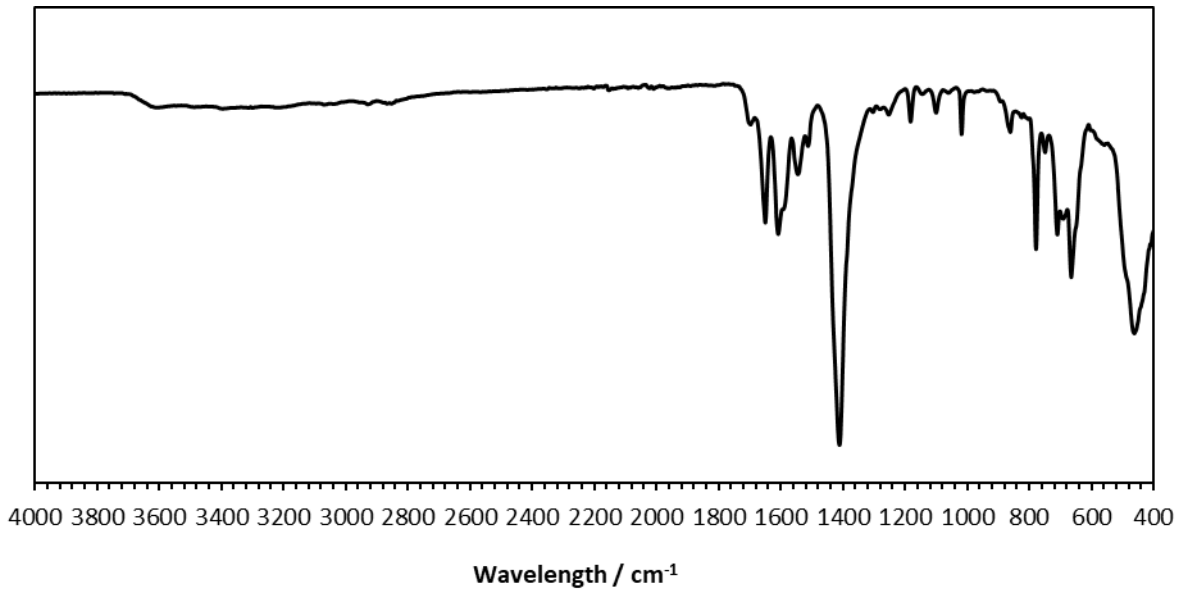

Figure S14: ATR-IR spectrum of Hf-BTB-NH_2

SEM

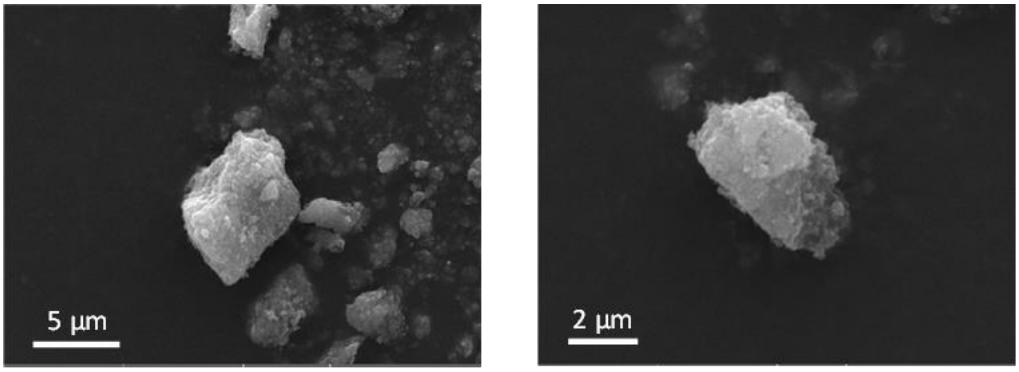

Figure S15: SEM of synthesised Hf-BTB-NH_2 bulk MOF

TGA

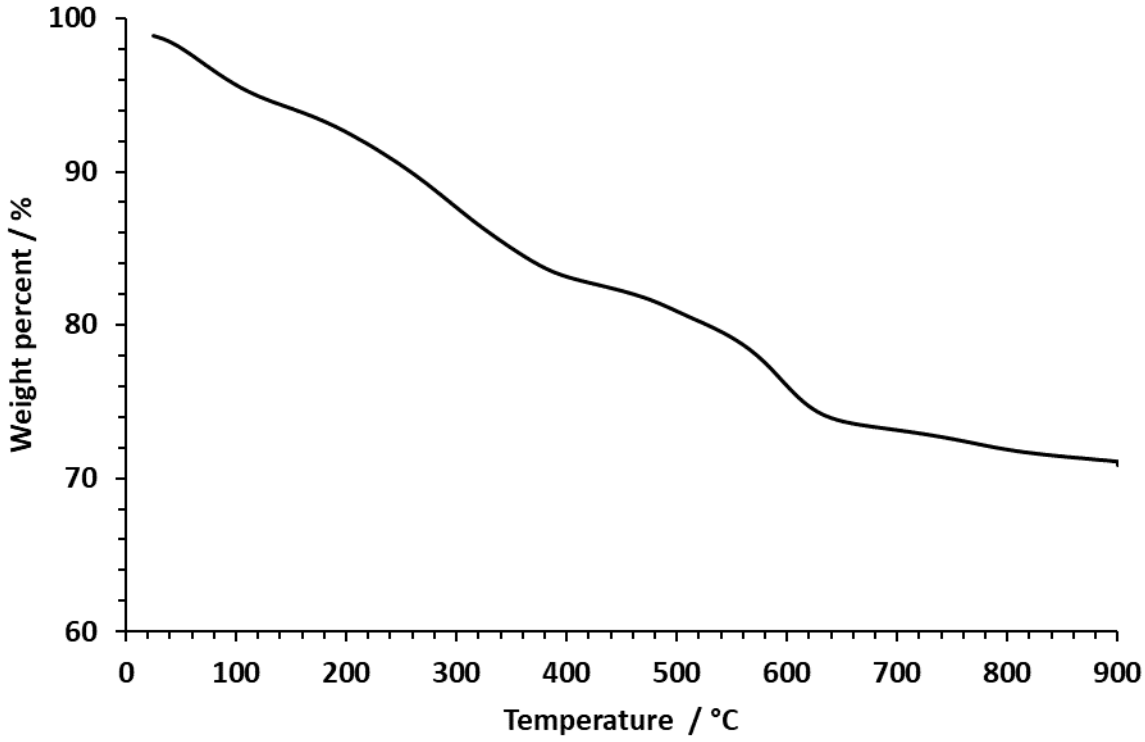

Figure S16: TGA plot for Hf-BTB-NH_2

4. MON Synthesis and Characterisation

4.1 Exfoliation of ZIF-7 and ZIF-7-NH_2 to access nanosheets

80 mg ZIF-7-III/ZIF-7-NH_2-III was ultrasonicated in 120 mL of a mixed solvent of methanol and n-propanol (1:1, v/v) at 80 KHz for 2 h to access nanosheets. After being centrifuged at 500 rpm for 5 min, the collected supernatant containing the nanosheets is the centrifuged at 12,000 30mins.

4.2 Exfoliation of Hf-BTB-NH_2 to access nanosheets

6 mg Hf-BTB-NH_2 was ultrasonicated in mL of water at 37 KHz for 12 h to access nanosheets. To prevent the stacking of the MON layers, Hf-BTB-NH_2 was kept in ethanol until needed for further studies.

4.3 Characterisation of ZIF-7, ZIF-7-NH_2 and Hf-BTB-NH_2 nanosheets

Tyndall Scattering

Figure S17: Tyndall scattering image of suspensions of ZIF-7, ZIF-7-NH_2 and Hf-BTB-NH_2

Atomic Force Microscopy

ZIF-7

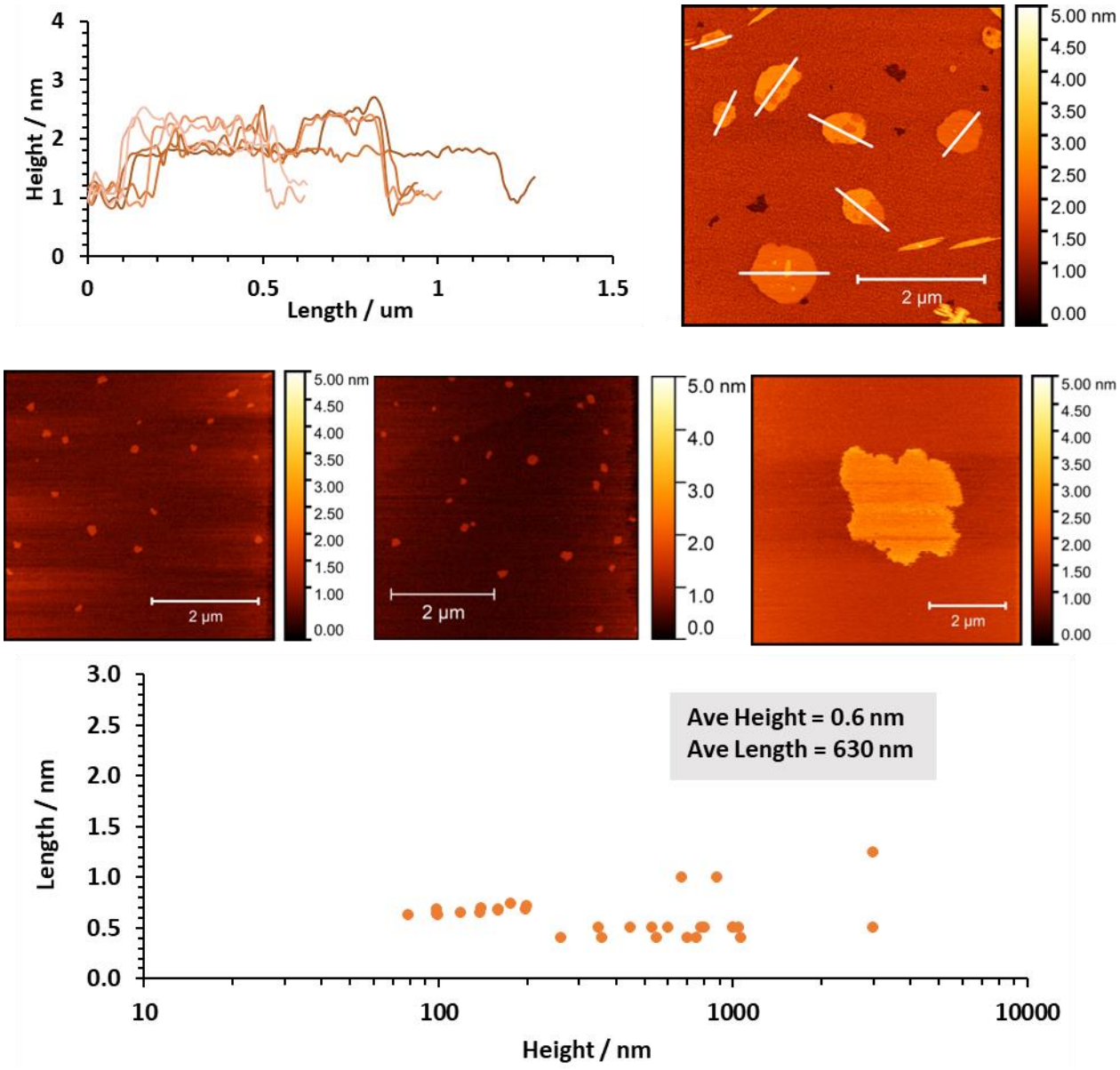

Figure S18: AFM images and associated height profiles of ZIF-7 nanosheets

ZIF-7-NH_2

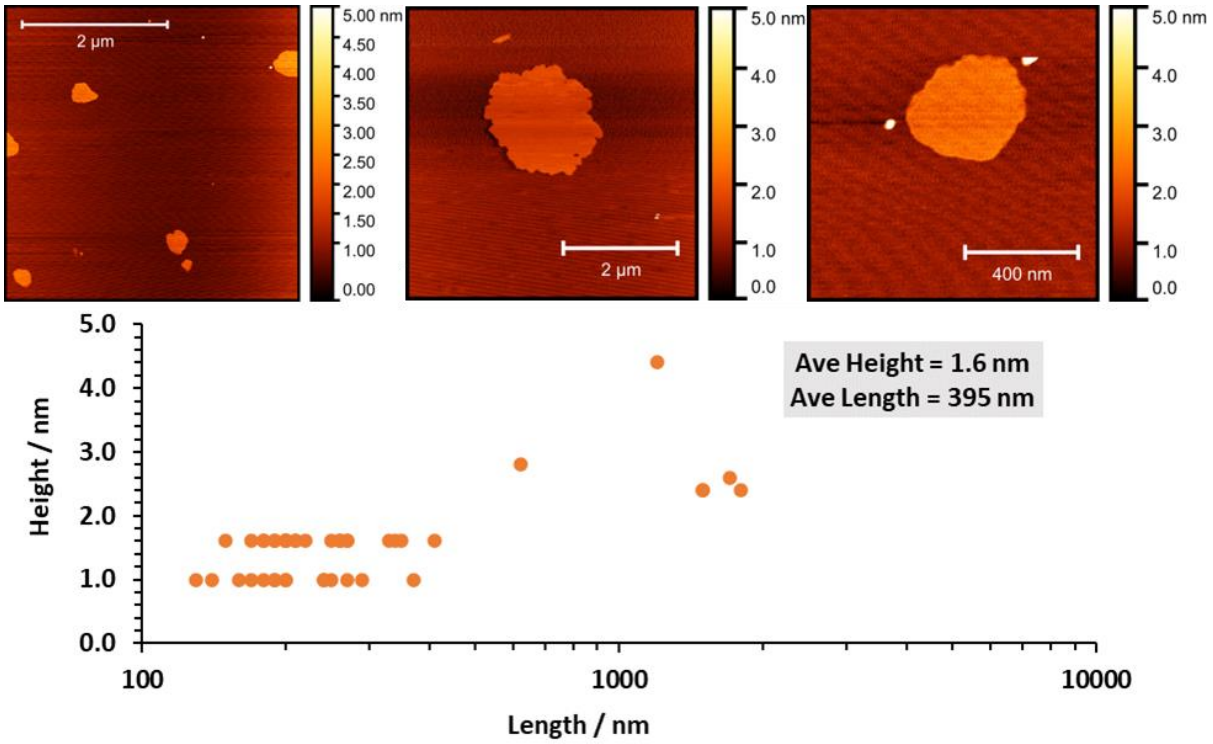

Figure S19: AFM images and associated height profiles of ZIF-7-NH_2 nanosheets

Hf-BTB-NH_2

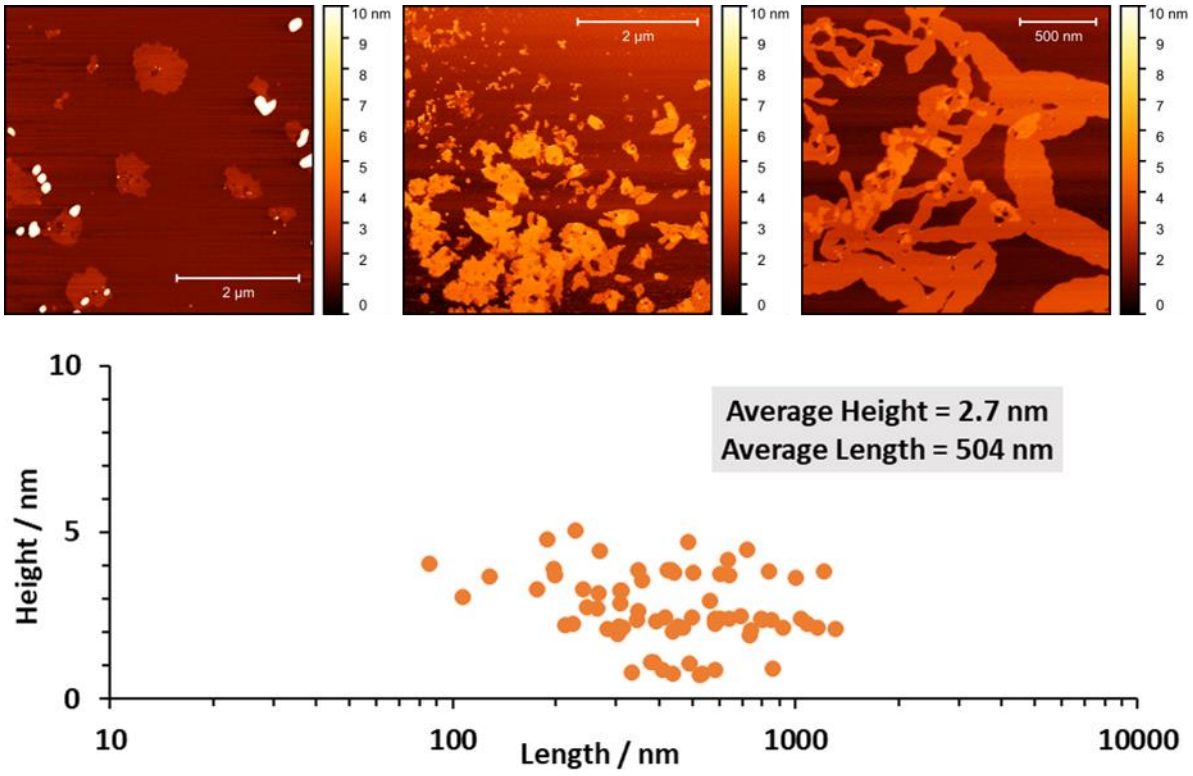

Figure S20: AFM images and associated height profiles of Hf-BTB-NH_2 nanosheets

Dynamic Light Scattering

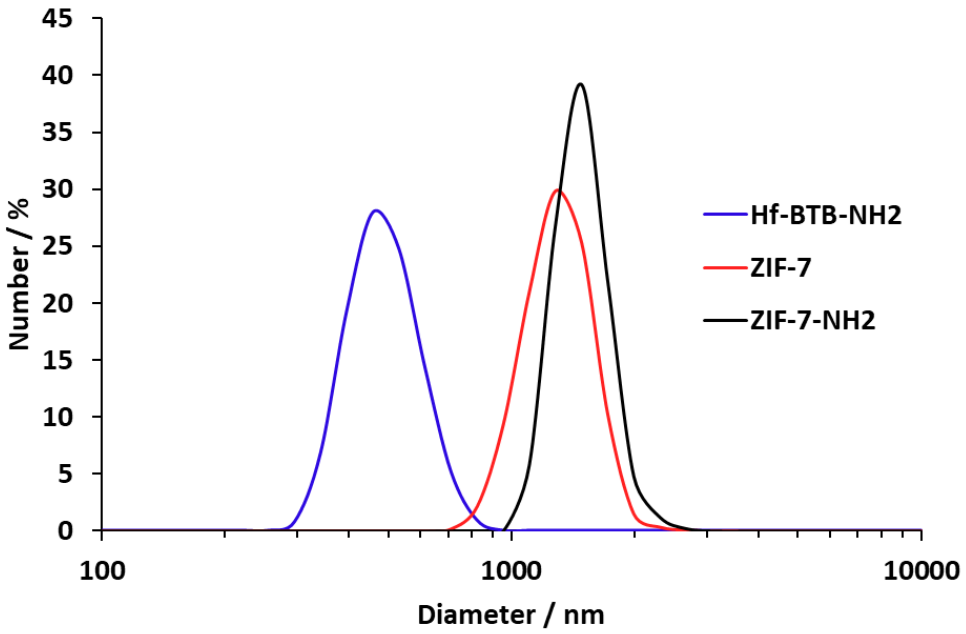

Figure S21: DLS number plot for MON suspensions of ZIF-7 (red) and ZIF-7-NH_2 (black) in methanol and Hf-BTB-NH_2 in ethanol.

Zeta Potential

Table S1: Zeta potential data obtained using the Smoluchowski method.

Sample Name	Temperature (°C)	Zeta Potential (mV)	Zeta Deviation (mV)	Mobility (µmcm/Vs)	Conductivity (mS/cm)
ZIF-7 1	20	-28.8	8.3	-2.043	0.206
ZIF-7 2	20	-30.5	7.47	-2.161	0.206
ZIF-7 3	20	-30.9	9.29	-2.194	0.207
	20	**-30.1**	**8.35**	**-2.13**	**0.21**
ZIF-7-NH_2 1	20.1	2.22	6.09	0.1574	0.246
ZIF-7-NH_2 2	20	2.51	6.05	0.1778	0.247
ZIF-7-NH_2 3	20	2.11	3.88	0.1493	0.248
	20	**2.3**	**5.34**	**0.16**	**0.25**
Hf-BTB-NH_2 1	20	-36.9	7.95	-2.615	0.231
Hf-BTB-NH_2 2	20	-37.2	7.04	-2.636	0.234
Hf-BTB-NH_2 3	20	-36.7	6.43	-2.605	0.236
	20	**-36.9**	**7.14**	**-2.62**	**0.23**

Contact Angle

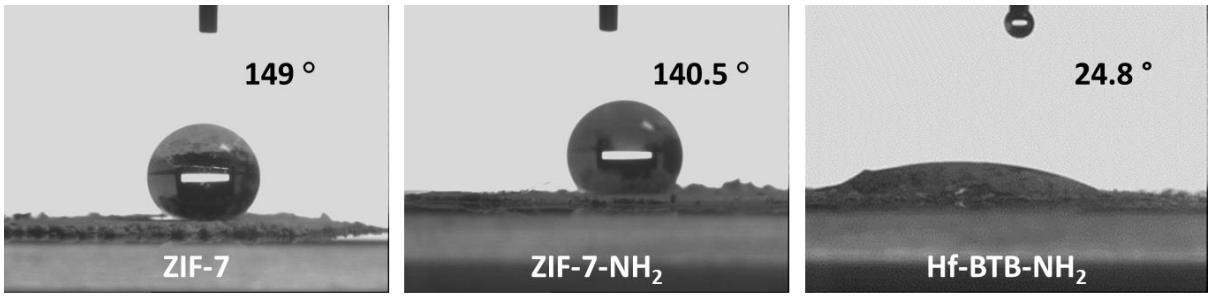

Figure S22: Contact angle data for ZIF-7, ZIF-7-NH_2 and Hf-BTB-NH_2.

PBS Stability Test

XRPD

ZIF-7

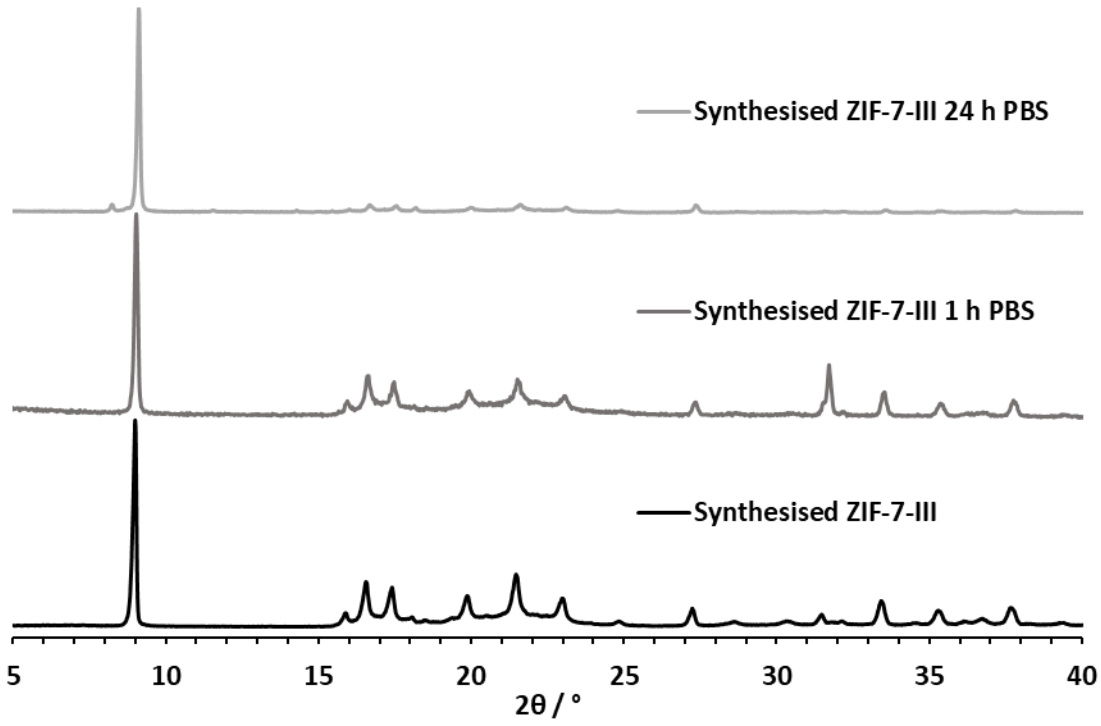

Figure S23: XRPD pattern of ZIF-7-III before (black) and after (grey) exposure to PBS for 1 h and 24 h.

ZIF-7-NH_2

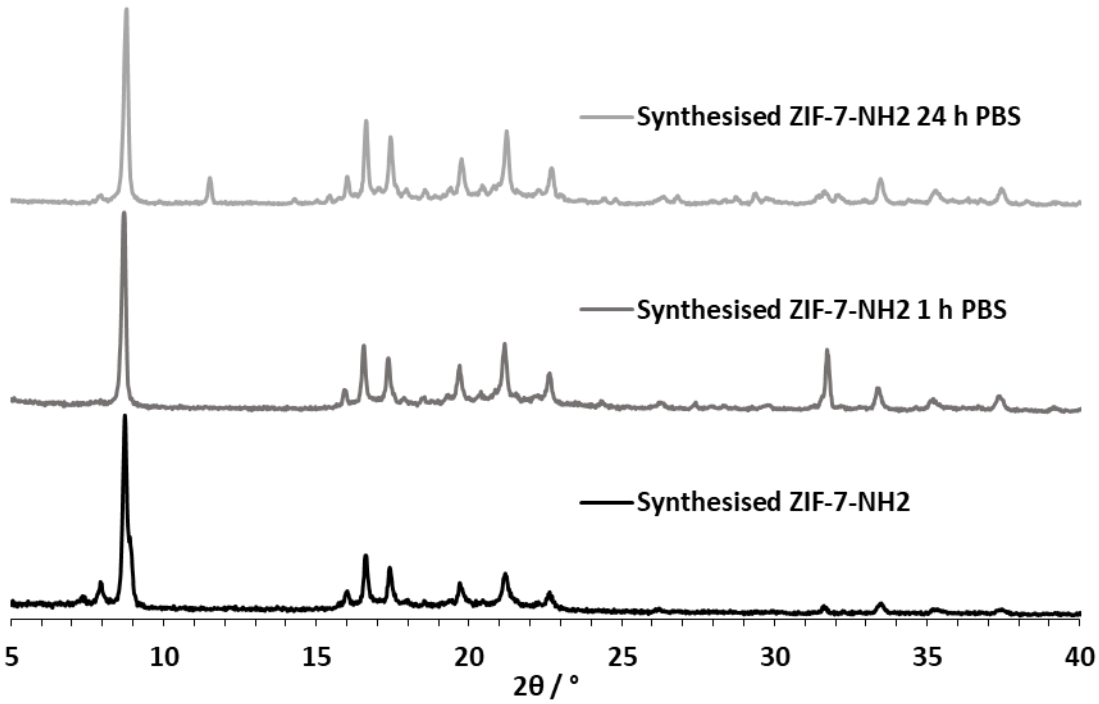

Figure S24: XRPD pattern of ZIF-7-NH_2 before (black) and after (grey) incubation with PBS for 1 h and 24 h.

Hf-BTB-NH_2

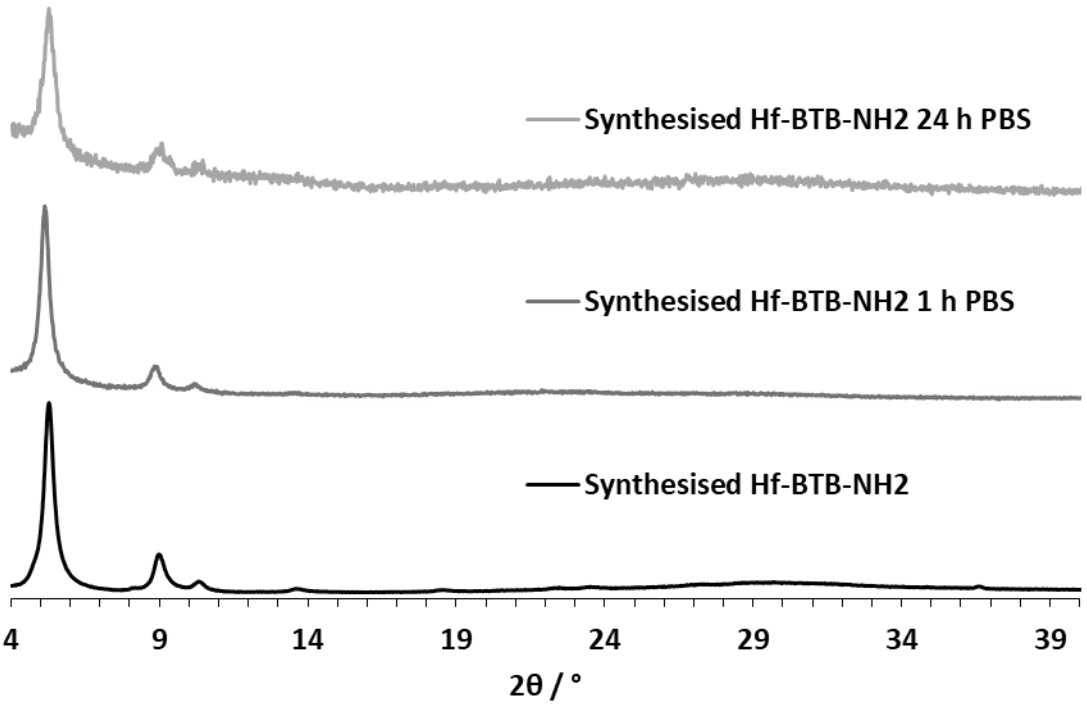

Figure S25: XRPD pattern of Hf-BTB-NH_2 before (black) and after (grey) incubation with PBS for 1h and 24 h.

AFM after PBS incubation

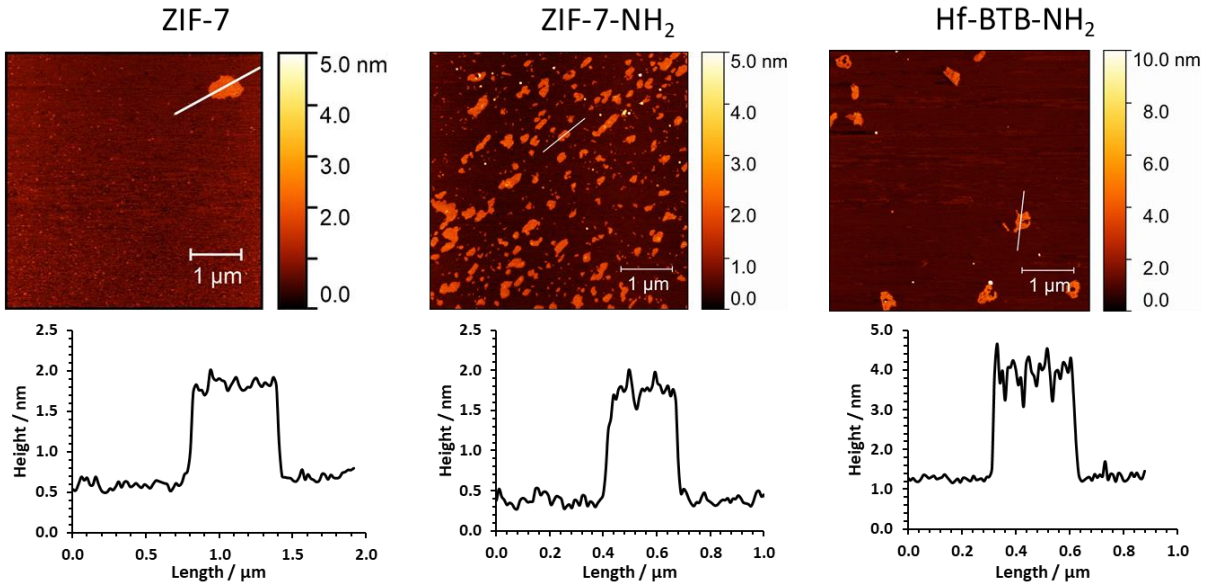

Figure S26: AFM images and height profile of nanosheets of each system after incubation in PBS for 1 h.

pH Stability Test

ZIF-7

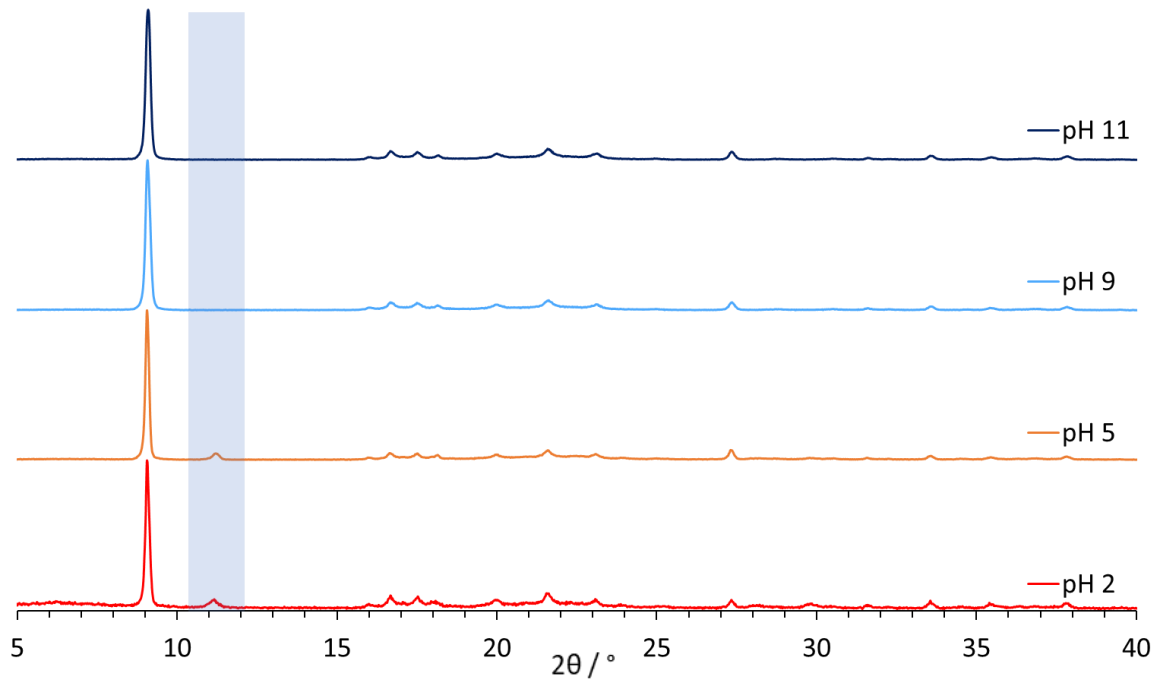

Figure S27: XRPD of ZIF-7 after incubation in aqueous solutions at different pHs

ZIF-7-NH_2

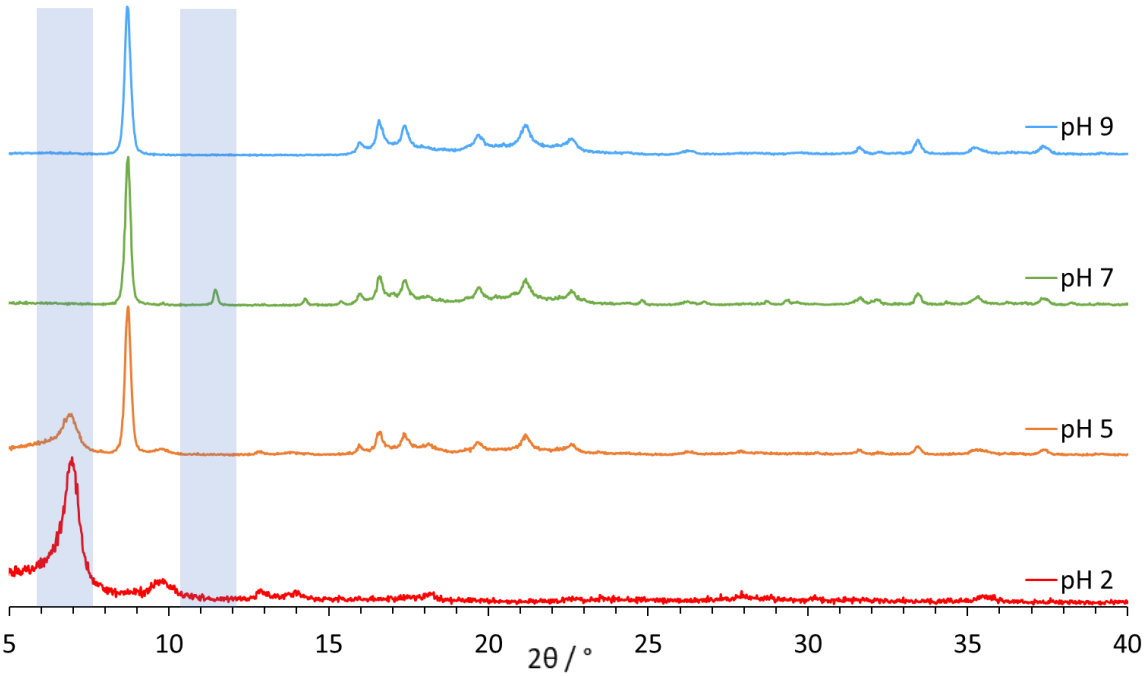

Figure S28: XRPD of ZIF-7-NH_2 after incubation in aqueous solutions at different pHs

Hf-BTB-NH_2

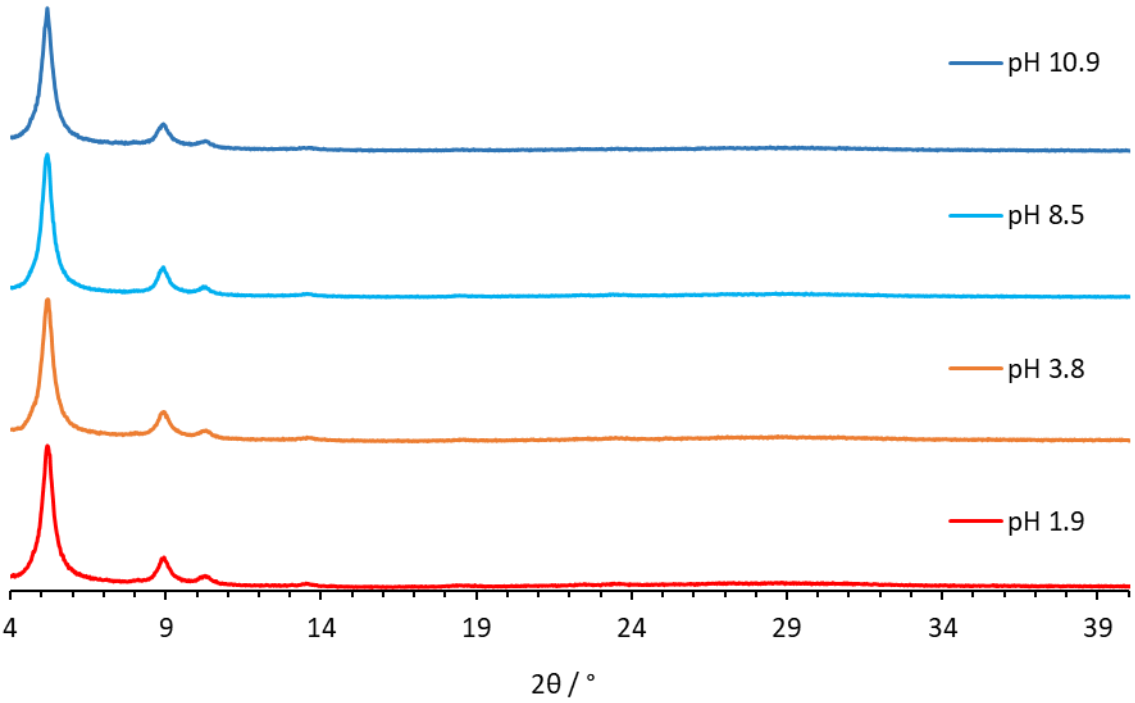

Figure S29: XRPD of Hf-BTB-NH_2 after incubation in aqueous solutions at different pHs

5. Phage Display

5.1 Binding studies

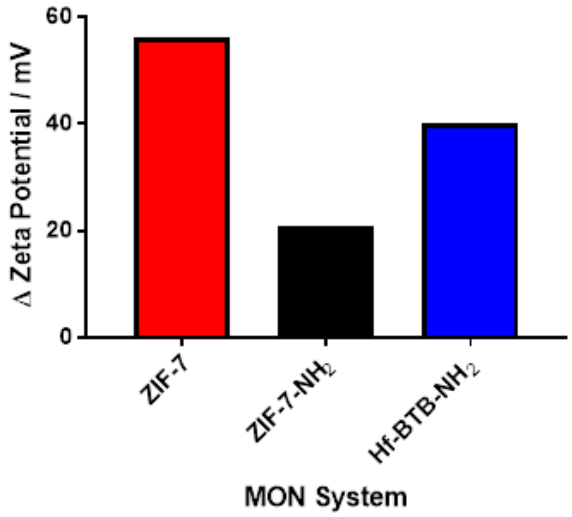

Figure S30: Change in Zeta Potential for each MON system on incubation with their phage display identified peptide (YNYRNLL - ZIF-7, NNWWAPA – ZIF-7-NH_2, FTVRDLS – Hf-BTB-NH_2)

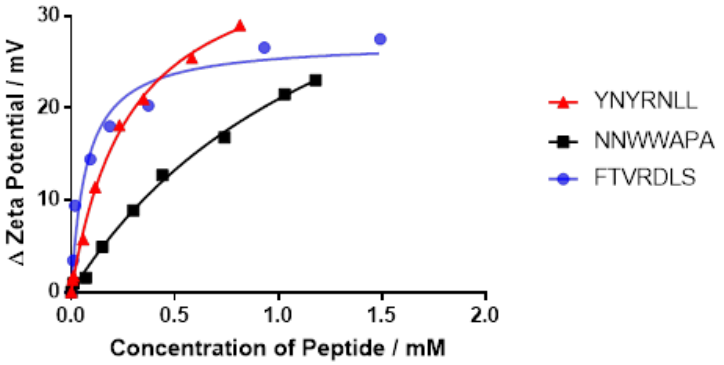

Figure S31: Zeta potential change when Hf-BTB-NH_2 is incubated with the peptides YNYRNLL (black), NNWWAPA (red) and FTVRDLS (blue)

Equation for Dissociation Constant – K_d: $Y = Bmax*X/(K_d + X)$

Bmax is the maximum specific binding, K_d is the ligand concentration needed to achieve a half-maximum binding at equilibrium.

5.2 Panning Round Data

Table S2: Panning round data for ZIF-7

MON System	Panning round	Peptide Binding Sequence (N'- C' amidated)	Peptide Isoelectric Point / pH	Predicted overall charge in PD
ZIF-7	3	YNYRNLL	10.15	+2
	1	TTFNLYP	9.53	+1
	1	LTNHIDM	7.81	+0.1
	1	GSWEHTT	7.81	+0.1
	1	TAKPIRE	11.39	+2
	1	SERLRTT	12.1	+2
	1	KVIELFS	9.91	+1
	1	EQLAVPL	6.87	+0
	1	MLPRQMT	14	+2
	1	WTRTVAN	14	+2

Table S3: Panning round data for ZIF-7-NH_2

MON System	Panning round	Peptide Binding Sequence (N'- C' amidated)	Peptide Isoelectric Point / pH	Predicted overall charge in PD
ZIF-7-NH_2	3	NNWWAPA	14	+1
	1	KMIDAFR	11.39	+2
	1	MRDHNLK	11.39	+2.1
	1	LWNPPNI	14	+1
	1	GSTMPIT	14	+1
	1	WIQQPFR	14	+2
	1	HAIFASN	14	+1.1
	1	SSPLGMA	14	+1

5.3 Isoelectric point calculations

The net charge (*Z*) of a peptide at a certain pH can be estimated by calculating:

$$Z = \sum_i N_i \frac{10^{pKa_i}}{10^{pH} + 10^{pKa_i}} - \sum_j N_i \frac{10^{pKa_j}}{10^{pH} + 10^{pKa_j}}$$

where N_i are the number, and pKa_i the pKa values, of the N-terminus and the side chains of Arginine, Lysine, and Histidine. The j-index pertain to the C-terminus and the Aspartic Acid, Glutamic Acid, Cysteine, Tyrosine amino acids.

6. References

(1) Pu, Y.; Yang, Z.; Wee, V.; Wu, Z.; Jiang, Z.; Zhao, D. Amino-Functionalized NUS-8 Nanosheets as Fillers in PIM-1 Mixed Matrix Membranes for CO2 Separations. *J. Memb. Sci.* **2022**, *641*, 376–7388. https://doi.org/10.1016/j.memsci.2021.119912.

Chapter 4:

Covalent Post-Synthetic Functionalisation of Metal-Organic Nanosheets

4.1 Introduction and Aims

The covalent post-synthetic functionalisation (PSF) of amine functionalised metal-organic materials is well documented due to the breadth of organic reactions in which aromatic amines can participate.[1,2] Chemical property tuning has been achieved following the modification of aromatic amine linkers with various electrophiles including carboxylic acids, anhydrides, isocyanates and isothiocyanates.[3–5]

This chapter explores using covalent PSF to incorporate biologically relevant binding sites onto the amine functionalised ZIF MONs discussed in chapter 2 (ZIF-7-NH_2 and ZIF-9-NH_2). Work carried out by Bonnefoy *et al*. demonstrated the functionalisation of a variety of amine functionalised MOFs (Al-MIL-101-NH_2, In-MIL-68-NH_2 and Zr-UiO-66-NH_2) with Boc (tert-butyloxycarbonyl)-protected amino acids and short peptides using microwave irradiation, a coupling agent and base (Figure 4.1).[6] The coupling agents were bromotripyrrolidinophosphonium hexafluorophosphate (PyBrOP), chlorotripyrrolidinophos-phonium hexafluorophosphate (PyClOP), and 2-chloro-N-methylpyridinium iodide, known as the Mukaiyama coupling agent combined with a base such as *N,N*-dimethylaminopyridine (DMAP) or *N,N*-diisopropylethylamine (DIPEA). The results showed vast improvements to functionalisation yields using microwave irradiation over traditional hot-plate heating. This approach to functionalisation required some optimisation of conditions for each type of small molecule attachment.

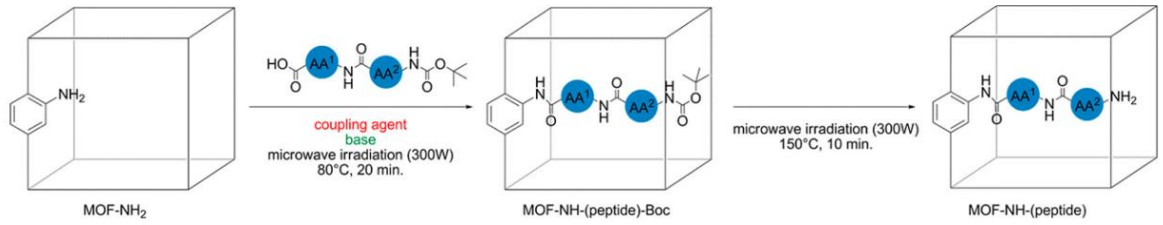

Figure 4.1: Reaction scheme adopted by Bonnefoy et al. for the PSF of various MOF-NH_2 with boc-protected amino acids and peptides. Figure adapted from reference 6.

Another approach to the amino acid functionalisation of MOF-NH_2 involving the coupling agent 2-(1H-benzotriazol-1-yl)-1,1,3,3-tetramethyluronium hexafluorophosphate (HBTU) and DIPEA was taken by Fracaroli *et al.* (Figure 4.2).[7] Through several consecutive steps, the authors were able to produce peptide functionalised MOFs at room temperature, demonstrating the scope of PSF for functionalising the surface of metal-organic materials with biomolecules. Also relevant to the work in this chapter was the functionalisation of ZIF-UC-6 demonstrated by Bumstead *et al.*.[8] The MOF glass incorporated bim-NH_2 as a linker component and was post-synthetically modified with octyl isocyanate. Demonstrating that even at low amine content (9 % of linkers) PSF can have a huge influence on surface properties such as hydrophobicity.

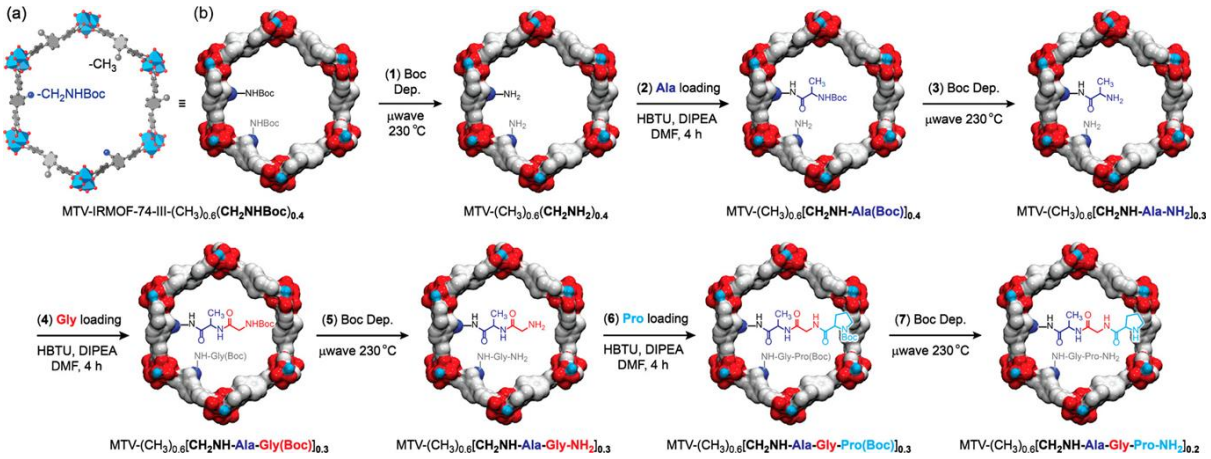

Figure 4.2: A scheme to show seven post-synthetic reactions to achieve enzyme-like complexity in the pores of MTV-IRMOF-74-III. Figure adapted from reference 7.

Whilst the majority of examples of covalent PSF involve MOFs, there are also some pertaining to their 2D counterpart's metal-organic nanosheets. The Foster Group published the first example of covalent PSF of MONs using 1,3-propanesultone to functionalise Cu-paddlewheel systems. Functionalisation was found to enhance top-down exfoliation into monolayer nanosheets as a result of disruption to interlayer interactions.[9] Since then click chemistry functionalisation has allowed a diverse array of surface chemistries to be introduced to the same MONs post-exfoliation.[10] Increased functionalisation was observed after exfoliation of the layered MOF due to the accessibility of binding sites. The only other example of covalent functionalisation of MONs was demonstrated by Ling *et al.* where the functionalisation of a Zr-BTB-NH_2 MON with isothiocyanate based fluorescent compounds introduced pH-sensitivity to the MON surface.[11] To the best of our knowledge, there are no examples of the covalent PSF of ZIF MONs.

In considering potential routes to the covalent attachment of amino acids to ZIF-7-NH_2 and ZIF-9-NH_2 MONs, it was important to consider the possible outcomes, including the undesirable (Figure 4.3). Due to the diatopic nature of amino acids, peptide bond formation between aromatic amine of the MON linker and carboxylic acid of the amino acid may not be the only reaction taking place. Polymerisation of the amino acid may occur either separately from the MON or on the MON itself (MON-NH-Poly-AA). With this in mind, an amine-protecting group was utilized, as is common within MOF PSF literature, to direct the desired functionalisation.[7,12] Tert-butyloxycarbonyl (Boc) was selected as the N-protecting group due to its thermolability, producing carbon dioxide and isobutene at temperatures above 110 °C.[13,14] Such properties, allows for its removal without the use of acids that could possibly degrade the MON, particularly the ZIF-based nanosheets.

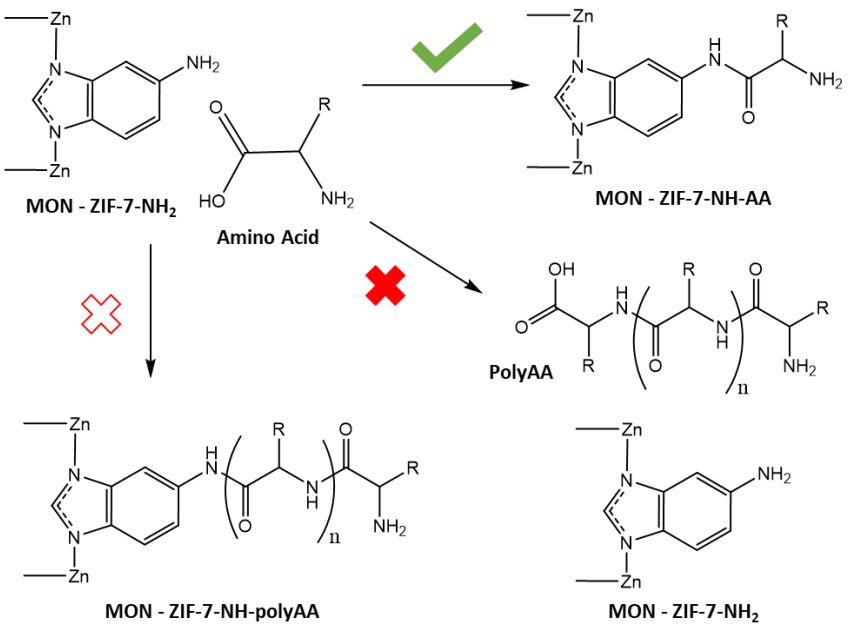

Figure 4.3: A simplified scheme to show potential amino acid functionalisation routes of an amine functionalised MON with using ZIF-7-NH_2 as an example.

The aim for this chapter is to establish routes to the covalent functionalisation of the amino functionalised ZIF-7-NH_2 and ZIF-9-NH_2 with amino acids in order to build a library of synthetic biomolecular recognition surfaces. The focus for this work is single residue functionalisation of the amine binding sites on previously synthesised MONs ZIF-7-NH_2 and ZIF-9-NH_2 (chapter 2). Exact positioning of specific sequences of amino acids results in the high degrees of biomolecular selectivity found in nature. Inspired by this, we hope to probe whether the periodic arrangement of binding sites on a MON can be manipulated to produce increasingly selective biointerfaces. Several different approaches will be investigated based on different literature reports used for the amino acid functionalisation of MOFs. Firstly, PSF which utilises microwave irradiation will be employed to functionalise ZIF-7-NH_2 MONs. The same system will also undergo PSF which utilises the coupling agent HBTU. Finally, ZIF-7-NH_2 and ZIF-9-NH_2 will undergo PSF with maleic anhydride which will then be used as the binding site for a second PSF step for the addition of amino acids.

4.2 Results and Discussion

4.2.1 PSF of ZIF-7-NH_2 with amino acids using Microwave Irradiation

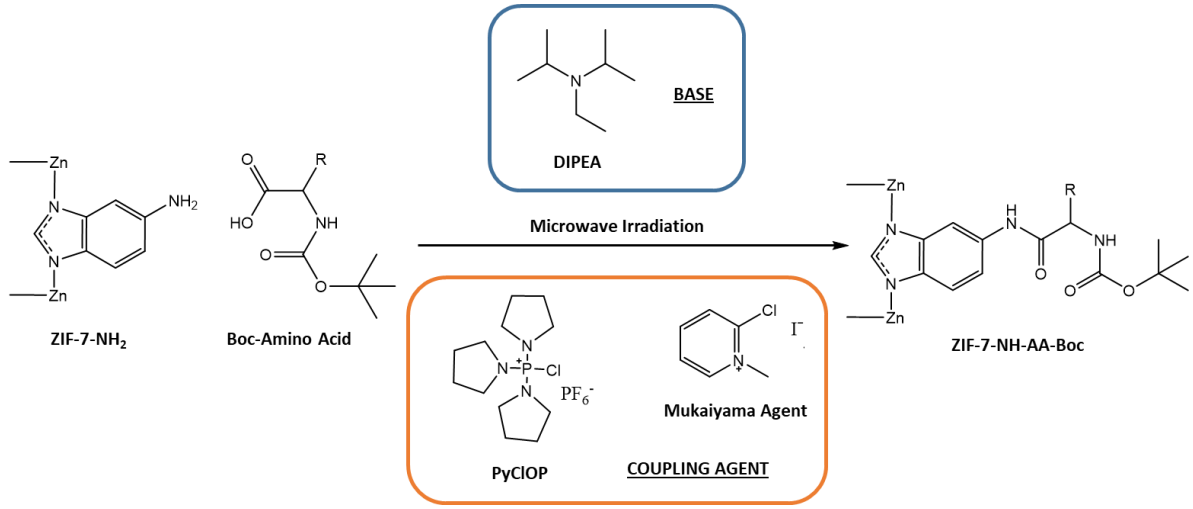

Figure 4.4: Reaction scheme for microwave irradiation based PSF for the functionalisation of ZIF-7-NH_2 nanosheets with boc-protected amino acids.

Initial attempts were made to covalently attach amino acids to ZIF-7-NH_2 via microwave-assisted PSF as shown schematically in Figure 4.4. This method was based on work performed by Bonnefoy *et al.* where different amine functionalised MOFs (Al-MIL-101-NH_2, In-MIL-68-NH_2 and Zr-UiO-66-NH_2) were incubated with coupling agent (0.45 mmol), base (0.6 mmol) and amino acid/peptides (0.45 mmol), microwave irradiation (300 W, 80 °C, 20 mins) in dichloromethane (DCM) was used to produce functionalised MOFs.[12] In this work, the optimisation of reaction conditions was required to determine the appropriate coupling agent and base combination as well as the molar ratios for the different amino acids. Boc-protecting groups on the amino acids were used, following the previous work., to prevent polymerization as the amino groups of ZIF-7-NH_2 have low nucleophilicity.[12] The density of the 3D layered ZIF-7-NH_2 MOFs meant it was difficult for reagents to pass through the pores (0.21 nm) and therefore after a few unsuccessful attempts exfoliated 2D MONs were used as the starting material to increase accessibility of the amine binding groups.[15]

ZIF-7-NH_2 MONs were successfully functionalised with Boc-Val-OH using PyCloP (Figure 4.4) as the coupling agent and DIPEA as the base in dichloromethane (DCM). A summary of the PyCloP experiments is shown in Table 4.1 with the conditions resulting in successful covalent attachment highlighted in green. The PSF of ZIF-7-NH_2 MONs with Boc-Val-OH was achieved upon doubling the reaction time (40 mins) and increasing the molar ratio of reagents to 20:40:20:1 (coupling agent : base : amino acid : MON-NH_2, CA:B:AA:NH_2).[6] The XRPD pattern (Figure 4.5Figure 4.1) of the resulting material (ZIF-7-NH-Val-Boc) showed that the crystal structure of the MONs was retained.

Table 4.1: Summary of experimental conditions for the covalent attachment of amino acids using PyClOP and microwave irradiation. Conditions that destroyed the MONs are highlighted in red and the conditions resulting in successful PSF are highlighted in green.

Amino Acid	Material	Method	Coupling Agent	Time / mins	Mol Equivalents			
					Coupling Agent	Base	Amino Acid	(MON-) NH_2
Boc-Valine-1	MON	Microwave	PyCloP	20	10	20	10	1
Boc-Valine-2	MON	Microwave	PyCloP	40	10	20	10	1
Boc-Valine-3	MON	Microwave	PyCloP	20	20	20	10	1
Boc-Valine-4	MON	Microwave	PyCloP	60	40	40	40	1
Boc-Valine-5	MON	Microwave	PyCloP	40	20	40	20	1
Boc-Valine-6	MON	Microwave	PyCloP	20	40	40	40	1
Boc-Valine-5B	MON	Microwave	PyCloP	40	20	40	20	1
Boc-Valine-5C	MOF	Microwave	PyCloP	40	20	40	20	1
Boc-Glycine-1	MON	Microwave	PyCloP	40	20	40	20	1
Boc-Alanine-1	MON	Microwave	PyCloP	20	20	40	20	1
Boc-Proline-1	MON	Microwave	PyCloP	40	20	40	20	1

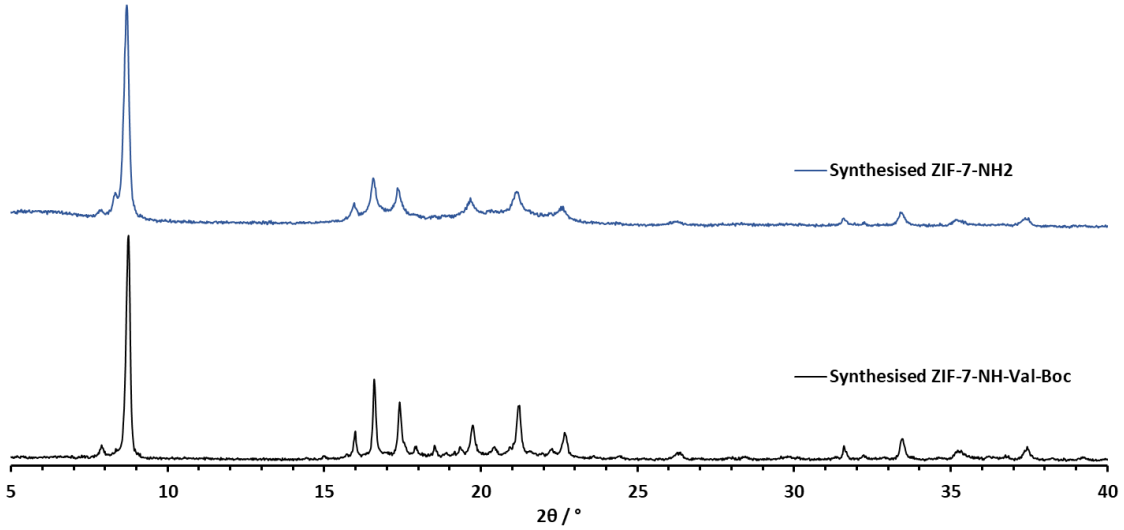

Figure 4.5: XRPD pattern of synthesised ZIF-7-NH_2 and ZIF-7-NH-Boc-Val nanosheets using PyClOP and microwave irradiation as the amino acid coupling mechanism.

The downfield section of ^{1}H NMR spectrum showed 60 % functionalisation of bim-NH_2 and 24 % of total linkers was achieved (Figure 4.6a). This is consistent with the work carried out by Bonnefoy *et al.* where 5-60 % functionalisation was reported.[12] Due to the presence of two new imidazole environments along with new phenyl peaks, it was predicted that a mixture of bim-NH-Val and bim-NH-Val-Boc was formed where partial Boc deprotection had occurred. This was corroborated with mass spectrometry which showed a peak at $[M]^+$ = 333.2, corresponding to Bim-NH-Val-Boc. The digestion conditions required for solution state NMR of MONs (DCl, DMSO) could hydrolyse the boc-group. There is evidence of this in the upfield section (Figure 4.6b) of the NMR spectrum as the degradation by-products (tert-butyl alcohol – 1.11 ppm and isobutene – 1.76 ppm) appear. The region assigned to the iso-propyl group of valine (1.05-0.64 ppm) integrates to double that expected from the integrals of the imidazole peaks, indicating an excess of amino acid. There was some evidence of MON

degradation as the ratio of bim to bim analogues decreased from 1 : 0.36 in ZIF-7-NH_2 to 1 : 0.45 in ZIF-7-NH-Val-Boc. Whilst there is evidence of covalent functionalization, there are limitations to the confidence in the degree in which this occurred as there is excess residue present.

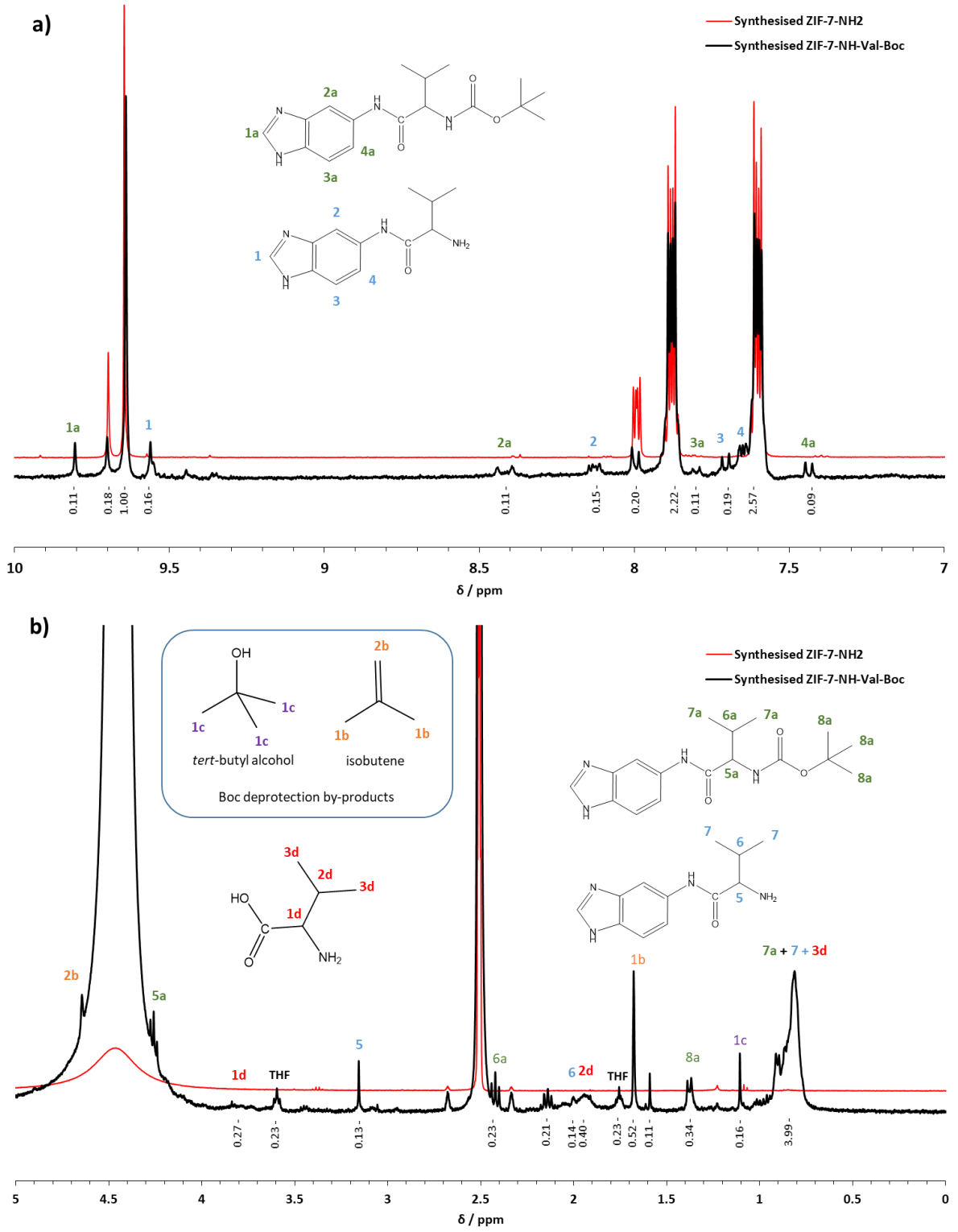

Figure 4.6: a) Downfield section (7-10 ppm) of ^{1}H NMR spectrum of synthesised ZIF-7-NH-Val-Boc compared to that of synthesised ZIF-7-NH_2, b) Upfield section (0-5 ppm) of of ^{1}H NMR spectrum of synthesised ZIF-7-NH-Val-Boc compared to that of synthesised ZIF-7-NH_2.

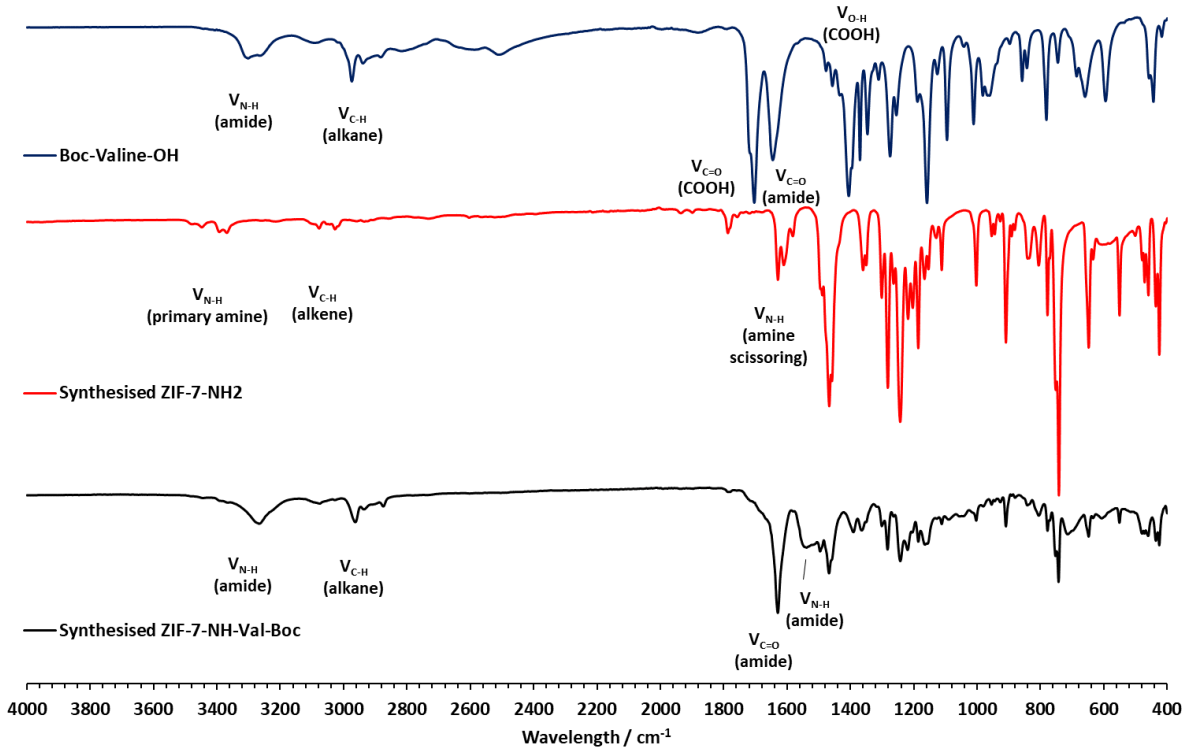

Figure 4.7: ATR-IR spectra of Boc-Val-OH (blue),synthesised ZIF-7-NH_2 (red) and synthesised ZIF-7-NH-Val-Boc (black).

The ATR-IR spectra (Figure 4.7) also indicated a clear difference between the synthesised ZIF-7-NH_2 and ZIF-7-NH-Val where an N-H secondary amide peak appears at 1539 cm^{-1} which doesn't appear on the spectra for Boc-Val-OH as well as a reduction in the amine peaks 3400-3600 cm^{-1}. The boc-protecting group introduces an amide group on the incoming amino acid therefore, it was not possible for successful PSF to be determined purely based on the appearance of an amide bond on the IR spectrum. The appearance of the characteristic secondary amide peak at 1500-1560 cm^{-1} (ν N-H) alongside a reduction in the amine peaks at 3100-3500 cm^{-1} was a positive indication of covalent attachment. As the material used for IR analysis had not undergone digestion it is predicted that there would be a larger presence of boc-protected amino acids (covalently attached or otherwise) therefore there would be a larger contribution of amide groups observed that for the NMR. Other peaks in the spectrum associated with the amino acid would appear with adsorbed residues that may not necessarily be covalently attached.

Attempts to increase the yield of functionalisation involved increasing the ratio of reagents further and increasing the reaction time. The material could withstand an excess up to 40 eq. of coupling agent before complete degradation with dissolution observed by loss of Tyndall scattering (Table 4.1 - Boc-Valine-4 and Boc-Valine-6). Three other amino acids (Boc-Gly-OH, Boc-Ala-OH and Boc-Pro-OH) were investigated using the same reaction conditions as for Boc-Valine-5 (Table 4.1) however, NMR, mass spectrometry (MS) and IR showed no evidence of functionalisation having taken place.

Bonnefoy *et al.* demonstrated that different systems worked well with different combinations of reagents, therefore another coupling agent was employed.[12] The Mukaiyama coupling agent (Figure 4.4) was also used along with DIPEA as the base in attempts at PSF of ZIF-7-NH_2 MONs with a range of residues and molar ratios of reagents but again there was no evidence of functionalisation according to NMR (Figure 4.19, experimental), MS and IR.

4.2.2 PSF of ZIF-7-NH_2 with amino acids using HBTU

Another approach to the covalent attachment of amino acids to the surface of MONs was the use of HBTU as a coupling agent following work carried out by Fracaroli *et al.* (Figure 4.8).[7] ZIF-7-NH_2 was incubated with different boc-AA-OH, HBTU (coupling agent) and DIPEA (base) in DMF overnight under ambient conditions and the resulting material was characterised by NMR, IR and MS. The ratio of reagents was again optimised where 20:40:20:1 molar equivalents of CA:B:AA:NH_2 resulted in a degree of functionalisation.

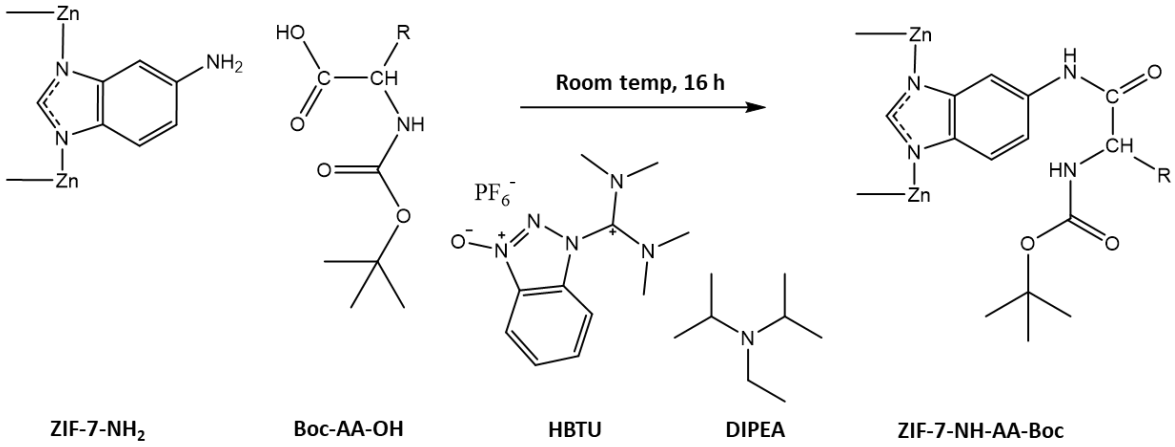

Figure 4.8: Reaction scheme for the functionalisation of ZIF-7-NH_2 nanosheets with boc-protected amino acids using HBTU.

The ^{1}H NMR spectra (Figure 4.9a) of the digested material also showed evidence of amino acid functionalised bim-NH_2 with new peaks appearing for the imidazolate hydrogen (~ 9.77 ppm) and around the aromatic region (~ 7.4 – 8.4 ppm). A closer look at the upfield region of the ^{1}H NMR spectra (Figure 4.9b) revealed the associated peaks for the corresponding amino acids (Gly, Ala and Val) as well as some evidence of the *tert*-butyl as a protecting group and *tert*-butyl alcohol. The degree of functionalisation was determined by ^{1}H NMR to be 35 % for ZIF-7-NH-Gly-Boc, 13.6 % for ZIF-7-NH-Ala-Boc and 13 % for ZIF-7-NH-Val-Boc with respect to the bim-NH_2 imidazolate aromatic peaks. The ATR-IR spectra for the synthesised ZIF-7-NH-Gly-Boc, ZIF-7-NH-Ala-Boc and ZIF-7-NH-Val-Boc all showed a new peak appearing at 1404 cm^{-1} which corresponds to the region for an sp^3 C-H vibration

(Figure 4.20 – Figure 4.22, experimental). Peaks at 3400-3600 cm^{-1}, assigned as aromatic amines, reduced in comparison to the synthesised ZIF-7-NH_2 MONs that indicated some successful attachment.

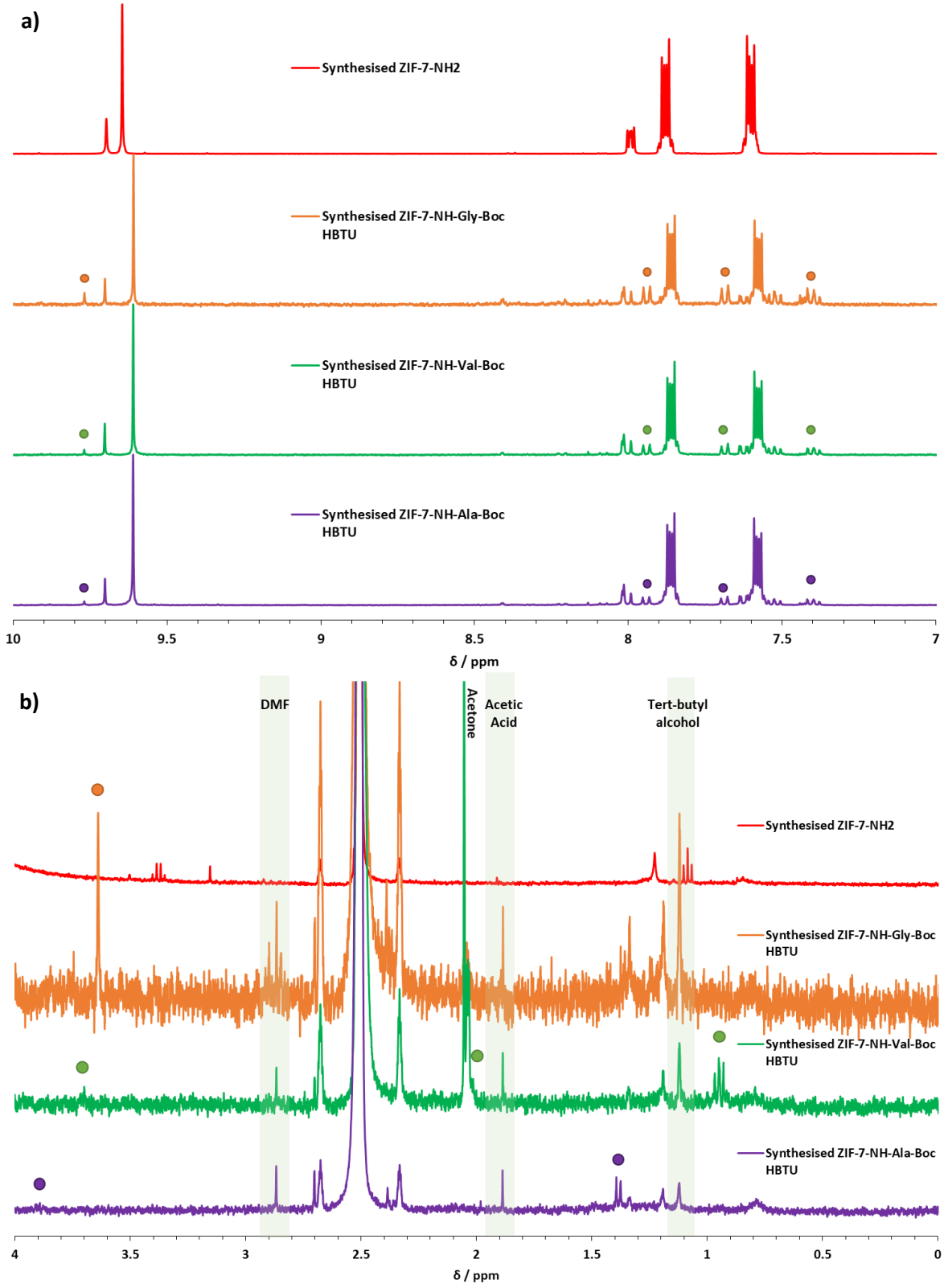

Figure 4.9: a) Downfield section (7-10 ppm) of the 1H NMR spectra of synthesised ZIF-7-NH_2 compared to synthesised ZIF-7-NH-Gly-Boc, ZIF-7-NH-Val-Boc and ZIF-7-NH-Ala-Boc using HBTU, b) upfield section (0-4 ppm) of the ^{1}H NMR spectra of synthesised ZIF-7-NH_2 compared to synthesised ZIF-7-NH-Gly-Boc, ZIF-7-NH-Val-Boc and ZIF-7-NH-Ala-Boc using HBTU.

As ZIF-7-NH_2 is a mixed linker system (20% amine functionality) a separate calculation revealed only 7.1 %, 2.5 % and 2.4 % of the total linkers existed as bim-NH-AA-Boc respectively. MS revealed that there was evidence of bim-NH-Gly formation with a peak at $[M]^+$ = 191.1 and bim-NH-Val formation with a peak at [M]+ = 235 but there was no evidence of bim-NH-Ala ($[M]^+$ = 205). Whilst this method seemed to demonstrate some success, it faces issues when calculating yields especially using a system that is only partially pre-synthetically functionalised with aromatic amines. For future attempts at PSF of ZIF-7-NH_2 we recommend using a primary amine group by introducing an alkyl spacer via 1H-benzimidazole-6-methanamine as suggested by Fracaroli *et al.* in order to increase the reactivity of the amine group sticking off the surface of the MON.[7]

4.2.3 A New Approach to the Covalent PSF of MONs with Amino Acids

In the previous attempts described above the coupling agents (PyClOP, Mukiayama, and HBTU) activated the residues through their carboxylate group in order to react with the amine functionalised MON. The following work describes functionalisation of the aromatic amines of ZIF-7-NH_2 and ZIF-9-NH_2 with maleic anhydride to introduce carboxylic acid functionalisation. We hypothesise that a surface functionalised with carboxylic acids can be activated using the coupling agents as described above to improve the likelihood of covalent PSF with amino acids. The following sections will first discuss the functionalisation of ZIF-7-NH_2 and ZIF-9-NH_2 with maleic anhydride and then attempts at amino acid PSF.

4.2.4 Maleic Anhydride

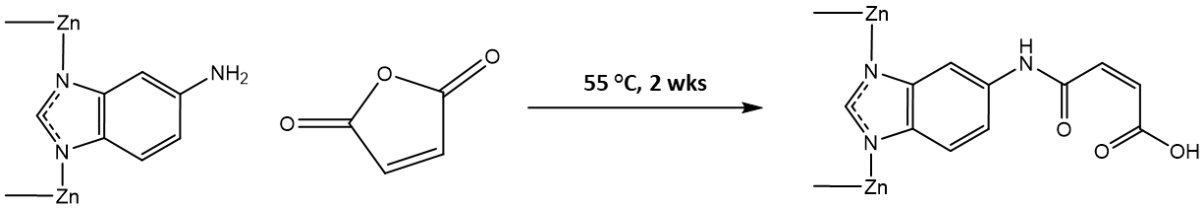

Figure 4.10: Schematic of the reaction of ZIF-7-NH_2 nanosheets with maleic anhydride.

The covalent attachment of maleic anhydride to the amine functionalised linkers within ZIF-7-NH_2 and ZIF-9-NH_2 unlocks a carboxylic acid group (Figure 4.10). The constrained ring of maleic anhydride makes it more reactive than amino acids therefore no additional reagents were required. The amide bond formed results in ring opening, introducing a new type of binding site to the material surface.

4.2.5 Post-Synthetic Functionalisation of ZIF-7-NH_2 with Maleic Anhydride

After the incubation of synthesised ZIF-7-NH_2 with maleic anhydride (MA) in chloroform the XRPD pattern of the resulting material revealed some changes in crystal structure (Figure 4.11). The major peak ~ 9 ° appeared to reduce in intensity and new peaks appeared at 10 ° and 18 °, indicating that the PSF resulted in some degradation of the crystalline material.

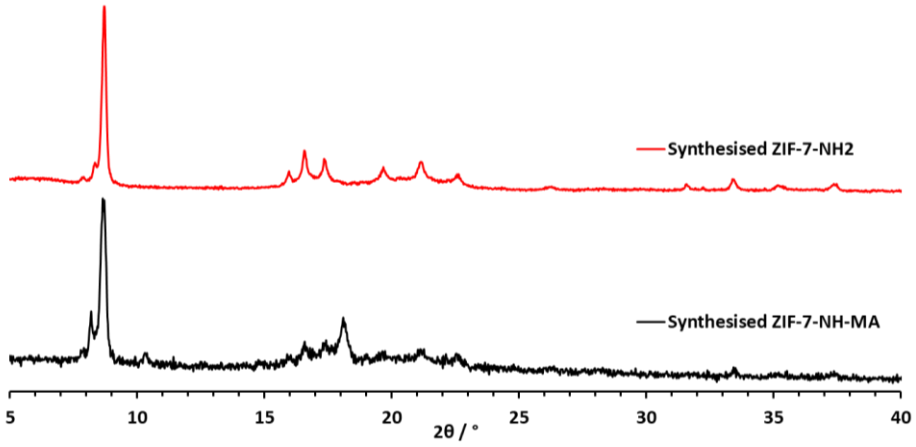

Figure 4.11: XRPD pattern of synthesised ZIF-7-NH_2-MA MONs compared to synthesised ZIF-7-NH_2 MONs.

To demonstrate successful PSF, ATR-IR (Figure 4.24, experimental) was used to indicate the presence of the carboxylic acid group and conversion of amine to amide. When comparing the IR spectra before and after the PSF there was a reduction in the peaks at 3400-3600 cm^{-1} which are associated with the amine groups indicating involvement in amide bond formation. A broad peak at 3000-3300 cm^{-1} indicated the presence of alcohol from the carboxylic acid. New peaks appeared at 1700 cm^{-1} for the carbonyl of the carboxylic acid and at 1560 cm^{-1} for the N-H bend of the amide.

^{1}H NMR was used to determine the presence of residual unreacted MA and the degree of functionalisation. Figure 4.12 shows the compared spectra of the resulting material after PSF and the two starting materials (ZIF-7-NH_2 and MA). The peak for MA did not appear on the synthesised ZIF-7-NH_2-MA spectrum and doublets appeared at 6.35 ppm and 6.60 ppm which correspond to the opened maleic anhydride. More aromatic peaks appeared in the region 7.5 – 8.4 ppm which could be assigned to the functionalised Bim-NH_2-MA. By comparing the integrals of the imidazolate hydrogens (1 and 1a) for Bim-NH_2-MA and Bim-NH_2 the level of functionalisation could be determined. 65 % of bim-NH_2 from the synthesised ZIF-7-NH_2 became functionalised with maleic anhydride. The overall formula for the material was determined to be $Zn_2(bim)_{2.9}(bim\text{-}NH_2)_{0.4}(bim\text{-}NH\text{-}MA)_{0.7}$.

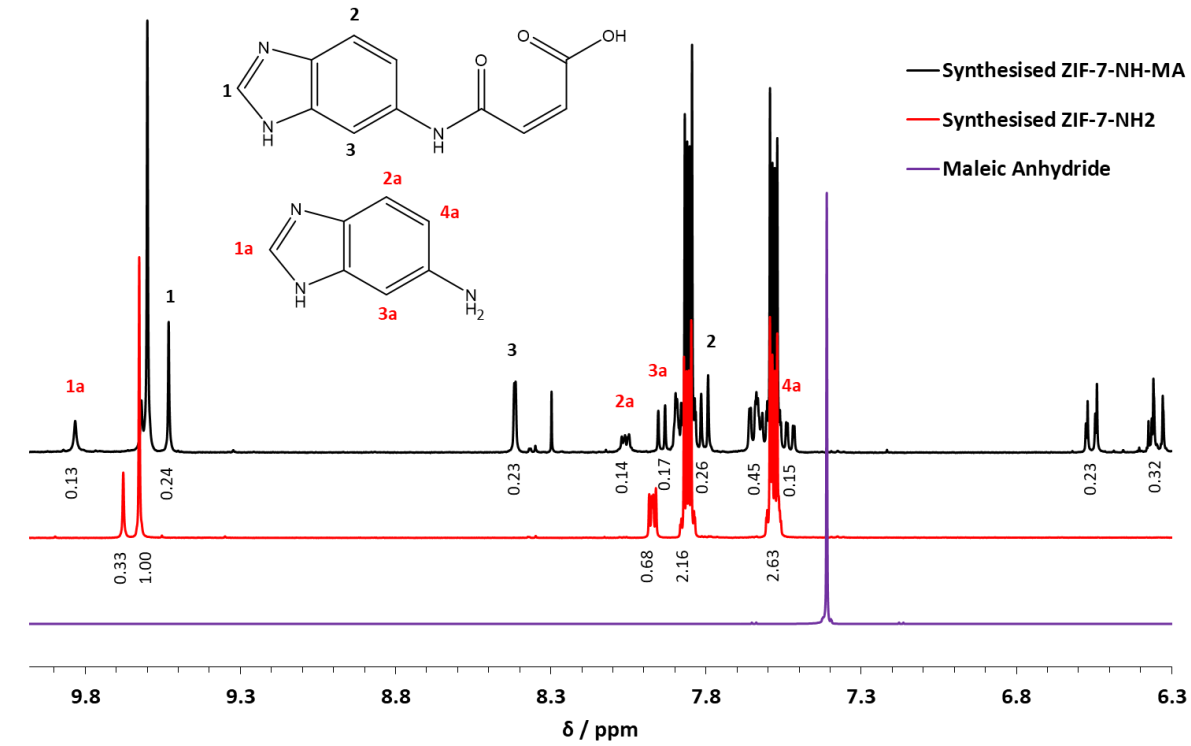

Figure 4.12: ^{1}H NMR spectra of maleic anhydride, synthesised ZIF-7-NH_2 and synthesised ZIF-7-NH_2-MA MONs.

Surface analysis revealed the extent to which MON hydrophobicity was altered by PSF with maleic anhydride. Contact angle measurements (Figure 4.13a+b) showed that hydrophobicity increased with angles measured at only 140.5 ° for ZIF-7-NH_2 but 153 ° for ZIF-7-NH-MA which is also larger than the angle for ZIF-7 (149 °). Interestingly the introduction of MA via PSF results in MONs that were more comparable in hydrophobicity to ZIF-7-CH_3 (154.9 °). This suggests that the alkene group was sterically hindering the carboxylate and may be introducing further hydrophobicity to the surface of the MON. The zeta potential measurements revealed that ZIF-7-NH-MA (-14.7 mV) had a significantly more negative surface than ZIF-7-NH_2 (7.7 mV) when in 1 mmol KCl solution, a good indication of the presence of carboxylate groups (Figure 4.13c).

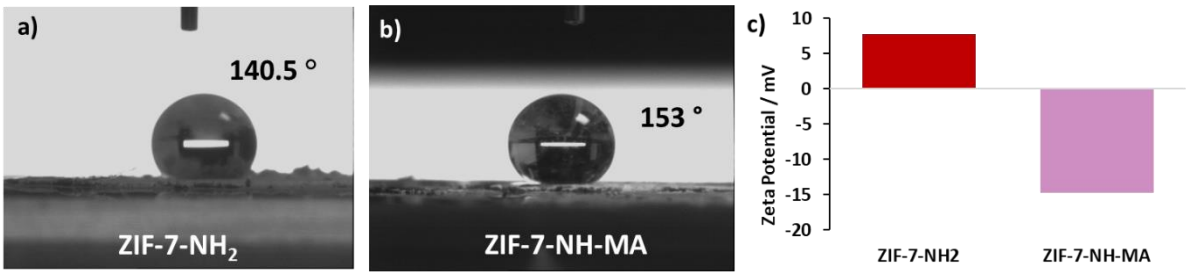

Figure 4.13: a) contact angle measurement of ZIF-7-NH_2 MONs, b) contact angle measurement of ZIF-7-NH-MA MONs and c) zeta potential measurements of synthesised ZIF-7-NH_2 and ZIF-7-NH-MA MONs.

4.2.6 Post-Synthetic Functionalisation of ZIF-9-NH_2 with Maleic Anhydride

The same method was used for the functionalisation of ZIF-9-NH_2 with maleic anhydride (MA). The XRPD pattern of the resulting material matched that of the unfunctionalized material suggesting crystallinity was maintained. The ATR-IR spectrum showed consistent changes in spectrum as observed for ZIF-7-NH_2-MA. Reduction in the in the peaks at 3400-3600 cm^{-1} which were associated with the amine groups of the linker and a broad peak alcohol peak appeared at 3000-3300 cm^{-1}. New peaks appeared at 1700 cm^{-1} which corresponds to the carbonyl of the carboxylic acid and at 1560 cm^{-1} for the N-H bend of the amide.

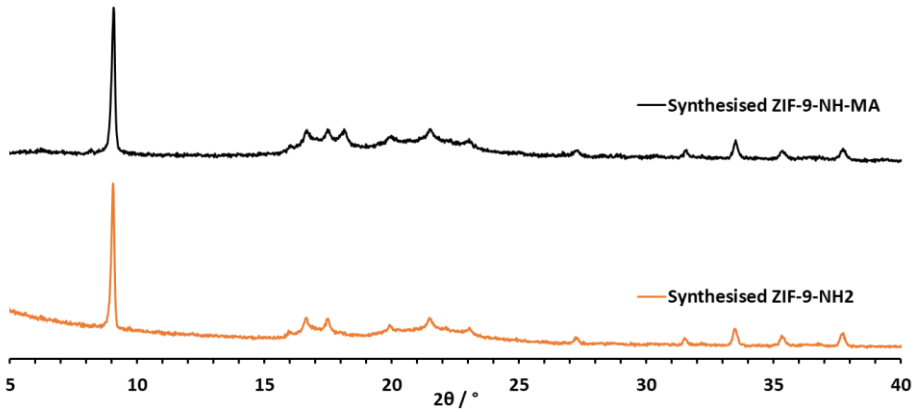

Figure 4.14: XRPD pattern of synthesised ZIF-9-NH_2-MA MONs compared to synthesised ZIF-9-NH_2 MONs.

The ^1H NMR spectrum of ZIF-9-NH_2-MA also showed the same changes with new peaks appearing at 6.35 ppm and 6.60 ppm for the new alkene C-H. Aromatic peaks appear in the region 7.5 – 8.4 ppm which can be assigned to the functionalised Bim-NH_2-MA. By comparing the ratio of the imidazole hydrogens, it was determined 53 % Bim-NH_2 became functionalised with maleic anhydride. The ratio of Bim-NH_2 and Bim-NH_2-MA to Bim increases after PSF indicating that there was some degradation and loss of material. The overall formula for the material was determined to be $Co_2(bim)_{2.5}(bim\text{-}NH_2)_{0.7}(bim\text{-}NH\text{-}MA)_{0.8}$.

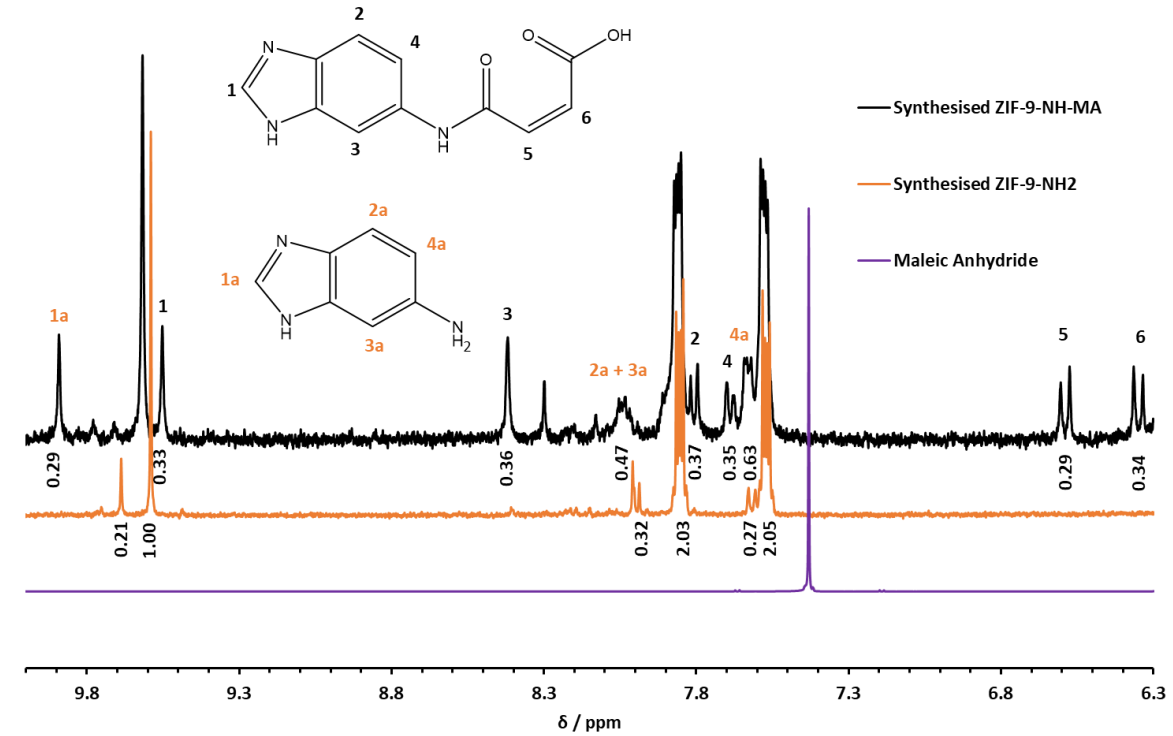

Figure 4.16: ^{1}H NMR spectra of maleic anhydride, synthesised ZIF-9-NH_2 MONs and synthesised ZIF-9-NH_2-MA MONs.

The surface properties of ZIF-9-NH-MA were also determined using contact angle and zeta potential measurements (Figure 4.15). The contact angle was determined to be 132.8 ° (Figure 4.15b) which is lower than ZIF-9 (145.9 °) indicating that the functionalised material is more hydrophilic, likely a result of the charged functional groups (mixture of amine and carboxylate). However, the angle is larger than for ZIF-9-NH_2 (Figure 4.15a, 94.5 °) making it a significantly more hydrophobic surface. When comparing the zeta potential of ZIF-9-NH_2 (20.3 mV) and ZIF-9-NH-MA (-12.3 mV) (1 mmol KCl solution), there is a significant decrease as seen in Figure 4.15b, further evidence of the carboxylic acid functionalised surface.

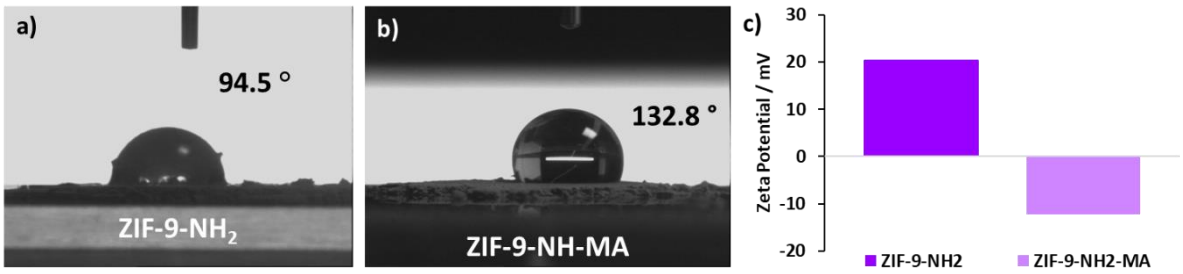

Figure 4.15: a) contact angle measurement of ZIF-9-NH_2 MONs, b) contact angle measurement of ZIF-9-NH-MA MONs and c) zeta potential measurments of synthesised ZIF-9-NH_2 and ZIF-9-NH-MA MONs.

4.2.7 Post-Synthetic Functionalisation of ZIF-9-NH-MA using HBTU

In preliminary studies to determine whether a carboxylic acid functionalised ZIF surface would lead to improved amino acid functionalisation, ZIF-9-NH-MA underwent the HBTU based PSF reaction with L-Val-OH. The new approach (Figure 4.17) to amino acid PSF of the ZIF systems no longer required Boc-protecting groups as the carboxylic acids groups on the MON surface could be activated by the coupling agent and forms a peptide bond with the amine group of the incoming residue. ZIF-9-NH-MA MONs were suspended in anhydrous DMF and a solution containing HBTU, DIPEA and L-Val-OH in DMF was added and left stirring for 16 h. After DMF washing the resulting material was characterised by NMR and IR.

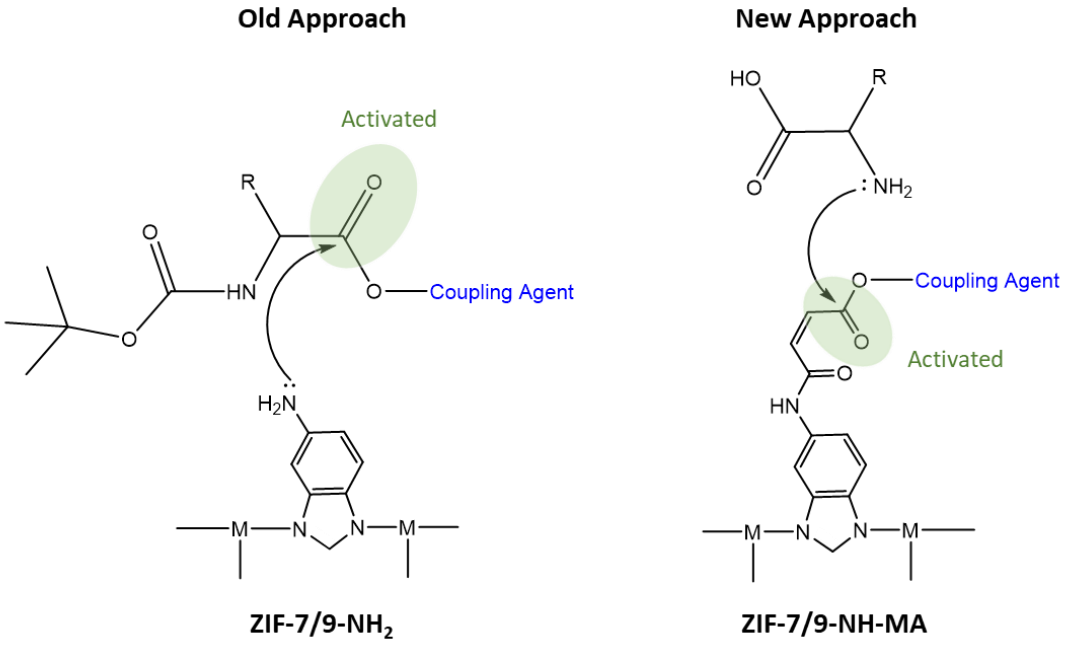

Figure 4.17: Simplified schematic of the different approaches to the amino acid PSF of amine functionlised ZIF MONs where the old approach involves the activation of residues, and the new approach involves the activation of the MON surface.

New peaks appeared in the ^{1}H NMR spectrum (Figure 4.18) that could not be assigned to free L-Val-OH or maleic anhydride at 9.71 ppm, 3.08 ppm, 1.75 ppm, 1.62 ppm and 1.23 ppm. This is evidence of successful PSF. However, it was predicted that there would be new peaks appearing for the alkene hydrogens from the anhydride on the ^{1}H NMR spectrum (Figure 4.18). This was not the case, as the peaks for the alkene hydrogens remained unchanged (6.3 ppm and 6.6 ppm). There was evidence of excess L-Val-OH both in the ^{1}H NMR and ATR-IR spectra (Figure 4.26, experimental). Through the comparison of the imidizolate hydrogen peaks with the new peak appearing at 9.71 ppm, a functionalisation of 9% of the total linkers was calculated. This was an increased degree of functionalisation compared to the same conditions used for the functionalisation of ZIF-7-NH_2 with

Boc-Val-OH where only 2.4 % functionalisation was observed. Due to the large amount of excess residue, it was difficult to assign peaks to successful covalent PSF in the ATR-IR spectrum (Figure 4.26). Further optimisation of this protocol by using the coupling agent PyClOP and microwave irradiation could enhance the level of observed functionalisation.

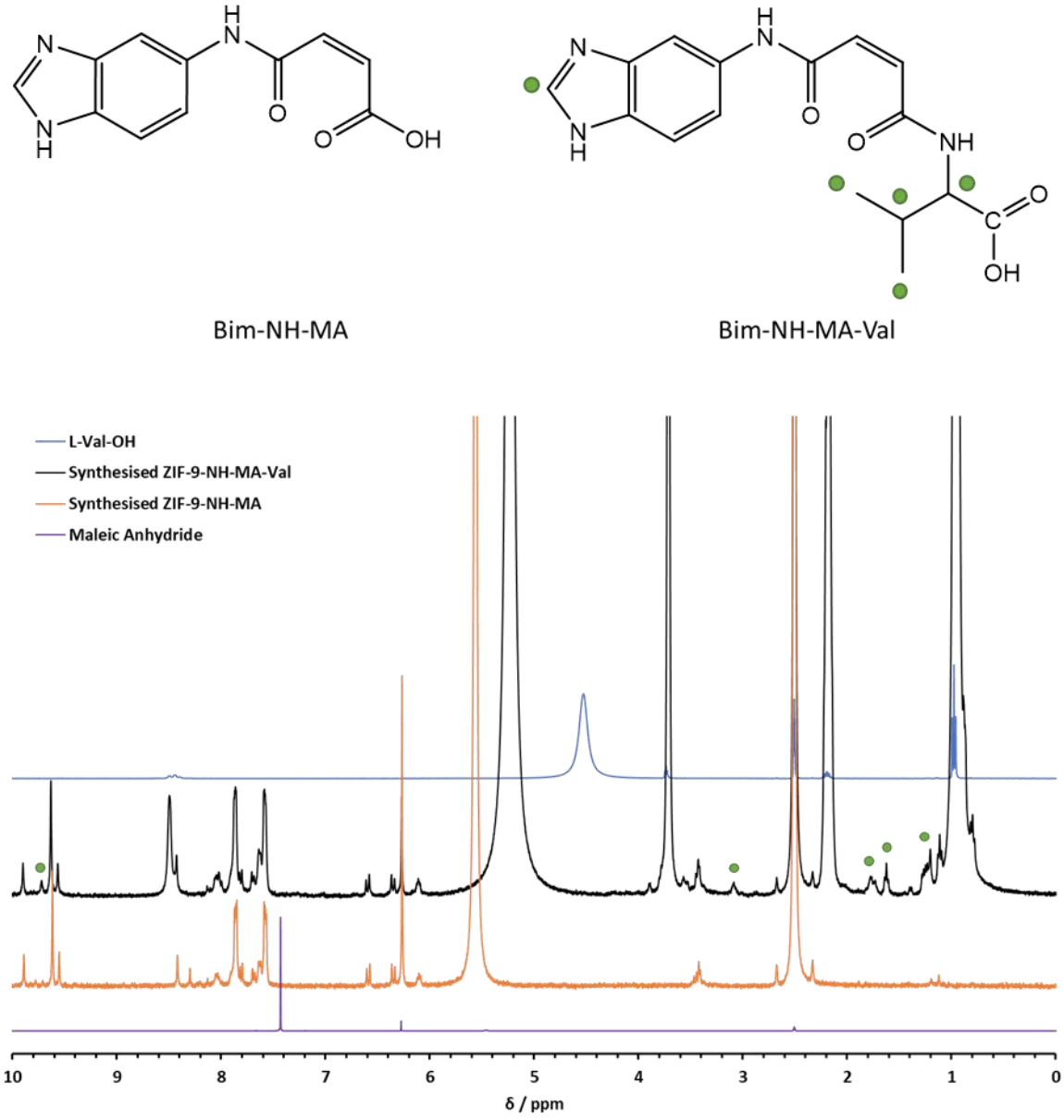

Figure 4.18: ^{1}H NMR spectra of maleic anhydride, synthesised ZIF-9-NH_2 MONs, synthesised ZIF-9-NH_2-MA MONs and L-Val-OH.

4.2.8 Conclusion

The aim of this chapter was to establish routes to the functionalisation of 2D MONs with amino acids to build a library of synthetic biomolecular recognition surfaces. Taking the amine functionalised MONs as discussed in the previous chapters, various previously published synthetic methods were followed to encourage peptide bond formation with amino acids. The residues were often boc-protected to minimize undesired homopolymerization.

For the functionalisation of ZIF-7-NH_2 which contained 20 % amine functionality, coupling agents were used along with microwave irradiation to successfully attach Boc-Val-OH reaching 19 %. Further optimization would be required for attaching other amino acids following the same route, varying the type of coupling agent and molar equivalents of reagents. Following work done by Fracaroli *et al.* the coupling agent HBTU was also utilized for a variety of aliphatic residues (Gly, Ala, Val) with overall functionalisation of 7.1 %, 2.5 % and 2.4 % of the total linkers under ambient conditions.[7]

For all reactions much larger quantities of reagents were required compared to the published work and resulted in only partial functionalisation. As PSF was carried out on MONs rather than the layered PSF it was predicted there would be elevated yields in functionalisation as found in previous work.[10] This is likely as a result of the difference in reactivity of the aromatic amine used in this work and primary amine used by Fracaroli *et al.*.[7] We recommend for the functionalisation of ZIF-7 to use a primary amine benzimidazole linker such as 1H-benzimidazole-6-methanamine that is predicted to be more easily functionalised.

The lack of reactivity of the aromatic amine posed a real problem for this work. Having a densely pack surface with few amine groups as is the case with ZIF-7-NH_2 and ZIF-9-NH_2 is likely to greatly impede PSF when the small reagents are first protected by a bulky boc group and are then activated by another bulky group. A solution to the problem was to create a surface that could be activated. The reaction of the ZIF-NH_2 MONs with maleic anhydride resulted in surfaces that were partially covered in carboxylate groups. This resulted in a change in hydrophobic character as well as decrease in zeta potential. It was hypothesised that the carboxylate groups could be activated using coupling agents, increasing the likelihood of PSF with residues. The further functionalisation of ZIF-9-NH-MA with valine resulted in unclear degrees of functionalisation where there was the appearance of new peaks within the ^{1}H NMR that could not be assigned to the starting material.

Overall, the covalent functionalisation of ZIF-NH_2 MONs proved to be difficult with determination of yields impeded by the low degree of amine functionalisation. The different attempts

at covalent amino acid functionalisation has highlighted the importance of the reactivity of the binding site on the MON surface.

4.3 Experimental

4.3.1 Synthesis of ZIF-7-NH-Val-Boc using PyClOP under microwave irradiation

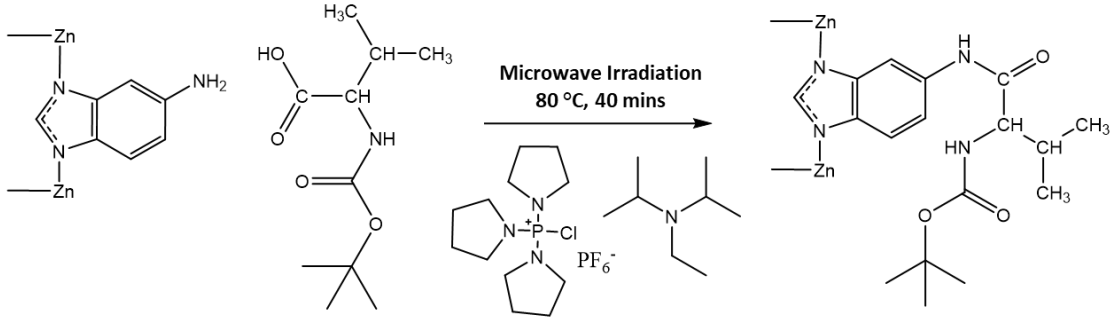

Chlorotripyrrolidinophosphonium hexafluoro-phosphate (PyClOP) (124 mg, 0.294 mmol), N-Ethyldiisopropylamine (DIPEA) (102.3 µL, 0.588 mmol), Boc-Valine-OH (63.9 mg, 0.294 mmol) and ZIF-7-NH_2 (15 mg, ca. 0.0147 mmol $–NH_2$) are suspended in 2 mL of anhydrous DCM. The resulting suspension was allowed to react under microwave irradiation for 40 min at 80 °C (300W) under air cooling. The suspension was then collected (4500 rpm 1 hr) and the solid obtained was washed with THF (3 × 8 mL, 4500 rpm 1 hr) with the final wash under stirring 1 hr. The material was then dried under vacuum at room temperature. (ESI-NEG): $[M]^+$ = 333.2 (Bim-NH-Val-Boc). ^{1}H NMR (DCl/DMSO-d_6): 9.80 (s, 1H, **Bim-NH-Val-Boc**), 9.70 (s, 1H, **Bim-NH_2**), 9.64 (s, 1H, **Bim**), 9.56 (s, 1H, **Bim-NH-Val**), 8.42 (d, J = 18.3 Hz, 4H), 8.11 (s, 4H), 8.03 (d, 1H, **Bim-NH_2**), 8.00 (s, 1H, **Bim-NH_2**), 7.92 – 7.83 (m, 2H, **Bim**), 7.64 (d, *J* = 2.0 Hz, 1H, **Bim-NH_2**), 7.63 – 7.55 (m, 2H, **Bim**), 7.44 (d, J = 8.5 Hz, 2H, **Bim-NH-Val-Boc**), 3.84 (s, 1H, **Val**), 3.16 (s, 1H, **Bim-NH-Val**), 2.4 (m, 1H, **Bim-NH-Val-Boc**), 2.00 (s, 1H, **Bim-NH-Val**), 1.94 (m, 1H, **Val**), 1.68 (s, 6H, **isobutene**), 1.38 (d, J = 8.2 Hz, 9H, **Boc**), 1.11 (s, 4H, **tert-butyl alcohol**), 1.05 – 0.64 (m, **Bim-NH-Val and Bim-NH-Val-Boc**).

4.3.2 Synthesis of ZIF-7-NH-Pro-Boc using Mukaiyama Agent

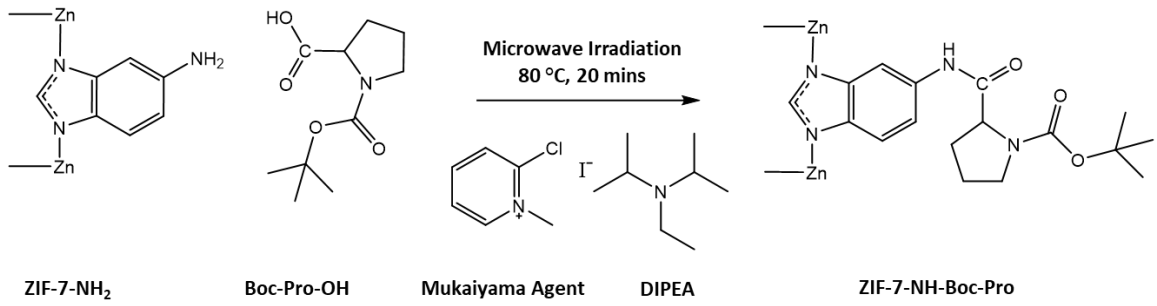

2-chloro-n-methylpyridinium iodide (Mukaiyama Agent) (12.5 mg, 0.049 mmol), N-Ethyldiisopropylamine (DIPEA) (17.1 µL, 0.098 mmol), Boc-Proline-OH (10.5 mg, 0.49 mmol) and ZIF-7-NH_2 (5 mg, ca. 0.0049 mmol $–NH_2$) are suspended in anhydrous DCM (500 µL). The resulting suspension was allowed to react under microwave irradiation for 20 min at 80 °C (300W) under air cooling. The suspension was then collected (4500 rpm 1 hr) and the solid obtained was washed with THF (3 × 8 mL, 4500 rpm 1 hr) with the final wash under stirring 1 hr. The material was then dried under vacuum at room temperature.

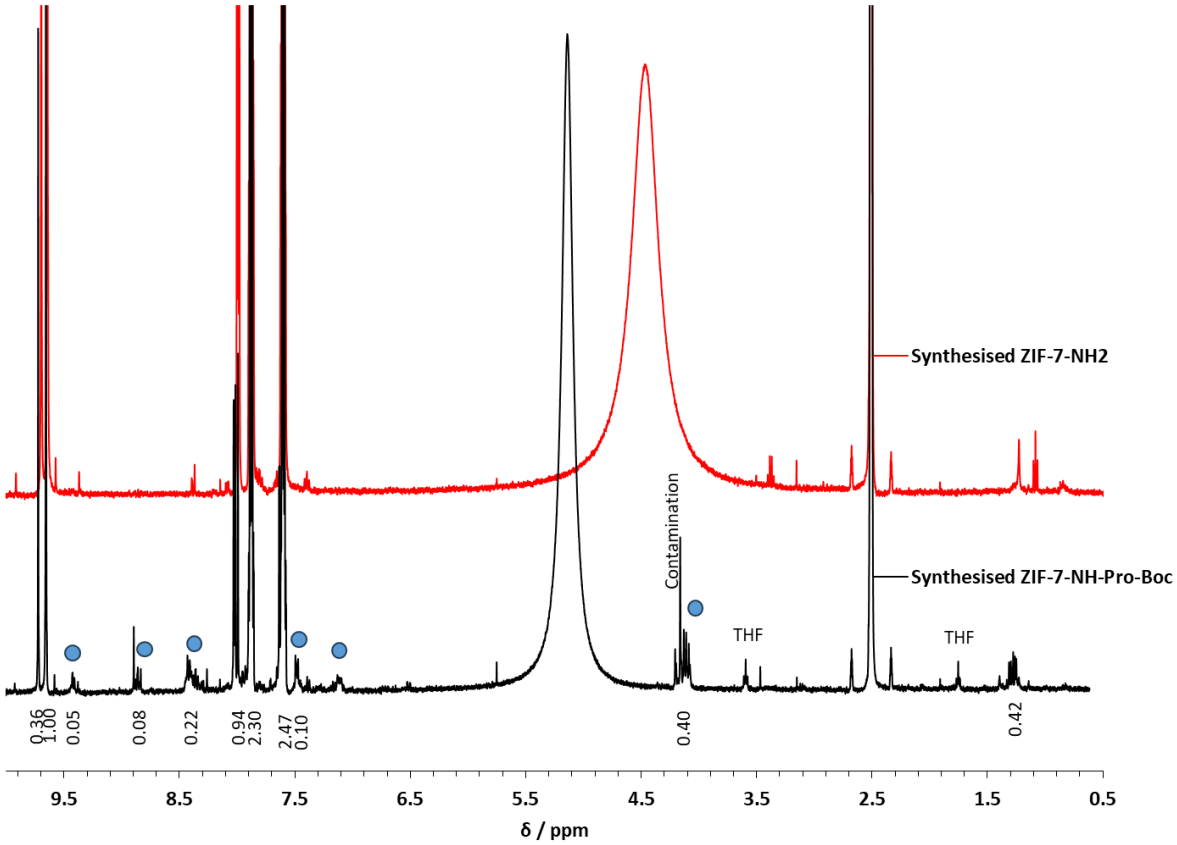

Figure 4.19: Zoomed in ^{1}H NMR spectra of synthesised ZIF-7-NH_2 (red) and ZIF-7-NH-Pro (black) with blue circles highlighting the new peaks assigned to bim-NH-Pro.

4.3.3 Synthesis of ZIF-7-NH-AA-Boc using HBTU

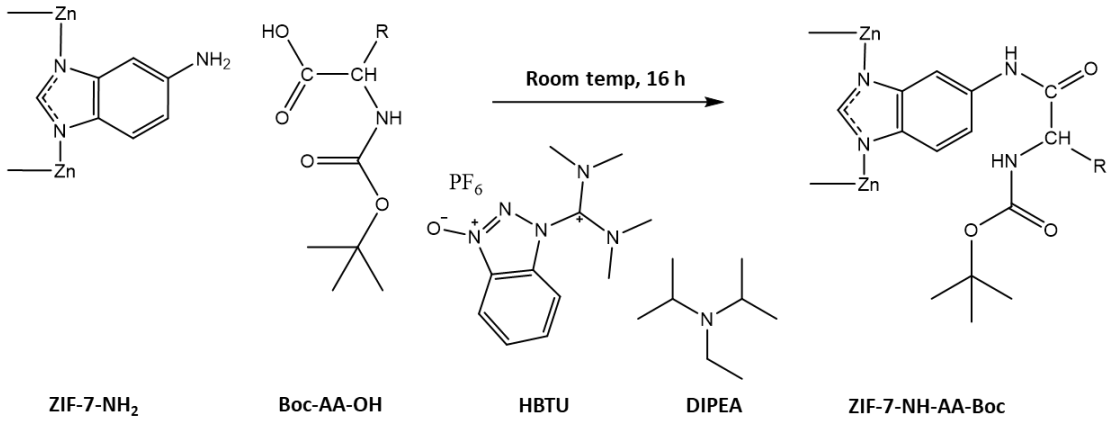

A suspension of ZIF-7-NH_2 (5 mg, 0.0049 mmol (NH_2)) in anhydrous DMF (500 µL) added dropwise to a 5 mL vial containing DMF (500 µL) solution of the corresponding boc-protected amino acid (20-fold excess with respect to MON-amine, 0.098 mmol), 2-(1H-benzotriazol-1-yl)uronium hexafluorophosphate (HBTU, 20-fold excess with respect to MON-amine, 37.16 mg, 0.098 mmol) and N,N-Diisopropylethylamine (DIPEA, 40-fold excess with respect to MON-amine, 17 µL, 0.196 mmol). The mixture was stirred mildly at room temperature for 16 hours, before washing with DMF (10 mL, 10,000 rpm for 1 h) three times.

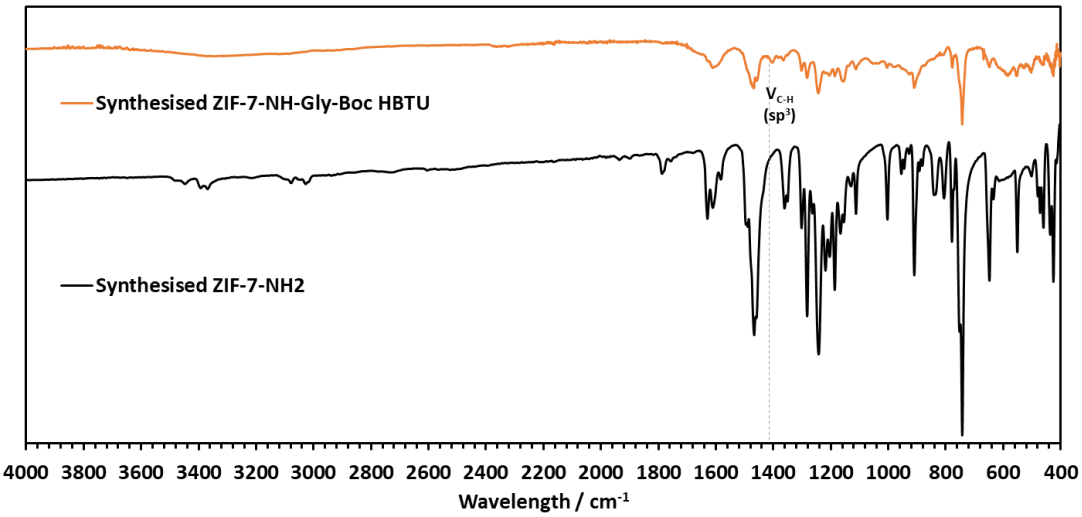

Figure 4.20: ATR-IR spectra of synthesised ZIF-7-NH_2 and ZIF-7-NH-Boc-Gly HBTU.

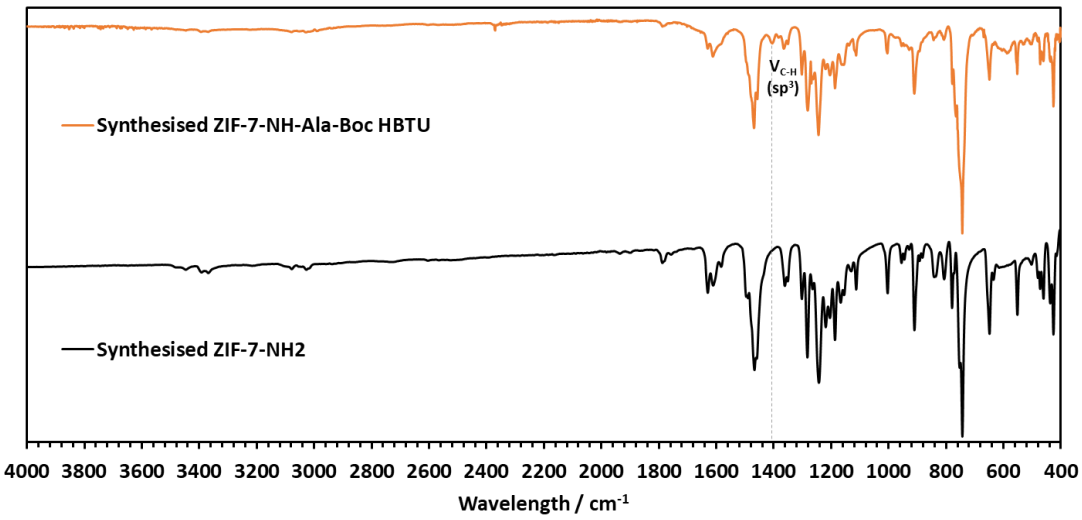

Figure 4.21: ATR-IR spectra of synthesised ZIF-7-NH_2 and ZIF-7-NH-Boc-Ala HBTU.

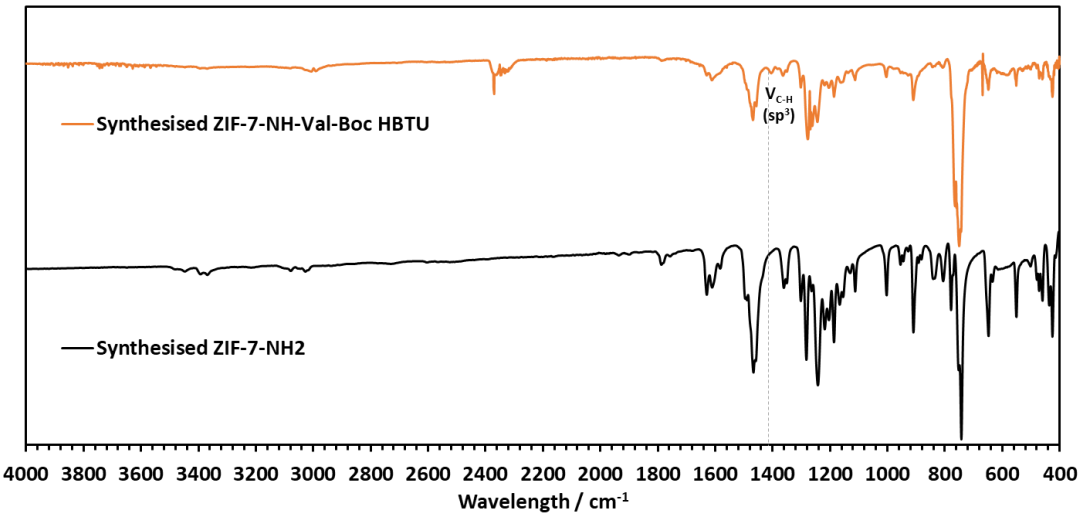

Figure 4.22: ATR-IR spectra of synthesised ZIF-7-NH_2 and ZIF-7-NH-Boc-Val HBTU.

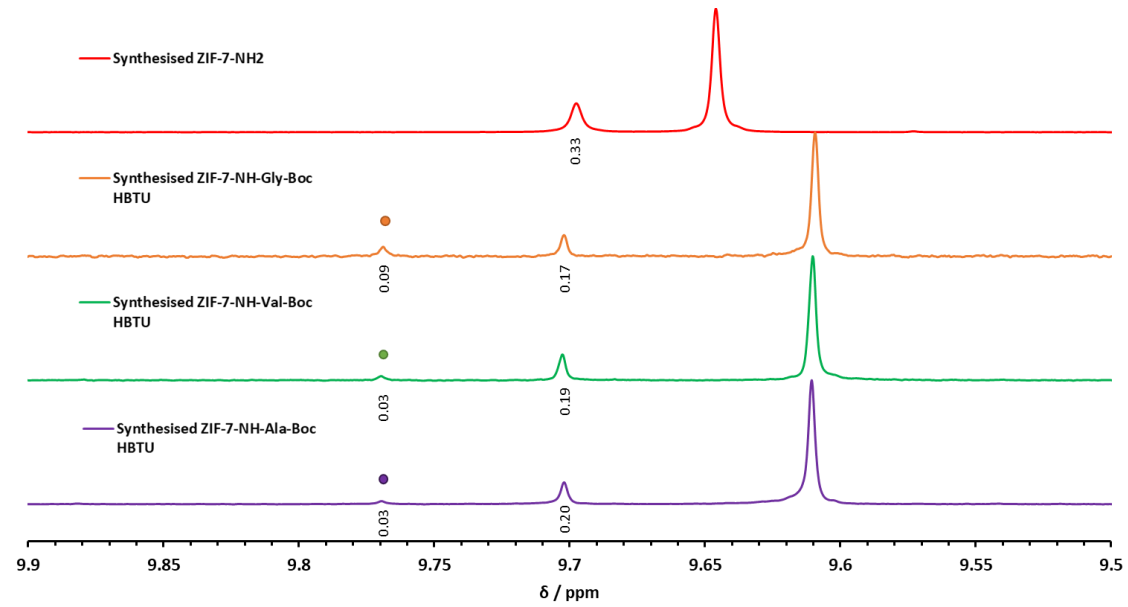

Figure 4.23: Downfield section (9.5-9.9 ppm) of the ^{1}H NMR spectra of synthesised ZIF-7-NH_2 compared to synthesised ZIF-7-NH-Gly-Boc, ZIF-7-NH-Val-Boc and ZIF-7-NH-Ala-Boc using HBTU

4.3.4 Synthesis of ZIF-7-NH-MA

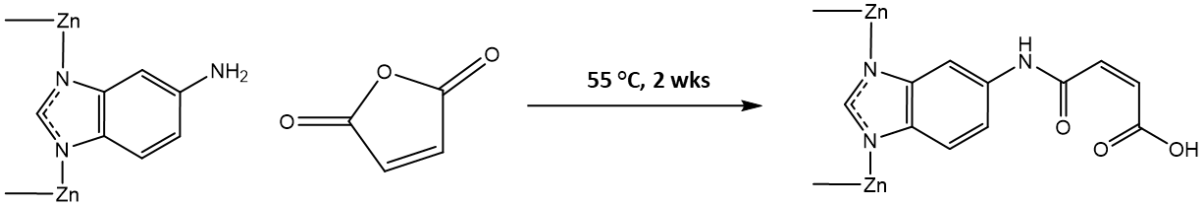

ZIF-7-NH_2 (20 mg, 0.0196 mmol (NH_2)) and maleic anhydride (19.82 mg, 0.196 mmol) were suspended in chloroform (3 mL). The mixture was stirred at 55 °C under nitrogen for 2 weeks. The reaction mixture was centrifuged (12,000 rpm, 30 mins), the supernatant removed, and the solids washed via centrifugation (12,000 rpm, 30 mins) in Chloroform (3 x 15 mL). The sample was dried under desiccation, producing ZIF-7-NH_2-MA as a lighter pink powder.

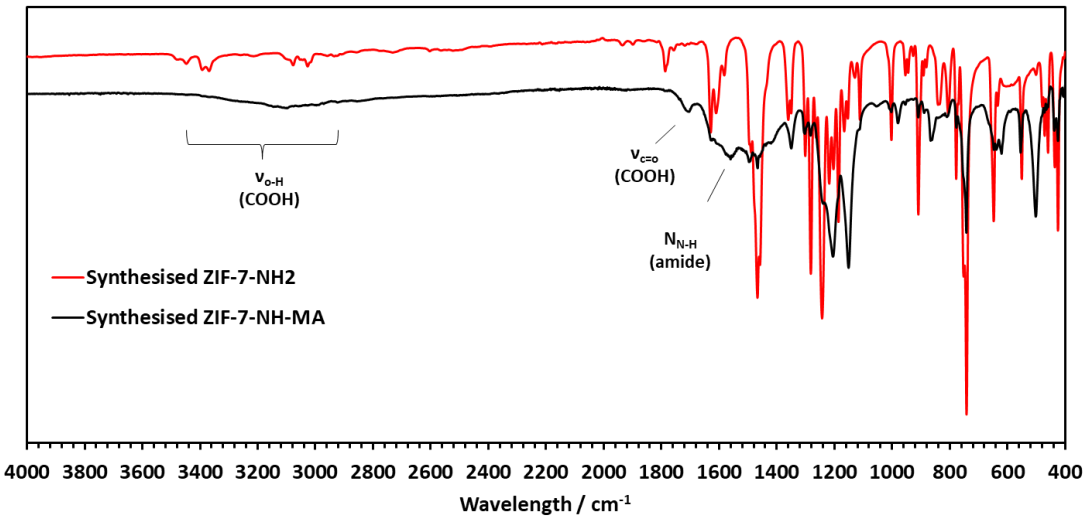

Figure 4.24: ATR-IR spectrum of synthesised ZIF-7-NH-MA compared to synthesised ZIF-7-NH_2.

4.3.5 Synthesis of ZIF-9-NH-MA

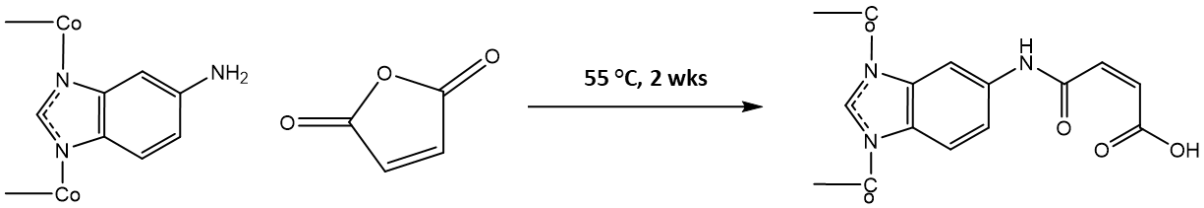

ZIF-9-NH_2 (20 mg, 0.0196 mmol (NH_2)) and maleic anhydride (19.82 mg, 0.196 mmol) were suspended in chloroform (3 mL). The mixture was stirred at 55 °C under nitrogen for 2 weeks. The reaction mixture was centrifuged (12,000 rpm, 30 mins), the supernatant removed, and the solids washed via centrifugation (12,000 rpm, 30 mins) in Chloroform (3 x 15 mL). The sample was dried under desiccation, producing ZIF-7-NH_2-MA as a lighter pink powder.

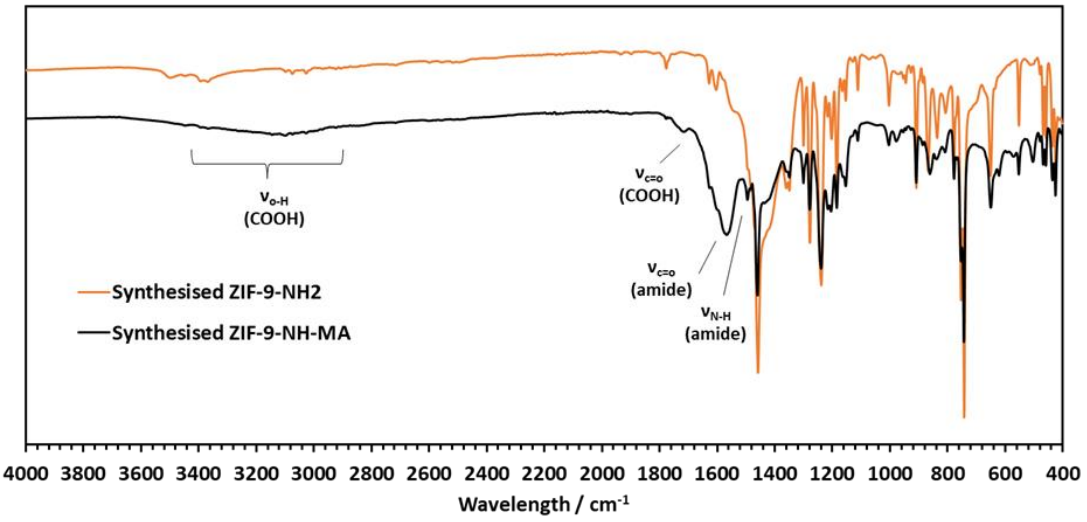

Figure 4.25: ATR-IR spectrum of synthesised ZIF-9-NH-MA compared to synthesised ZIF-9-NH_2.

4.3.6 Synthesis of ZIF-9-NH-MA-Val

A suspension of ZIF-9-NH-MA ($Co_2(bim)_{2.5}(bim\text{-}NH_2)_{0.7}(bim\text{-}NH\text{-}MA)_{0.8}$, 5 mg, 0.006 mmol -COOH), 2-(1H-benzotriazol-1-yl)uronium hexafluorophosphate (HBTU, 45.5 mg, 0.12 mmol) and N,N-Diisopropylethylamine (DIPEA, 40-fold excess with respect to MON-amine, 21 µL, 0.24 mmol) in anhydrous DMF (500 µL) was left stirring for 30 mins. A solution containing valine (20-fold excess with respect to MON-COOH, 0.098 mmol) in DMF (500 µL) was added dropwise. The mixture was stirred mildly at room temperature for 16 hours, before washing with DMF (10 mL, 10,000 rpm for 1 h) three times.

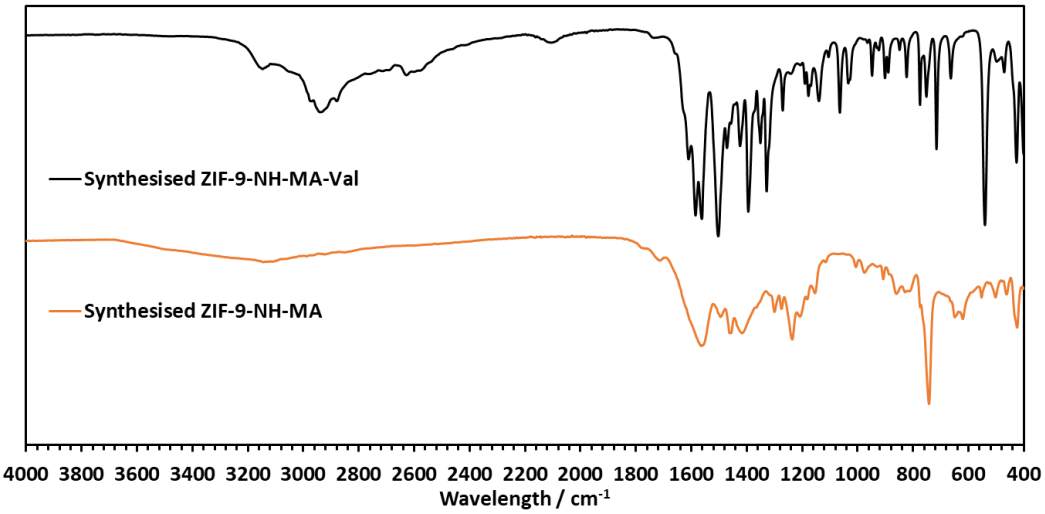

Figure 4.26: ATR-IR spectrum of synthesised ZIF-9-NH-MA compared to synthesised ZIF-9-NH-MA-Val.

4.4 References

1 K. K. Tanabe and S. M. Cohen, *Chem. Soc. Rev.*, 2011, **40**, 498–519.

2 Z. Wang and S. M. Cohen, *Chem. Soc. Rev.*, 2009, **38**, 1315–1329.

3 J. S. Costa, P. Gamez, C. A. Black, O. Roubeau, S. J. Teat and J. Reedijk, *Eur. J. Inorg. Chem.*, 2008, 1551–1554.

4 M. Kandiah, S. Usseglio, S. Svelle, U. Olsbye, K. P. Lillerud and M. Tilset, *J. Mater. Chem.*, 2010, **20**, 9848–9851.

5 E. Dugan, Z. Wang, M. Okamura, A. Medina and S. M. Cohen, *Chem. Commun.*, 2008, **29**, 3366–3368.

6 J. Bonnefoy, A. Legrand, E. A. Quadrelli, J. Canivet and D. Farrusseng, *J. Am. Chem. Soc.*, 2015, **137**, 9409–9416.

7 A. M. Fracaroli, P. Siman, D. A. Nagib, M. Suzuki, H. Furukawa, F. D. Toste and O. M. Yaghi, *J. Am. Chem. Soc.*, 2016, **138**, 8352–8355.

8 A. M. Bumstead, I. Pakamorė, K. D. Richards, M. F. Thorne, S. S. Boyadjieva, C. Castillo-Blas, L. N. McHugh, A. F. Sapnik, D. S. Keeble, D. A. Keen, R. C. Evans, R. S. Forgan and T. D. Bennett, *Chem. Mater.*, 2022, **34**, 2187–2196.

9 J. Nicks, J. Zhang and J. A. Foster, *Chem. Commun.*, 2019, **55**, 8788–8791.

10 J. Nicks and J. A. Foster, *Nanoscale*, 2022, **14**, 6220–6227.

11 X. Ling, D. Gong, W. Shi, Z. Xu, W. Han, G. Lan, Y. Li, W. Qin and W. Lin, *J. Am. Chem. Soc.*, 2021, **143**, 1284–1289.

12 J. Bonnefoy, A. Legrand, E. A. Quadrelli, J. Canivet and D. Farrusseng, *J. Am. Chem. Soc.*, 2015, **137**, 9409–9416.

13 D. J. Lun, G. I. N. Waterhouse and S. G. Telfer, *J. Am. Chem. Soc.*, 2011, **133**, 5806–5809.

14 C. Kutzscher, H. C. Hoffmann, S. Krause, U. Stoeck, I. Senkovska, E. Brunner and S. Kaskel, *Inorg. Chem.*, 2015, **54**, 1003–1009.

15 R. Tatewaki, T. Yamaki, M. Yoshimune, H. Negishi, T. Imura, H. Sakai and N. Hara, *Colloids Surfaces A Physicochem. Eng. Asp.*, 2020, **603**, 125157.

Chapter 5:

Post-Synthetic Functionalisation of Hf-BTB-NH_2 with Amino Acids

5.1 Introduction and Aims

Creating a library of MONs with different surface chemistries will expand the prospects of MONs in biosensing as we build knowledge on which surfaces attract specific sequences of amino acids. This will facilitate nanoscopic tuning of a sensor surface to a given target biomolecule through pre and post synthetic modifications. Building upon work done in chapter 3 to identify the specific peptide sequences that are attracted to different MON systems, this chapter aims to further probe the tuning of surface properties. Determining efficient methods to tune surface chemistry combined with the knowledge already built about specific binding interactions will enable the targeting of biomedically important peptides.

The NUS-8 based MON Hf-BTB-NH_2 was selected for investigation due to the inherent stability of the system in aqueous media, specifically PBS which has been demonstrated in chapter 3.[1] There are also various opportunities for post-synthetic modifications through covalent attachment to the amine group on the linker as discussed in chapter 4 or coordination of new molecules to the metal clusters. This chapter will focus on the modification of the metal cluster components by exchanging the formate modulating agent with various amino acids.

Work done by Lan et al. has demonstrated the use of metal cluster coordination modification to generate well-defined and complex active sites on hafnium based metal-organic nanosheets.[2] Through the precise arrangement of amino acids and ferric protoporphyrin haemin around Hf_{12} clusters artificial photosynthesis was achieved. This is attributed to the specific arrangement of the modifiers as a result of the MONs structure. Amino acids are known to coordinate to the Zr and Hf clusters where work by Marshall *et al.* demonstrated the particular efficiency of L-proline for MOF modulation.[3] Introducing biologically relevant functionality such as amino acids onto the MON surface may enhance the inherent affinity to specific target peptide sequences. MONs in biosensing have typically been involved in complex detection pathways with multiple components including bioreceptor functionalisation which doesn't exploit the density of metal cluster and ligand binding sites.

This chapter aims to demonstrate whether the Hf-BTB-NH_2 surface can be modified post-synthetically with biologically relevant molecules in order to further tune the surface for biosensing applications. Using XRPD to determine whether structural integrity is maintained after PSF, the degree of functionalisation will be verified using NMR. The effect of PSF on MON size, zeta potential and hydrophobicity will also be uncovered in order to establish trends for future MON-based biosensor design.

5.2 Results and Discussion

5.2.1 Synthesis and Characterisation of Hf-BTB-NH_2

Hf-BTB-NH_2 was synthesised by modifying the procedure reported by Ling et. al. by replacing zirconium clusters with hafnium clusters (discussed in chapter 3).[4] The synthesis (Figure 5.1) involved the sonication of hafnium chloride and BTB-NH_2 linker in DMF followed by the addition of water and formic acid as the modulating agent. After 48 h at 120 °C, the resulting pale viscous colloidal suspension once washed becomes a homogenous suspension.

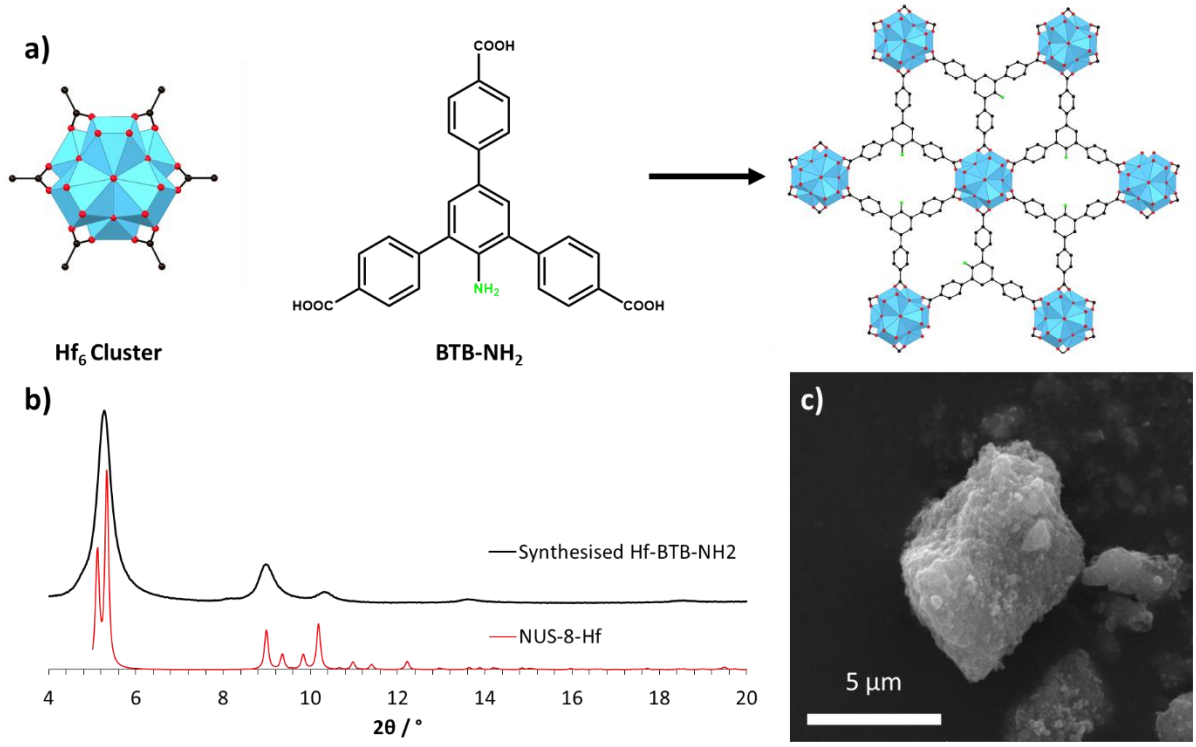

Figure 5.1: a) Schematic of the one-pot synthesis of Hf-BTB-NH_2 where Hf6 clusters react with BTB-NH_2 linker, b) XRPD of Synthesised Hf-BTB-NH_2 (black) and NUS-8-Hf (red) CCDC (1567189), c) SEM of synthesised Hf-BTB-NH_2

The layered material was characterised using XRPD and SEM (Figure 5.1b+c). The powder pattern for the synthesised Hf-BTB-NH_2 matched that of the NUS-8-Hf powder pattern with the only difference being the lack of the amine group on the central benzene on the linker. This is consistent with work done by Ling *et al.* and Lan *et al.* where 2D Zr_6/Hf_6-based MONs with tricarboxylate ligands produce peaks at 5 ° and 9 °.[4,5]

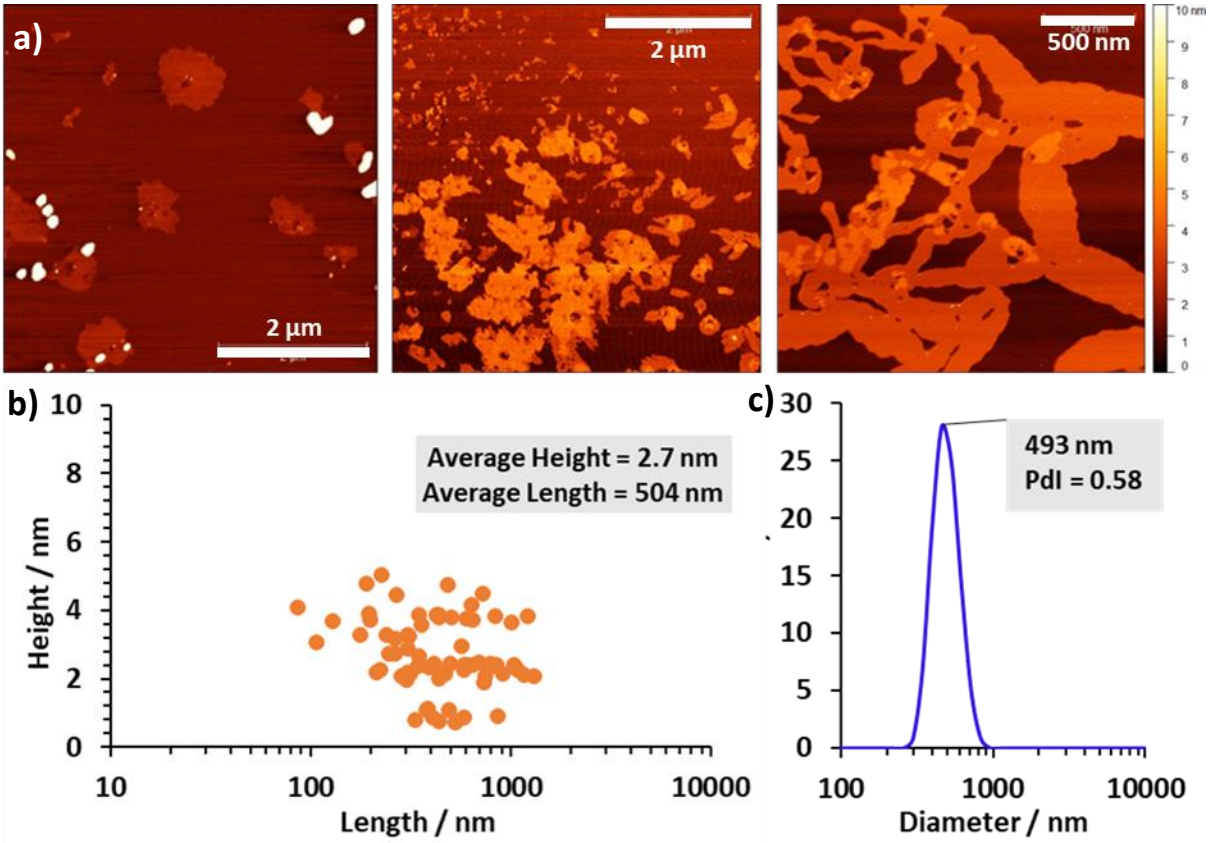

Figure 5.2: a) AFM images and b) the associated dimensions data of Hf-BTB-NH_2 nanosheets with c) the associated DLS data

After confirmation that the material was the correct phase, nanosheets were imaged using AFM (Figure 5.2a). The particle size analysis (Figure 5.2b) of the imaged Hf-BTB-NH_2 nanosheets revealed that they were up to five layers thick with the majority ~2.5 nm and the thinnest nanosheets were ~0.9 nm. The average length was 504 nm which is consistent with the DLS measurement of 493 nm (Figure 5.2c).

The 6-connected Hf_6 SBUs are predicted to be linked by 3-connected BTB-NH_2 ligands to form a 3,6-connected network of $Hf_6(\mu_3\text{-}O)_4(\mu_3\text{-}OH)_4(HCOO)_6(BTB\text{-}NH_2)_2$ with Kagome topology (Figure 5.1 a). The metal cluster in this case is complex, in that there are multiple metal atoms and coordinated modulating agents. The elemental analysis of the synthesised material showed that carbon and nitrogen were underrepresented, and hydrogen was overrepresented. The ideal formula was also not reflected by the ^1H NMR (Figure 5.23, experimental) after digestion where an integration ratio of 1 : 1.77 of linker and formic acid was identified, not the ideal 1 : 3. The predicted formula based on the NMR is therefore $Hf_6(\mu_3\text{-}O)_4(\mu_3\text{-}OH)_4(HCOO)_{4.4}(BTB\text{-}NH_2)_{2.5}$ to satisfy the 12-connectivity.[6] However, this did not match the elemental analysis and therefore it is likely that rather than excess linker in place of the missing formate groups it is hydroxyl and water molecules to account for the extra hydrogen.

The modulating agent can be replaced as demonstrated by Lan et. al., where through room temperature exchange trifluoroacetate (TFA) was replaced by different amino acids.[2] This post-synthetic modification allows for immense diversification of MON surface properties and can be optimised depending on the desired application.

5.2.2 Synthesis and Characterisation of Amino Acid Functionalised Hf-BTB-NH_2

Eight different amino acids (Figure 5.3) were selected for the post-synthetic functionalisation of Hf-BTB-NH_2, each with a variety of chemical properties to introduce to the nanosheet surface. The material as synthesised in section 5.2.1 was left suspended in DMF before undergoing a room temperature reaction to introduce the residues onto the system taking inspiration from work by Lan

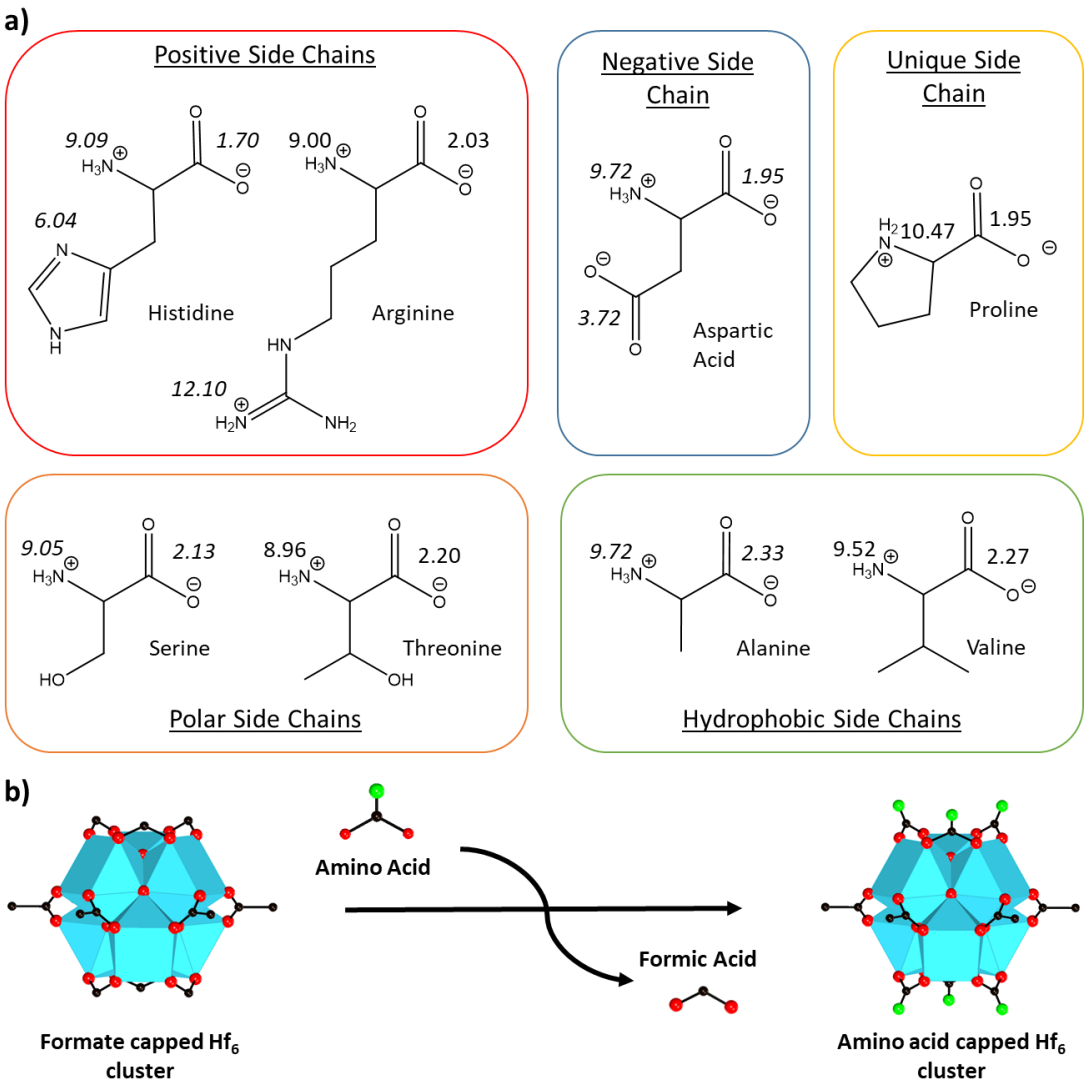

Figure 5.3: a) Structures of the eight amino acids selected for the post-synthetic functionalisation of Hf-BTB-NH_2 with pK_a values shown and charge shown at pH 7.4, b) a simplified scheme to show the proposed post-synthetic exchange reaction of the replacement of formate capping groups with the aforementioned amino acids on a Hf_6 cluster created via the modification of the NUS-8 CIF(CCDC 1444733) using crystal maker software by Dr Ram Prasad.

et. al..[2] The amino acid was expected to replace the formic acid groups on the metal cluster introducing different surface properties.

For the post-synthetic modification, six equivalents of amino acid (with respect to the linker) was added to the suspension of Hf-BTB-NH_2 in DMF (5 mg / mL) and left stirring overnight. After three DMF washes (one left overnight) and three ethanol washes (last one left over 72 h) the resulting material was then characterised. This was a modification of the method by Lan *et al.* that only reported three DMF washes.

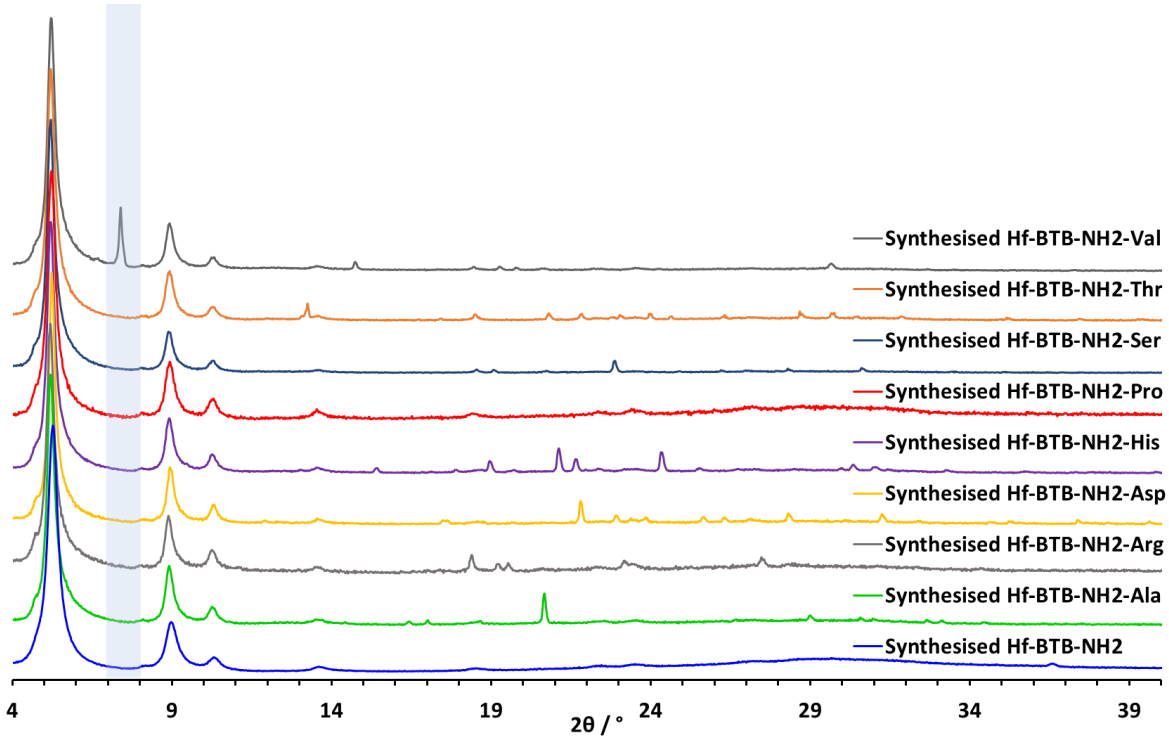

Figure 5.4: XRPD of amino-acid functionalised Hf-BTB-NH_2

XRPD patterns (Figure 5.4) of the resulting material after incubation with the eight different amino acids showed that no significant changes to the main peaks within the crystal structure occurred, indicating that the supramolecular coordination structure was maintained. The majority of amino acid functionalised Hf-BTB-NH_2 showed extra peaks that match well with crystal data for the particular residue indicating excess uncoordinated material that had not been washed away. For example, the synthesised Hf-BTB-NH_2-Val a peak appears at 7.39 ° on this spectra which is likely an indicator of the presence of excess crystallised L-valine which has a peak at 7.40 °.[7] The data is summarised in Table 5.1 where peaks appearing in the XRPD pattern for the synthesised materials are compared to those of the corresponding amino acid (full spectral comparison in the experimental).[8] In each case the amino acid peaks match within 0.1 ° of expected peaks of amino acids in zwitterion form. The peaks in the table are only the peaks that appear in the Hf-BTB-NH_2-AA pattern that aren't

assigned to Hf-BTB-NH_2. There may be other peaks in the expected pattern for the amino acid that don't appear on MON pattern due to lack of intensity. For proline, no additional peaks were observed other than those for Hf-BTB-NH_2 indicating no excess amino acid was present.

Table 5.1: Peaks associated with amino acids for the as synthesised Hf-BTB-NH_2-AA and also the expected peaks from CCDC for the amino acids.

Amino Acid	As Synthesised Peaks (2θ/ °)	Expected Peaks (2θ/ °)
	16.42	16.36
Alanine	17.02	16.92
	20.68	20.60
Arginine	18.39	18.36
	19.22	19.18
	19.57	19.50
	23.11	23.14
	27.47	27.48
Aspartic Acid	21.80	21.86
Histidine	15.42	15.42
	17.92	17.92
	18.96	18.96
	21.13	21.13
	21.66	21.66
	24.32	24.32
Proline	n/a	n/a
Serine	18.55	18.50
	19.08	19.22
	22.88	22.84
Threonine	13.25	13.14
	18.49	18.42
	20.80	20.70
	21.81	21.72
	23.05	22.96
Valine	7.40	7.40

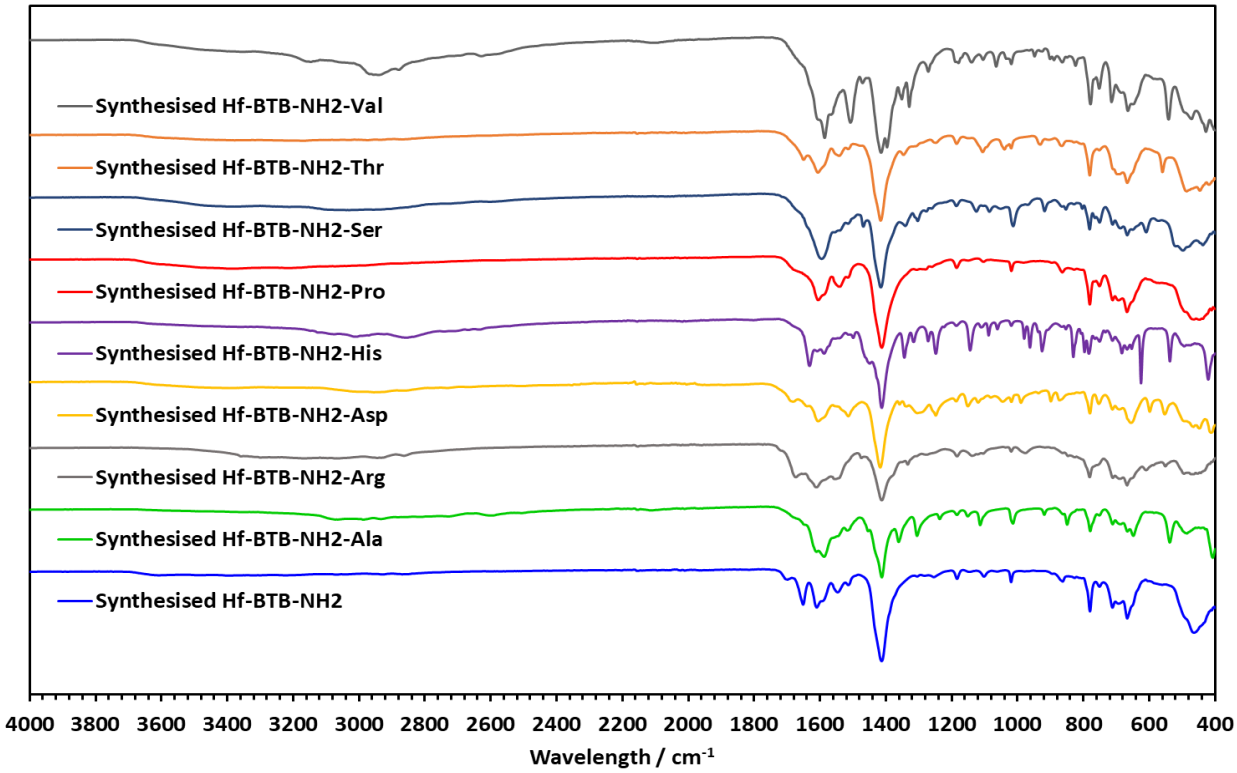

Figure 5.5: ATR-IR spectra of all synthesised Hf-BTB-NH2-AA compared to synthesised Hf-BTB-NH_2

Having determined that after post-synthetic functionalisation MON crystallinity was retained, further characterisation was carried out. ATR-IR was used to confirm the presence of the amino acid side chains (Figure 5.5). Weak bands were observed for all Hf-BTB-NH_2-AA MONs in the region of 3600–2600 cm^{-1}, associated with introduced C–H stretches, O-H stretches and N-H stretching. This was particularly strong for valine which has an isopropyl side chain, likely due to excess residue. The strongest band which appeared at 1412 cm^{-1} for all spectra is associated with the O-H bending of the carboxylic acids present in both the BTB-NH_2 linker and amino acids. For Hf-BTB-NH_2-His and Hf-BTB-NH_2-Arg, C=N stretching appears at 1630 cm^{-1} and 1675 cm^{-1} respectively. There are differences between the Hf-BTB-NH_2-AA spectra and Hf-BTB-NH_2 but as many of the functional groups introduced are the same (amine/carboxylic acid) or appear in a similar position on the IR spectrum further analysis was used to properly determine the extent of functionalisation.

The ^{1}H NMR spectrum for each MON system determined the ratio of amino acid to linker and formic acid. The predicted post-synthetic functionalisation mechanism was the replacement of the formic acid (FA) groups that occupy Hf_6-cluster binding sites with the amino acids through coordination of the carboxylic acid group. The ratio of all components was determined using one linker (BTB-NH_2) to calculate the integrals of all H environments. An intense digestion process was of 24 hr ultrasonication in a solution of NaOD diluted by D_2O is used due to the stability of the MON system.

The ^{1}H NMR spectra for each Hf-BTB-NH_2-AA system is shown in the appropriate experimental section, with a comparison to the NMR spectrum for Hf-BTB-NH_2 and the corresponding amino acid. In all cases there was still formic acid present after PSF therefore the direct replacement of all FA groups was not achieved. However, there was a general trend of decreasing ratio of FA with increasing ratio of AA compared to linker. Further optimisation of the synthetic process could be carried out where the incubation period is extended, or the system is heated to maximise the exchange.

Table 5.2: Ratio of amino acid and formic acid for each Hf-BTB-NH_2-AA system determined by NMR after digestion.

Amino Acid	Ratio of AA vs linker (Ideal (3-FA):1)	Ratio of FA vs linker (ideal 3:1)
Alanine	5.8	0.4
Arginine	2.0	1.0
Aspartic Acid	7.8	0.5
Histidine	7.7	0.7
Proline	1.1	1.1
Serine	7.2	0.6
Threonine	7.1	0.5
Valine	5.8	0.8

When comparing the level of functionalisation, aspartic acid, and histidine showed the highest ratios (7.8 and 7.7), followed closely by serine and threonine (7.2 and 7.1). Interestingly aspartic acid, serine and threonine all appear in the specific binding peptide for Hf-BTB-NH_2 identified in chapter 3 (FTVRDLS). Whilst within the peptide the carboxylic acid group is captured in a peptide bond, the residues have carboxylate or hydroxyl side chain groups that can also undergo metal centre coordination. It is also important to consider the solubility of each amino acid in DMF which will influence the trends discussed below.

Arginine also appears in the binding peptide sequence but does not achieve the same level of functionalisation. The predicted binding mode of arginine is with the aromatic linker through cation – π interactions and not with the metal centre. Indicating that whilst this binding may occur, interactions of the surrounding residues within the specific binding peptide might be essential for this to take place. Accumulative interactions from the specific combination and ordering of amino acids within the peptide results in the highly selective affinity. However, the binding conditions for the amino acid PSF (DMF) were different to that of the peptide binding studies (PBS) as an aprotic solvent was used.

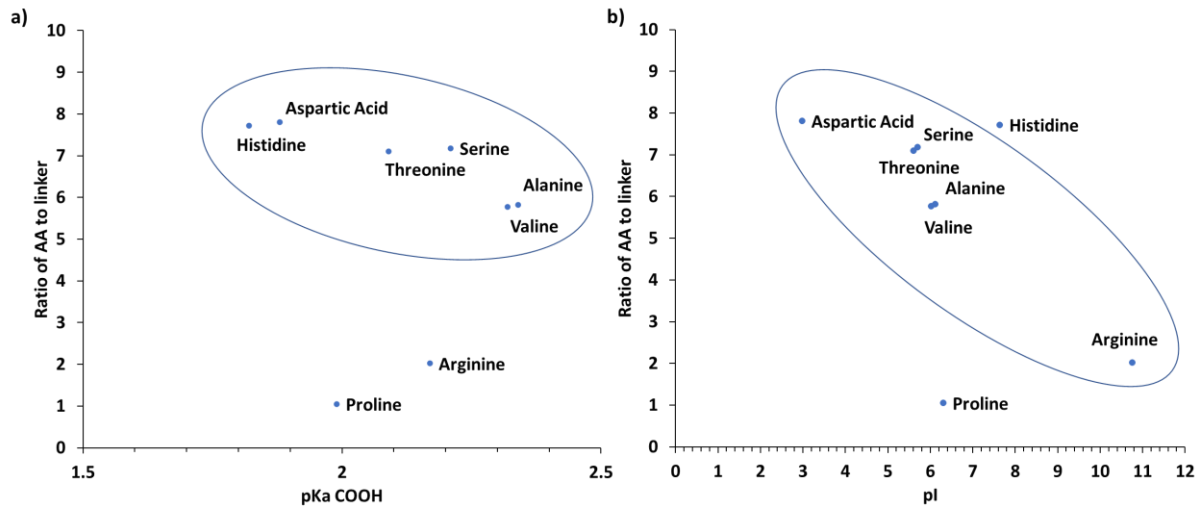

Figure 5.6: a) Effect of the pKa of the amino acids carboxylate on the ratio of amino acid to linker, b) effect of the pI of the amino acid on the ratio of amino acid to linker.

Valine, which also appears in the binding peptide, has a slightly reduced level of functionality (5.8) when compared to residues with carboxylate and hydroxyl side chains. Alanine has the same level of functionalisation (5.8) which is likely due to the similarity in aliphatic nature of the two residues. The pKa values for the carboxylate on alanine and valine are 2.34 and 2.32 respectively. Figure 5.6a shows the effect of carboxylate pKa on the ratio of amino acid to linker found from the NMR. There is a general trend of increasing level of functionalisation with decreasing pKa. Arginine and proline are outliers in the trend therefore other factors are likely to influence the degree of functionalisation here. In the study by Lan *et al.*, the pka of the carboxylate for all amino acids was considered in regard to metal centre coordination, specifically in comparison to the modulator TFA that they were replacing.[2] The authors state that a pKa ~ 2.00 which is larger than TFA ~ 0.23 results in the facile exchange of TFA for amino acids. As the pKa of formic acid is 3.75, carboxylic acid exchange was therefore less facile due to the electron-rich carboxylate in the FA. The residual FA peaks after the PSF in this work are likely as a result of the difference in carboxylate pKas. Selecting a different modulator, with a smaller pKa could result in larger levels of amino acid functionalisation, the amino acids themselves could be used.[3] When considering the effect of the isoelectric point (pI – in water) of the amino acids there is also a general trend of increasing level of functionalisation on decreasing pI (Figure 5.6b). As the MON surface is negatively charged it would be predicted that residues with a larger pI would have a higher affinity over those with pIs under 7.4. This is not what is observed, likely due to repulsion from the positive metal clusters making carboxylate coordination more difficult. Proline is again an outlier which could be due to the unique structure of proline and its solubility in DMF. As there is no appearance of proline peaks in the XRPD it could be considered the level of functionality identified by ^{1}H NMR is a true representation of coordinated residue.

Having established the presence of the amino acids within the Hf-BTB-NH_2-AA systems particle size analysis was carried out in order to determine the effect of PSF. Synthesised Hf-BTB-NH_2 nanosheets were accessed down to 0.9 nm and averaged at ~ 500 nm in length. The incorporation of amino acids via PSF was predicted to increase the thickness of the nanosheets whilst still maintaining the same overall topology according to the XRPD data.

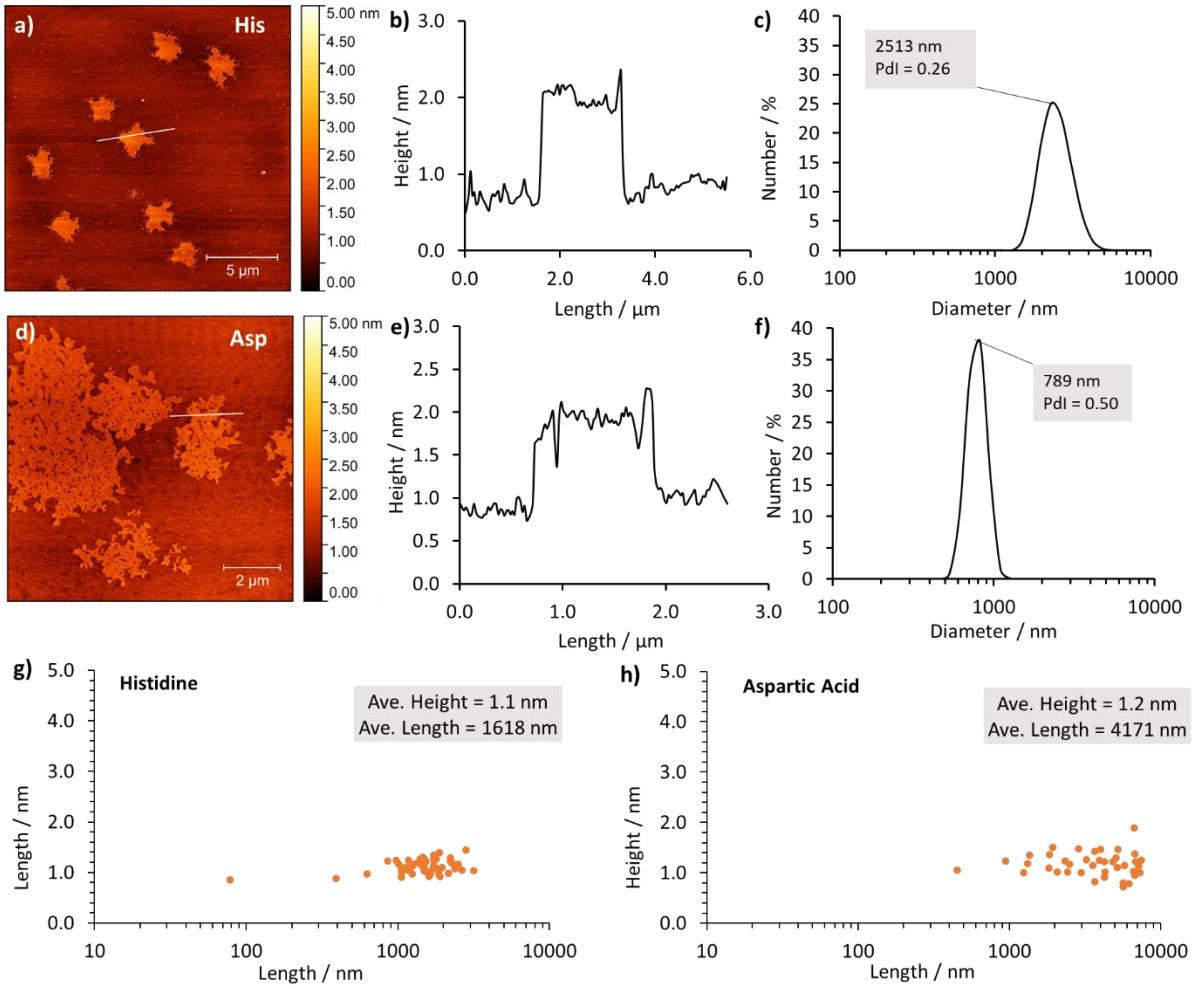

Figure 5.7: a + d) AFM image of Hf-BTB-NH_2-His and Hf-BTB-NH_2-Asp, b + e) height profile of a nanosheet from the AFM image (a + d), c + f) DLS data for Hf-BTB-NH_2-His and Hf-BTB-NH_2-Asp, g + h) associated dimensions of the nanosheets imaged by AFM

Hf-BTB-NH_2-His and Hf-BTB-NH_2-Asp were the most functionalised MONs according to ^{1}H NMR. AFM was used to image the resulting nanosheets to determine the impact of functionalisation on particle size (Figure 5.7). For both systems ultrathin nanosheets were accessed down to 1.1 nm and 1.2 nm on average, slightly thicker than the thinnest functionalised Hf-BTB-NH_2 nanosheets at 0.9 nm. This increase is good evidence to support the functionalisation of the clusters. Both systems produced similar lateral dimensions typically > 1 µm, with Hf-BTB-NH_2-Asp nanosheets being on average larger reaching 7.5 µm. Figure 5.7d shows the ultrathin Asp functionalised MONs are highly defected. This may be due to the ditopic nature of the amino acid.

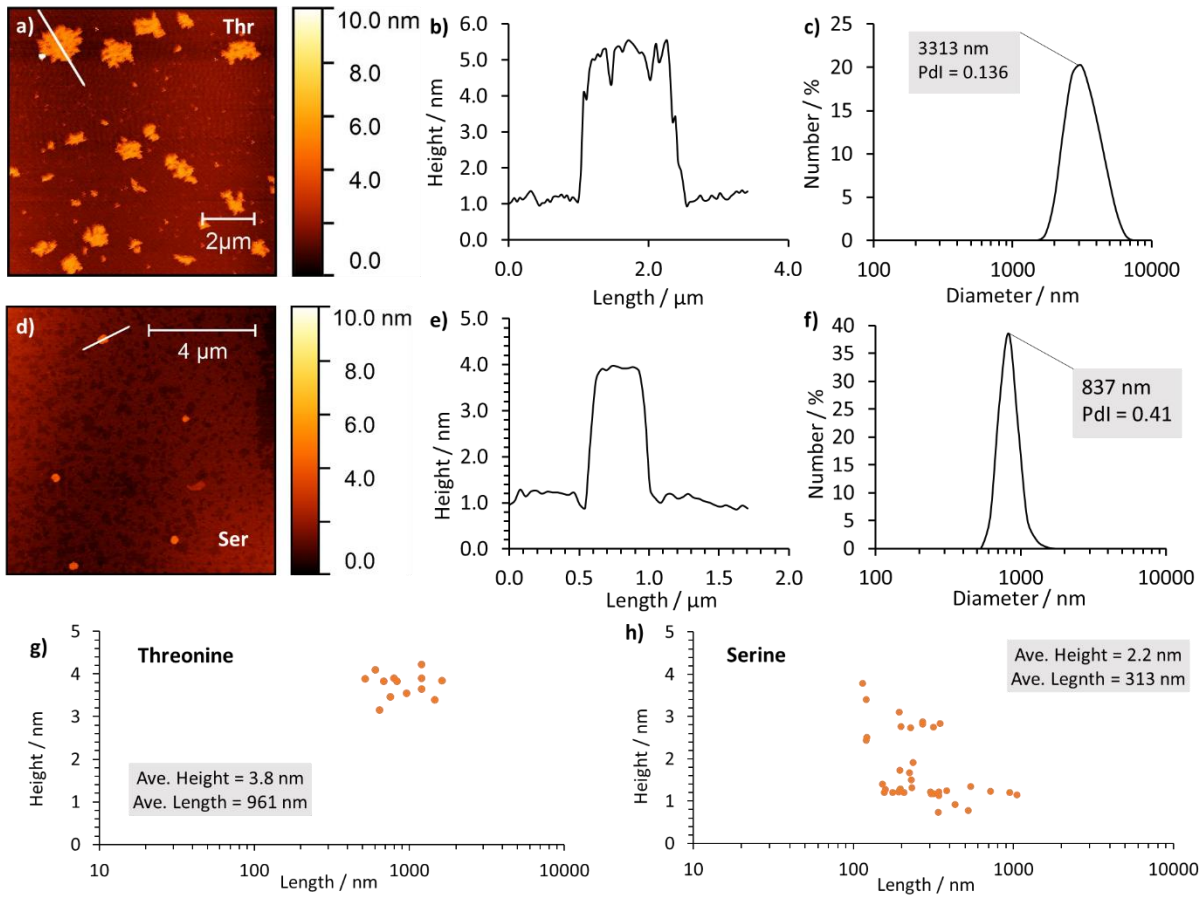

Figure 5.8: a + d) AFM image of Hf-BTB-NH_2-Thr and Hf-BTB-NH_2-Ser, b + e) height profile of a nanosheet from the AFM image (a + d), c + f) DLS data for Hf-BTB-NH_2-Thr and Hf-BTB-NH_2-Ser, g + h) associated dimensions of the nanosheets imaged by AFM.

Threonine and serine functionalised Hf-BTB-NH_2 nanosheets where on average 3.8 nm and 2.2 nm in height respectively (Figure 5.8). The thinnest Hf-BTB-NH_2-Ser nanosheets were 1.2 nm which is consistent with Asp and His functionalised MONs. Threonine, which has a bulkier side chain, produced nanosheets that were on average thicker than the average Hf-BTB-NH_2 MONs (2.7 nm). The extra thickness here might be inter-layer interactions from two residues that are known to have high affinity with the Hf-BTB-NH_2 surface as identified in chapter 3. Hf-BTB-NH_2-Thr MONs were ~ 1 µm in length, the increased interactions might provide greater stability enabling larger nanosheets to be accessed when compared to unfunctionalized MON which averages ~ 500 nm. Hf-BTB-NH_2-Ser MONs were smaller on average (313 nm) but reached aspect ratios ≥ 100. The DLS analysis in this instance corroborated that of the AFM analysis in indicating Hf-BTB-NH_2-Thr MONs were larger but significantly overestimated the average size.

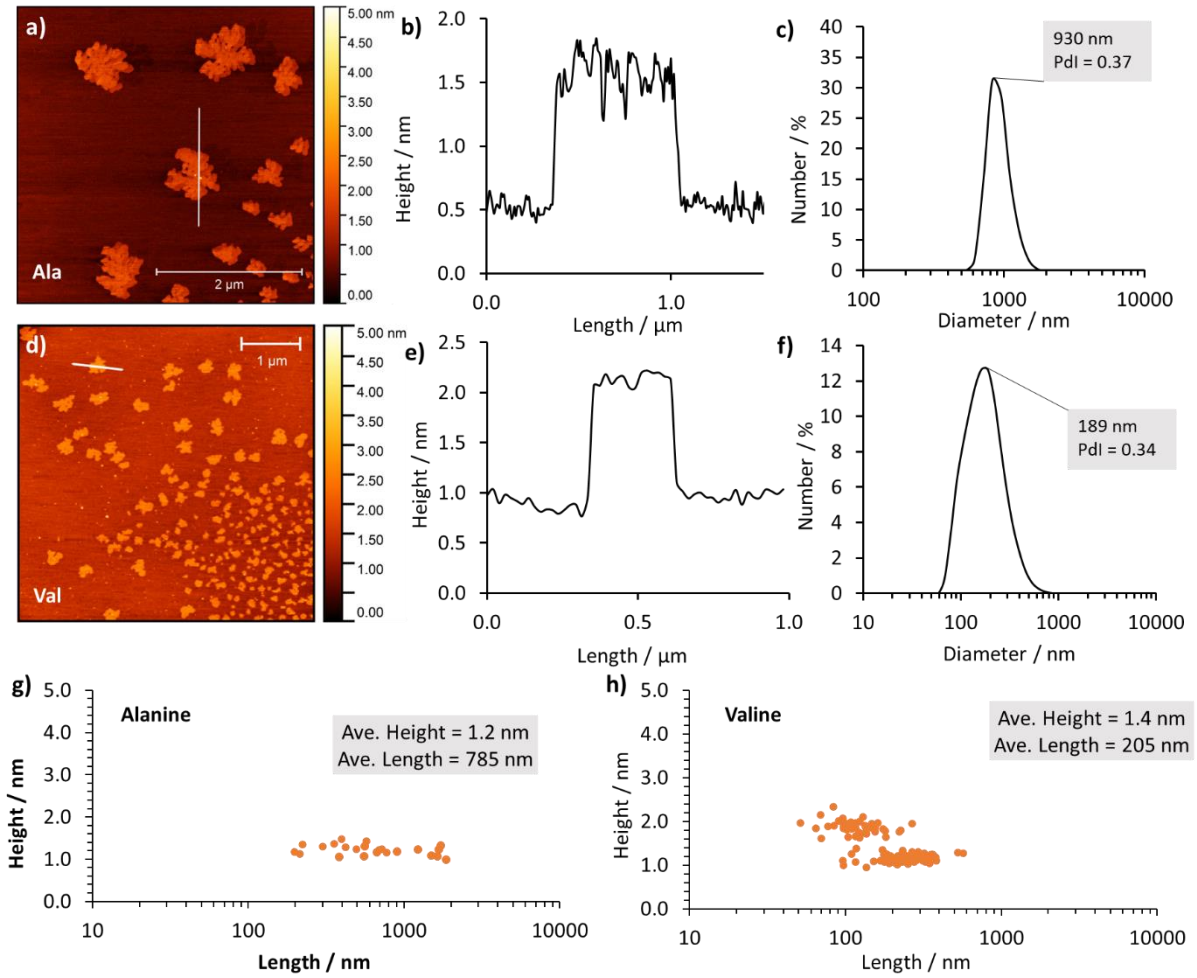

Figure 5.9: a + d) AFM image of Hf-BTB-NH_2-Ala and Hf-BTB-NH_2-Val, b + e) height profile of a nanosheet from the AFM image (a + d), c + f) DLS data for Hf-BTB-NH_2-Ala and Hf-BTB-NH_2-Val, g + h) associated dimensions of the nanosheets imaged by AFM.

The two aliphatic amino acids alanine and valine also produced ultrathin nanosheets that were both at their thinnest 1.2 nm corresponding to the AFM data (Figure 5.9). This is a consistent increase on the height of Hf-BTB-NH_2 nanosheets after amino acid functionalisation. Valine functionalisation resulted in two groups of nanosheets one and two layers thick (Figure 5.9h). Due to the nature of the side chain chemistries for both residues it is unlikely that they will contribute to increased inter-layer interactions. The majority of nanosheets for both systems were between 100 – 1000 nm but the average length was larger for Hf-BTB-NH_2-Ala (785 nm) than for Hf-BTB-NH_2-Val (205 nm). The DLS data matches closely in this case with a large particle size distribution for both systems around 930 nm for ala and 189 nm for val.

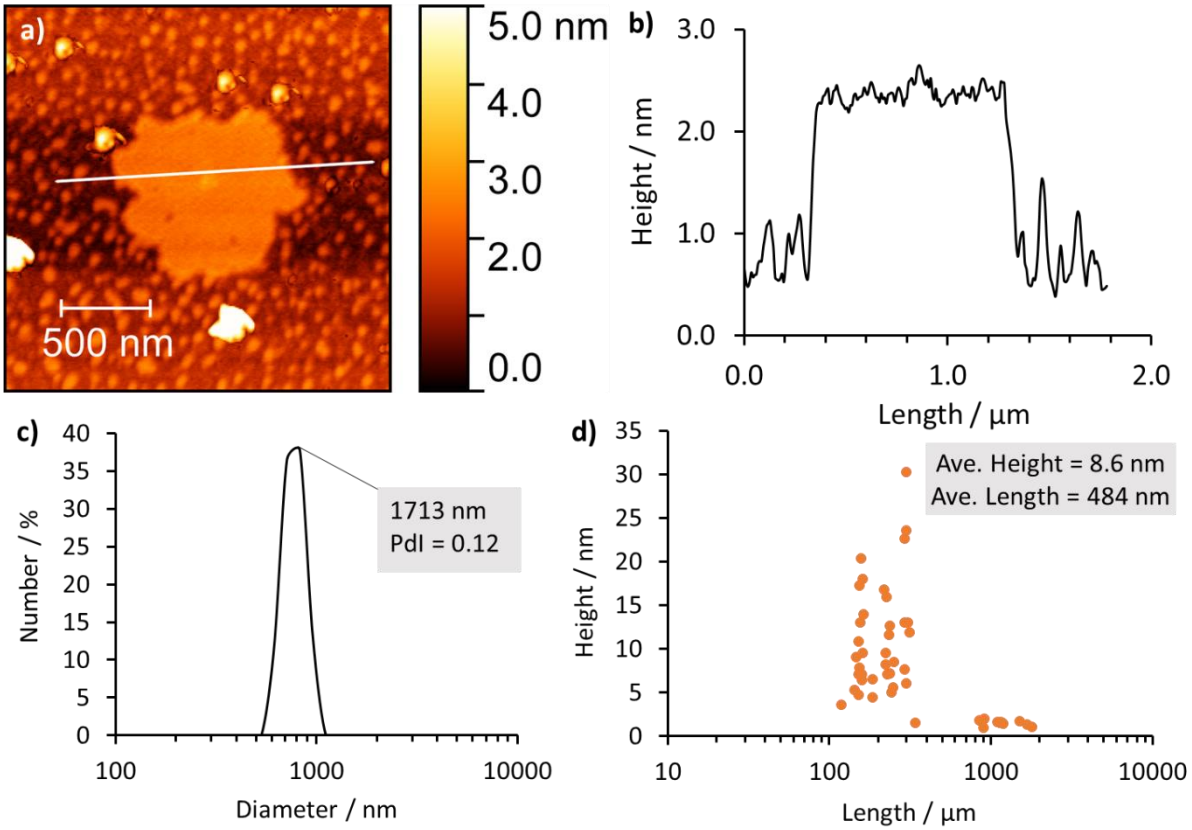

Figure 5.10: a) AFM image of Hf-BTB-NH_2-Arg, b) height profile of a nanosheet from the AFM image (a), c) DLS data for Hf-BTB-NH_2-Arg, d) associated dimensions of the nanosheets imaged by AFM.

Hf-BTB-NH_2-Arg nanosheets had a large range in heights up to 30.3 nm, with the thinnest nanosheets averaging at 1.6 nm (Figure 5.10d). Arginine is one of the largest amino acids and therefore was likely to introduce more height to the surface than others.[9] The range in heights of the MONs might be as a result of interlayer interactions between the guanidinium side chain and linkers in other MONs as indicated by phage display in chapter 2. The ultrathin MONs reach microns in length but the thicker MONs are ~200 nm in length.

The majority of Hf-BTB-NH_2-Pro nanosheets were ~ 5 nm in height, making them a few layers thick. With the thickest Hf-BTB-NH_2 nanosheets existing at ~ 4 nm, functionalisation with proline indicated that interlayer interactions increased (Figure 5.11). The added height from the presence of one proline molecule is predicted to be 0.56 nm therefore it can be inferred the difference is a result of functionalisation. On average the Hf-BTB-NH_2-Pro nanosheets were ~ 950 nm, larger than Hf-BTB-NH_2 nanosheets, indicating an increase in stability as a result of interlayer interactions which resulted in thicker and larger MONs.

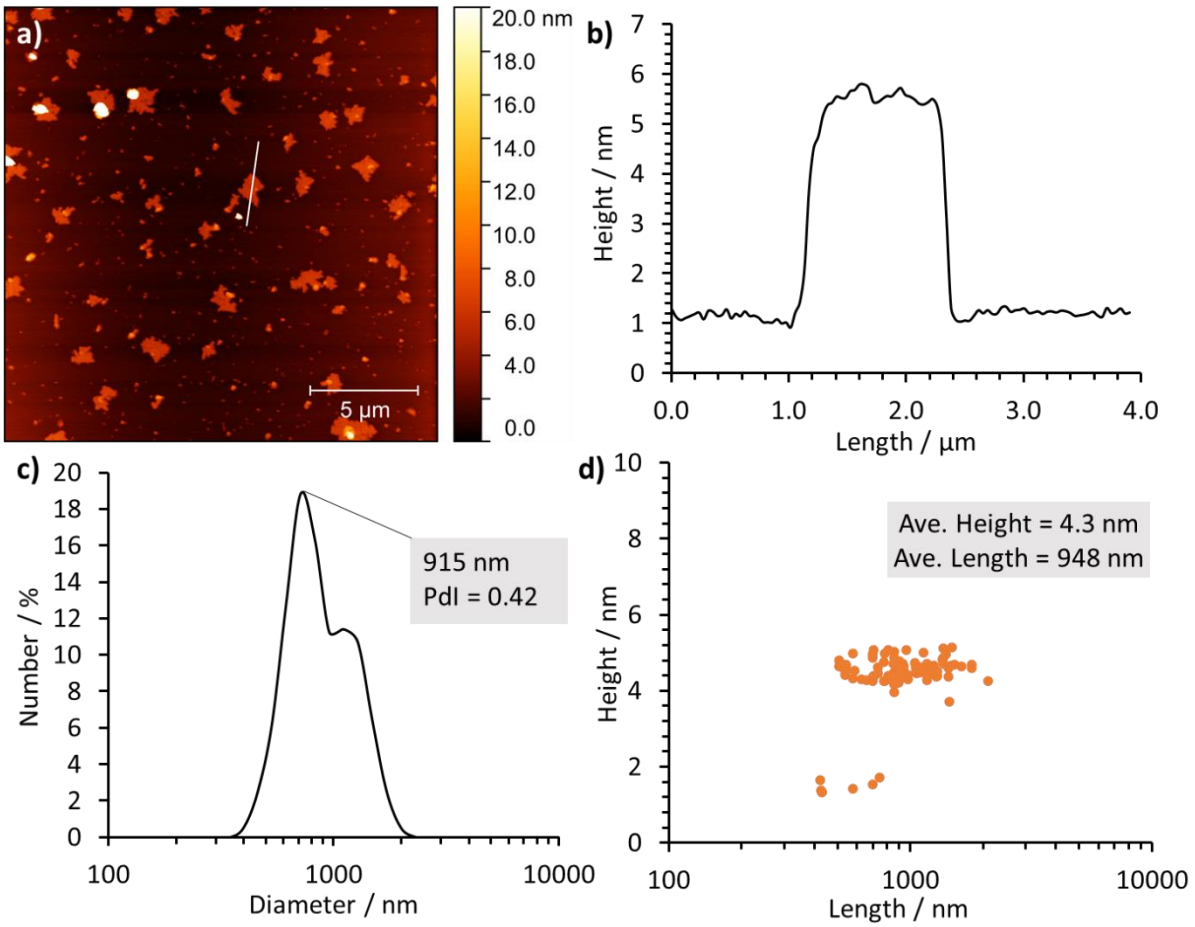

Figure 5.11: a) AFM image of Hf-BTB-NH_2-Pro, b) height profile of a nanosheet from the AFM image (a), c) DLS data for Hf-BTB-NH_2-Pro, d) associated dimensions of the nanosheets imaged by AFM.

Overall ultrathin nanosheets were accessed for each Hf-BTB-NH_2-AA with a slight increase in height observed as a result of the PSF. His and asp produced the longest nanosheets where the majority were ultrathin (1.1/1.2 nm), thinner on average than the unfunctionalised MON (2.5 nm). The asp functionalised MONs are highly defected potentially due to its ditopic nature or it may be crystallised amino acid. Ser, thr, arg and pro based nanosheets were on average thicker than Hf-BTB-NH_2 likely a result of the presence of residues themselves and the interlayer interactions they achieve through their side chains encouraging stacking. The aliphatic amino acids ala and val produced shorter nanosheets on average than Hf-BTB-NH_2-His/Asp but were around the same thickness.

Having determined the dimensions of the Hf-BTB-NH_2-AA nanosheets, the next step was to determine the effect of PSF on surface chemistry. Changes to surface charge were determined through zeta potential measurements where MONs were suspended in diluted PBS. The addition of each amino acid resulted in an increase in zeta potential when compared to Hf-BTB-NH_2 (-36 mV ± 0.8) as shown in Figure 5.12. The amine group for each amino acid was accessible and likely to be positively charged under the analytical conditions (pH 7). The only side chain groups that would carry charge are

arginine, aspartic acid and histidine. The functionalisation with these residues resulted in the largest changes in zeta potential.

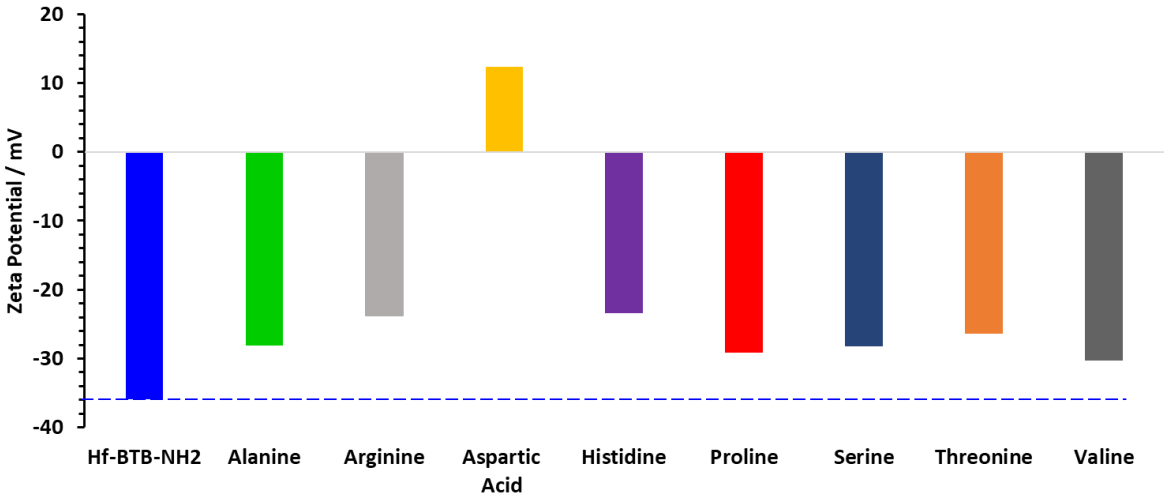

Figure 5.12: Zeta potential values for all Hf-BTB-NH_2-AA

Arginine and histidine, which have basic side chain groups, increased the zeta potential to –23.7 mV ± 1.3 and - 23.4 ± 0.45 mV respectively from the - 36 mV ± 0.8 of Hf-BTB-NH_2 under these conditions. Whilst the pKa of the side chain for arginine (12.48) is significantly greater than that for histidine (6), the addition of histidine results in the larger change in zeta potential (ΔZP). This is likely a result of the difference in the degree of functionalisation of the two, with Hf-BTB-NH_2-His having 3.82-fold more residues per linker than Hf-BTB-NH_2-Arg. Figure 5.13a shows the relationship between the ratio of amino acid to linker and zeta potential, where generally as the ratio increases there is a greater increase in zeta potential likely due to the increasing amount of amine groups. Within the comparison there are two groups, one contains residues with side chains unlikely to possess a charge under the analytical conditions and one with charged side chain groups. For PSF using these residues there is a greater effect on zeta potential even with reduced levels of functionalisation as a result of charged side chains.

Figure 5.13a+b indicate the change in zeta potential for Hf-BTB-NH_2-His may be a result of both the high level of functionalisation and the isoelectric point of histidine. Unpredictably aspartic acid increases the zeta potential the most to 12.4 ± 2.7 mV. It was hypothesised that introducing carboxylate groups onto the MON surface would decrease the zeta potential. This result indicates that both carboxylate groups of the residue are involved in interactions and therefore are not bringing additional negative charge to the surface. The AFM image of Hf-BTB-NH_2-Asp (Figure 5.7d) shows highly defected nanosheets and the ditopic nature of Asp could be an explanation for both

observations. Aspartic acid has previously been utilized as a linker in work synthesising the metal-organic framework MIP-202(Zr) therefore indicating that it is possible.[10]

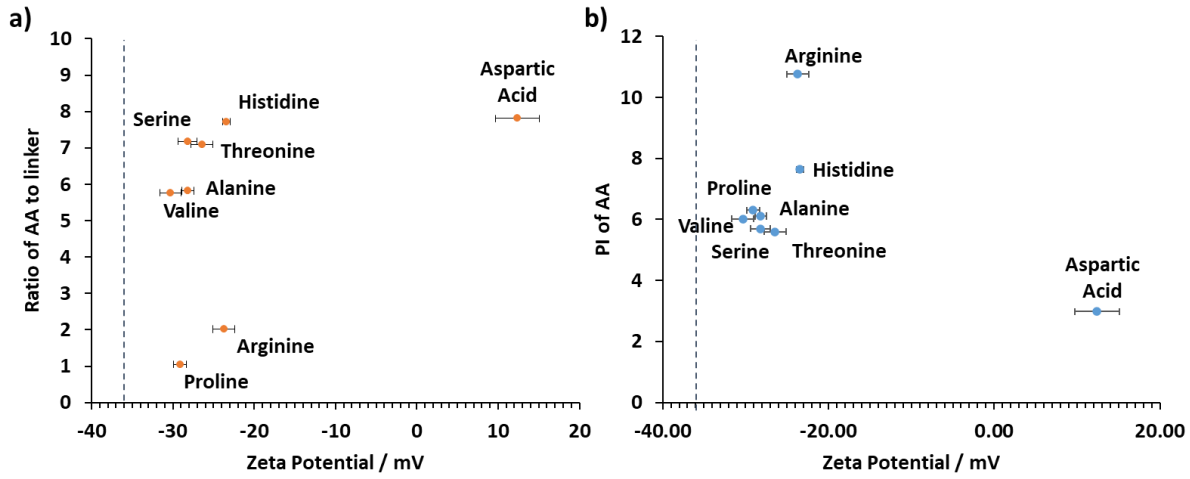

Figure 5.13: a) Comparison of Hf-BTB-NH_2-AA to show the effect of the ratio of amino acid to linker on the zeta potential of the system, b) Comparison of Hf-BTB-NH_2-AA to show the effect of the pI of amino acid on the zeta potential of the system. Dashed line is zeta potential of Hf-BTB-NH_2 in both graphs.

For the rest of the Hf-BTB-NH_2-AA systems, the level of functionalisation is likely what determines the zeta potential of the system due to the amount of positively charged amine groups and blocking the access of negative phosphate ions binding to metal clusters. Direct comparison of the zeta potentials is difficult due to the varying levels of functionalisation however changes in zeta potential are apparent and can assist in the further tuning of the MONs surface towards a given target.

The contact angle measurements for Hf-BTB-NH_2 and all Hf-BTB-NH_2-AA are shown in Figure 5.14. When compared to unmodified Hf-BTB-NH_2, the residue functionalised MONs resulted in a change in contact angle and therefore change in hydrophobicity. Amino acids with hydrophobic side groups such as valine and alanine increased the contact angle measurement to 51.2 ° and 32.7 ° respectively. Interestingly proline significantly increased the hydrophobicity of the surface with the smallest amount of functionalisation (1.05 per BTB-NH_2), this is likely a result of it not having a free primary amine like the other residues. Arginine also slightly increased the contact angle measurement which is surprising considering its basic nature however this could be evidence of side chain involvement in interlayer interactions.

Histidine on the other hand significantly increased the hydrophilicity of the surface, reducing the contact angle measurement to 2.5 °. Hf-BTB-NH_2-His was one of the most functionalised surfaces (7.72 per BTB-NH_2) which will have contributed to the significant change in surface properties. Aspartic acid also increased the hydrophilicity of the surface with a similar amount of functionality compared to histidine (7.81 per BTB-NH_2). Serine and threonine, with alcohols in their side chains, also had a reduced contact angle compared to Hf-BTB-NH_2 but not as significantly as the charged residues. Although there is a clear difference in hydrophobicity for each Hf-BTB-NH_2-AA MON system, there is evidence to suggest this is a combination of adsorbed and coordinated residues. Further interrogation of the MONs was required in order to determine their applicability in biosensing.

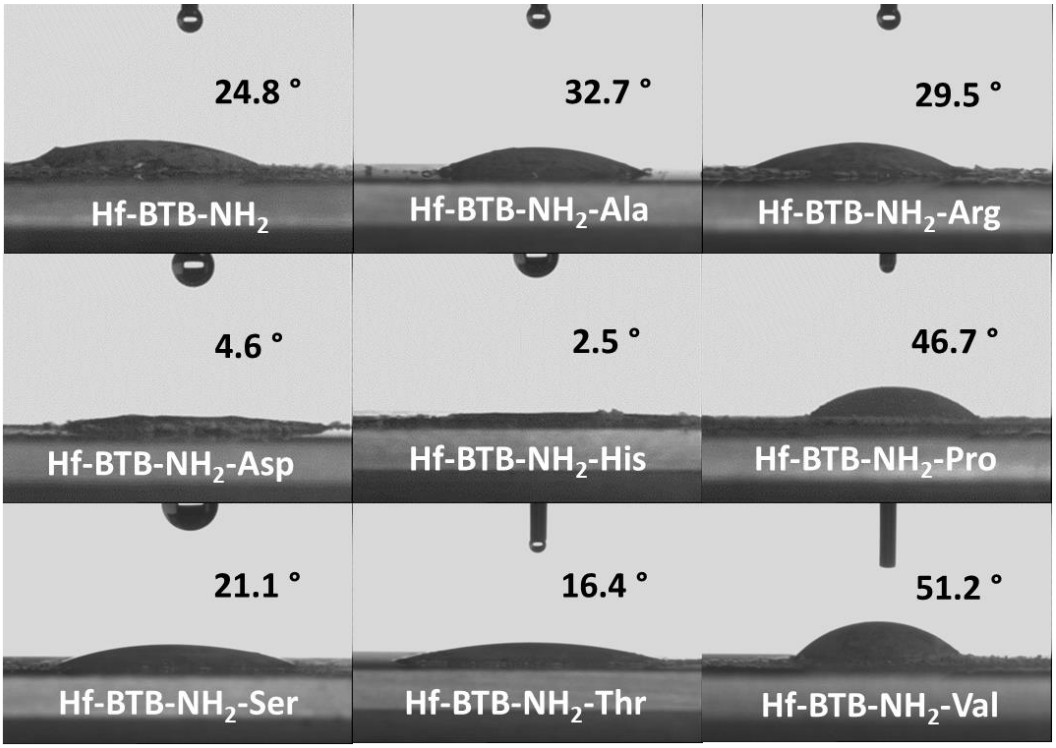

Figure 5.14: Contact angle measurements for all amino acid functionalised Hf-BTB-NH_2

5.2.3 Stability Testing

The stability of the Hf-BTB-NH_2-AA MONs was determined in order to confirm applicability in biosensing. After incubation in PBS for 24 hr the resulting material was characterised using XRPD (Figure 5.15). The resulting pattern indicated the extra peaks previously shown on Hf-BTB-NH_2-AA XRPD patterns for the appropriate amino acid were no longer visible. This indicated that the PBS wash had removed any adsorbed residues that had not coordinated to the MON. ^{1}H NMR spectra revealed there was still residue remaining after PBS incubation (Table 5.3), indicating some suitability to QCM sensing conditions. Limited data was available due to lost sample as a result of the harsh degradation conditions required for solution state NMR preparation. There was data for Ala, Arg, His and Ser with all experiencing a significant reduction in functionalisation compared to the originally synthesised Hf-BTB-NH_2-AA materials.

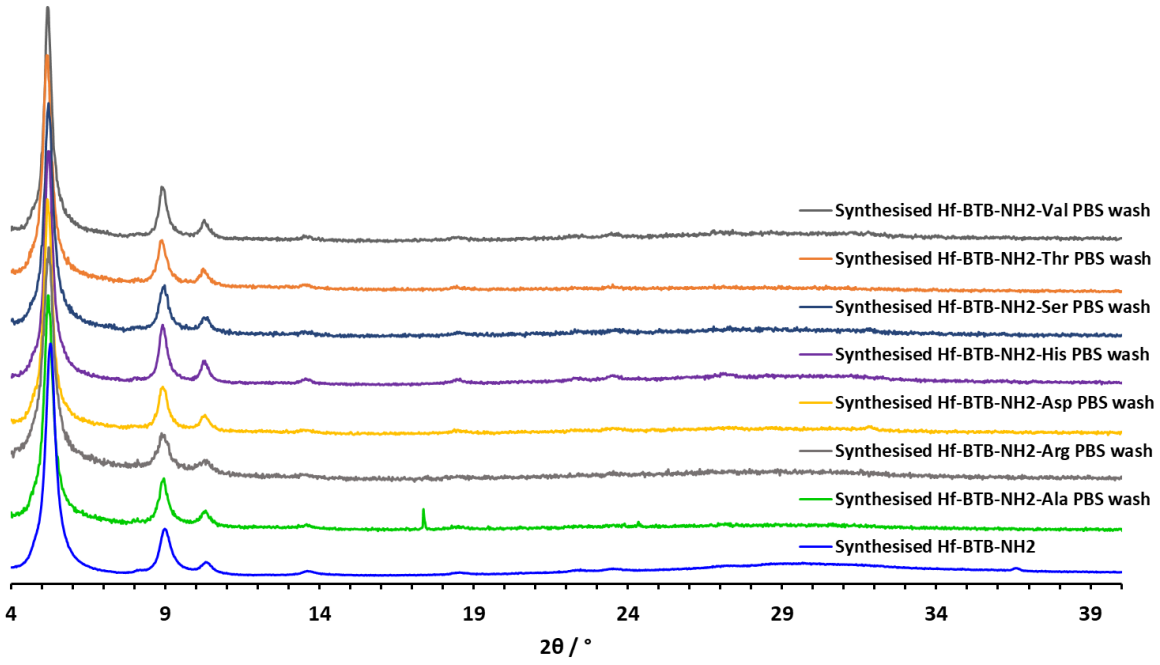

Figure 5.15: XRPD of synthesised Hf-BTB-NH_2-AA after incubation in PBS compared to synthesised Hf-BTB-NH_2.

Table 5.3: Ratio of amino acid to linker for each Hf-BTB-NH_2-AA system determined by NMR after incubation in PBS for 24 h.

Amino Acid	Ratio of AA vs linker	Ratio of AA vs linker post PBS incubation
Alanine	5.82	0.23
Arginine	2.02	0.75
Histidine	7.72	0.56
Serine	7.18	0.54

Another assessment of the ratio of amino acid to linker was made comparing values to the pKa of the carboxylate and pI of the residue (Figure 5.16). The same general trend in increasing pKa of the carboxylate and decreasing ratio of residue to linker was observed. The opposite trend was found in Figure 5.16b where there was a positive correlation between isoelectric point and the ratio of residue to linker. The MON has a negative charge (- 36.9 mV), therefore residues that were positively charge would have a higher affinity for the surface through electrostatic interactions as discussed in chapter 3.

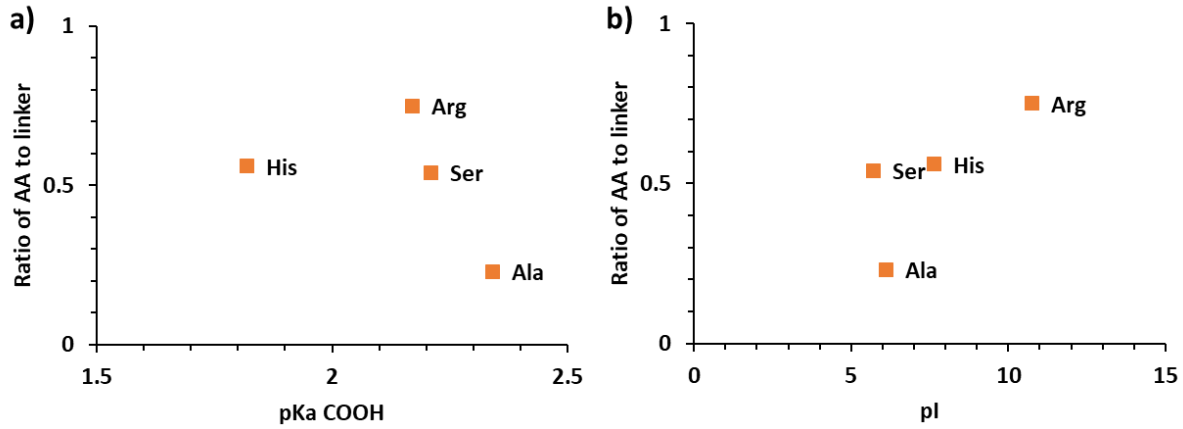

Figure 5.16: a) Effect of the pKa of the amino acids carboxylate on the ratio of amino acid to linker after PBS incubation, b) effect of the pI of the amino acid on the ratio of amino acid to linker after PBS incubation.

This inspired a more rigorous washing procedure where the synthesised Hf-BTB-NH_2-AA MONs underwent a third washing step using DI water (3 X 10 mL wash with one overnight, 4,500 rpm 30 mins). We hypothesised that after the water wash that any remaining residue is likely coordinated to the MON and will remain stable under the aqueous conditions required for biosensing such as the QCM set up mentioned in chapter 3.

5.2.4 Washing Optimisation

Hf-BTB-NH_2-Val had a clear residue peak at 7.4 ° (Figure 5.4) which is in a key area of the XRPD pattern and Hf-BTB-NH_2-Asp had the highest ratio of residue to linker from the NMR. Therefore, these two systems were selected to be the focus of the new washing procedure. The same synthetic process of Hf-BTB-NH_2 incubation with the corresponding amino acid in DMF overnight was followed. The three DMF washes which included an overnight wash was followed by the extra three DI water washes (3 X 10 mL wash with one overnight, 4,500 rpm 30 mins) and then the same ethanol washes as described previously. The resulting material was characterised using XRPD (Figure 5.17) where the extra residue peaks seen originally were no longer present.

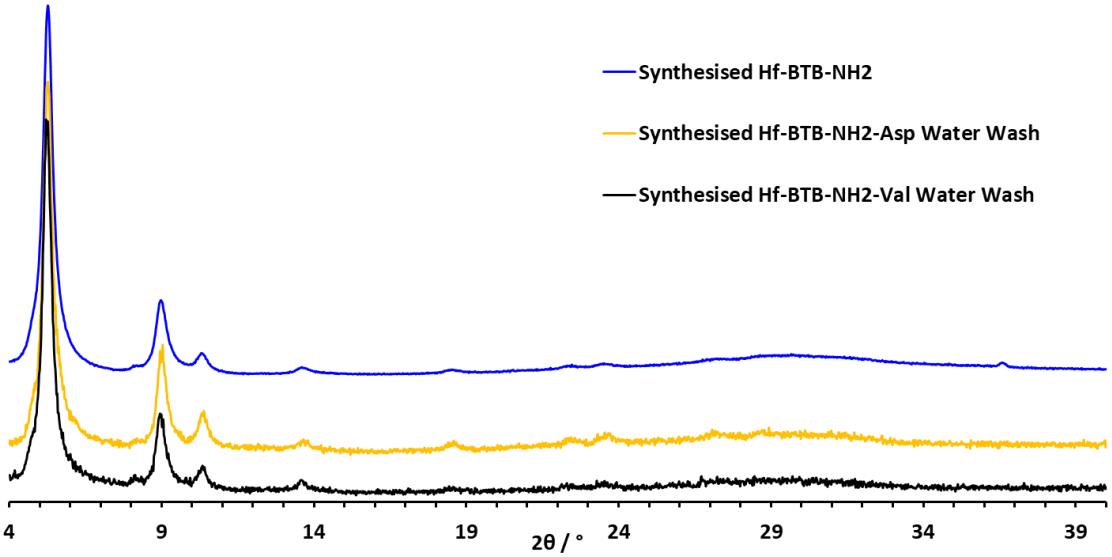

Figure 5.17: XRPD pattern of synthesised Hf-BTB-NH_2 and Hf-BTB-NH_2-Asp and Hf-BTB-NH_2-Val after the water wash

A reduction in the peaks associated with the amino acids was observed on the ATR-IR spectra (Figure 5.18) also evidence of the removal of excess residue. For both Hf-BTB-NH_2-Val and Hf-BTB-NH_2-Asp there were changes to the spectra compared to Hf-BTB-NH_2 at 1650 cm^{-1} where a peak no longer appeared. The ^1H NMR spectra showed a significant decrease in the ratio of amino acid to linker with Asp falling from 7.81 per linker molecule to 1.56 and Val falling from 5.35 per linker to 0.35. Indicating a total functionalisation of 3.12 and 0.7 residues per MON subunit respectively.

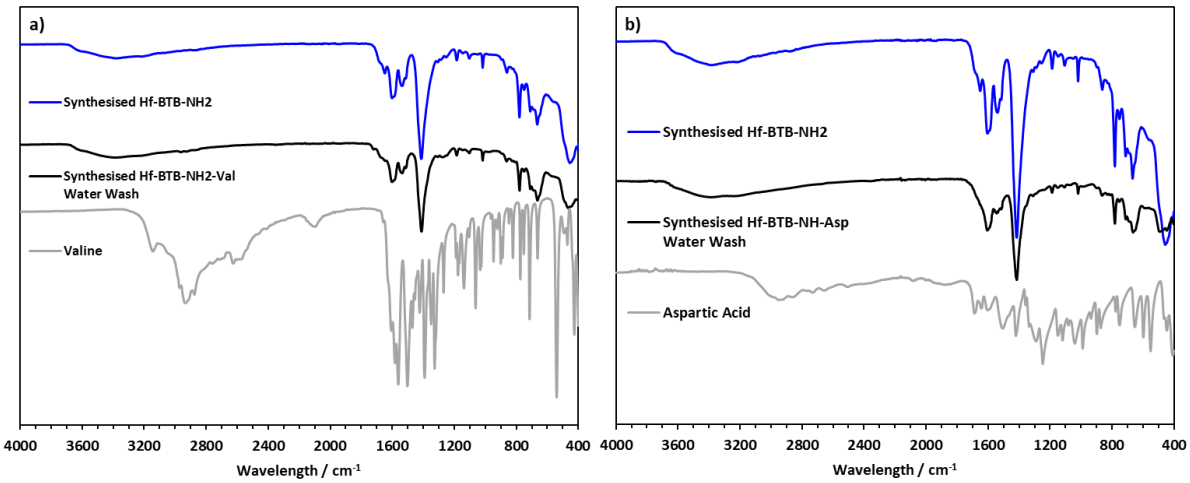

Figure 5.18: ATR-IR spectra of a) synthesised Hf-BTB-NH_2-Val compared to synthesised Hf-BTB-NH_2 and L-valine, b) synthesised Hf-BTB-NH_2-Asp compared to synthesised Hf-BTB-NH_2 and aspartic acid.

Particle size analysis was performed in order to determine the effect of the water wash. AFM images (Figure 5.19a) of Hf-BTB-NH_2-Val revealed MONs that were on average 1.2 nm in height and 1094 nm in length. This is consistent with the height of single layer Hf-BTB-NH_2-Val nanosheets that were identified earlier (Figure 5.9). For Hf-BTB-NH_2-Asp nanosheets were on average 15 nm in height and 200 nm in length (Figure 5.19b+c). This is a drastic difference in size compared to the previous size analysis, which is evidence that the AFM images of Hf-BTB-NH_2 in Figure 5.7d could be crystalline aspartic acid.

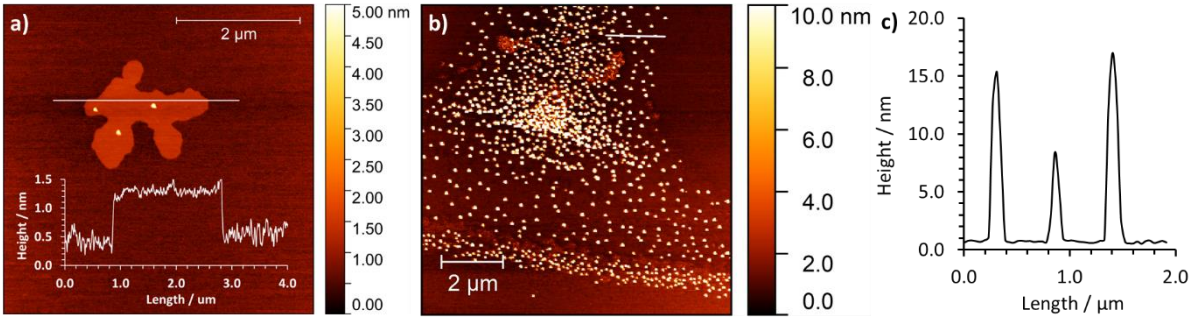

Figure 5.19: a) AFM image of Hf-BTB-NH_2-Val with inserted height profile, b) AFM image of Hf-BTB-NH_2-Asp, c) height profile from AFM b.

Having confirmed the presence of the amino acid after the new washing step, further surface characterisation was carried out in order to determine whether there would be significant changes to the surface properties as a result of the removal of excess adsorbed material. Zeta potential measurements (Figure 5.20) were performed to determine the impact of the more rigorous washing on the surface charge of the MONs. There was no significant change of the zeta potential of Hf-BTB-NH_2-Val post water wash (-29.5 ± 0.4 mV) compared to that with only DMF washes (-30.3 ± 1.3 mV). This is likely a result of the measurement environment being aqueous and therefore uncoordinated residue in the first instance was desorbed therefore didn't impact the initial zeta potential reading. The isopropyl side chain of Val does not carry charge and therefore is unlikely to have a significant effect on the overall zeta potential as discussed above. There is a slight change in the zeta potential observed for Hf-BTB-NH_2-Asp as the average reading falls from 12.4 ± 2.7 mV to 2.1 ± 0.3 mV. However, the material is still significantly more positively charged than the starting material (-36 mV for Hf-BTB-NH_2) with the amine group from the residue introducing the positive charge as the carboxylates coordinate to the metal. Considering that there was a significant decrease in the ratio of Asp to linker after the extra washing steps, the change in zeta potential is minimal and the same prediction that both carboxylate groups are involved in metal centre coordination stands. Trends regarding the relationship between the ratio of AA to linker and zeta potential drawn previously should be reconsidered as it is likely the ratio is an overestimation.

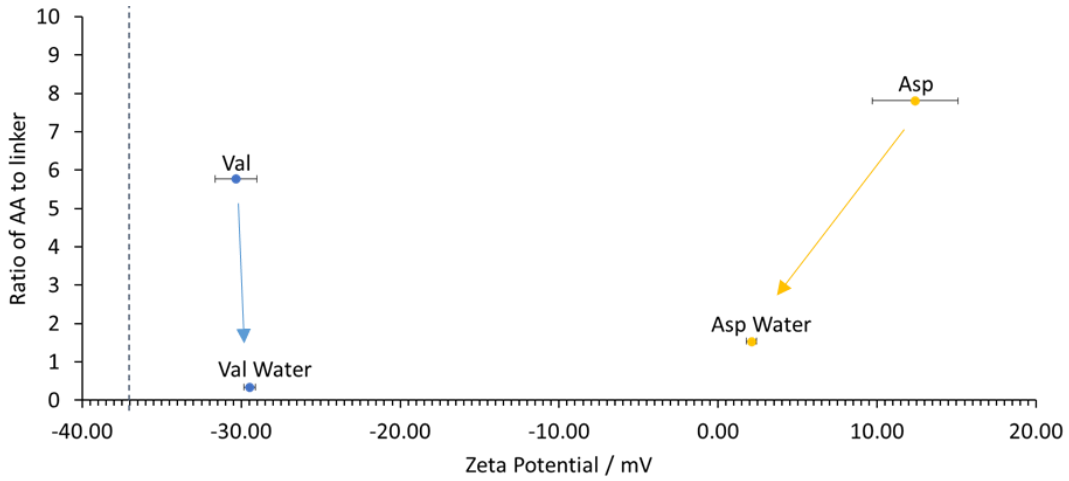

Figure 5.20: Zeta potential measurements of Hf-BTB-NH_2-Val (blue) and Hf-BTB-NH_2-Asp (yellow) with and without the extra water washing step.

Contact angle measurements (Figure 5.21) were also carried out in order to ascertain whether there was any difference in the hydrophilicity of the surface of the functionalised MON after the rigorous washing step. On comparison to the unfunctionalized MON (Hf-BTB-NH_2) and previously functionalised material, the extra washing step has little impact upon the contact angle of Hf-BTB-NH_2-Asp and a significant impact on Hf-BTB-NH_2-Val. For the aspartic acid functionalisation there is a change from 4.6 ° to 0 ° which indicates the material is slightly more hydrophilic, but this may be as a result of slightly different packing onto the glass slide. There is a significant drop in the hydrophobicity of the surface for Hf-BTB-NH_2-Val (51.2 ° to 20.7 °) which showed similar hydrophobic character as Hf-BTB-NH_2. This is likely a result of the low degree of functionalisation with excess adsorbed valine no longer contributing the hydrophobic character of its side chain.

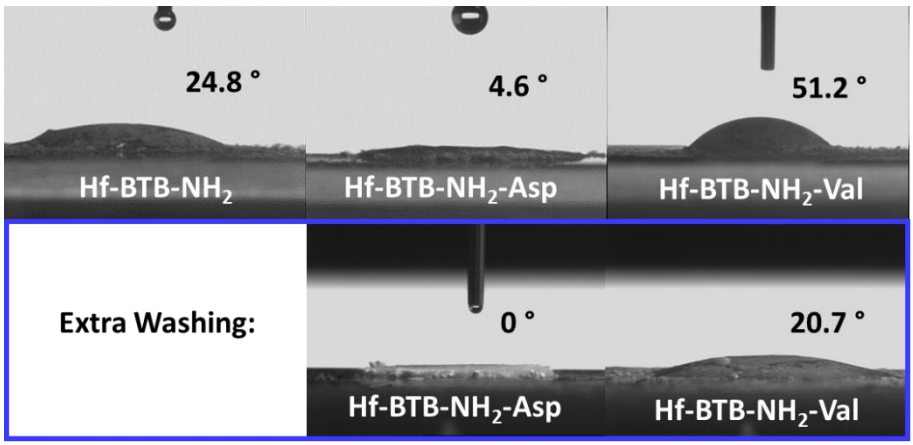

Figure 5.21: Contact angle measurements of synthesised Hf-BTB-NH_2, Hf-BTB-NH_2-Asp and Hf-BTB-NH_2-Val both with (bottom line) and without (top line) the extra water washing step.

Further stability testing through PBS incubation showed some peak broadening on the XRPD pattern (Figure 5.22) indicating reduction in crystallite size. The material was digested and ^{1}H NMR revealed that for both Hf-BTB-NH_2-Val and Hf-BTB-NH_2-Asp residue remained. There was no significant change in the ratio of valine to linker (~ 0.3 Val per linker) whereas there was a significant reduction in the amount aspartic acid which reduced to ~ 0.4 per linker from ~ 1.5, which indicates that PBS influences the PSF stability.

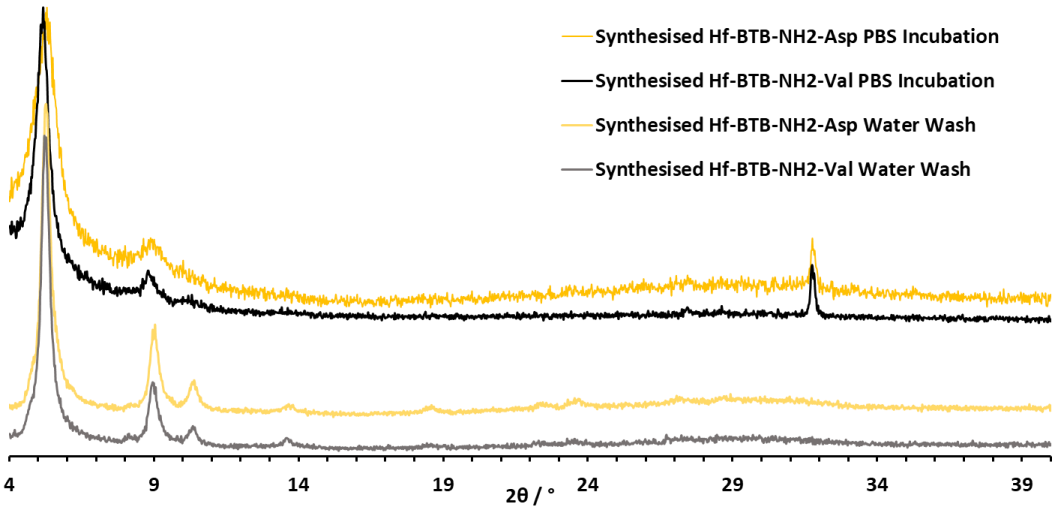

Figure 5.22: XRPD pattern of synthesised Hf-BTB-NH_2-Val and Hf-BTB-NH_2-Asp with water washing before and after incubation in PBS for 24 h.

Residue did remain in both cases however, the stability of Hf-BTB-NH_2-Asp in PBS remains uncertain. There is a strong possibility that Hf-BTB-NH_2-Val would remain stable under phage display and the QCM sensor conditions. One test of stability would be to functionalise the QCM sensor with Hf-BTB-NH_2-Val as described in chapter 3. Exposing the system to a flow of PBS and measuring the change in frequency would reveal any drift associated with the set up. This would indicate whether the system was suitable for sensor preparation.

5.3 Conclusions

The aim for this chapter was to determine whether Hf-BTB-NH_2 surfaces could be modified post-synthetically with biologically relevant molecules and to establish the prospects of the resulting material as biosensor surfaces. Whilst incubation of Hf-BTB-NH_2 with various amino acids produced surfaces with a variety of properties, it was likely a result of the combination of both coordinated and adsorbed residues. For certain applications such as controlled drug delivery, the range in surface functionality accessed in this way may be suitable.[11] However, for the construction of synthetic biosensor surfaces, an excellent stability is required. The noncovalent interactions between the MON

surface and adsorbed residues is likely to not meet the stability standards essential for highly selective and sensitive biosensors. The predictability over the binding sites on the MON surface becomes lost.

The most promising cases of coordination PSF came from Hf-BTB-NH_2-Val after water washing and Hf-BTB-NH_2-Pro. Hf-BTB-NH_2-Val with water washing retained the same level of functionalisation after PBS incubation. As this simulates the conditions of the QCM sensor set up, it is a good indication of compatibility. This also indicates that if water washing was used for PSF with the other residues the same stability would be observed. This is backed up by the initial PBS stability experiment for the Hf-BTB-NH_2-AA without water washing where the was evidence of the presence of Ala, Arg, His and Ser after PBS incubation. Hf-BTB-NH_2-Asp showed less stability therefore an extra PBS wash might also be required before sensor preparation. Hf-BTB-NH_2-Pro showed no evidence of crystallised proline in the XRPD pattern and had a subtle functionalisation of 1.07 per linker. Whilst there was no significant change to the zeta potential, Hf-BTB-NH_2-Pro produced a significant change in hydrophobic character.

The general trends observed included a decreasing level of functionalisation on increasing the pKa of the carboxylate of the residue. The level of amino acid functionalisation increased as the zeta potential increased as a result of exposed amine groups. Residues with charged side chains will had a greater influence on zeta potential (arginine, histidine and aspartic acid). After incubation of Hf-BTB-NH_2-AA in PBS there was a general trend of increasing ratio of residue to linker on increasing isoelectric point indicating electrostatic interactions are involved where residues with positive side chains have a higher affinity for the negative MON surface in aqueous conditions. The height of the functionalised MONs increased overall where: His, Ala and Val subtly increased the average height to 1.2 – 1.4 nm; Ser, Thr and Pro increased the average height to 2.2 – 4.3 nm and Arg and Asp post water wash increased the average height to 8.3 – 15 nm.

5.4 Future Work

Immediate experiments would involve repeating the water washing steps on the other Hf-BTB-NH_2-AA systems and carrying out the PBS incubation experiment. To increase the level of coordinative PSF and replace more formate groups there are further optimisations to the procedure that could be undertaken. Increasing temperature (60 °C) and prolonging the experiment have been showed to work previously.[1213] Hf-BTB-NH_2 could also undergo activation via heat treatment or exposure to HCl in order to remove the formic acid groups before residue incubation.

5.5 Experimental

5.5.1 Synthesis and exfoliation of Hf-BTB-NH_2

To prepare Hf-BTB-NH_2 MONs $HfCl_4$ (34.59 mg, 0.108 mmol) and BTB-NH_2 (32.87 mg, 0.072 mmol) were added to a 20 mL screw-cap glass vial. After the addition of 12.5 mL DMF, the mixture was ultrasonically dissolved to obtain clear solution. To the resulting solution, 2.5 mL formic acid and 0.7 mL H_2O was added and placed in a preheated oven at 120 °C for 48 h. After completion of the reaction, the vial was taken out of the oven and cooled down to room temperature. The turbid solution was centrifuged to collect Hf-BTB-NH_2 as a pale yellow precipitate and washed three times with DMF. To prevent the stacking of the MON layers, Hf-BTB-NH_2 was kept in DMF until needed for further studies. For analysis purposes, the solid was collect via centrifugation and dried 120 °C overnight. Elemental Analysis Expected Mass %: C 27.3, H 2.04, N 1.18, Found Mass %: C 24.8, H 2.9, N 1.0. ^{1}H NMR (NaOD/D_2O, 24 hr sonication): 8.24 (s, 2H), 7.72 – 7.65 (m, 4H), 7.58 (d, J = 8.4 Hz, 2H), 7.21 (d, J = 8.3 Hz, 2H), 7.11 (d, J = 8.2 Hz, 4H), 7.03 (s, 2H). Phase purity confirmed by XRPD with a comparison to NUS-8-Hf found in CCDC (1567189).

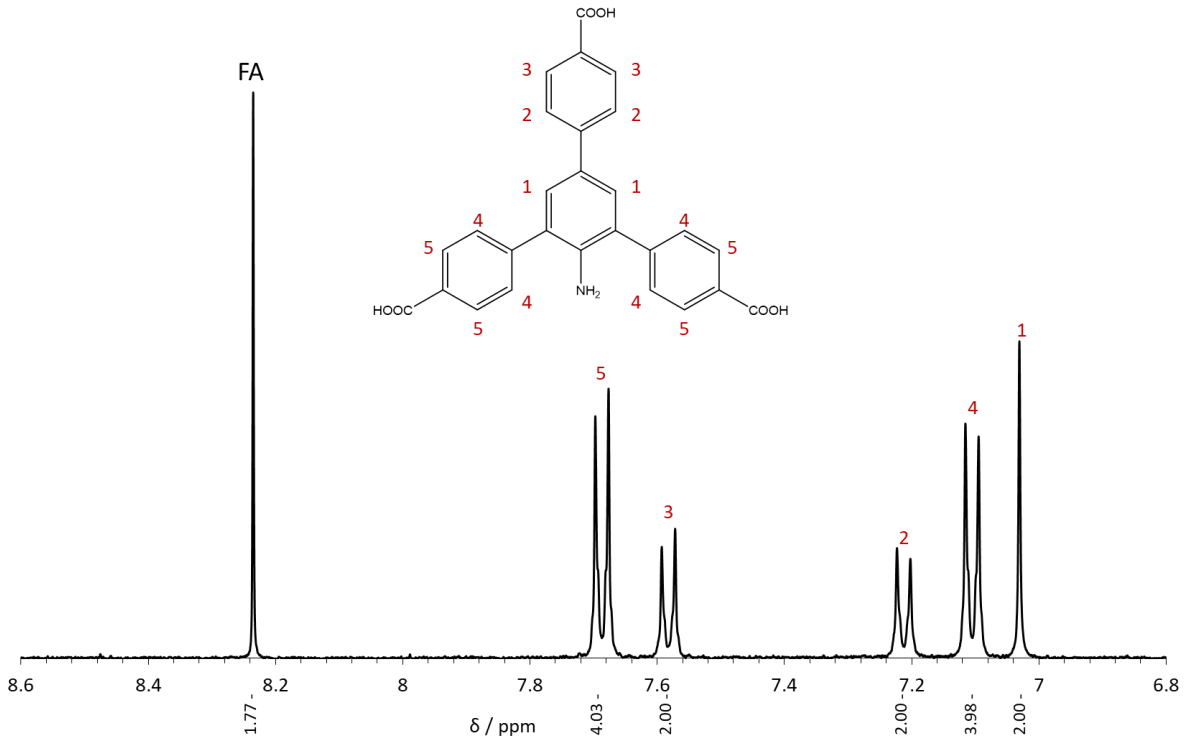

Figure 5.23: ^{1}H NMR spectrum of Hf-BTB-NH_2 digested with NaOD/D_2O and a 24 hr sonication, with peaks assigned according to the inset molecular structure of BTB-NH_2.

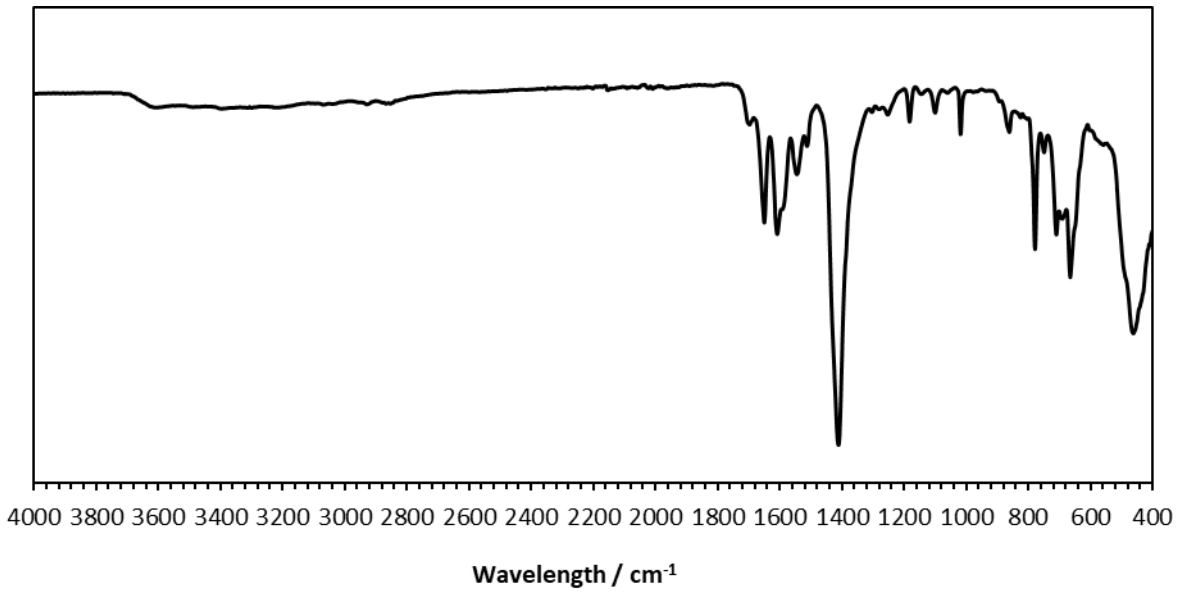

Figure 5.24: ATR-IR spectrum of Hf-BTB-NH_2

5.5.2 Synthesis and exfoliation of Hf-BTB-NH_2-Ala

Six equivalents of alanine (0.0756 mmol, 6.7 mg) was added to Hf-BTB-NH_2 (0.0126 mmol, 15 mg) in DMF (3 mL) and was left stirring overnight. After three DMF (10 mL) washes (one left overnight) and three ethanol (10 mL) washes (last one left over the weekend) the resulting material was collect via centrifugation and dried 120 °C overnight. ^{1}H NMR ($NaOD/D_2O$, 24 hr sonication): 8.24 (s, 2H), 7.72 – 7.65 (m, 4H), 7.58 (d, *J* = 8.4 Hz, 2H), 7.21 (d, *J* = 8.3 Hz, 2H), 7.11 (d, *J* = 8.2 Hz, 4H), 7.03 (s, 2H), 3.08 (q, *J* = 7.0 Hz, 6H), 0.99 (dd, *J* = 7.0, 0.6 Hz, 18H). Phase purity confirmed by XRPD with a comparison to NUS-8-Hf found in CCDC (1567189).

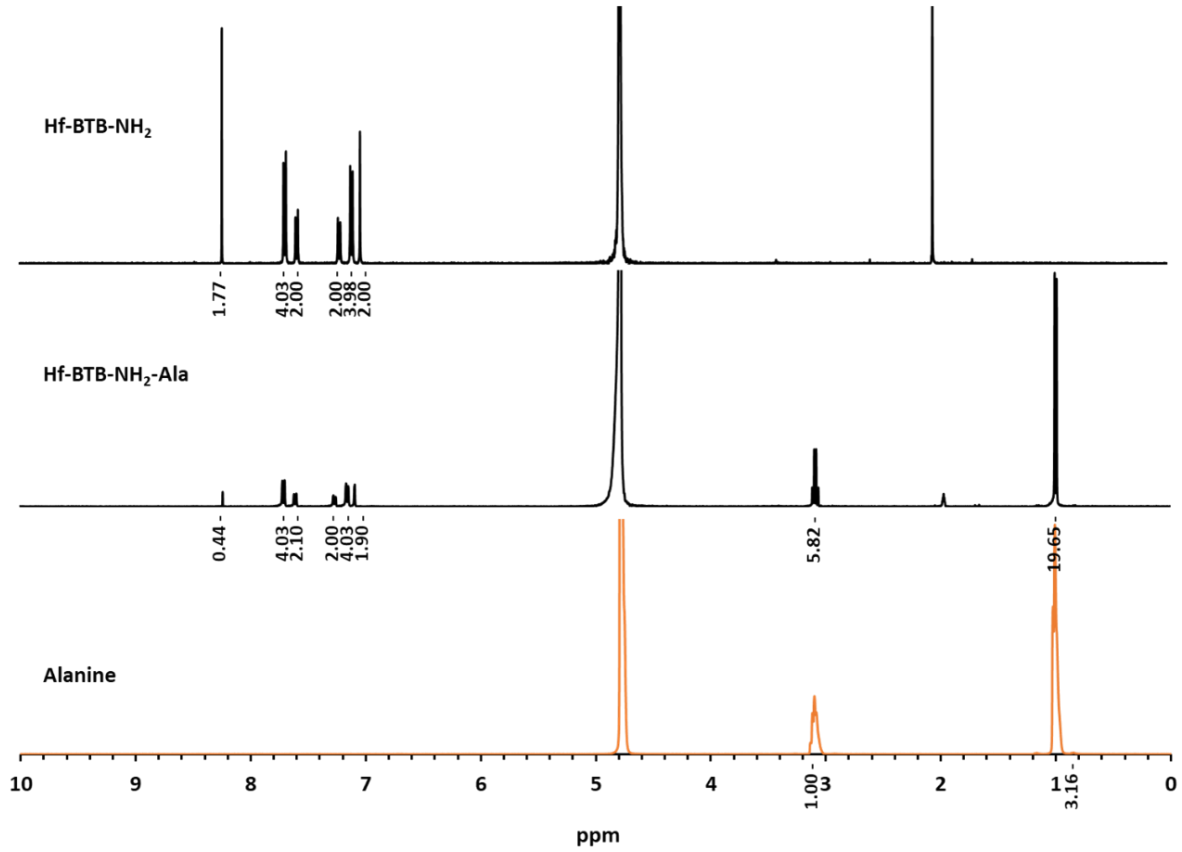

Figure 5.25: ^{1}H NMR data for synthesised Hf-BTB-NH_2, synthesised Hf-BTB-NH_2-Ala, and alanine

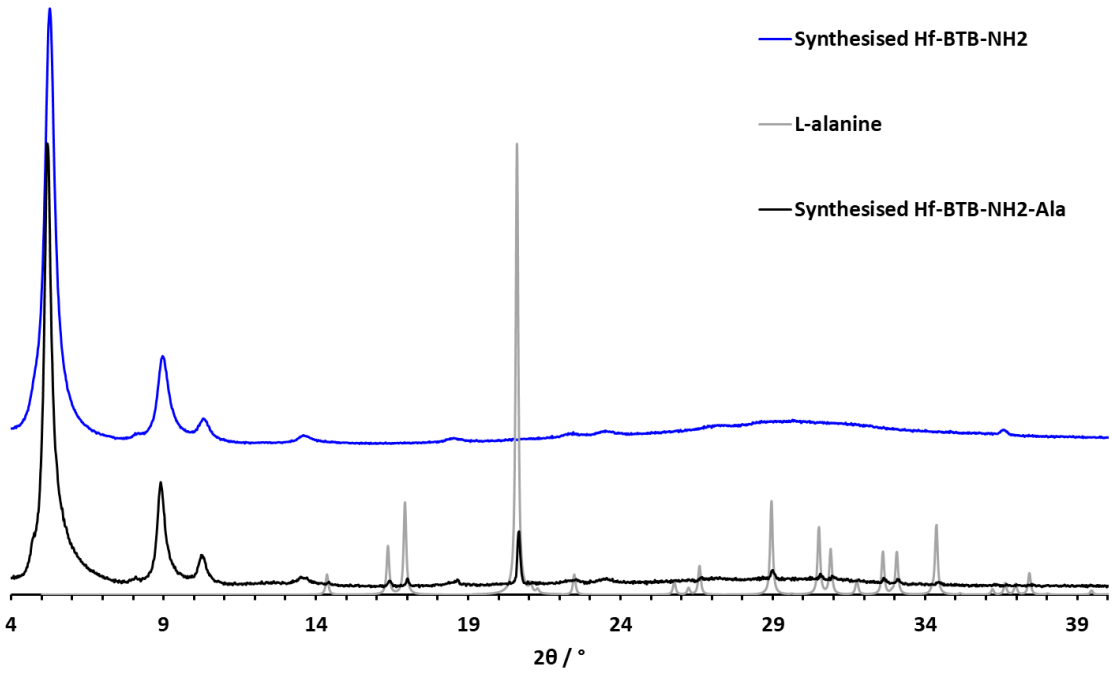

Figure 5.26: Comparison of XRPD pattern of synthesised Hf-BTB- NH_2, synthesised Hf-BTB-NH_2-Ala and L-alanine (CCDC- 1203203)

5.5.3 Synthesis and exfoliation of Hf-BTB-NH_2-Arg

Six equivalents of arginine (0.0756 mmol, 13.2 mg) was added to Hf-BTB-NH_2 (0.0126 mmol, 15 mg) in DMF (3 mL) and was left stirring overnight. After three DMF (10 mL) washes (one left overnight) and three ethanol (10 mL) washes (last one left over the weekend) the resulting material was collect via centrifugation and dried 120 °C overnight. ^{1}H NMR (NaOD/D_2O, 24 hr sonication): 8.24 (s, 2H), 7.72 – 7.65 (m, 4H), 7.58 (d, *J* = 8.4 Hz, 2H), 7.21 (d, *J* = 8.3 Hz, 2H), 7.11 (d, *J* = 8.2 Hz, 4H), 7.03 (s, 2H), 3.06 – 3.02 (m, 2H), 2.86 (t, J = 6.7 Hz, 4H), 1.50 – 1.14 (m, 8H). Phase purity confirmed by XRD with a comparison to NUS-8-Hf found in CCDC (1567189).

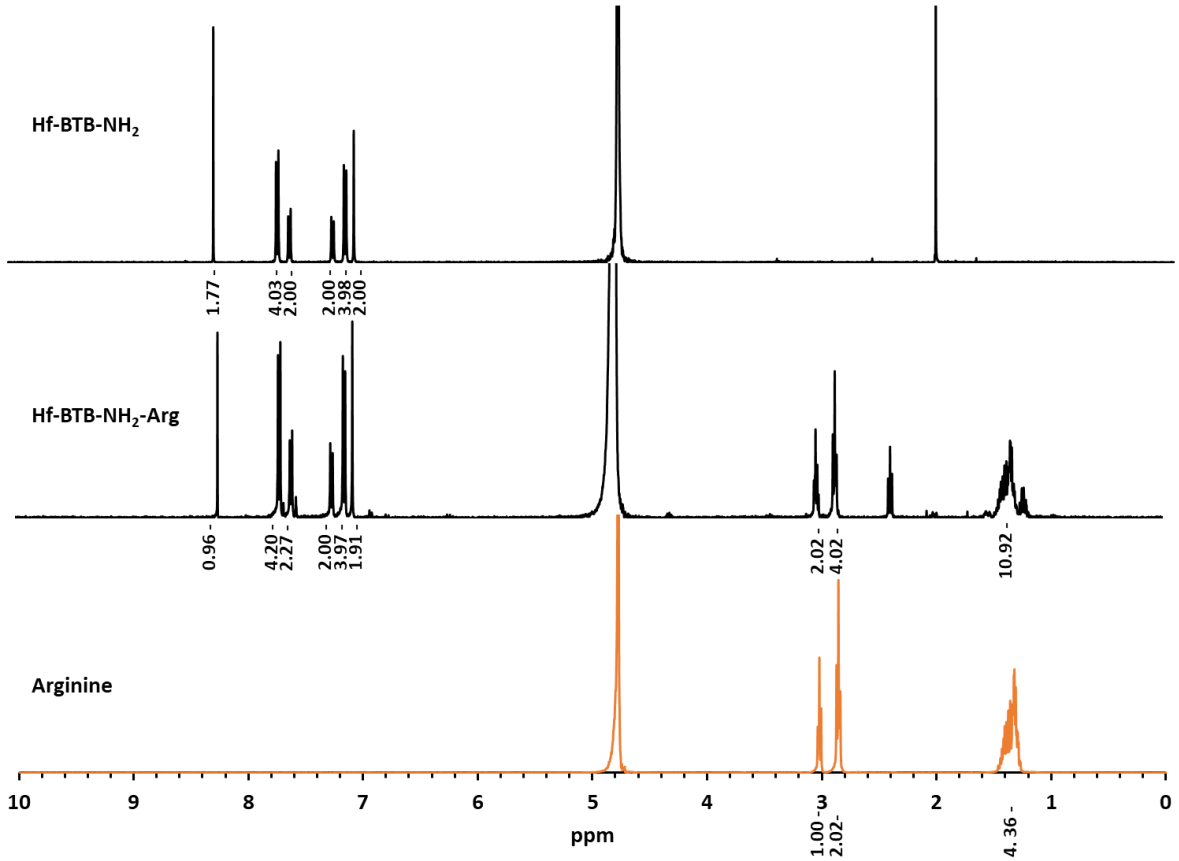

Figure 5.27: ^{1}H NMR data for synthesised Hf-BTB-NH_2, synthesised Hf-BTB-NH_2-Arg, and arginine

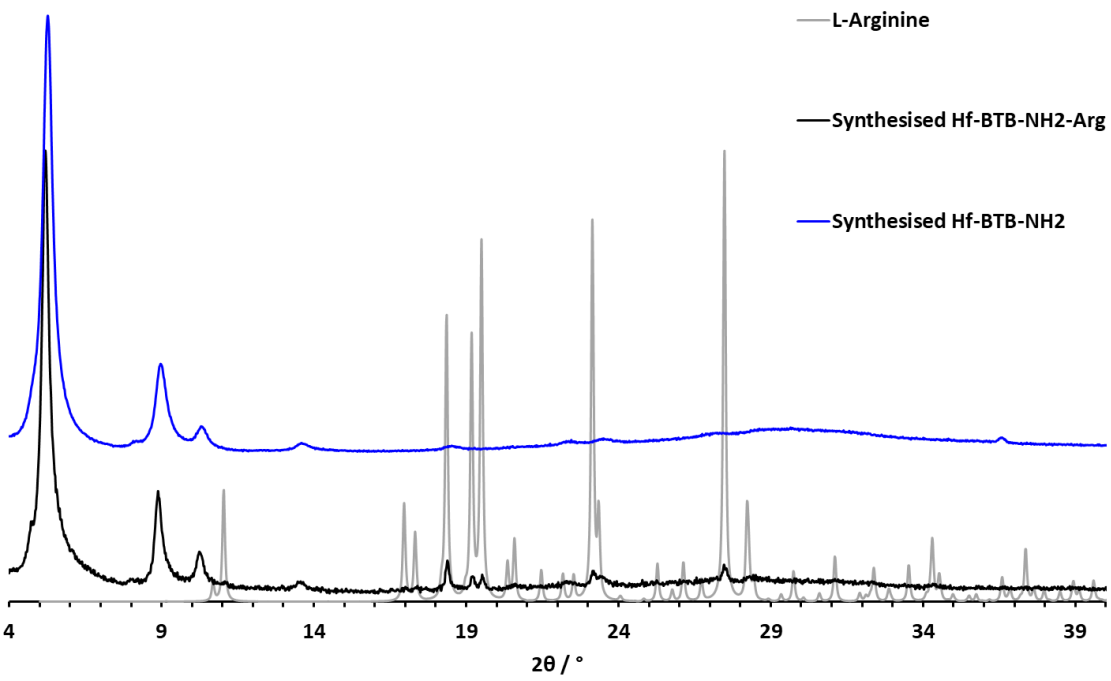

Figure 5.28: Comparison of XRPD pattern of synthesised Hf-BTB- NH_2, synthesised Hf-BTB-NH_2-Arg and L-arginine (CCDC-855058)

5.5.4 Synthesis and exfoliation of Hf-BTB-NH_2-Asp

Six equivalents of aspartic acid (0.0756 mmol, 10.1 mg) was added to Hf-BTB-NH_2 (0.0126 mmol, 15 mg) in DMF (3 mL) and was left stirring overnight. After three DMF (10 mL) washes (one left overnight) and three ethanol (10 mL) washes (last one left over the weekend) the resulting material was collect via centrifugation and dried 120 °C overnight. ^{1}H NMR (NaOD/D_2O, 24 hr sonication): 8.24 (s, 2H), 7.72 – 7.65 (m, 4H), 7.58 (d, *J* = 8.4 Hz, 2H), 7.21 (d, *J* = 8.3 Hz, 2H), 7.11 (d, *J* = 8.2 Hz, 4H), 7.03 (s, 2H), 3.32 (dd, J = 9.8, 3.9 Hz, 8H), 2.41 (dd, J = 15.3, 4.0 Hz, 8H), 2.07 (dd, J = 15.3, 9.7 Hz, 8H). Phase purity confirmed by XRPD with a comparison to NUS-8-Hf found in CCDC (1567189).

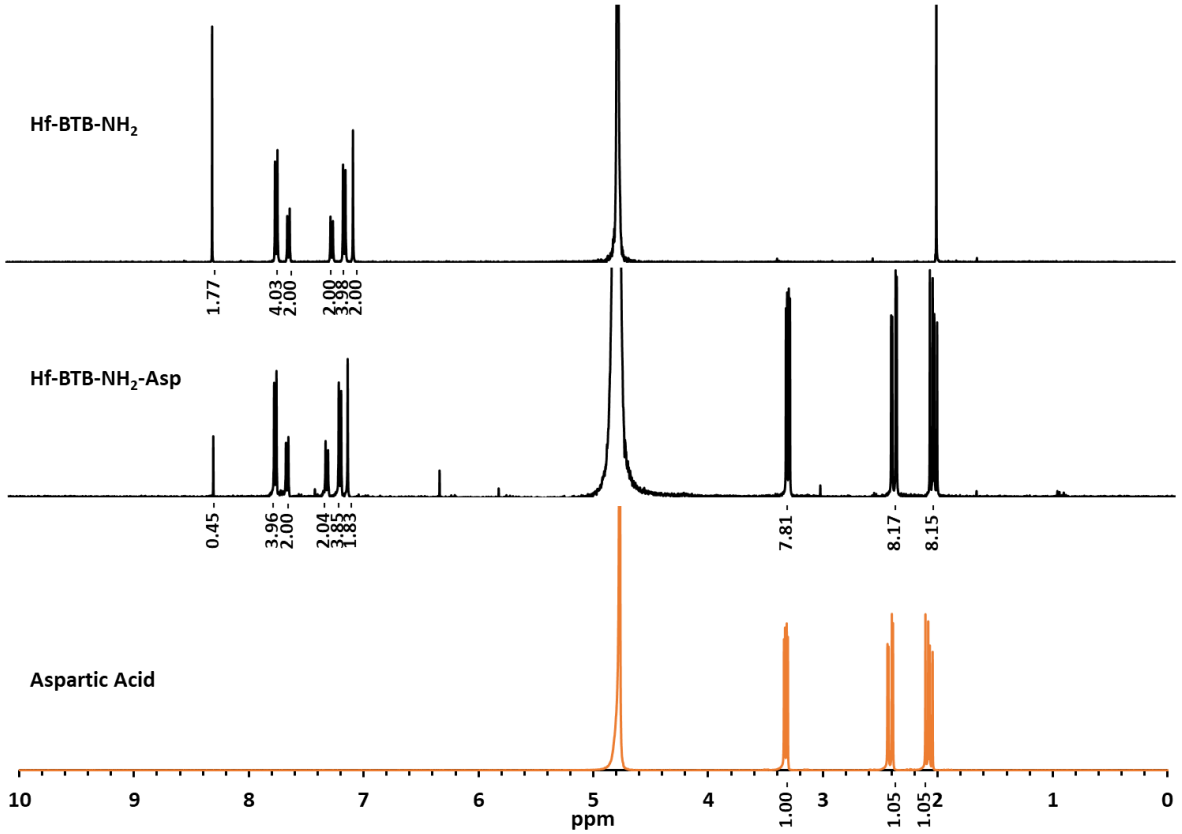

Figure 5.29: ^{1}H NMR data for synthesised Hf-BTB-NH_2, synthesised Hf-BTB-NH_2-Asp, and aspartic acid.

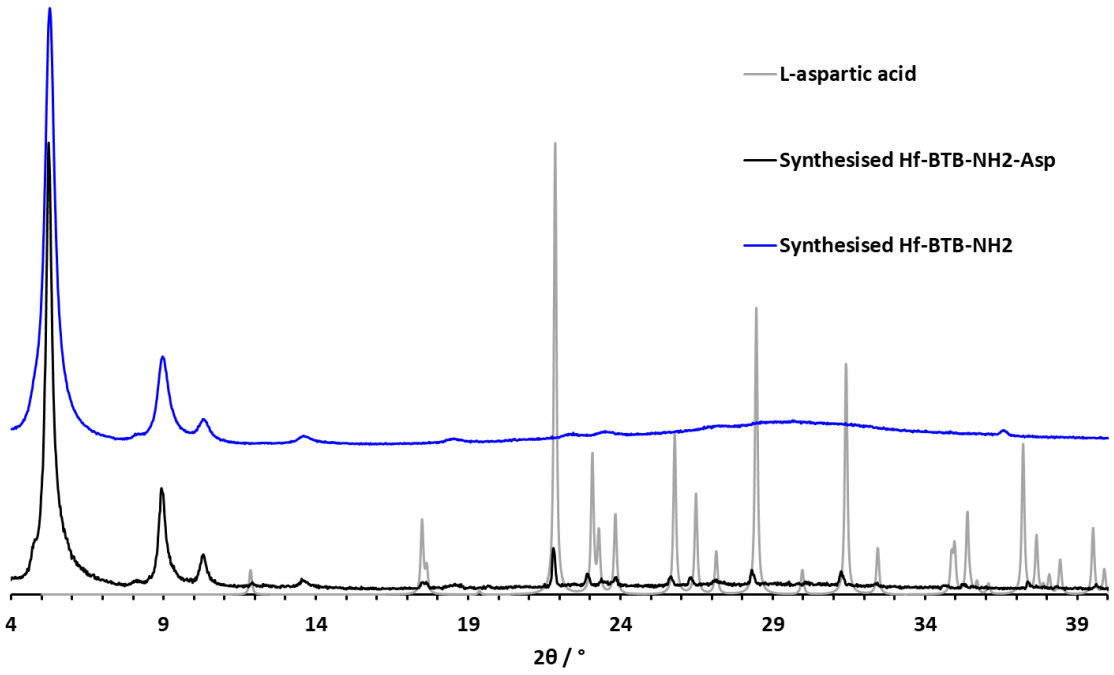

Figure 5.30: Comparison of XRPD pattern of synthesised Hf-BTB- NH_2, synthesised Hf-BTB-NH_2-Asp and L-aspartic acid (CCDC- 652520)

5.5.5 Synthesis and exfoliation of Hf-BTB-NH_2-His

Six equivalents of histidine (0.0756 mmol, 11.7 mg) was added to Hf-BTB-NH_2 (0.0126 mmol, 15 mg) in DMF (3 mL) and was left stirring overnight. After three DMF (10 mL) washes (one left overnight) and three ethanol (10 mL) washes (last one left over the weekend) the resulting material was collect via centrifugation and dried 120 °C overnight. ^{1}H NMR (NaOD/D_2O, 24 hr sonication): 8.24 (s, 2H), 7.72 – 7.65 (m, 4H), 7.58 (d, *J* = 8.4 Hz, 2H), 7.31 (d, J = 1.1 Hz, 7H), 7.21 (d, *J* = 8.3 Hz, 2H), 7.11 (d, *J* = 8.2 Hz, 4H), 7.03 (s, 2H), 6.62 (s, 7H), 3.25 (dd, J = 8.2, 4.9 Hz, 7H), 2.74 (dd, J = 14.5, 4.9 Hz, 7H), 2.52 (dd, J = 14.5, 8.3 Hz, 7H). Phase purity confirmed by XRPD with a comparison to NUS-8-Hf found in CCDC (1567189).

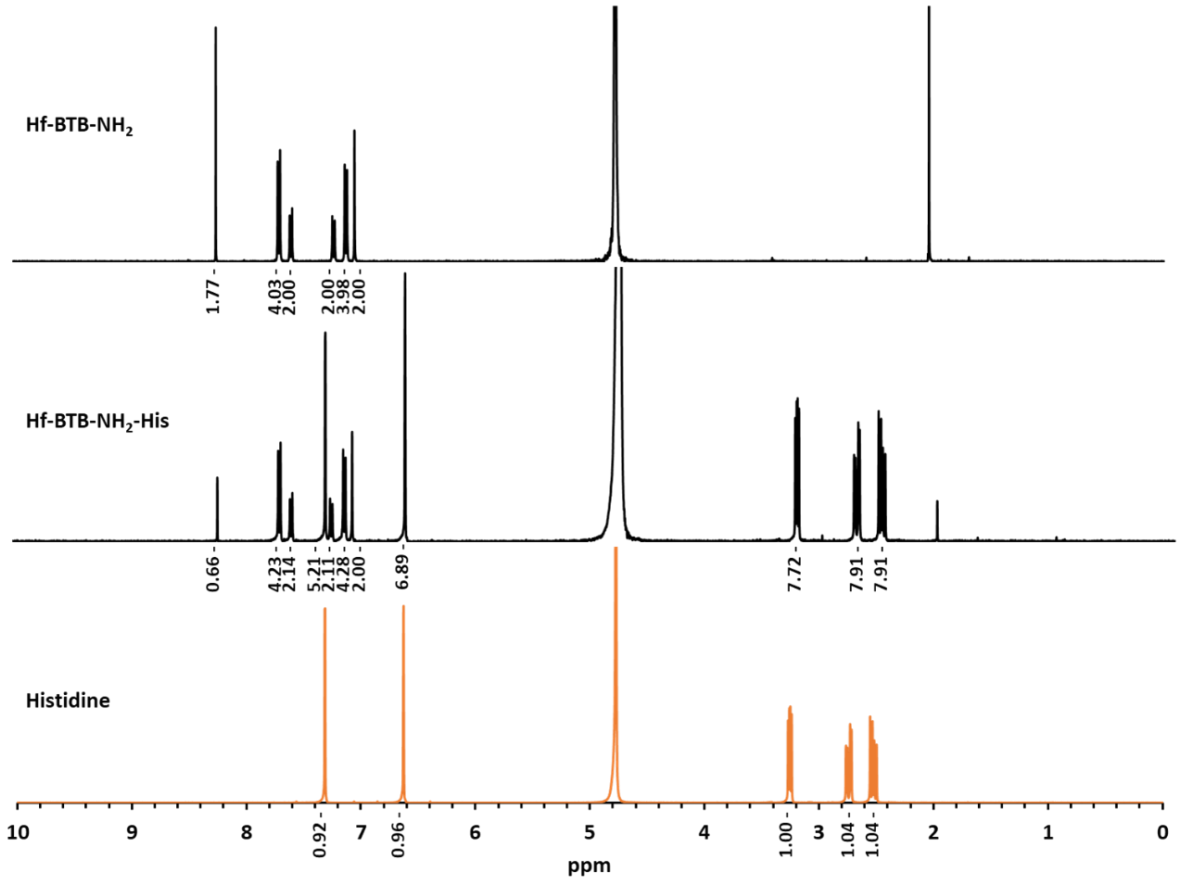

Figure 5.31: ^{1}H NMR data for synthesised Hf-BTB-NH_2, synthesised Hf-BTB-NH_2-His, and histidine.

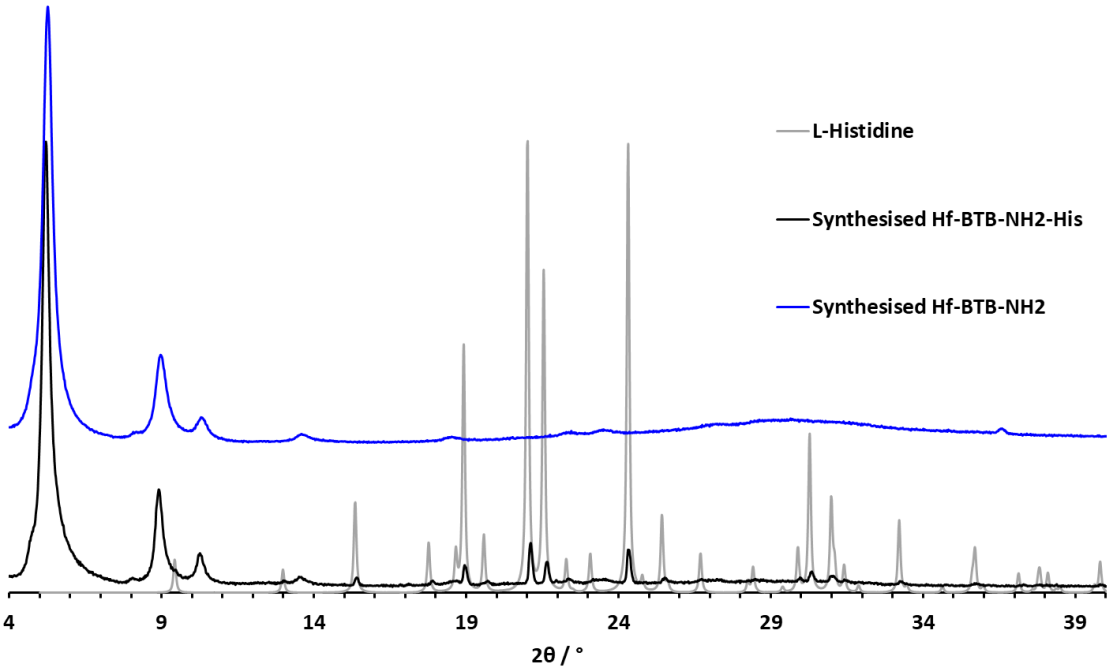

Figure 5.32: Comparison of XRPD pattern of synthesised Hf-BTB-NH_2, synthesised Hf-BTB-NH_2-His and L-histidine (CCDC- 1206542)

5.5.6 Synthesis and exfoliation of Hf-BTB-NH_2-Pro

Six equivalents of proline (0.0756 mmol, 17.4 mg) was added to Hf-BTB-NH_2 (0.0126 mmol, 15 mg) in DMF (3 mL) and was left stirring overnight. After three DMF (10 mL) washes (one left overnight) and three ethanol (10 mL) washes (last one left over the weekend) the resulting material was collect via centrifugation and dried 120 °C overnight. ^{1}H NMR (NaOD/D_2O, 24 hr sonication): 8.24 (s, 2H), 7.72 – 7.65 (m, 4H), 7.58 (d, *J* = 8.4 Hz, 2H), 7.21 (d, *J* = 8.3 Hz, 2H), 7.11 (d, *J* = 8.2 Hz, 4H), 7.03 (s, 2H), 3.19 (d, J = 6.5 Hz, 1H), 2.78 – 2.69 (m, 1H), 2.45 (dt, J = 11.5, 6.5 Hz, 1H), 1.83 (d, J = 8.1 Hz, 1H), 1.48 – 1.41 (m, 3H). Phase purity confirmed by XRPD with a comparison to NUS-8-Hf found in CCDC (1567189).

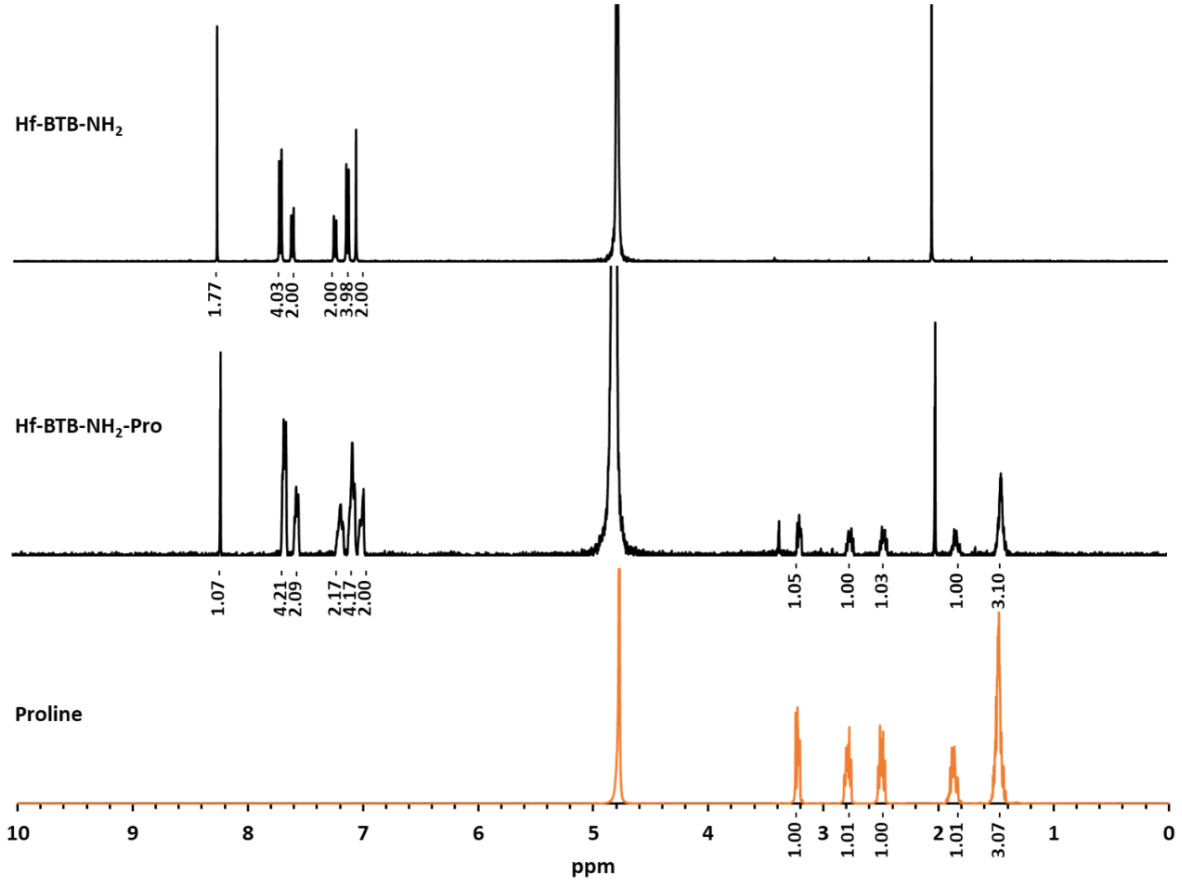

Figure 5.33: ^{1}H NMR data for synthesised Hf-BTB-NH_2, synthesised Hf-BTB-NH_2-Pro, and proline.

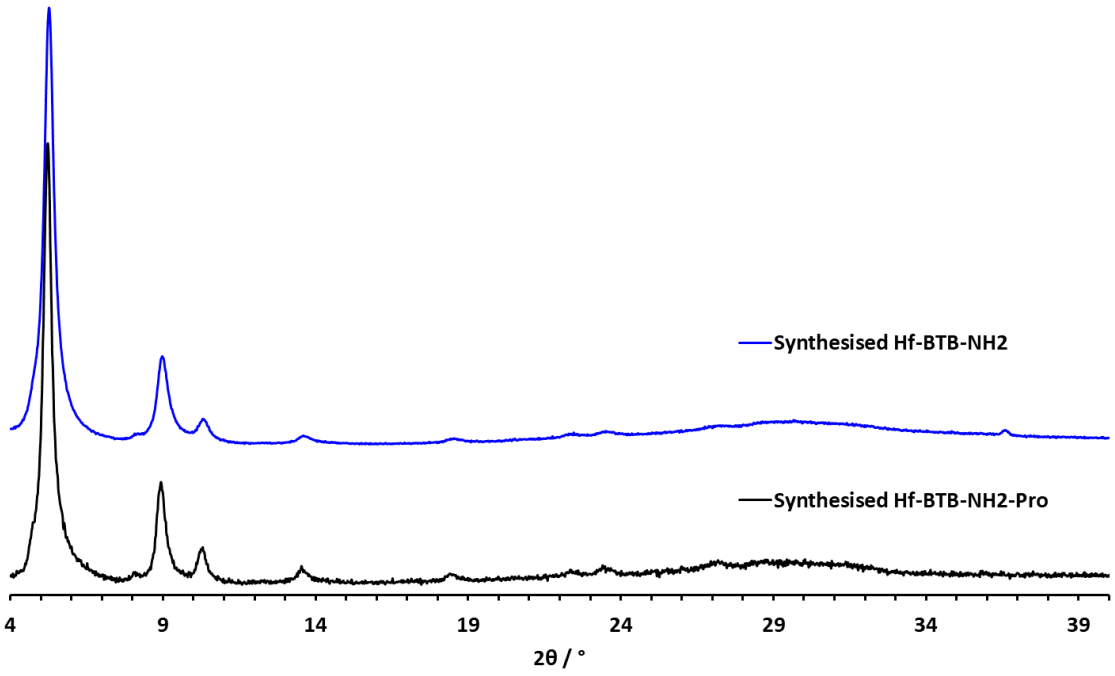

Figure 5.34: Comparison of XRPD pattern of synthesised Hf-BTB-NH_2 and synthesised Hf-BTB-NH_2-Pro

5.5.7 Synthesis and exfoliation of Hf-BTB-NH_2-Ser

Six equivalents of serine (0.0756 mmol, 7.9 mg) was added to Hf-BTB-NH_2 (0.0126 mmol, 15 mg) in DMF (3 mL) and was left stirring overnight. After three DMF (10 mL) washes (one left overnight) and three ethanol (10 mL) washes (last one left over the weekend) the resulting material was collect via centrifugation and dried 120 °C overnight. ^{1}H NMR (NaOD/D_2O, 24 hr sonication): 8.24 (s, 2H), 7.72 – 7.65 (m, 4H), 7.58 (d, *J* = 8.4 Hz, 2H), 7.21 (d, *J* = 8.3 Hz, 2H), 7.11 (d, *J* = 8.2 Hz, 4H), 7.03 (s, 2H), 3.53 (dd, J = 11.1, 4.1 Hz, 7H), 3.39 (dd, J = 11.1, 6.4 Hz, 7H), 3.09 (dd, J = 6.4, 4.1 Hz, 7H). Phase purity confirmed by XRPD with a comparison to NUS-8-Hf found in CCDC (1567189).

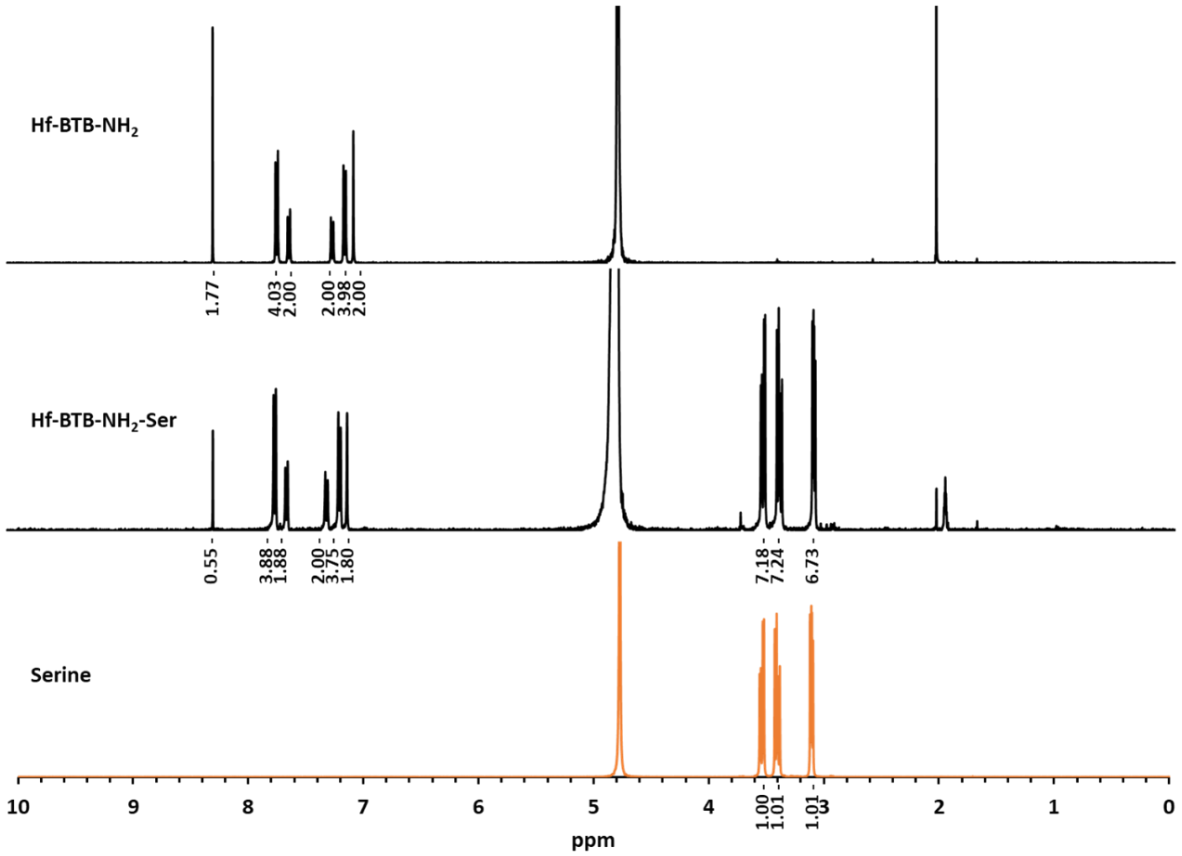

Figure 5.35: ^{1}H NMR data for synthesised Hf-BTB-NH_2, synthesised Hf-BTB-NH_2-Ser, and serine.

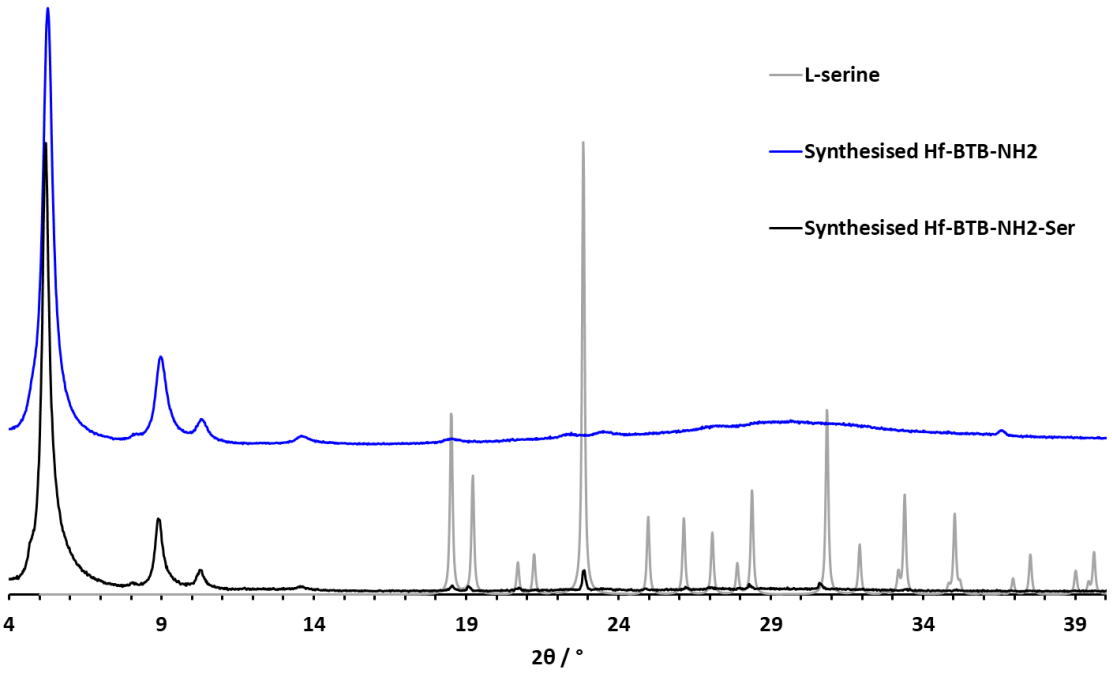

Figure 5.36: Comparison of XRPD pattern of synthesised Hf-BTB-NH_2, synthesised Hf-BTB-NH_2-Ser and L-serine (CCDC- 889401)

5.5.8 Synthesis and exfoliation of Hf-BTB-NH_2-Thr

Six equivalents of threonine (0.0756 mmol, 9.0 mg) was added to Hf-BTB-NH_2 (0.0126 mmol, 15 mg) in DMF (3 mL) and was left stirring overnight. After three DMF (10 mL) washes (one left overnight) and three ethanol (10 mL) washes (last one left over the weekend) the resulting material was collect via centrifugation and dried 120 °C overnight. ^{1}H NMR (NaOD/D_2O, 24 hr sonication): 8.24 (s, 2H), 7.72 – 7.65 (m, 4H), 7.58 (d, *J* = 8.4 Hz, 2H), 7.21 (d, *J* = 8.3 Hz, 2H), 7.11 (d, *J* = 8.2 Hz, 4H), 7.03 (s, 2H 3.68 (qd, J = 6.4, 5.2 Hz, 7H), 2.84 (d, J = 5.2 Hz, 7H), 0.96 (d, J = 6.5 Hz, 21H). Phase purity confirmed by XRPD with a comparison to NUS-8-Hf found in CCDC (1567189).

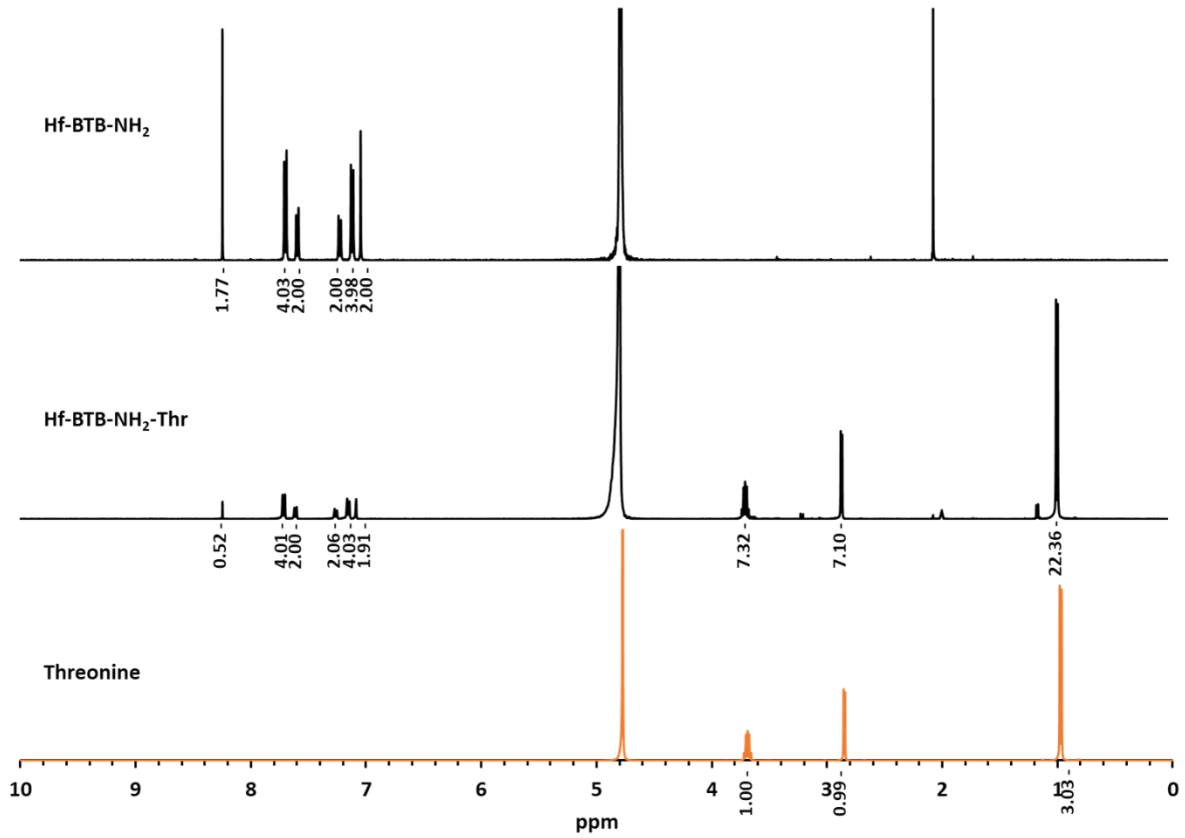

Figure 5.37: ^{1}H NMR data for synthesised Hf-BTB-NH_2, synthesised Hf-BTB-NH_2-Thr, and threonine.

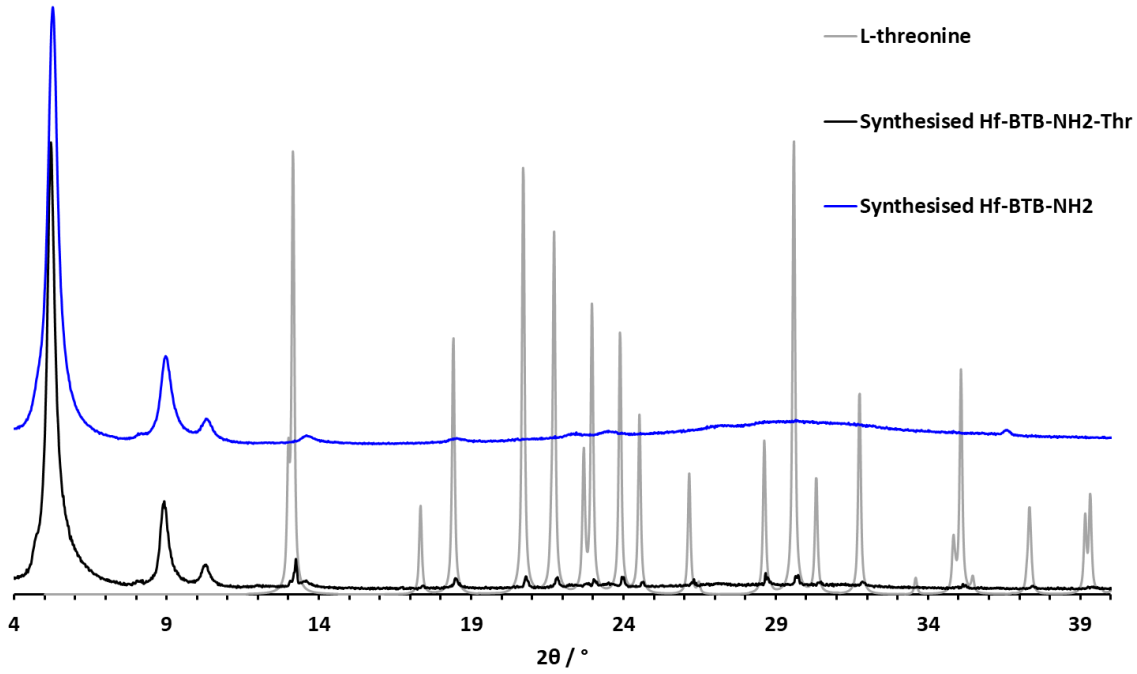

Figure 5.38: Comparison of XRPD pattern of synthesised Hf-BTB-NH_2, synthesised Hf-BTB-NH_2-Thr and L-threonine (CCDC - 2072836)

5.5.9 Synthesis and exfoliation of Hf-BTB-NH_2-Val

Six equivalents of valine (0.0756 mmol, 13.2 mg) was added to Hf-BTB-NH_2 (0.0126 mmol, 15 mg) in DMF (3 mL) and was left stirring overnight. After three DMF (10 mL) washes (one left overnight) and three ethanol (10 mL) washes (last one left over the weekend) the resulting material was collect via centrifugation and dried 120 °C overnight. ^{1}H NMR (NaOD/D_2O, 24 hr sonication): 8.24 (s, 1H), 7.72 (d, J = 8.3 Hz, 4H), 7.63 (d, J = 8.5 Hz, 2H), 7.31 (d, *J* = 8.3 Hz, 2H), 7.19 (d, *J* = 8.2 Hz, 4H), 7.14 (s, 2H), 2.81 (d, *J* = 5.3 Hz, 6H), 1.75 – 1.58 (m, 6H), 0.70 (d, *J* = 6.9 Hz, 18H), 0.63 (d, *J* = 6.9 Hz, 18H). Phase purity confirmed by XRPD with a comparison to NUS-8-Hf found in CCDC (1567189).

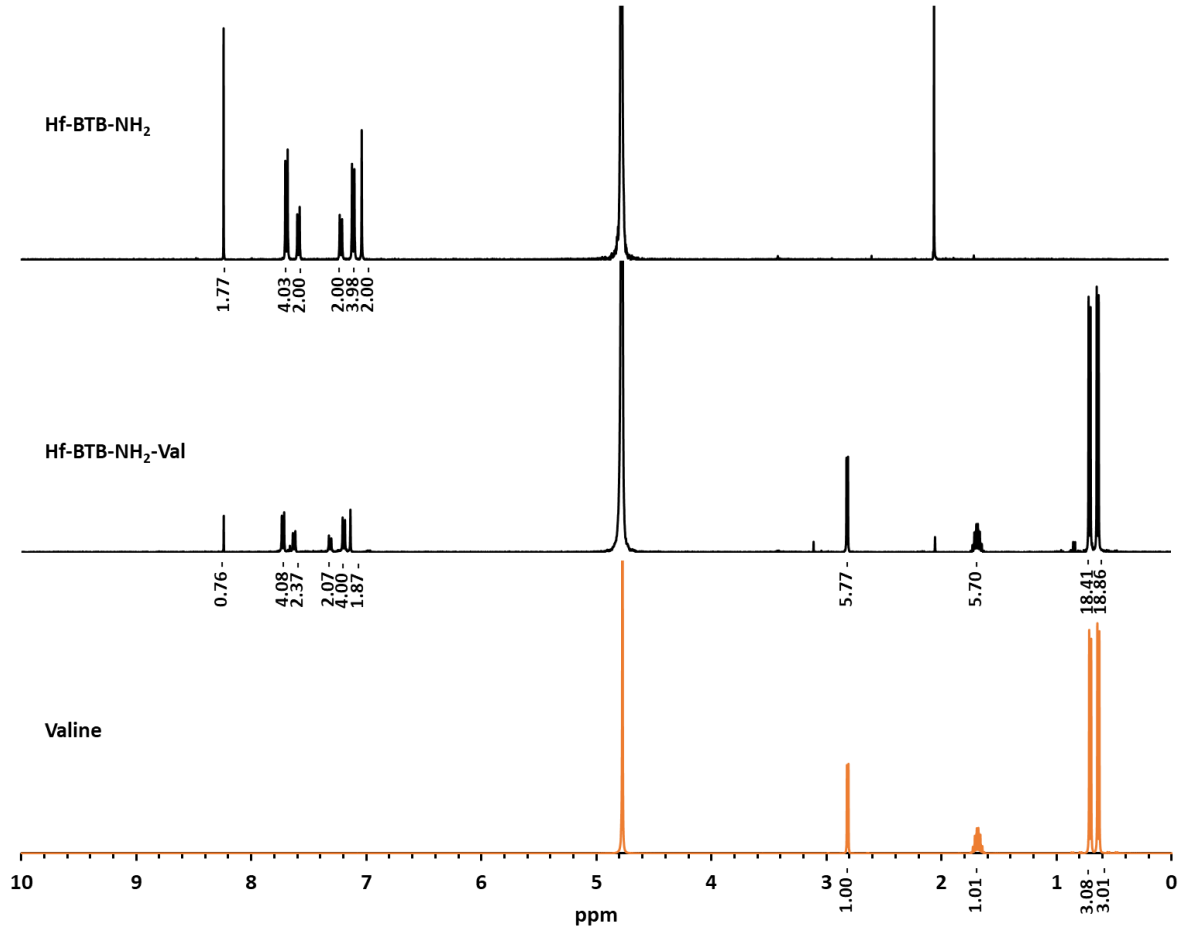

Figure 5.39: ^{1}H NMR data for synthesised Hf-BTB-NH_2, synthesised Hf-BTB-NH_2-Val, and valine.

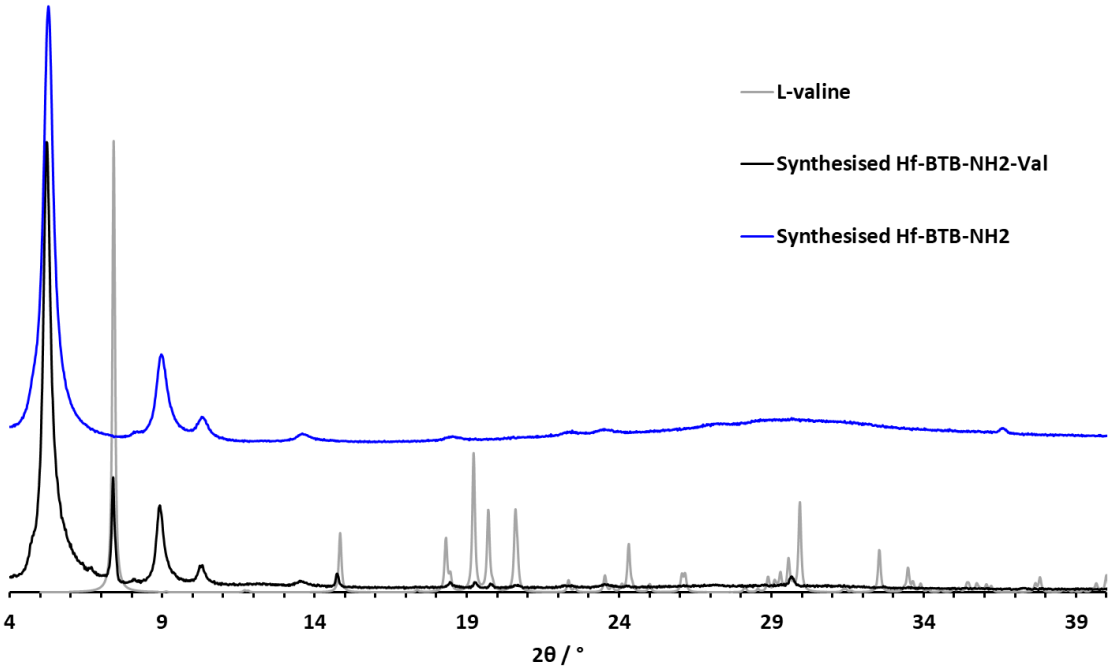

Figure 5.40: Comparison of XRPD pattern of synthesised Hf-BTB-NH_2, synthesised Hf-BTB-NH_2-Val and L-valine (CCDC - 1208818)

5.5.10 PBS Stability Test

Hf-BTB-NH_2-AA MON (5 mg) was suspended in PBS solution (5 mL) and left stirring for 24 hr. The resulting material was collected (4,500 rpm, 30 mins) and washed with water (10 ml, 4,500 rpm, 30 mins). Phase purity confirmed by XRPD with a comparison to NUS-8-Hf found in CCDC (1567189).

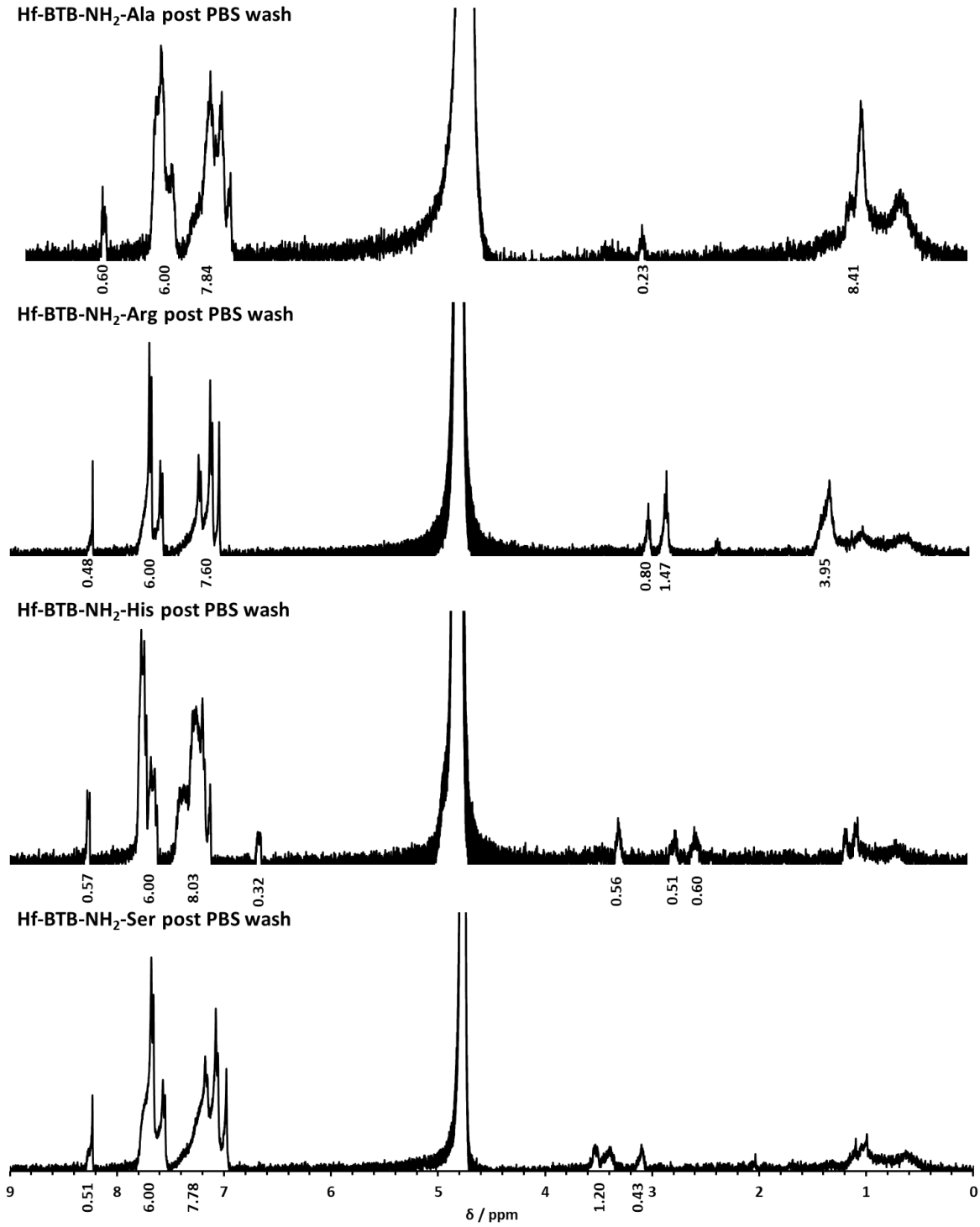

Figure 5.41: ^{1}H NMR spectra of Hf-BTB-NH_2-AA after incubation in PBS for 24 hr.

5.5.11 Synthesis of Hf-BTB-NH_2-Asp - Water Wash

Six equivalents of arginine (0.0756 mmol, 13.2 mg) was added to Hf-BTB-NH_2 (0.0126 mmol, 15 mg) in DMF (3 mL) and was left stirring overnight. After three DMF (10 mL) washes (one left overnight), three DI water (10 mL) washes (one left overnight), and three ethanol washes (last one left over the weekend) the resulting material was collect via centrifugation and dried 120 °C overnight. ^{1}H NMR (NaOD/D_2O, 24 hr sonication): 8.24 (s, 2H), 7.72 – 7.65 (m, 4H), 7.58 (d, *J* = 8.4 Hz, 2H), 7.21 (d, *J* = 8.3 Hz, 2H), 7.11 (d, *J* = 8.2 Hz, 4H), 7.03 (s, 2H), 3.32 (dd, J = 9.8, 3.9 Hz, 1.5H), 2.41 (dd, J = 15.3, 4.0 Hz, 1.6 H), 2.07 (dd, J = 15.3, 9.7 Hz, 1.9 H). Phase purity confirmed by XRPD with a comparison to NUS-8-Hf found in CCDC (1567189).

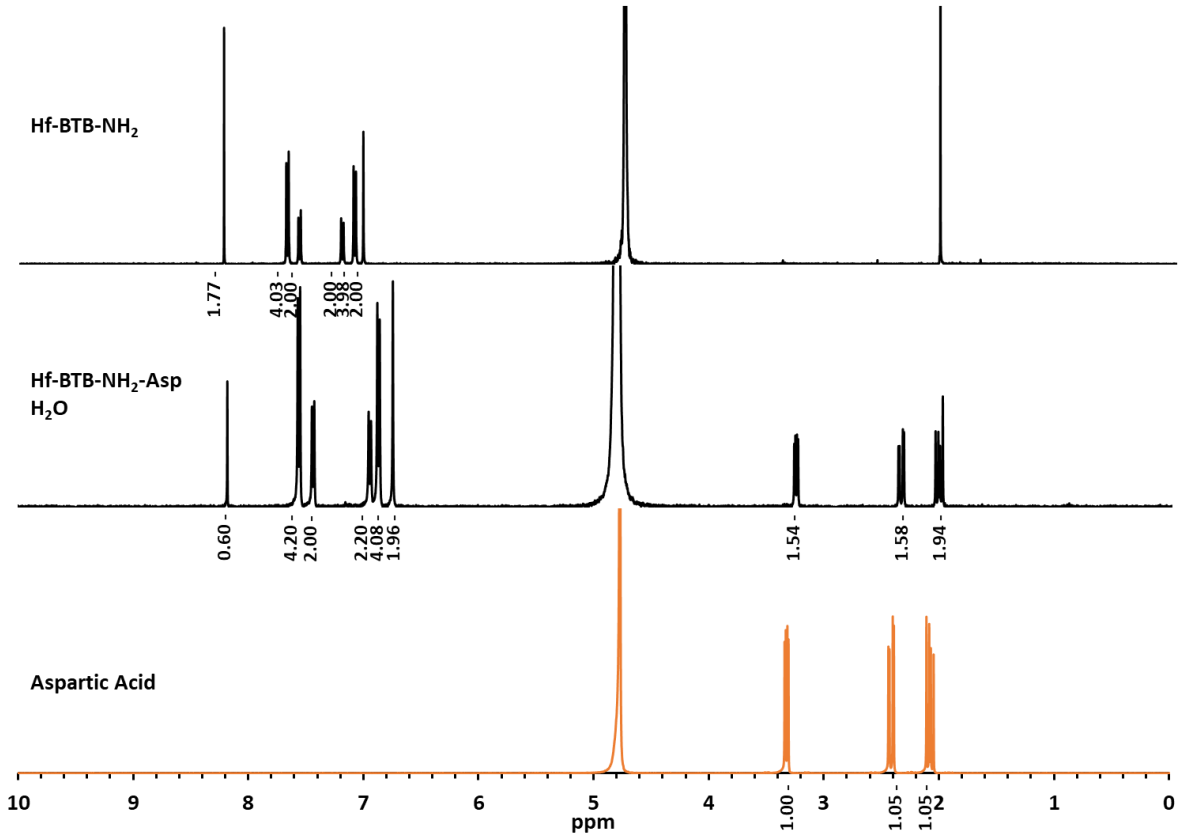

Figure 5.42: ^{1}H NMR data for synthesised Hf-BTB-NH_2, synthesised Hf-BTB-NH_2-Asp (water wash), and aspartic acid.

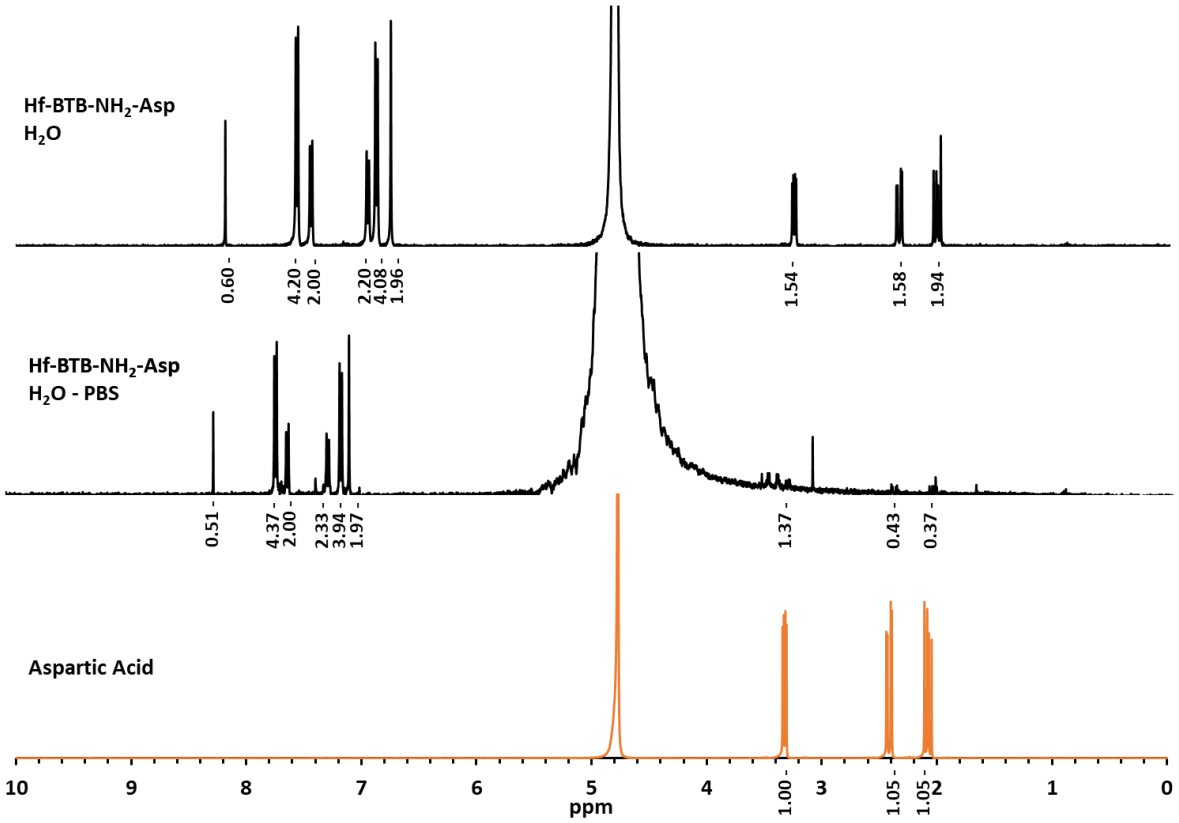

Figure 5.43: ^{1}H NMR data for synthesised Hf-BTB-NH_2-Asp (water wash) before and after PBS incubation for 24 h, and aspartic acid.

5.5.12 Synthesis of Hf-BTB-NH_2-Val - Water Wash

Six equivalents of valine (0.0756 mmol, 13.2 mg) was added to Hf-BTB-NH_2 (0.0126 mmol, 15 mg) in DMF (3 mL) and was left stirring overnight. After three DMF (10 mL) washes (one left overnight), three DI water (10 mL) washes (one left overnight), and three ethanol (10 mL) washes (last one left over the weekend) the resulting material was collect via centrifugation and dried 120 °C overnight. ^{1}H NMR (NaOD/D_2O, 24 hr sonication): 8.24 (s, 1H), 7.72 (d, J = 8.3 Hz, 4H), 7.63 (d, J = 8.5 Hz, 2H), 7.31 (d, *J* = 8.3 Hz, 2H), 7.19 (d, *J* = 8.2 Hz, 4H), 7.14 (s, 2H), 2.81 (d, *J* = 5.3 Hz, 0.34H), 1.75 – 1.58 (m, 0.37H), 0.70 (d, *J* = 6.9 Hz, 1.2H), 0.63 (d, *J* = 6.9 Hz, 1.1H). Phase purity confirmed by XRPD with a comparison to NUS-8-Hf found in CCDC (1567189).

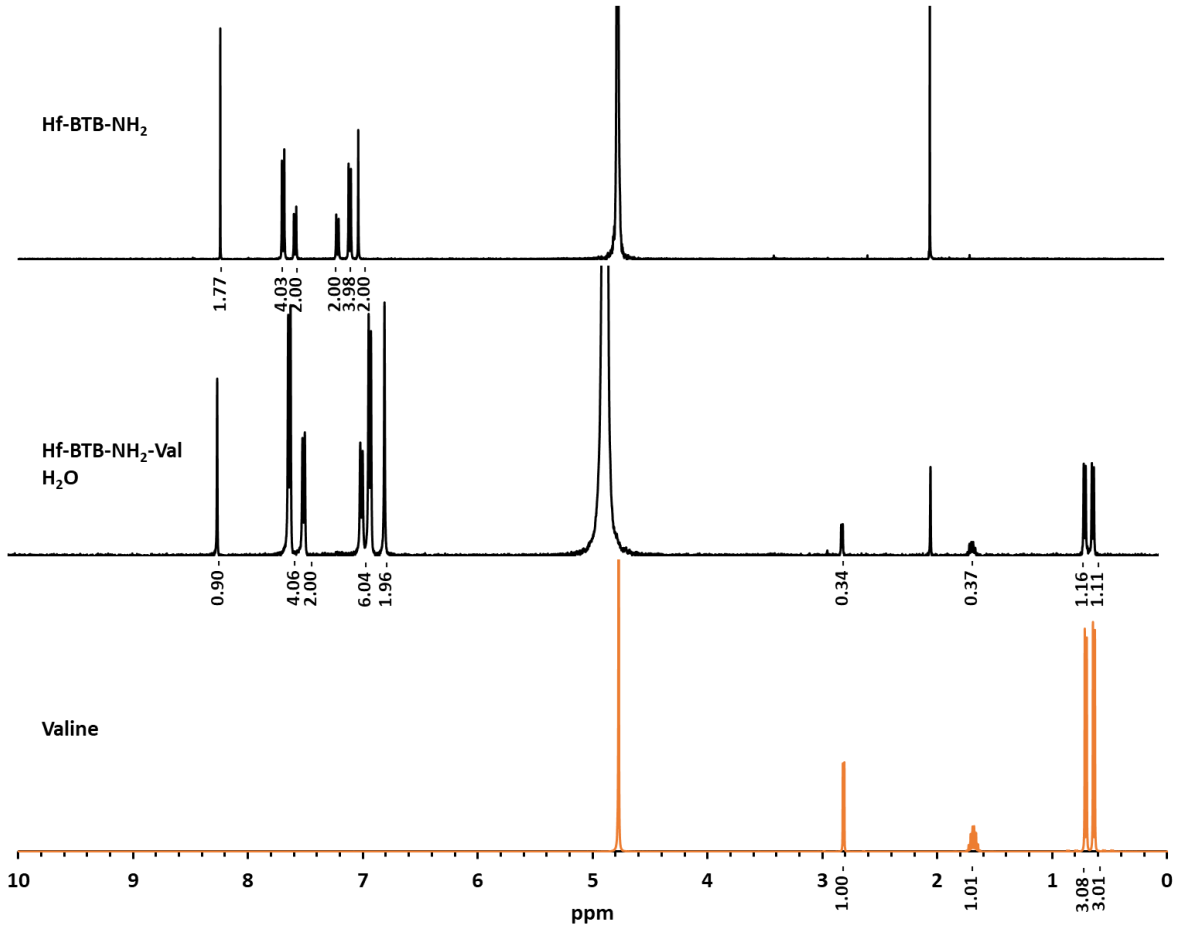

Figure 5.44: ^{1}H NMR data for synthesised Hf-BTB-NH_2, synthesised Hf-BTB-NH_2-Val (water wash), and valine.

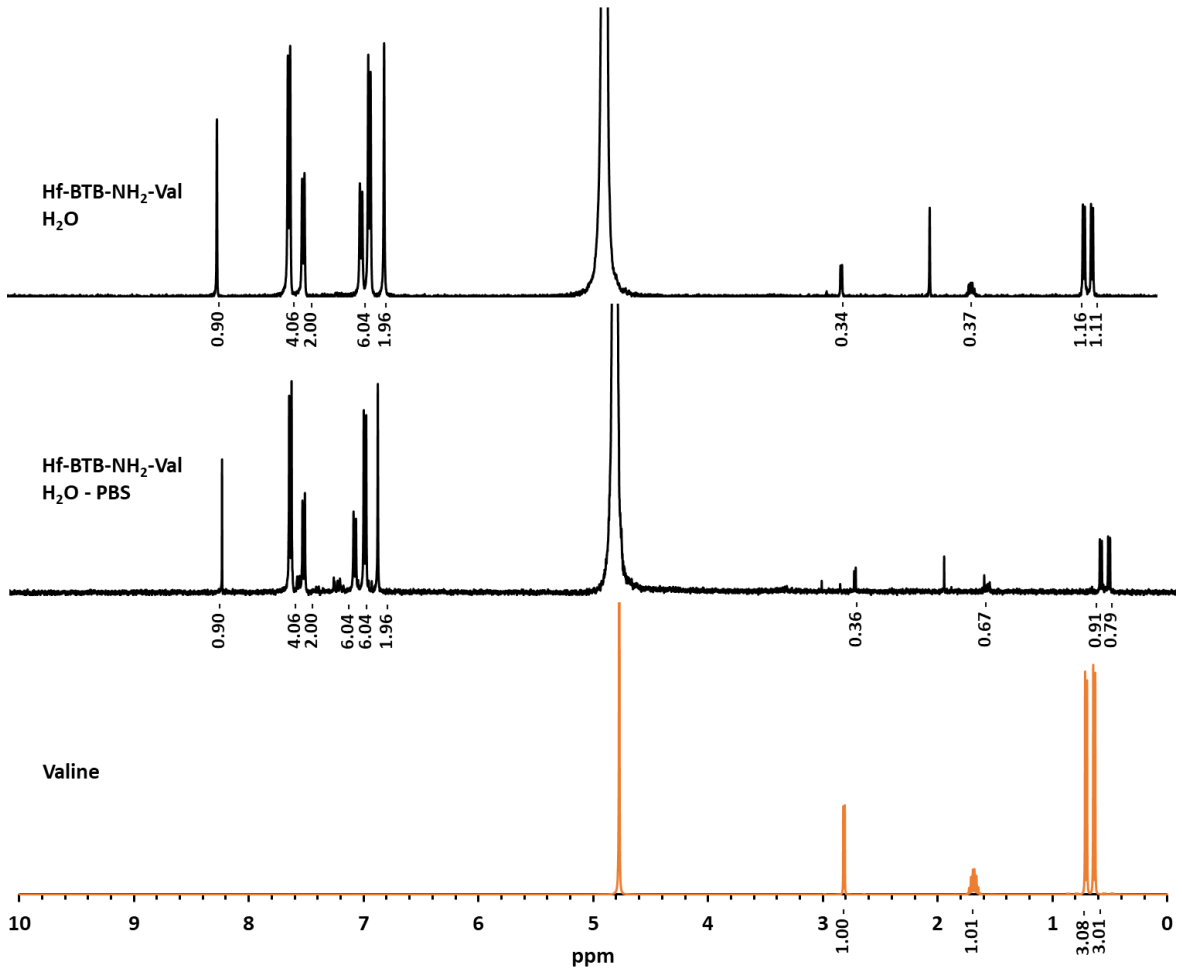

Figure 5.45: ^{1}H NMR data for synthesised Hf-BTB-NH_2-Val (water wash) before and after PBS incubation for 24 h and valine.

5.6 References

1 Z. Hu, E. M. Mahdi, Y. Peng, Y. Qian, B. Zhang, N. Yan, D. Yuan, J. C. Tan and D. Zhao, *J. Mater. Chem. A*, 2017, **5**, 8954–8963.

2 G. Lan, Y. Fan, W. Shi, E. You, S. S. Veroneau and W. Lin, *Nat. Catal.*, 2022, **5**, 1006–1018.

3 R. J. Marshall, C. L. Hobday, C. F. Murphie, S. L. Griffin, C. A. Morrison, S. A. Moggach and R. S. Forgan, *J. Mater. Chem. A*, 2016, **4**, 6955–6963.

4 X. Ling, D. Gong, W. Shi, Z. Xu, W. Han, G. Lan, Y. Li, W. Qin and W. Lin, *J. Am. Chem. Soc.*, 2021, **143**, 1284–1289.

5 G. Lan, K. Ni, R. Xu, K. Lu, Z. Lin, C. Chan and W. Lin, *Angew. Chemie*, 2017, **129**, 12270–12274.

6 M. Taddei, R. J. Wakeham, A. Koutsianos, E. Andreoli and A. R. Barron, *Angew. Chemie - Int. Ed.*, 2018, **57**, 11706–11710.

7 M. K. Sangeetha, M. Mariappan, G. Madhurambal and S. C. Mojumdar, *J. Therm. Anal. Calorim.*, 2015, **119**, 907–913.

8 M. R. S. Kumar, H. J. Ravindra, A. Jayarama and S. M. Dharmaprakash, *J. Cryst. Growth*, 2006, **286**, 451–456.

9 C. B. Ching, K. Hidajat and M. S. Uddin, *Sep. Sci. Technol.*, 1989, **24**, 581–597.

10 S. Wang, M. Wahiduzzaman, L. Davis, A. Tissot, W. Shepard, J. Marrot, C. Martineau-Corcos, D. Hamdane, G. Maurin, S. Devautour-Vinot and C. Serre, *Nat. Commun.*, 2018, **9**, 4937.

11 P. Horcajada, T. Chalati, C. Serre, B. Gillet, C. Sebrie, T. Baati, J. F. Eubank, D. Heurtaux, P. Clayette, C. Kreuz, J. S. Chang, Y. K. Hwang, V. Marsaud, P. N. Bories, L. Cynober, S. Gil, G. Férey, P. Couvreur and R. Gref, *Nat. Mater.*, 2010, **9**, 172–178.

12 Y. Yang, G. B. Hu, W. Bin Liang, L. Y. Yao, W. Huang, R. Yuan and D. R. Xiao, *Nanoscale*, 2019, **11**, 10056–10063.

13 W. Shi, L. Cao, H. Zhang, X. Zhou, B. An, Z. Lin, R. Dai, J. Li, C. Wang and W. Lin, *Angew. Chemie - Int. Ed.*, 2017, **56**, 9704–9709.

Chapter 6: Conclusions

6.1 Summary

Since 2015 there has been growing interest in the use of MONs in biosensing. From optical to electrochemical based sensor set ups, MONs have been utilised for their unique surface chemistries and two dimensional nature. However, the exploitation of the periodic array of binding sites presented by MONs, namely unsaturated metal clusters and functionalisable organic linkers, has not been thoroughly investigated.

This chapter reflects on the progress made towards the interrogation of MONs for application as biomolecular recognition components and explores the opportunities and potential barriers associated with the development of this work. Discussing first the design, synthesis, and characterisation of the library of MONs presented. The chapter will then go on to discuss the insights gained into the use of MONs in biomolecular recognition including the use of biopanning for the identification of high affinity binding peptides.

6.2 Design, Synthesis, and Characterisation of MONs

The ability to predictably control surface chemistry in order to fine-tune properties for a given application is an attractive prospect. Across the thesis a number of approaches to introduce different functional groups onto the surface of the MONs were therefore investigated, each with their own advantages and disadvantages. In chapter 2, ligands with different functional groups were added to the reaction mixture in a pre-synthetic functionalisation approach. Six different ZIF MON systems were synthesised and characterised with four of those never before reported. Here the advantage is that successful functionalisation is easily characterised by digesting the MONs and analysing the linker. In some cases, 100 % functionalisation was achieved (bim-Br), but in other cases lower degrees of functionalisation (bim-NH_2 and bim-CH_3) were achieved which was attributed to decreased basicity of the imidazolate linker. A mixed linker approach to include functionalised linkers that are less reactive in MOF formation should be taken when designing MONs to have specific surface chemistries.

In later chapters the nanosheets were first synthesised then either covalently (chapter 4) or datively (chapter 5) functionalised. Covalent PSF of the ZIF systems demonstrated that functionalisation with amino acids and maleic anhydride is possible but does require optimisation of reaction conditions depending on the MON system and incoming substituent. For PSF with amino acids the microwave assisted synthesis is the most promising approach but a maximum of 19 % of total linkers were functionalised. A reaction time of two weeks was required for MON-NH_2 functionalisation with maleic anhydride where 53-65 % functionalisation was achieved. Functionalisation of the MONs rather than the bulk layered MOF, facilitated the highest degrees of

covalent attachment. Coordinative amino acid PSF of Hf-BTB-NH_2 was limited by perceived high degrees of functionalisation in chapter 5. General trends of increasing pKa of the residue carboxylate showed decreased functionalisation. Further water washing steps proved useful in the removal of excess Val and Asp and therefore it is advised to be carried forward in the synthesis of Hf-BTB-NH_2-AA systems. Optimisation through pre-treating the MON with HCl or heat to displace formate groups and increasing the reaction temperature could see improved yields.

Overall, the pre-synthetic incorporation of bim analogues proved to be the most well defined method of functionalisation however there are limitations to the size of functional group available to be introduced by this approach. In general, the post-synthetic functionalisation procedures faced issues of excess adsorbed residue which made determining the true degree of functionalisation difficult. The exchange of modulating agent for the Hf-BTB-NH_2 system was the most promising form of amino acid PSF where there was evidence of stability after PBS incubation and the opportunity for higher degrees of functionalisation (6 amino acids per cluster).

Having introduced different functional groups onto the surface of MONs by these different methods, developing different approaches to characterise the resulting properties of the nanosheets was a key theme throughout this thesis. Surface charge is one key property which was investigated using Zeta potential analysis and the MON surface charge was found to range from -36 mV (Hf-BTB-NH_2) to 14.8 mV (Hf-BTB-NH_2-Asp). Introducing charged amino acids had the greatest effect on MON surface charge, especially aspartic acid where both carboxylates can coordinate to metal clusters. Covalent PSF with maleic anhydride was shown to reduce the zeta potential of the amino-functionalised ZIF systems, this could reduce the surface charge of Hf-BTB-NH_2 further. The pre-synthetic functionalisation of the ZIF systems accessed a range from -30.1 mV (ZIF-7) to 2.3 mV (ZIF-7-NH_2). Blending linkers with subtle and dramatic effect on surface charge could allow an excellent degree of control over the average surface charge.

The second general property of the nanosheets investigated is their hydrophobicity which was studied throughout the thesis using contact angle measurements. A direct comparison can be made between the different ZIF analogues synthesised. Contact angles ranged between 94.5 ° for the most polar ZIF-9-NH_2 system to 161.3 ° for the more hydrophobic ZIF-7-Br. Switching zinc for cobalt had no effect on hydrophobicity with both having an intermediary value of ~ 140 °. The Hf-BTB-NH_2 system was significantly more polar at 24.8 °. Coordination PSF provides a good opportunity to systematically modify the hydrophobicity of the nanosheets, with residues such as aspartic acid producing more polar nanosheets whilst proline could create more hydrophobic systems.

The methods developed within this thesis to introduce different functional groups and measure their surface properties have applications in a variety of fields from drug delivery and bioimaging,[1–3] where such properties control cell uptake to catalysis where synergistic active sites facilitate tandem catalysis.[4–6] The new, ultrathin, water stable MONs developed within this thesis have already been explored by other members of the group for applications including water-purification, corrosion inhibition, phosphate sensing and polymer grafting.

6.3 Applicability of MONs as Biomolecular Recognition Components

Evaluating the potential of MONs for biorecognition was a key theme across the thesis and one of the first considerations investigated was their stability in biologically relevant conditions. The biostability of the library of MON systems was evaluated through incubation in PBS (1 mg / mL, 24 h). Hf-BTB-NH_2 MONs showed the greatest stability where there was no significant changes to the XRPD pattern observed (chapter 3), making it able to withstand potential disruption from phosphates.[7] ZIF-7-Br and ZIF-7-CH_3 also showed no changes to the XRPD pattern but there was the appearance of new peaks observed for the other ZIF systems indicating the formation different crystalline material. Beyond their stability in suspension, the stability of the nanosheets on the surface of the QCM sensors is another key consideration. The high hydrophobic character of ZIF-7 and ZIF-7-NH_2 made QCM preparation difficult therefore it is predicted to be an issue for ZIF-7-Br and ZIF-7-CH_3 as their surfaces were more hydrophobic. Hf-BTB-NH_2-AA systems saw a reduction in residue functionalisation after incubation with PBS therefore further optimisation of reactions and washing steps are required to ensure stability within a QCM sensor set up.

Previous examples of MON-based biosensors involve complex detection pathways where the MON acts as a nanozyme to H_2O_2 or quenches the fluorescent bioreceptors for “signal-on” detection. In this work, the periodic array of binding sites presented by MONs, particularly unsaturated metal clusters and functionalised organic linkers, were exploited for binding. This thesis presents the interrogation of the affinity between peptide sequences and different physiologically stable MONs via the high throughput screening technique phage display. The investigation revealed that ZIF-7 MONs with negative surface charge and hydrophobic character attracted a peptide sequence with majority aromatic and hydrophobic residues. Arginine was also present which could be involved in electrostatic interactions. ZIF-7-NH_2 MONs with neutral surface charge and hydrophobic character had affinity for a peptide that again contained largely hydrophobic and aromatic residues with hydrophobic interactions thought to drive selectivity. Hf-BTB-NH_2 MONs with negative surface charge and hydrophilic character had affinity for a peptide with a greater range of residues resulting in a more polar peptide. Electrostatic interactions play a role through arginine and there was opportunity for

side chain coordination of aspartic acid to the Hf_6 metal cluster. An interaction not available to the ZIF systems. It was clear the 20 % amine functionality of ZIF-7-NH_2 offered a distinctly different surface to that of ZIF-7 where a different high affinity binding peptide was identified. A consensus binding sequence was accessed for a MON with a non-periodic array of functional groups, indicating a blend of linkers is a viable approach to take for MON-based biosensor design. The binding peptides don't just contain all basic residues when the surface is negative, or all hydrophobic residues when the surface is hydrophobic. Multiple interactions are possible, and the aqueous binding environment is thought to require peptides to contain some polar residues for stability. The different surfaces offer different binding modes, even the ZIFs where the metal node is packed within a dense system. When predicting peptide binding sequences for other MON systems it is important to consider the type interactions that will drive selectivity: 1) electrostatic interactions, 2) hydrophobic interactions, 3) specific R-group interactions.

Based on the work presented in chapter 3, we hypothesise that the negatively charged ZIF-7-CH_3, ZIF-9, and ZIF-9-NH_2 and Hf-BTB-NH_2-AA MONs would also have affinity for basic residues such as arginine. The range in hydrophobic character of the MONs would then inform the composition of remaining residues with the hydrophobic and aromatic residues likely to feature more for the ZIF systems. Phage display was attempted with ZIF-9 and ZIF-9-NH_2 but there were issues with wild phage infections preventing further studies. Due to the similarity of the measured surface properties of ZIF-7 and ZIF-9 it is predicted that the consensus binding peptide would contain similar residues. However, ZIF-9-NH_2 showed a significant increase in hydrophilic character even with reduced bim-NH_2 loading compared to the ZIF-7-NH_2 system therefore the binding peptide in this instance is predicted to be more polar and contain a larger variety of residues.

As mentioned, the peptide sequence for Hf-BTB-NH_2 contained aspartic acid where the carboxylate side chain is capable of coordinating to the Hf_6-clusters. The coordinative functionalisation of the MON surface with different amino acids produced material with a range in surface properties. Hf-BTB-NH_2-Val showed minimal change in surface properties compared to Hf-BTB-NH_2 therefore a similar binding peptide would be expected but the coordinated valine could disrupt metal centre coordination of acidic residues. Hf-BTB-NH_2-Asp offers a neutral/positive surface charge with an increase in hydrophilic character. This system would be the most interesting to undergo phage display as long as functionalisation remained stable due to its unique surface properties compared to the systems previously investigated. It is likely polar and acidic residues will appear within the binding peptide. Confirmation of this would allow a broader degree of predictability over the sequences of amino acids that different MONs have affinity to.

6.4 Outlook

Overall, it is clear the complex nature of MON composition facilitates specific recognition on the molecular scale. Biopanning can be used to identify peptides that bind to MON surfaces with high affinity. Different MON surfaces interact differently with different peptide sequences, even those with similar chemical components. The peptide sequences contained a multitude of residues indicating that multiple interactions with the MON and aqueous environment are responsible for the selectivity observed. A diverse range of water stable MONs can be synthesised, and their surfaces functionalised with a wide range of different groups. Such functional groups affect surface properties in subtle and extreme ways, with mixed linker systems giving access to tunable surfaces. MONs therefore have significant potential to be used as biosensing components with predictable, controllable surface chemistry, which can be fine-tuned for specific biomolecular recognition.

6.5 References

1 Y. Zhang and J. Wang, *Inorganica Chim. Acta*, 2018, **477**, 8–14.

2 W. Xie, F. Zhou, X. Li, Z. Liu, M. Zhang, Z. Zong and L. Liang, *Arab. J. Chem.*, 2022, **15**, 103672.

3 S. Arun Kumar, B. Balasubramaniam, S. Bhunia, M. K. Jaiswal, K. Verma, Prateek, A. Khademhosseini, R. K. Gupta and A. K. Gaharwar, *WIREs Nanomedicine and Nanobiotechnology*, 2021, **13**, e1674.

4 Y. Quan, G. Lan, Y. Fan, W. Shi, E. You and W. Lin, *J. Am. Chem. Soc.*, 2020, **142**, 1746–1751.

5 J. Nicks, J. Zhang and J. A. Foster, *Chem. Commun.*, 2019, **55**, 8788–8791.

6 Y. Quan, G. Lan, W. Shi, Z. Xu, Y. Fan, E. You, X. Jiang, C. Wang and W. Lin, *Angew. Chemie - Int. Ed.*, 2021, **60**, 3115–3120.

7 Y. Liu, Y. Zhao and X. Chen, *Theranostics*, 2019, 9, 3122–3133.